27
10-20-82
JMB

J-5985 (1)

Dr. 923

Mirror Fusion

UCID-19359

MASTER

Physics Basis for an Axicell Design for the End Plugs of MFTF-B

Editors:

D. E. Baldwin

B. G. Logan

April 21, 1982

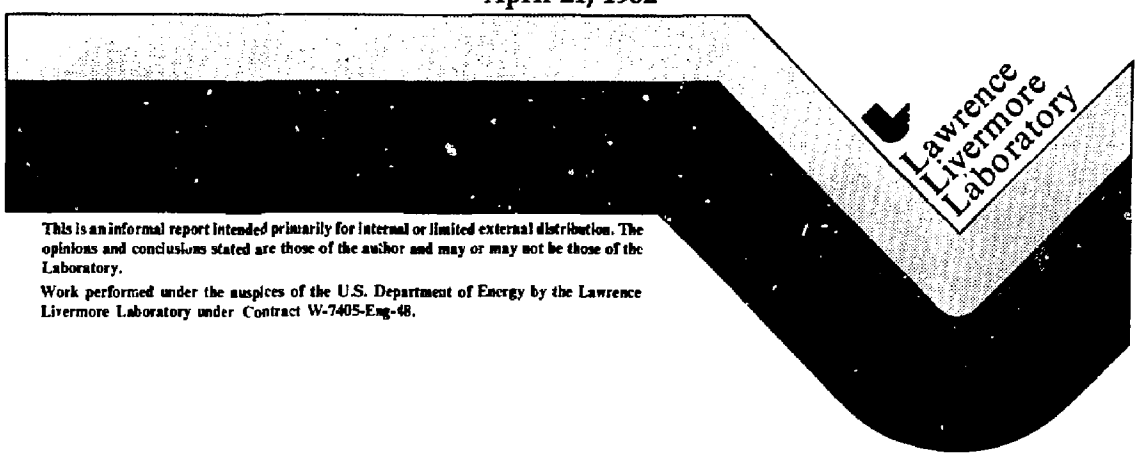

UCID--19359

DE83 001161

UCID-19359

PHYSICS BASIS FOR AN AXICELL DESIGN FOR THE END PLUGS OF MFTF-B

D. E. Baldwin and B. G. Logan

Editors

April 21, 1982

PHYSICS BASIS FOR AN AXICELL DESIGN FOR THE END PLUGS OF MFTF-B

CONTENTS

List of Figures iii
List of Tables vii
1. Introduction and Physics Summary 1
1.1. Physics Overview 1
1.2. Central-Cell Confinement 5
1.3. Magnetohydrodynamic (MHD) Equilibrium 5
1.4. Low-Frequency Stability - MHD 6
1.5. Low-Frequency Stability - Electrostatic 9
1.6. Microstability 11
References 14
2. Scenarios for MFTF-B Axicell Operation 17
2.1. Introduction and Summary 17
References 23
2.2. Axicell Reference-Case Operation (MARS Mode) 27
2.2.1. Description of Reference-Case MARS Mode 27
2.2.2. Suitability of Reference Case for Reactor Operation 28
2.2.3. Operating Scenario for MARS Mode at Steady State 37
2.2.4. Start-Up Scenario for the MARS Mode 53
References 60
2.3. Alternate Operating Modes 63
2.3.1. Kelley TDF-like Mode 63
2.3.2. TMX-U-like Mode 69
2.3.3. TARA-like Mode 72
References 75
2.4. Physics Models for Calculations of Parameters 79
2.4.1. Central-Cell Parameters 79
2.4.2. Axicell Parameters 79
2.4.3. Barrier Parameters 82
2.4.4. Warm-Electron and Confining-Potential Parameters 84
2.4.5. Anchor-Cell Beam Requirements 88
2.4.6. Microwave Power Requirements 92

2.4.7. Central-Cell Ion-Particle and Energy Balance 93
2.4.8. Central-Cell Electron-Particle and Energy Balance 96
References 98

Appendices
A. Analytic Equilibria with Quadrupole Symmetry in the Paraxial Limit 103
B. Gyrokinetic Magnetohydrodynamics (MHD) 115
C. Some Effects of Hot-Electron Stability in Tandem-Mirror Geometry 139
D. Electrostatic Ballooning Modes 147
E. Sloshing Ions in the MFTF-B Anchor 163
F. Ion Microstability 181
G. Electron Microstability 195
H. Radial Transport 207
I. Barrier Potential Model 219

LIST OF FIGURES

1-1. Comparison of A-cell and axicell designs for MFTF-B. 2
1-2. Field, density, and potential profiles for the MARS-mode reference case of the MFTF-B Axicell design. 3
2.1-1. Magnet set for MFTF-B Axicell. 18
2.1-2. Thermal-barrier MARS-mode reference case for MFTF-B Axicell. 20
2.1-3. Improved MARS axicell reactor. 21
2.2-1. A-cell Tandem-Mirror Reactor (TMR). 31
2.2-2. Axicell TMR. 32
2.2-3. Modified cusp TMR. 33
2.2-4. Typical central-cell particle balance for MARS mode of MFTF-B. 41
2.2-5. Typical central-cell ion-energy balance for MARS mode of MFTF-B. 42
2.2-6. Typical central-cell electron-energy balance for MARS mode of MFTF-B. 43
2.2-7. Comparison of passing ions and electrons in MFTF-B yin-yang anchor. 46
2.2-8. Variation of overall Q and of ion fraction passing into the yin-yang anchor as a function of axicell- and pump-beam power. 50
2.2-9. MARS-mode (vacuum) flute interchange. 52
2.2-10. Operating window during start-up of MFTF-B. 54
2.2-11. Start-up of MFTF-B Axicell with thermal barriers. 56
2.2-12. Approximate central-cell power balance used for start-up. 59
2.3-1. Axial profiles in Kelley mode of MFTF-B Axicell. 64
2.3-2. Central-cell power flow for alternate modes. 68
2.3-3. Axial profiles in TMX-U mode of MFTF-B Axicell. 70
2.3-4. Axial profiles in the TARA-like configuration of MFTF-B. 73
2.4-1. Loss boundary and distribution-function contours for sloshing-ion injection in yin-yang anchor. 86

2.4-2. Potential and density profiles obtained for sloshing-ion injection in yin-yang anchor. 87
2.4-3. Loss boundary and distribution-function contours for passing and trapped ions in the transition region. 89

FIGURES IN APPENDICES

B-1. Critical value of β_c as a function of ψ. 120
B-2. Critical value of β as a function of Γ. 120
B-3. Phase-space trajectory and invariant toroid for two degrees of freedom. 124
B-4. Example of an integrable ballooning ray orbit. 126
B-5. Example of a stochastic orbit. 127
B-6. Line spectrum characteristic of a system with well-separated time scales. 129
B-7. Marginal stability boundary in the β_c, Ω^* plane. 132
B-8. A plot of S_θ vs β_c at marginal stability. 132

C-1. Frequency dependence of right and left sides of the dispersion relation. 142

D-1. Field, density, and potential profiles in the MFTF-B Axicell design, showing worst EB ballooning mode, which occurs when the density in the transition is very low. 151
D-2. Field, density, and potential profiles in the MFTF-B Axicell design, showing the trial function at low plasma density in the transition. 153
D-3. Field, potential, and density profiles at one end of MFTF-B when operated with A-cell-type thermal barriers. 157

E-1. Axial magnetic-field profile in anchor. 164
E-2. Potential profile in anchor. 166
E-3. Loss-cone boundaries in midplane velocity space of anchor. 170
E-4. Ion density as a function of magnetic field for four values of n_m. 173

E-5. Contour plots of ion-distribution function, $f_0(v_\perp, v_\parallel)$, at anchor midplane for four values of n_m. 174
E-6. Distribution of perpendicular velocities at anchor midplane for four values of n_m. 175
E-7. Distribution of parallel velocities at anchor midplane for four values of n_m. 176

F-1. Stability of axicell configuration to loss-cone modes. 182
F-2. Marginal stability for two worst modes and for configuration with a 20% broader ECRH profile. 184
F-3. Ion-distribution function f as a function of perpendicular velocity at midplane of anchor at marginal stability. 186
F-4. Amplitude and phase of the eigenfunction of marginal stability for the $n_z = 0$ mode and for the $n_z = 1$ mode. 187

G-1. Contour plot of the electron distribution found in Fokker-Planck studies of the ECRH plasma in the TMX-U experiment. 196
G-2. Model electron distribution formed by superposing five separable distributions. 198
G-3. Temporal growth rate of the upper-hybrid loss-cone instability for the electron distribution shown in Fig. G-2. 200
G-4. Growth rates, maximized over $\underline{k}$, of the whistler and upper-hybrid loss-cone (UHLC) instabilities as a function of the temperature anisotropy. 202
G-5. Constant-growth-rate curves for the whistler and UHLC modes. 203
G-6. Convective-absolute instability boundary for whistler mode. 103

H-1. Resonant diffusion coefficients, D_0, D_1, D_2 and lifetime estimate τ_2, for MFTF-B preliminary design, all as a function of electric field. 212

I-1. Magnetic-field strength and ambipolar potential for a typical thermal-barrier cell in a tandem mirror. 220
I-2. Thermal-electron phase space. 220
I-3. Thermal-ion phase space. 222
I-4. Profiles of Mod-B, ambipolar potential, thermal-ion density, and sloshing-ion density for $\alpha = 1.5$. 228
I-5. The same profiles as in Fig. I-4 but with $\alpha = 3$. 228
I-6. Various equilibrium quantities as a function of $g(R_M)$. 230

LIST OF TABLES

2.1-1. Key parameters for operating modes of MFTF-B with thermal barriers. 22
2.2-1. Plasma parameters for reactor types. 29
2.2-2. Reactor power balance (all powers in megawatts). 34
2.2-3. Reactor costs in millions of dollars ($M). 35
2.2-4. Reactor costs in dollars per kilowatt-electric ($/kWe). 35
2.2-5. Key parameters of axicell tandem reactors. 36
2.2-6. Plasma parameters for the MARS mode of the MFTF-B Axicell. 38
2.2-7. Trapped-particle stability parameters for MFTF-B and for axicell tandem-mirror reactors. 49
2.3-1. Central-cell plasma parameters. 65
2.3-2. Parameters for MFTF-B Axicell in the TARA-like mode (for an earlier design), $Q = 0.37$, $Q_c = 1$, $P_{fusion} = 330$ kW. 74

TABLES IN APPENDICES

Table B-1. Critical beta values for the central cell. 116

Table E-1. Input parameters for sloshing-ion anchor. 171
Table E-2. Effect of passing-ion density on anchor parameters. 172

PHYSICS BASIS FOR AN AXICELL DESIGN FOR THE END PLUGS OF MFTF-B

1. INTRODUCTION AND PHYSICS SUMMARY

The primary motivation for conversion of MFTF-B to an axicell configuration lies in its engineering promise as a reactor geometry based on circular high-magnetic-field coils (see Ref. 1.1). In comparing this configuration to the previous A-cell geometry, we find a number of differences that might significantly affect the physics performance. The purpose of the present document is to examine those features and to assess their impact on the performance of the axicell, as compared to the A-cell configuration, for MFTF-B. In so doing, we address only those issues thought to be affected by the change in geometry and refer to the original report[1.2] "Physics Basis for MFTF-B," for discussion of those issues thought not be affected.

In Sec. 1, we summarize these physics issues. In Sec. 2, we describe operating scenarios in the new configuration. In the Appendices, we discuss those physics issues that require more detailed treatment.

1.1. PHYSICS OVERVIEW

The magnet set for the axicell version of MFTF-B is shown in Fig. 1-1. The central cell is terminated at either end by an axisymmetric mirror cell called the axicell. This configuration was inspired by the geometry of TARA, which is under construction at MIT.[1.3] However, to accommodate the MFTF-B reference mode of operation, the axicell in MFTF-B has a lower mirror ratio and a different B profile from TARA.

In the plasma configuration that forms the reference mode (MARS mode) for MFTF-B, the axicell throttles the flow of ions to the end cell. This is done by a combination of magnetic constriction and reflection from a potential peak formed by ions mirror-trapped in the axicell. The final and higher plugging potential peak and the associated thermal barrier are found in the minimum-B anchor, as shown in Fig. 1-2. Those ions confined to the central cell by the axicell see only axisymmetric magnetic and electrostatic fields.

Situated outside of the axicells and separated by transition sections, the MFTF ying-yang magnets act as magnetohydrodynamic (MHD) anchors to the whole system. Electrical contact between the axicell/central-cell combination

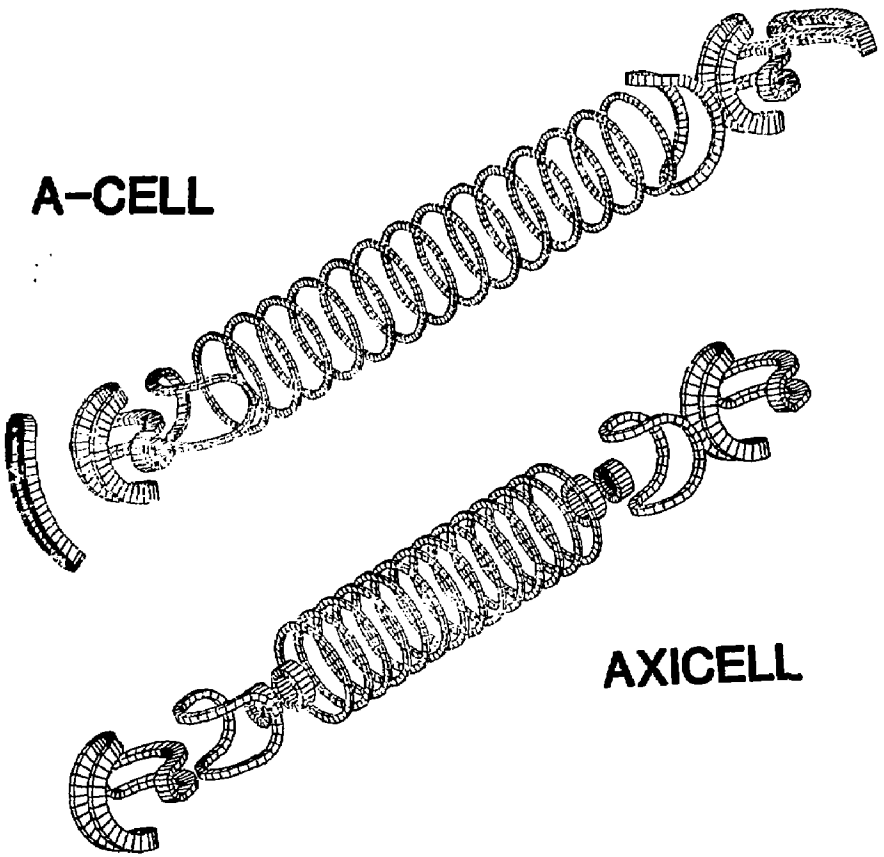

Fig. 1-1. Comparison of A-cell and axicell designs for MFTF-B.

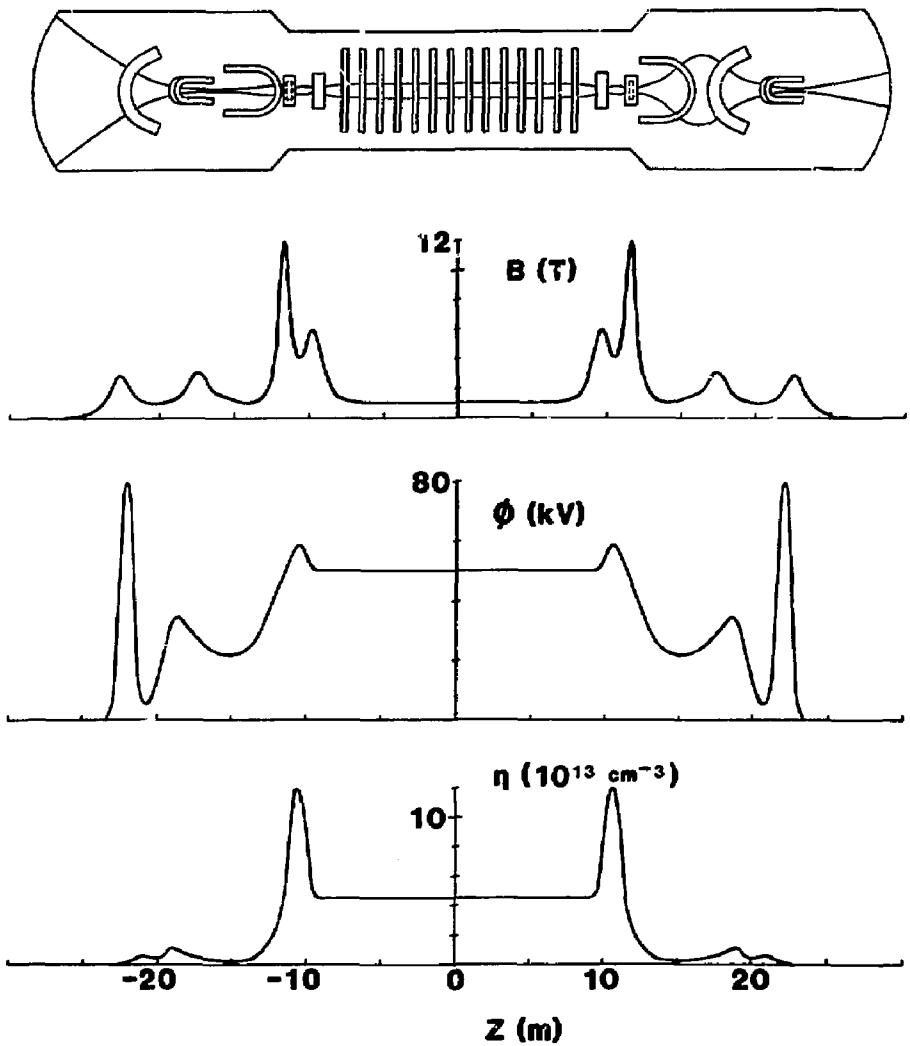

Fig. 1-2. Field, density, and potential profiles for the MARS-mode reference case of the MFTF-B Axicell design.

and the minimum-B anchor cell is maintained through the transition region by a plasma of relatively low density and pressure. Model axial profiles for the density and potential are also shown in Fig. 1-2.

In assessing the physics performance of this configuration, we have identified three critical parameters. Their significance is discussed in the following sections, and more detail is given in the Appendices.

One parameter is set by the degree of coupling of the curvature-driven trapped-particle mode in the central cell to a drift wave. A minimum coupling is required for stability. At high azimuthal-mode numbers this comes about by finite ion Larmor radius effects. For low-mode numbers, there is a coupling induced by details of the charge-particle confinement by the end cells. This sets a minimum for the fraction of central-cell ions that are confined by the end cell. This constraint is met in the MFTF-B design and is less restrictive in reactor extrapolations. For MFTF-B, about 2% of the central-cell ions are confined by the outer potential peak in the reference design. With this fraction, MFTF-B is calculated to be marginally stable to the trapped-particle mode.

Another critical parameter is the achievable β-value in the central cell as determined by both equilibrium and stability considerations. An important new element in determining the central-cell β limit is the density (and therefore β) in the transition between the yin yang and axicell regions that is required to stabilize the trapped-particle mode. The final magnetic-design is not yet complete, particularly regarding the minimization of the parallel currents in the equilibrium. Even so, with an intermediate design we find that central-cell β-values ranging from 36% in the equilibrium field to 53% in the vacuum field can be sustained and are consistent with an anchor β of 55% and axicell β of 20%.

The third critical parameter is the ratio of the density of warm ions that penetrate into the midplane of the yin-yang anchor to the density of energetic sloshing ions that possess a loss cone. Such a coexistence of warm and hot ions is necessary for stability of the latter to loss-cone modes. We find that a warm-ion midplane-density fraction $\gtrsim 0.6$ at a T_{warm}/T_{hot} ratio $\gtrsim 0.3$ should be nominally stable, as compared to the reference-case design parameters where $n_{warm}/n_{hot} = 0.8$ and $T_{warm}/T_{hot} = 0.32$.

1.2. CENTRAL-CELL CONFINEMENT

From the point of view of confinement physics, a primary advantage of the axicell configuration is the reduction of radial transport in the central cell. The dominant radial-loss mechanism in the original MFTF-B central cell was a resonant transport of ions having half-integer-related axial bounce and azimuthal-drift frequencies and suffering radial displacements because of the nonsymmetric field components. In the axicell geometry, only the passing particles experience nonsymmetric fields. Most of the central-cell ions see symmetric fields so that their transport is classical in the absence of symmetry-breaking field errors or fluctuations. Ions entering the end regions suffer radial steps because of the same geodesic curvature that drives parallel currents. Once the parallel current is largely eliminated (a design constraint), the overall transport will be reduced compared to the A-cell. Details of this improvement are given in Appendix H.

1.3. MAGNETOHYDRODYNAMIC (MHD) EQUILIBRIUM

Finite-β equilibria in nonaxisymmetric mirror geometries are dominated by the currents parallel to B, which are generated by the nonvanishing divergence of the diamagnetic current. These currents are analogous to the Pfirsch-Schluter currents in tokamaks and produce closed plasma-current loops that can roughly image the external yin-yang or baseball magnet currents. In a multicell system such as a tandem geometry, these loops can internally close over either the full axial extent of the system as a whole or separately in each cell.

A tandem-mirror system with a long central cell must have small quadrupole axial current in the central cell. Otherwise it would generate B_θ, B_r, and large flux-tube distortions proportional to the central-cell length. An important constraint on a magnet-set design is that all current loops must at least close in each end region. Our reference design satisfies this condition. A much preferred solution has current loops closing separately in each mirror cell of an end region, which avoids a required balancing of adjacent cell properties, particularly pressures, and permits a wider parameter space of central-cell axial-current-free operation. We also have an

in-principle solution that meets the latter more stringent condition but do not as yet have a satisfactory design from the engineering point of view.

Our design code for this problem is TEBASCO, which solves for plasma equilibrium to linear order in β, using magnet fields generated by our engineering magnet design code EFFI. TEBASCO is routinely used by the magnet design team to iterate magnet designs to adjust the central-cell axial current to zero while satisfying acceptable flute-stability criteria [β (central-cell) > β (plug)]. Details of the theory and examples of the code results are given in Appendix A.

1.4. LOW-FREQUENCY STABILITY - MHD

Modes in the drift-frequency range are conveniently distinguished by (1) whether the parallel electric field $\tilde{E}_{||}$ vanishes by virture of an inductive vector potential $\tilde{A}_{||}$, cancelling the longitudinal field $\partial\tilde{\phi}/\partial s$, or (2) whether $\tilde{E}_{||} = -\partial\tilde{\phi}/\partial s$ can exist in spite of the pressure plasma. The first is characteristic of MHD behavior, with or without finite Larmor radius (FLR) corrections. The second is characteristic of electrostatic ballooning behavior, which is very similar to that of trapped-particle modes in tokamaks.

When calculated by pure MHD theory, the axicell configuration has a central-cell β limit even below that of the A-cell configuration. The worst modes in this description are highly localized, bending the thin dimensions of the fan-shaped region between the plug and anchor with little expenditure of bending energy. In the long solenoid, FLR has a strong stabilizing effect on such highly localized modes. When the worst modes have large enough azimuthal variation to justify an eikonal approximation, the full 3-D FLR stability problems can be analyzed using the procedures described in Appendix B. However, these calculations show such a strong FLR stabilization that, for most parameters of interest, only very low azimuthal-mode numbers could be unstable; these, of course, lie outside the validity of the theory.

A proper treatment of this problem requires a full 3-D stability analysis, including the nonsymmetric anchors and rotation in the central cell. This theoretical capability is currently under development at LLNL. Lacking this tool to date, we neglected the high-m modes and used the flute-interchange stability condition as a figure of merit in magnetic-field design.

Recent PHAEDRUS results support our neglect of high-m modes[1.4]. In that experiment, only m = 1 was observed, and the stability limits agreed with those of the flute condition. Beta values were too low to expect ballooning in PHAEDRUS, but finite β experiments in the Wisconsin octupole[1.5] demonstrated increased ballooning β limits consistent with FLR theory.

The low-m stability problem is complicated by several features, in addition to the 3-D character of the equilibrium, namely:

- A powerful energy principle, as in MHD, is no longer available so that eigenmodes and frequencies must be calculated.
- An eikonal treatment is no longer valid.
- The rotation drive in the central cell occurs in the same order as FLR.
- The mode structure is richer, particularly in the presence of hot electrons as described in the following.

As just discussed, our analysis so far has been eikonal, and the curvature-driven response has been treated in the high-frequency limit, as in MHD. In a number of important circumstances, this analysis remains valid in the presence of fast drifting hot electrons if the curvature-driven response is properly modified. This procedure is outlined in the following and detailed in Appendix C.

Following the idea developed for the TARA tandem mirror at MIT[1.3], the anchor cells in MFTF-B will derive most of their pressure from an anisotropic population of hot electrons. Ample experience in the Elmo Bumpy Torus (EBT), ELMO, and INTEREM experiments demonstrates that local β-values of several tens of percent can be generated with relatively low-power electron-cyclotron-resonance heating (ECRH) and a considerable parameter space of (electron) microstable operation.

Because of their fast precessional drift frequencies, these electrons do not behave as an MHD fluid and, therefore, would not by themselves contribute a positive pressure weighting to, for example, a flute-stability integral. These electrons also should be "rigid" in a minimum-B anchor and not contribute to stability under conditions similar to those where electron rings in EBT are "rigid" (i.e., do not have an unstable MHD response in a simple mirror). However, consistent with EBT results, the warm (or slow-drifting) plasma coexisting with the hot electrons has an MHD-like response in the well that is dug (or enhanced) by the hot electrons. The anchor β value is divided

between a hot component β_h and a lower pressure warm component β_w ("hot" and "warm" being defined by frequencies of species' drift relative to the central-cell MHD frequencies). The contribution to flute stability is given by

$$\int \frac{d\ell}{r} k \left(\frac{\beta_w (\beta_h + \beta_w)}{\beta_w + 2r_n k} \right) \quad , \tag{1.1}$$

where $r_n > 0$ is the density scale length, and k is the component of curvature normal to the pressure-level surfaces. For $\beta_w \gg 2r_n k$, this expression becomes

$$\int \frac{d\ell}{r} k \, (\beta_h + \beta_w) \quad ,$$

which is the appropriate weighting when all species are treated as having an MHD response. For finite $\beta_w / 2r_n k$, the region containing hot electrons can still be treated as if it had an MHD response, provided the local β-value is degraded by a factor $\beta_w (\beta_w + 2r_n k)^{-1}$. (In this example flute perturbation is assumed, but a similar result would hold for a ballooning perturbation.) Thus, by this replacement, eikonal balloon-code results, including FLR as the only kinetic effect, can describe tandem systems that have anchors containing fast-drifting electrons.

This change in behavior with β_w compared to $2r_n k$ is directly analogous to the Van Dam-Lee-calculated limit[1,6] on the core β in EBT. There $k < 0$, so the denominator and, therefore, the sign of the response changes as β_w exceeds $|2r_n k|$. The emergence of an MHD response for the hot electrons in a negative-curvature well, therefore, implies instability; whereas in a positive curvature well it implies increased anchoring.

Our picture of low-frequency stability can be summarized as follows. Finite Larmor radius in the central cell stabilizes all but very low-m modes. A proper three-dimensional theory for these has not yet been developed. In our magnet design, the flute-interchange condition is being used as a figure of merit with experimental support. If appropriate effective β values are used, and even with hot electrons in the anchor, ballooning and flute-average calculations can be carried out.

1.5. LOW-FREQUENCY STABILITY - ELECTROSTATIC

The electrostatic ballooning modes, first identified by Berk and Rosenbluth[1.7], are closely related to trapped-particle modes in tokamaks. Because of their recent arrival to the tandem-mirror scene, we give more detail to their properties in this overview.

In such an instability, particles trapped in regions of bad curvature can drive an electrostatic perturbation that excludes good-curvature regions. Particles passing between the two regions can Debye-shield the perturbed potential, but this is a fairly weak effect if only a small fraction of particles are passing.

When the electron-bounce frequency throughout the machine length greatly exceeds the wave frequency, the resulting nonvanishing $\tilde{E}_{\parallel}$ does not drive a parallel electron current, as it would do in an infinite medium.

Because all tandem mirrors only have good magnetic curvature in a line-averaged sense, they are predicted to be susceptible to such modes, as are tokamaks. The tandem-miror central cells are separated from the end cells by large mirror ratios--10 or more for experiments and about 5 for a reactor--and the passing-particle fraction is small by at least the inverse of these mirror ratios. For such passing fractions, the calculated electrostatic-mode growth rates are relatively small, the azimuthal m-values relatively large, and the modes are perhaps benign. However, thermal-barrier efficiency can be increased by further decreasing the passing-particle fraction. Berk and Rosenbluth[1.7] showed that, in the extreme of such cases, the electrostatic mode growth rate can rise to that of the MHD value of the central cell alone, and the m-value can drop to unity. In such a circumstance, the central cell would be expected to tear loose from the anchors until limited by a nonlinear process. The severity of this worst-case scenerio for electrostatic modes warrants paying close attention to their properties to find means of stabilization.

The stability of the electrostatic ballooning mode can be modelled by the quadratic equation, as shown in Appendix D,[1.8,1.9]

$$\left(1 + \frac{A_1}{m^2}\right)\omega^2 - \omega m\omega_{*i}\left(\frac{m-1}{m} + \frac{A_2}{m^2}\right) + \gamma_c^2 = 0 \quad , \tag{1.2}$$

where m is an azimuthal mode number, ω_{*i} is the ion-diamagnetic-drift frequency, and γ_c^2 is the MHD flute-averaged pressure-weighted growth rate including all regions except the minimum-B anchors. The (m-1) term is the familiar FLR-stabilizing effect. The coefficients $A_{1,2}$ are configuration- and geometry-dependent: A_1 measures the Debye-shielding because of particles passing between regions of vanishing and nonvanishing perturbed potential; A_2 measures the difference between the bounce-averaged, perturbed E x B drift of ions and electrons and takes the sign of the charge having the lowest such drift speed. This difference does not occur in tokamaks but does in tandem mirrors where there is an important electrostatic aspect to parallel confinement separating the turning points of positive and negative charges. The coefficient A_2 can support or cancel the FLR term, depending on its sign. Cancellation when $A_2 < 0$ leads to electrostatic instability at some value or range of m. Preferred designs use $A_2 > 0$. When this is the case, the worst mode is usually $m = 1$, and stability then requires

$$\frac{\omega_{*i}^2}{\gamma_c^2} > \frac{4(1 + A_1)}{A_2^2} \quad . \tag{1.3}$$

In the axicell design,

$$A_1 = A_2 \left[\frac{r_c^2}{\rho_i^2} \frac{n_{pass}}{n_c} \frac{2}{L_c} \frac{B_c}{B_a} (L_a + L_t) \right] ,$$

where r_c/ρ_i is the number of ion Larmor radii in the central cell; L_c, L_t, and L_a are, respectively, the central-cell, transition, and anchor lengths. For L_c = 16 m, L_t = 5 m, L_a = 2.5 m in the MFTF-B axicell design, and

$$A_{1,2} = 0.56 \frac{r_c^2}{\rho_i^2} \frac{n_{pass}}{n_c} \quad .$$

Thus, taking values for MARS-mode of MFTF-B described in Sec. 2, $r_c/\rho_i \approx 13$, a ratio $n_{pass}/n_c > 5\%$ is stable for $\omega_{*i}^2 \approx \gamma_c^2$, whereas $n_{pass}/n_c > 1.6\%$ is stable for $\omega_{*i}^2 \approx 2\gamma_c^2$. The parameter $A_{1,2}$ is the important physics parameter determining the coupling to the anchor. In the MFTF-B Axicell design, this ratio can be varied by about 100 through variation of r_c/ρ_i and n_{pass}/n_c.

In the original A-cell design, the worst perturbation is one that eliminates only the yin yang. Both ions and electrons have access to the yin yang, although the ions are depressed by a potential $\Delta\varphi_p$ resulting from neutral-beam injected ions trapped in the yin yang. The coefficient A_1 takes the form

$$A_1 = \frac{1}{R_c}\left(\frac{T_{ic}}{T_{ec}}\right) + e^{-\Delta\varphi_p/T_{ic}}\left(\frac{r_c^2}{\rho_i^2}\right)\frac{2(L_a + L_A)}{L_c} \quad ,$$

when R_c is the central-cell mirror ratio, T_{ic} and T_{ec} the central-cell temperatures, and L_a is the effective yin-yang (anchor) length. The coefficient A_2 is negative because of the free penetration of the central-cell electrons into the anchor,

$$A_2 = -\frac{1}{R_c}\left(1 - e^{-\Delta\varphi_p/T_{ic}}\right)\frac{r_c^2}{\rho_i^2}\,\frac{2(L_a + L_A)}{L_c} \quad .$$

If we use L_c = 32 m, R_c = 4, T_{ic}/T_{ec} = 1.7, L_A = 4 m, and $\Delta\varphi \approx T_{ic}$, and the parameters above, we find $A_1 \approx 38$ and $A_2 \approx -12$. Thus, by Eq. 1.2, we would expect an instability with $m \approx 3$.

In the absence of charge-separation effects, obtained by setting $\omega_{*i} = 0$ in Eq. 1.2, all magnet designs would yield an unstable mode with growth rates differing only by $A_1^{-1/2}$ for fixed m. This is analogous to the situation in tokamaks, except A_1 is usually much larger in tokamaks if only because of the increased number of Larmor radii in the cross section.

In summary, as in other average-minimum-B-stabilized systems, localized electrostatic ballooning, resulting from particles trapped in regions of unfavorable curvature, appears to be a distinct possibility. In a tandem mirror, there is a charge-separation mechanism that couples the basic mode to a drift wave. By this means, the mode can be stabilized with parameter constraints compatible with good confinement.

1.6. MICROSTABILITY

Instabilities near the ion-cyclotron frequency or its multiples have been a predominant feature of all neutral-beam-heated mirror machines. Control of these instabilities in the plugs and anchors must be considered the

primary physics challenge in the development of a tandem-mirror fusion reactor. As the tandem-mirror concept has come to employ a magnetically trapped subpopulation of energetic electrons, the microstability of this group becomes equally important. However, the relatively increased stability of electrons (as opposed to ions) observed in the EBT experiment lends hope that this latter problem may be easier to solve.

We identify two possible drives for instability: first, the "loss-cone" drive due to an inverted perpendicular energy ($E_\perp$) population; and second, anisotropy, the excess of perpendicular energy over parallel energy ($E_\parallel$) (directions are measured relative to $\underline{B}$). Although there are similarities of treatment, it is convenient to discuss ion and electron modes separately.

As regards the ion microstability issue in MFTF-B, we find little difference between the original A-cell design and the axicell design if the yin yang is stretched to produce a vacuum mirror ratio of three. In both cases, the barrier and plugging potentials exist in the same mirror cell. The outer lobe of the sloshing-ion distribution has hotter electrons and consequently a higher potential peak. Ions from the central cell that are confined by this outer peak will supply more than enough warm ions to stabilize the sloshing hot ions at the cell midplane to loss-cone modes. Only near the potential peak does an energy inversion appear, and any modes that might appear are resonant there. A description of Fokker-Planck studies of sloshing-ion distribution is given in Appendix E.

The most sensitive region for ion modes is the yin-yang anchor. As discussed in Appendix F, we find that stability to loss-cone modes can be achieved within the range of operating parameters. However, an extreme sensitivity of calculated stability boundaries to axial equilibrium profiles is indicative of the theoretical uncertainty. The axicell also contains hot ions, but the distribution is always made monotonic in perpendicular energy because of the passing ions confined by the outer potential peak.

The principal anisotropy-driven mode, the Alfvén ion-cyclotron mode (AIC), has been fairly firmly identified in TMX. Its presence there is well explained theoretically by the extreme anisotropy induced by the normal injection. As described in Appendix F, we find the low β value and sloshing nature of the ions in the anchor to be very stabilizing. The most susceptible regions for this mode are the axicell and the central cell under intense neutral-beam heating. Maintenance of low β in the axicell and the very large

mirror ratio of the central cell are both stabilizing, but detailed stability analyses of Fokker-Planck solutions remain to be done. This problem is virtually unchanged by the magnet-design change.

We identify two modes of concern in the electron-cyclotron-frequency range: first, the upper hybrid mode of the bulk electrons, driven by a nonmonotonic hot-electron population (essentially a loss-cone mode); and, second, the whistler mode, driven by the anisotropy. Our analysis (described in Appendix G) has to date been nonrelativistic, care being taken in matching Fokker-Planck solutions by a series of analytic functions. We find a rather small parameter span for stability, and we calculate fairly short convective-growth lengths in typical Fokker-Planck profiles. At issue is the narrowness of the hot-electron distribution, relative to that of the sloshing ions, that is required to assure good barrier formation. This problem holds for both axicell and A-cell configurations. Relativistic effects are known to be stabilizing and need to be included in the description.

REFERENCES

1.1. K.I. Thomassen and V.N. Karpenko, An Axicell Design for the End-Plugs of MFTF-B, LLNL Report, UCID-19318 (1982).

1.2. D.E. Baldwin, B.G. Logan, and T.C. Simonen, eds., Physics Bas's for MFTF-B, LLNL Report, UCID-18496 (1980).

1.3. J. Kesner, R.S. Post, B.D. McVey, and D.K. Smith, A Tandem Mirror with Axisymmetric Central Cell Ion Confinement, MIT Report, PFC/JA81-11 (1981); to be published in Nucl. Fusion.

1.4. A.W. Molvik, et al., Phys. Rev. Lett. 48, 742 (1982).

1.5. S.C. Prager, Bull. Am. Phys. Soc. 26(7), 951 (1981).

1.6. J.W. Van Dam and Y.C. Lee, Proceedings of the Workshop on EBT Ring Physics, Oak Ridge, TN, 471 (1979).

1.7. H.L. Berk and M.N. Rosenbluth, private communication.

1.8. M.N. Rosenbluth, H.L. Berk, H.V. Wong, D.E. Baldwin, and T. Antonsen, "Fast-Growing Trapped Particle Modes in Tandem Mirrors", presented at 1982 Sherwood Meeting, Annual Controlled Fusion Theory Conference, Santa Fe, NM, April 25-28, 1982.

1.9. L.D. Pearlstein, D.E. Baldwin, R.H. Cohen, T.K. Fowler, and B.G. Logan, "Stabilization of Tandem Mirror Trapped Particle Modes by Incomplete Cancellation of Trapped Particle Drifts", presented at 1982 Sherwood Meeting, Annual Controlled Fusion Theory Conference, Santa Fe, NM, April 25-28, 1982.

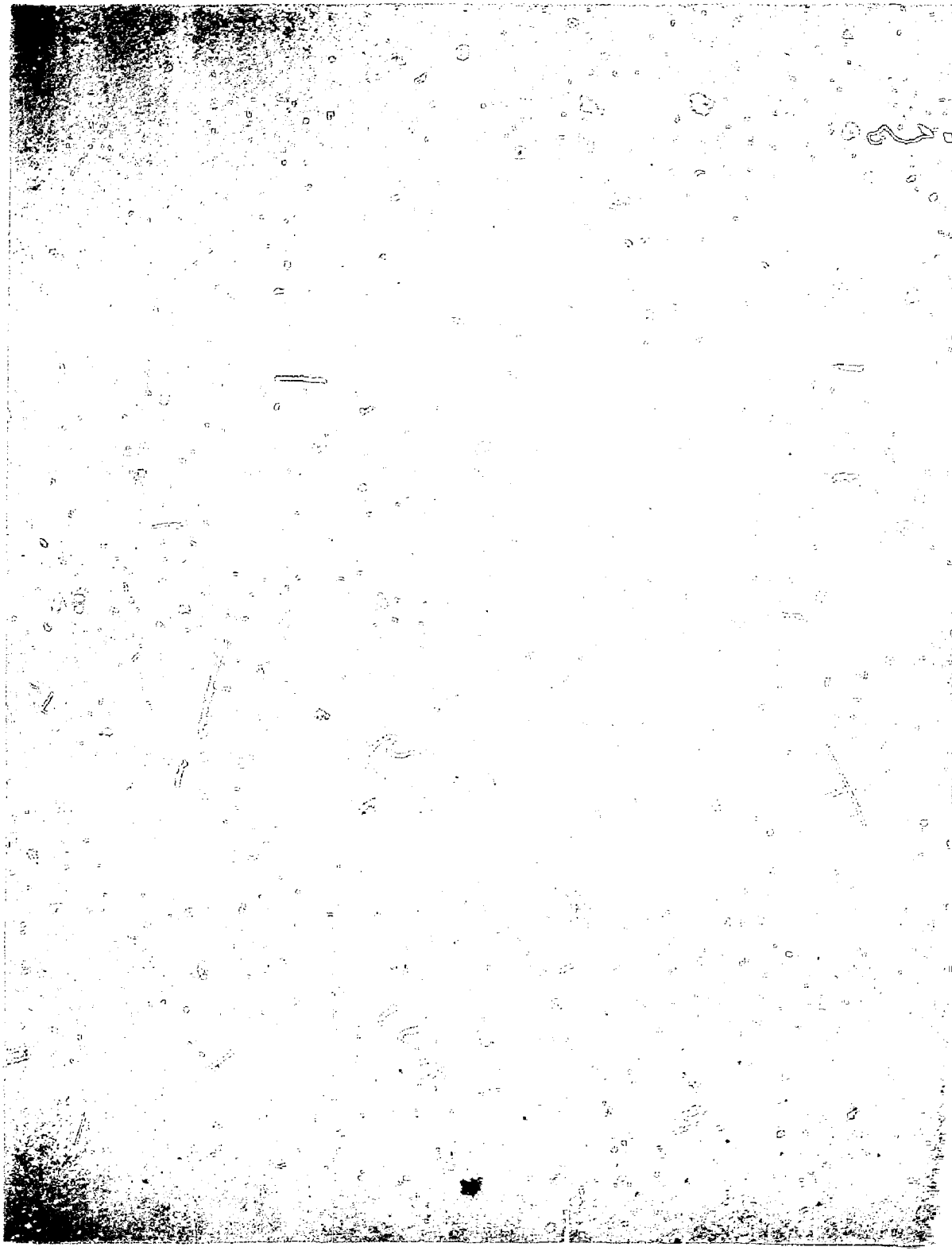

2. SCENARIOS FOR MFTF-B AXICELL OPERATION

B. G. Logan, R. A. Jong, D. L. Correll, and A. W. Molvik

2.1. INTRODUCTION AND SUMMARY

The primary motivation for the proposed modification of MFTF-B to the axicell-plug-magnet configuration[2.1] (shown in Fig. 2.1-1) is that, compared to the A-cell, this configuration when scaled to a reactor[2.2] is expected to improve performance in terms of higher Q, lower plug-magnet capital cost, and reduced radial transport. These reactor improvements are reviewed briefly in Sec. 2.2.2. Using essentially the same plasma models described in the original MFTF-B proposal[2.3] but updated where needed (Sec. 2.3), we estimate that operation with thermal barriers (Sec. 2.2 following) in the modified axicell magnet set would achieve the same physics objectives and equivalent performance as the original A-cell design. Specifically, we can do the following:

(1) Generate maximum center-cell ion-confining potentials ($\phi_c \sim 30$ kV) sufficient for confinement, $(n\tau)_c \sim 5 \times 10^{13}$ cm^{-3}·s, equivalent to achieving $Q \sim 0.5$ with D-T.

(2) Achieve sufficiently high plasma temperatures ($T_{ic} \sim 15$ keV, $T_{ec} \sim 9$ keV) to test physics of thermal barriers and radial transport in appropriate collisionless reactor regimes.

(3) Demonstrate high beta MHD equilibrium and stability ($\beta_c \sim 0.5$).

(4) Design for microstable sloshing ions and thermal barriers in the MFTF-B yin yangs, using theoretical models developed for the A-cell design and TMX-U.

In addition to the above physics-design criteria, we also require the operating scenarios for the MFTF-B Axicell to satisfy presently understood theoretical criteria for trapped-particle stability[2.4] and to insure MHD response of hot electrons (Lee-Van Dam constraints)[2.5], even though these theoretical criteria are still evolving and, therefore, are not yet quantitative. Indeed, consideration of trapped-particle stability led to designing the thermal barrier in the yin yang rather than in the axicell, so that more central-cell passing ions can reach the stabilizing yin-yang region. We believe this is the best mode of operating the MFTF-B Axicell in

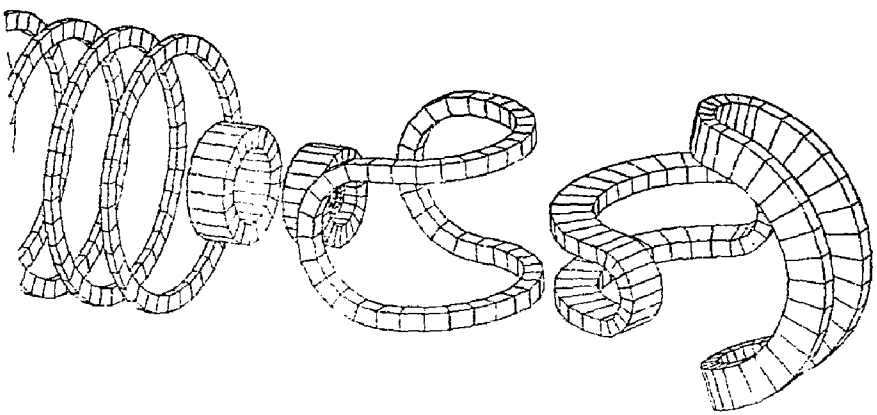

Fig. 2.1-1. Magnet set for MFTF-B Axicell.

the on-going Mirror Advanced Reactor Study (MARS), so we can refer to it simply as the thermal-barrier MARS-mode of MFTF-B. This reference-case operating mode is discussed in detail in Sec. 2.2. Description of the plasma model used for this mode is detailed in Sec. 2.4. In Figs. 2.1-2 and 2.1-3 we compare axial profiles of field, density, and potential for the MARS-mode of MFTF-B and for the MARS reactor, respectively.

In a two-component mode of operation, one can achieve an equivalent $Q > 0.5$ with lower confining potentials and, therefore, with relaxed beam-species-mix requirements. This alternative-operation mode uses the same magnet coils with 0.5-s beams, mostly injected into the central cell. The thermal-barrier potentials are one-half of those in the reference-case MARS mode (Sec. 2.3.1). Figure 2.3-1 of that section shows the axial profiles of field, potential, and density for this case, which are very similar to those used in the present design of the Technology Demonstration Facility (TDF) engineering-test reactor. The plugs only augment the basic mirror confinement in the central cell, as originally suggested by Kelley.[2.6] Thus, we refer to this case as the Kelley-TDF-like mode.

To allow for uncertainties in low-frequency stability (particularly the trapped-particle stability), we have also considered (in Sec. 2.3.2) a backup mode of running the axicell MFTF-B magnet set without injecting the axicell or pumping the transition region, so that a plasma configuration very similar to the TMX-U can be obtained (see Fig. 2.3-3). With respect to ballooning MHD and trapped-particle stability, this mode of operation (naturally called TMX-U-like mode) is probably at least as stable as the original A-cell design of MFTF-B. In fact, one can operate MFTF-B almost continuously between the TMX-U and the MARS modes and obtain increasing central-cell density, increasing Q, and decreasing margin of MHD and trapped-particle stability when going toward the MARS-mode. This continuum of operating points is discussed further in Sec. 2.2. A summary of key parameters comparing these various operation modes of MFTF-B is given in Table 2.1-1.

Finally, in Sec. 2.3.3, we discuss the option of operating MFTF-B with thermal barriers in the axicell if the axicell coils are spread apart to obtain a larger mirror ratio. This would generate a plasma configuration (see Fig. 2.3-4) similar to the original proposed TARA experiment.[2.1] Operation in this mode is possible only if trapped-particle stability is much better

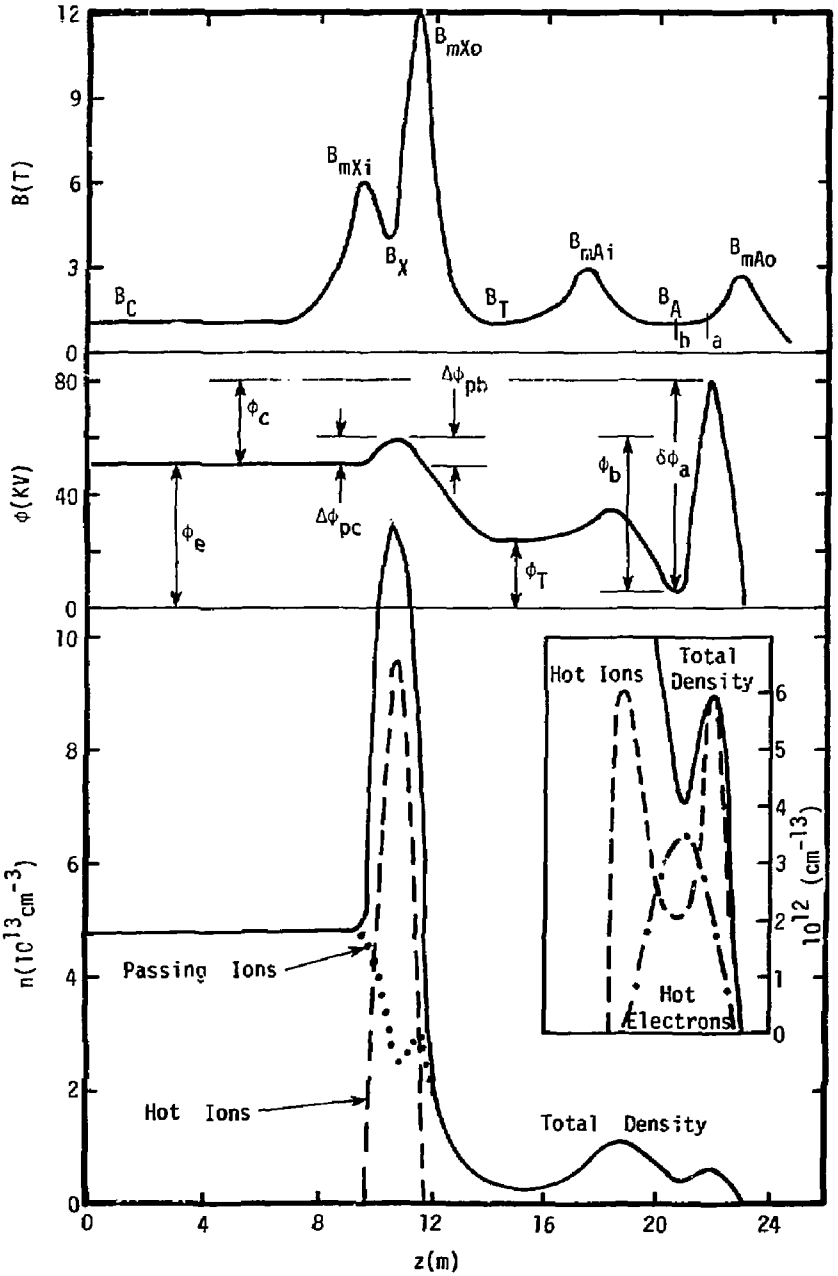

Fig. 2.1-2. Thermal-barrier MARS-mode reference case for MFTF-B Axicell.

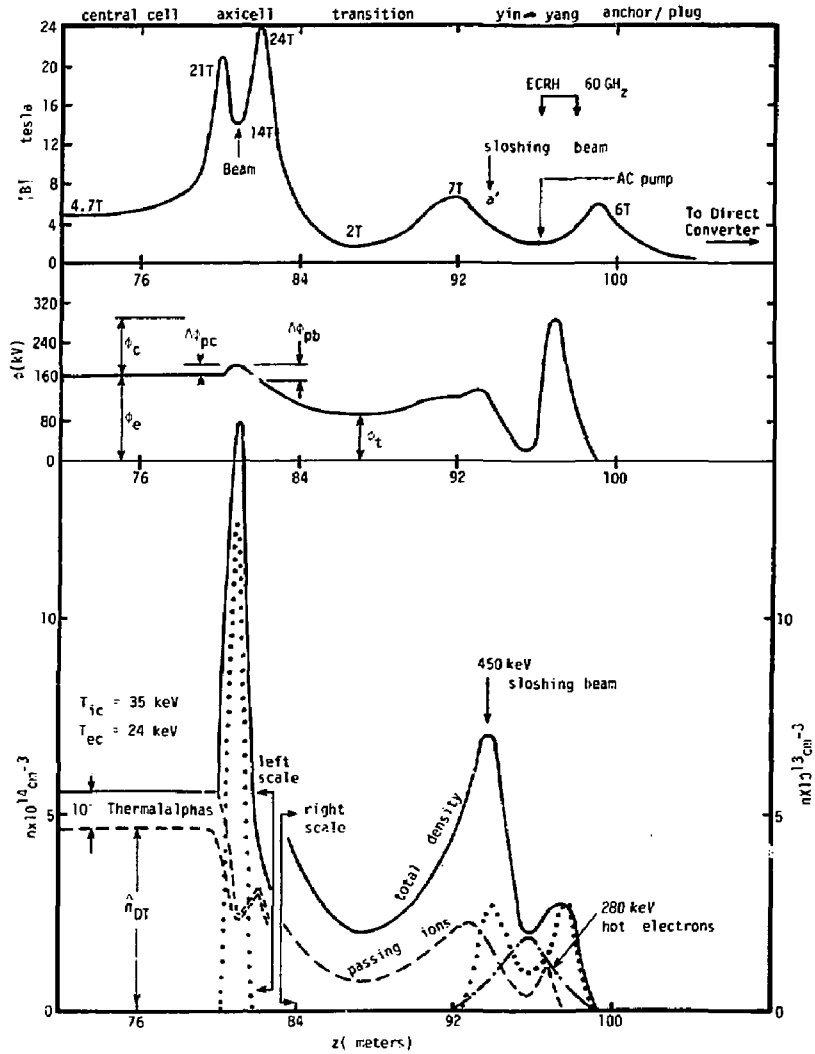

Fig. 2.1-3. Improved MARS axicell reactor.

TABLE 2.1-1. Key parameters for operating modes of MFTF-B with thermal barriers.

Parameter	Mode		
	MARS-like	TDF-like	TMX-U like
Q (overall)[a]	0.40	0.6	0.06
T_{ihC} (keV)	-	35	-
T_{iwC} (keV)	15	10	15
T_{eC} (keV)	9	6	9
B_C (T)	1.0	1.6	1.0
β_C	0.5	0.54	0.12
n_C (cm^{-3})	4.8×10^{13}	9.1×10^{13}	1.2×10^{13}
$(n\tau)_C$(cm^{-3} s)	5×10^{13}	1.4×10^{13}	5×10^{13}
P_{fus} (kW)	830	4200	80

[a]Equivalent for D-T.

than we now estimate. The magnet set for use with thermal barriers in the yin yang (MARS mode) is designed so that the MFTF-B can be operated in a TARA mode with only a 3-month turnaround (during which the axicell coils are spread and beams and ECRH rearranged).

REFERENCES

2.1. J. Kesner, Nuclear Fusion 20, 557 (1980). See also J. Kesner, R. S. Post, D. D. McVey, and D. K. Smith, "A Tandem Mirror with Axisymmetric Central Cell Confinement," to be published in Nuclear Fusion; also see MIT Rept. PFC/JA81-11 (1981).

2.2. G. A. Carlson, W. L. Barr, B. M. Boghosian, R. S. Devoto, J. N. Doggett, G. W. Hamilton, B. M. Johnston, W. N. Kumai, J. D. Lee, B. G. Logan, R. W. Moir, W. S. Neef, and R. B. Campbell (TRW, Inc.), Comparative End-Plug Study for Tandem Mirror Reactors, LLNL Report, UCID-19271 (1981).

2.3. D. E. Baldwin, B. G. Logan, and T. C. Simonen, Eds., Physics Basis for MFTF-B, LLNL Report, UCID-18496 (1980).

2.4. M. N. Rosenbluth, H. L. Berk, H. V. Wong, D. E. Baldwin, and T. Antonsen, "Fast-Growing Trapped Particle Modes in Tandem Mirrors;" also L. D. Pearlstein, D. E. Baldwin, R. H. Cohen, T. K. Fowler, and B. G. Logan, "Stabilization of Tandem Mirror Trapped Particle Modes by Incomplete Cancellation of Particle Drifts." Both papers presented at the 1982 Sherwood Meeting, Annual Controlled Fusion Theory Conference, Santa Fe, NM, April 25-28, 1982.

2.5. J. W. Van Dam and Y. C. Lee, Proceedings of the Workshop on EBT Ring Physics, Oak Ridge, TN (1979), p. 471.

2.6. G. G. Kelley, "Elimination of Ambipolar Potential-Enhanced Loss in a Magnetic Trap," Plasma Phys. 9, 503 (1967).

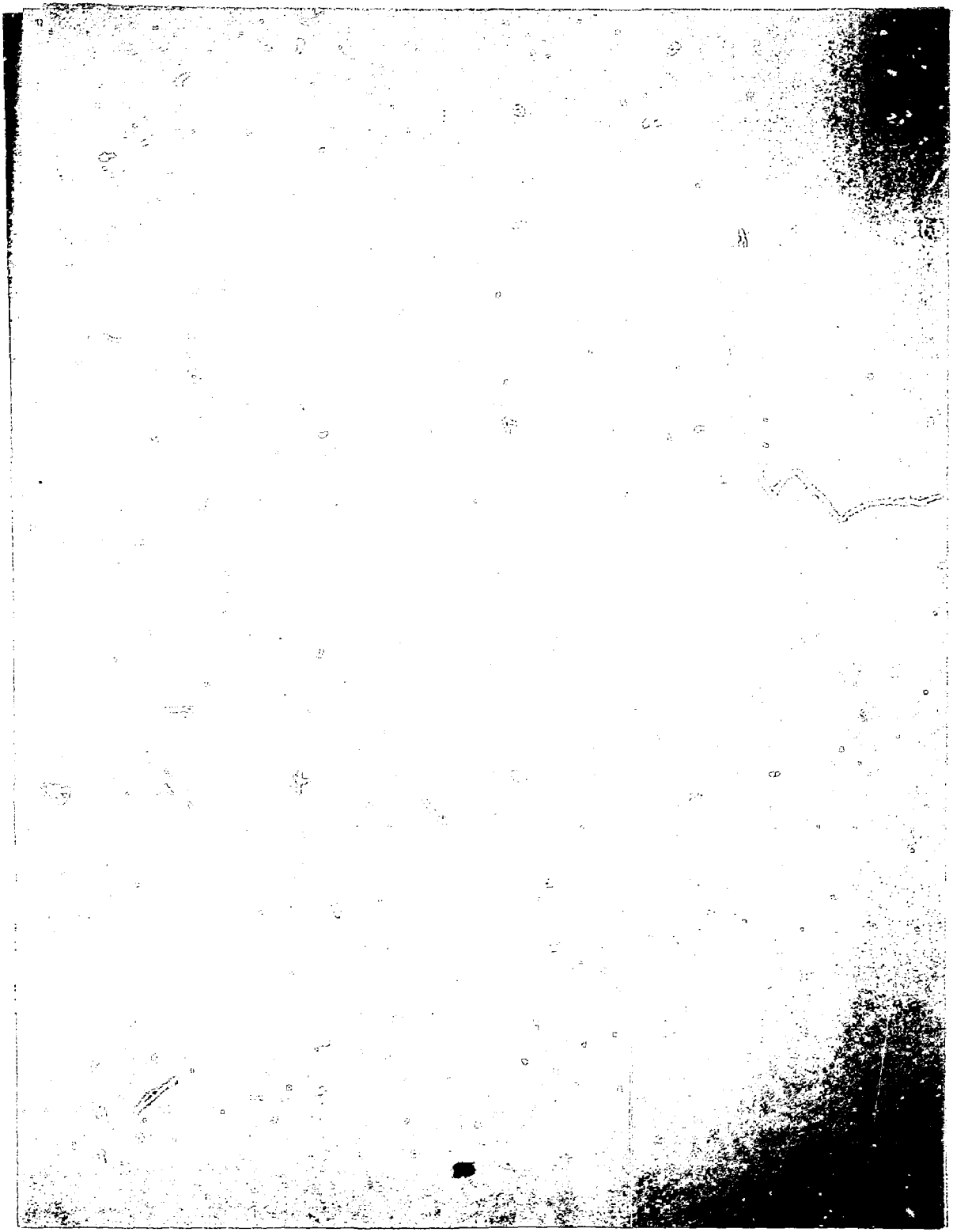

2.2. AXICELL REFERENCE-CASE OPERATION (MARS MODE)

2.2.1. DESCRIPTION OF REFERENCE-CASE MARS MODE

We require a thermal-barrier mode of operation that satisfies the physics and stability constraints mentioned in Sec. 2.1 and that can be scaled to a high-performance reactor. The key features required are the following:

- A high-field circular coil between the central cell and plug to obtain a sufficiently high central-cell density relative to plug density (high Q).
- A moderately high ($R \geq 3$), outward mirror ratio to make thermal barriers and confine sloshing ions, wherever the plug is located.
- Trapped-particle stability, obtained by charge separation. This last feature requires a significant number of ions (orders of magnitude above the end-leakage streaming density), which pass from the central cell through the good curvature regions of the yin-yang anchors.

These requirements are met by the following:

- Adding a high-field circular coil at each end of the central cell (see Fig. 2.1-1).
- Increasing the MFTF-B yin-yang separation to raise its vacuum mirror ratio from 2 to 3.
- Putting the thermal-barrier plugs into the extended yin yangs.

The high-field circular coil will produce a field of 12 T, using Nb_3Sn inserts. The thermal-barrier plugs will include sloshing ions, with the ion-confining potential produced by ECRH applied to the outermost sloshing-ion density peaks. These features are included in the axial field, potential, and density profiles shown in Fig. 2.1-2.

To make this scheme adequate for pumping the transition to a desirable low density, axicells are created by adding another circular coil (but low field) inboard of the high-field circular coils, with beams injected perpendicularly into the axicells to create local density and potential bumps there. The axicells thus serve as electrostatic attenuators, aiding the high-field circular coils in reducing the passing-ion density, relative to the central-cell density, by an additional factor of roughly $\exp(-\Delta\phi_{pc}/T_{iwC})$.

Therefore, the amount of collisional trapping and pump-beam power in the transition and barrier regions is reduced. In this role the axicells perform the same function as the density and potential bumps of the yin yangs in the original MFTF-B A-cell design and can be used as experimental "valves" to vary the passing-ion fraction.

Fokker-Planck calculations, recently performed by Archer Futch, for cases without axicells and with axicells having equal central-cell densities and 12-tesla mirrors, indicates that axicells reduce barrier-filling rates by about a factor of 2 to 3. This reduction leads to an important reduction in pumping in MFTF-B and in reactors. In addition, the passing-ion pressure is reduced in the transitions, easing MHD interchange and parallel-current drives there. With respect to trapped-particle stability, raising the central-cell density by exp $(\Delta\phi_{pc}/T_{iwC})$ factors allows the use of smaller plasma radius for the same fusion power; the smaller plasma radius in turn increases ω^*/γ_{MHD}, thus enhancing drift stabilization of trapped-particle modes.

2.2.2. SUITABILITY OF REFERENCE CASE FOR REACTOR OPERATION

By comparing Figs. 2.1-2 and 2.1-3, one can envision a tandem reactor with fields, potentials, and densities that follow in nearly constant ratios to those of MFTF-B. The reactor fields would be higher everywhere by about a factor of two, except for the being four times higher central-cell field. The reactor potentials are all about four times higher (likewise beam voltages), and the reactor densities about ten times higher in the central cell, and five times higher in the transitions and anchors. The plasma radial dimensions, however, would only be slightly larger in the reactor because of high density. Thus the end plug magnets, especially the yin yangs, need only be a little larger than in MFTF-B.

We have already examined the impact of trapped-particle stability on the mode of operation (e.g., location of the thermal barriers) in the axicell-magnet configuration and have shown that the same regime of trapped-particle stability ($\omega^* > \gamma_{MHD}$ for high density, small radius) can be achieved in axicell reactors as well as in the axicell MFTF-B (Table 2.2-1). The following question naturally arises, however: Why use axicells for reactors, rather than A-cells or other plug configurations, since reactor suitability is a key motivating issue for MFTF-B. We addressed this

TABLE 2.2-1. Plasma parameters for reactor types.

	A-Cell	Modified-Cusp	Axicell	Axicell with EBT Stabilization
P_{FUSION}	3500 MW	3500	3500	3500
Q	10.3	19.7	22.3	12.2
Γ_{fw}	2.3 MW/m^2	2.3	2.3	2.2
Central Cell				
r_c	1.0 m	1.0	1.0	1.0
$r_{c,inner}$	--	0.5 m	--	--
r_{fw}	1.3 m	1.3	1.3	1.3
L_c	150 m	150	150	150
β_c	0.56	0.7	0.7	0.7
n_{ic}	$1.6x10^{14} cm^{-3}$	$2.2x10^{14}$	$1.6x10^{14}$	$1.6x10^{14}$
T_{ic}	40 keV	40	40	40
T_{ec}	36 keV	33	32	33
ϕ_e	270 keV	260	240	240
Barrier/Plug				
L_B	8 m	7	8.6	8.6
β_B	0.63	0.61	0.71	0.36
n_{pass}	$5.0x10^{12} cm^{-3}$	$5.5x10^{12}$	$3.4x10^{12}$	$4.4x10^{12}$
$E_{inj,B}$	350 keV	300	250	250
E_{eh}	520 keV	390	750	240
T_{ew}	93 keV	110	82	150
ϕ_B	230 keV	190	210	170
ϕ_c	150 keV	150	140	140
Anchor				
r_A	0.84 m		1.2	
β_A	0.7		0 3	
n_{iA}	$1.7x10^{14} cm^{-3}$		$1.5x10^{13}$	
$E_{inj,A}$	200 keV		150	
E_{iA}	310 keV		150	
T_{eA}	--		32 keV	
ϕ_A	--		160 keV	
ϕ_{pc}	19 keV		--	

question in a recently completed comparative study (Ref. 2.2 Sec. 2.1) at LLNL of four plug configurations: A-cell (Fig. 2.2-1), axicell (Fig. 2.2-2), modified-cusp (Fig. 2.2-3), and hot-electron-ring (EBT) stabilized axicell (Fig. 2.2-2., but without the yin-yang anchor). While these four configurations do not constitute an exhaustive list of possible plug configurations, their physics characteristics are probably generic to the three known means of providing minimum-B for MHD stability in open systems: quadrupoles, cusps, and diamagnetic wells created by fast-drifting electrons. The basic results of that study are summarized in Tables 2.2-2 to 2.2-4. These tables show significantly lower plug-magnet cost and higher Q (less plug beams and ECRH) for the axicell and modified-cusp plugs compared to the A-cell design. The axicell with EBT stabilization had the smallest plug-magnet cost, but the additional ECRH required to maintain the EBT rings still gave it a higher overall capital cost per kilowatt. The main reason for the lower plug-magnet cost and higher Q of both axicell (with yin-yang anchors) and modified-cusp plugs (compared to the A-cell) was that higher fields could be designed in the circular mirror coils and could be augmented by normal copper coils to permit fields even above superconducting limits with modest electric-power consumption. The high mirror fields, together with barrier pumping, increased the allowed ratio of central-cell density to plug density, thus increasing Q and lowering other plug magnetic fields and costs. An additional advantage of the circular mirror coils can be expected in the reduction of radial transport in the central cell (although credit for this was not taken in the study comparisons). Although the magnet cost and Q of the modified-cusp was comparable to the axicell, the axicell with quadrupole anchors was chosen as the favored-candidate reactor configuration for the ongoing Mirror-Advanced-Reactor Study (MARS). This was primarily because of greater confidence in the MHD stability of quadrupoles employed in many past and present mirror experiments and because of the forthcoming data base that will be provided by TMX-U at LLNL, TARA at MIT, Gamma-10 in Japan, and AMBAL-1 in the USSR.

Since the comparative study, the MARS axicell-reactor design has been further developed in four important areas:

(1) Preliminary engineering analyses by General Dynamics, LLNL, and the University of Wisconsin on the neutron damage, water cooling, power consumption, and stress-analysis of the normal coil inserts

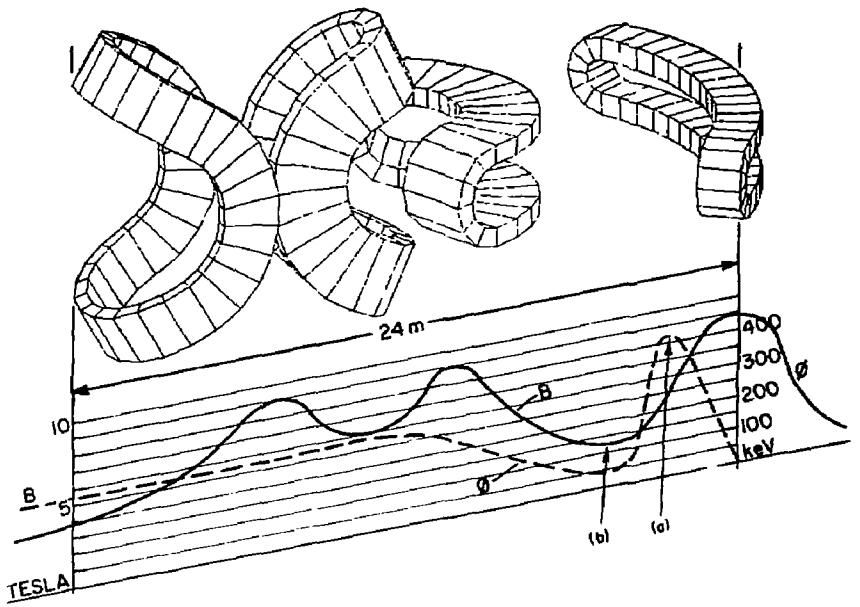

Fig. 2.2-1. A-cell Tandem-Mirror Reactor (TMR).

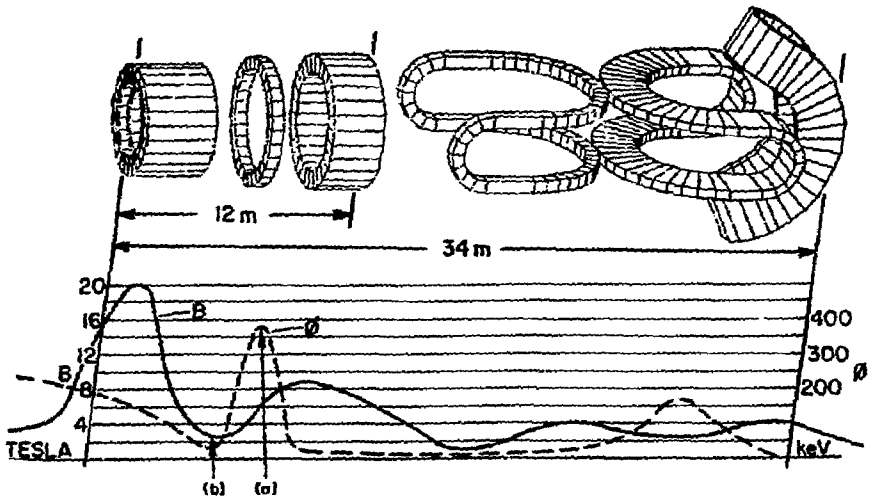

Fig. 2.2-2. Axicell TMR.

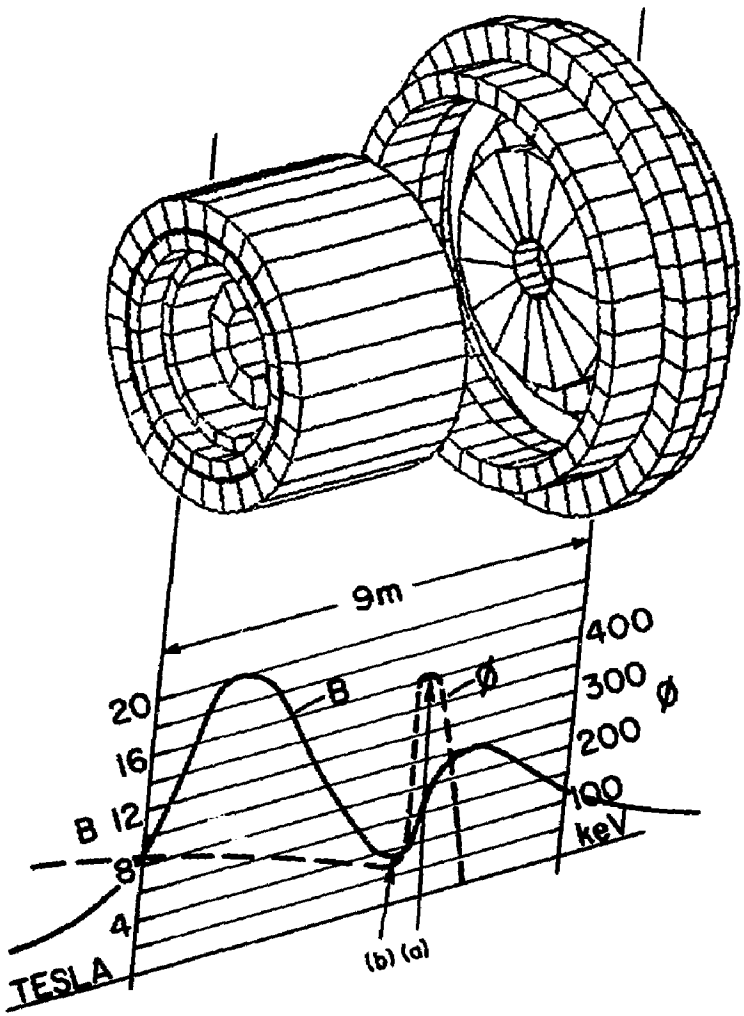

Fig. 2.2-3. Modified cusp TMR.

TABLE 2.2-2. Reactor power balance (all powers in megawatts).

	A-Cell	Modified-cusp	Axicell	Axicell with EBT stabilization
Trapped powers:				
ECRH	97	60	47	154
Pump beams	148	98	93	97
Sloshing beams	66	20	12	35
Anchor beams	29	--	5	--
TOTAL	340	178	157	286
Injected powers:				
ECRH	108	67	52	171
Pump beams	177	118	115	105
Sloshing beams	122	83	52	159
Anchor beams	30	--	15	--
TOTAL	437	268	234	435
Recirculated powers:				
ECRH	216	134	104	342
Pump beams	354	236	230	210
Sloshing beams	244	166	104	318
Anchor beams	60	--	30	--
Copper coils	--	72	72	72
TOTAL	874	608	540	942
Thermal converter output	1176	1176	1176	1176
Direct converter output	520	439	429	493
TOTAL (Gross electrical)	1696	1615	1605	1669
$f_{REC} = \frac{\text{Recirculated power}}{\text{Gross electrical}}$	0.52	0.38	0.34	0.56
Net electrical power	822	1007	1065	727

TABLE 2.2-3. Reactor costs in millions of dollars ($M).

	A-Cell	Modified-Cusp	Axicell	Axicell with EBT Stabilization
Beams @$2/W injected	658	402	364	528
ECRH @$5/W injected	540	335	260	855
Plug magnets	628	251	302	175
Direct converter	158	83	152	127
Central cell	450	450	450	450
Reactor bldg.	165	154	162	149
BOP	470	470	470	470
TOTAL	3069	2145	2160	2754

TABLE 2.2-4. Reactor costs in dollars per kilowatt-electric ($/kWe).

	A-Cell	Modified-Cusp	Axicell	Axicell with EBT Stabilization
Beams @$2/W injected	800	399	342	639
ECRH @$5/W injected	657	333	244	1176
Plug magnets	764	249	284	212
Direct converter	192	82	143	152
Central cell	547	447	423	545
Reactor bldg.	201	153	152	180
BOP	572	467	441	569
TOTAL	3733	2130	2029	3473

TABLE 2.2-5. Key parameters of axicell tandem reactors.

	FY81 Study UCID 19271 (TARA Mode) (no thermal alphas)	Higher Field Axicell (TARA Mode) (with thermal alphas)	1982 MARS Study (New Operating Mode) (with thermal alphas)
P_{FUSION}	3500 MW	3500	3500
L_c	150 m	150	150
$L_{barrier}$	8.6 m	8.0	7.0
B_c	3.0 T	4.7	4.7
B_{mirror}	20 T	24	24
r_c	1.0 m	0.38	0.38
r_{FW}	1.3 m	0.56	0.56
n_{ic}	$1.6 \times 10^{14} cm^{-3}$	4.6×10^{14}	4.6×10^{14}
n_{pass}	$3.4 \times 10^{12} cm^{-3}$	1.0×10^{13}	3.6×10^{12}
Q	*22.3*	*16.8*	*17.0*
Γ_{FW}	2.3 MW/m^2	5.3	5.3

indicates that high field mirror coils as high as 28 T are probably feasible, with the cost-effectiveness optimum being about 24 T.

(2) Blanket modules capable of operating at 5 MW/m^2 of neutron wall loading permit us to raise the central-cell field and density, shrinking the plasma size down to the point where the yin-yang anchor need be only slightly larger than the MFTF-B coil, using NbTi conductor.

(3) Equilibrium concentrations of thermalized alphas were included in the plasma model (resulting in reduced Q by nearly a third) with provision being made for dc grad-B radial transport (akin to an optimized resonant transport in the central cell). On the plus side, the ignited central cell now provides 50 to 100 MW of power to sustain a halo dense enough to shield the plasma core from gas and impurities and provides a handle on reducing the central-cell radial electric field and associated E x B rotation.

(4) Conversion of the axicell-plug operating mode, from the TARA-like mode of the previous year to the more stable regime (with respect to trapped-particle instabilities) of thermal-barrier operation in the yin yang, has been successfully completed. Minimal perturbation occurred with respect to the central-cell design and plug magnets (with the single exception being the transition coil design, which is still being optimized to null parallel current). For comparison, key parameters of the FY81 axicell design [the first (TARA-mode) MARS design] and the recently modified axicell MARS design are given in Table 2.2-5. Note that conversion to the modified axicell MARS design made very little difference in the performance. The drop in Q from FY81 axicell to the MARS design was a consequence of properly including thermal alphas in the plasma model and power balance.

2.2.3. OPERATING SCENARIO FOR MARS MODE AT STEADY STATE

We now examine the plasma parameters and power balances for the MARS mode, using plasma models described in detail in Sec. 2.4, and will shortly consider the stability aspects of this case. Parameters for the central-cell, axicell, transition, and anchor plugs (Table 2.2-6) are consistent with the following key engineering choices for MFTF-B:

TABLE 2.2-6. Plasma parameters for the MARS mode of the MFTF-B Axicell.

Region	Parameter	Value
Central-cell	T_{iwC}	15 keV
	T_{eC}	9 keV
	n_{iwC}	4.8×10^{13} cm^{-3}
	β_C	0.5
	ϕ_C	30 kV
	ϕ_e	50 kV
	$(n\tau)_{Pastukhov}$	5×10^{13} cm^{-3} s
	Q_C	0.6
	Q_{tot}	0.4
	L_C	16.5 m
Yin-yang	$n_{iA}(b)$	3.4×10^{12} cm^{-3}
	ϕ_b	51 kV
	E_{eh}	470 keV
	β_A	0.55
	ϕ_p	80 kV
	T_{ew}	72 keV
	$\delta\phi_a$	72 kV
	$n_{ihA}(a)$	5.6×10^{12} cm^{-3}
Transition	ϕ_T	26 kV
	n_T	2×10^{12} cm^{-3}
	β_T	0.05 (0.01 perpendicular, and 0.09 parallel)
Axicell	n_{iX}	1.2×10^{14}
	$\Delta\phi_{pc}$	9.0 kV
	$\Delta\phi_{pb}$	10 kV
	β_X	0.20

TABLE 2.2-6 (continued)

Trapped current and rf power:

Neutral Beams	Trapped current (A)
Each axicell (80 kV)	3.4
Each transition (30 kV)	6.0
Each anchor (80 kV)	0.30
Each pump beam (80 kV)	2.4
ECRH	**Absorbed power (kW)**
Anchor (28, 35, 56 GHz)	610
ICRH	
Central cell (15-17 MHz)	210

- 12-T maximum high-field circular coils (limited by the superconducting Nb_3Sn insert).
- An R_{vac} = 3 yin yang with B_{mirror} = 3 T (∿ the maximum separation manageable with the MFTF-B structure).
- An 80-kV max, 30-s beam with 90% atomic-species fraction, and 28-, 35-, and 56-GHz gyrotrons.

The parameters in Table 2.2-6 are also consistent with the performance levels of the previous A-cell design, namely: $(n\tau)_c \approx 5 \times 10^{13}$ cm^{-3} s, T_{ic} = 15 keV, T_{ec} = 9 keV, $\phi_c \approx 30$ keV, $Q \sim 0.5$ and $P_{fusion} \sim 1$ MW (equivalent for D-T). Using definitions in the previous A-cell proposal (Refs. 2 and 3 of Sec. 2.1), we find:

$$Q_c \equiv \frac{P_{fusion}}{I_{pastukhov\ loss}\,(\phi_c + \phi_e + T_{ic} + T_{ec})} \approx 0.6 \ ,$$

$$\text{and } Q_{overall} \equiv \frac{P_{fusion}}{\Sigma_{\substack{\text{all beams, ECRH and ICRH} \\ \text{trapped in the plasma}}}} \approx 0.4 \ ,$$

for this axicell MARS mode of operation of MFTF-B. The fusion power $P_{fusion} \approx 640$ kW from the central cell and 190 kW from the two dense axicells. The fact that similar Q's and fusion power obtain for this case in spite of shorter central-cell length (L_c (eff) = 16.5 m versus 32 m for the A-cell design) and smaller central-cell radius ($r_c \approx 0.3$ m, max allowed by 12-T insert, versus $r_c \approx 0.56$ m for the A-cell design) is due to higher central-cell density ($n_c = 4.8 \times 10^{13}$ cm^{-3} versus 2×10^{13} cm^{-3} in the A-cell design). The higher central-cell density is made possible by the higher 12-T circular coil compared to the previous 4-T yin-yang mirror which played the same role. Mapping of densities in thermal-barrier machines leads one to expect higher central-cell/plug density ratios in proportion to the maximum mirror field. However, the central-cell density is not exactly three times higher than in the A-cell design because of the effect of the outer potential drop $\Delta\phi_{pb}$ in the axicell (see Fig. 2.1-2) which accelerates the passing ions through the high-field mirror (see Eq. 14 in Sec. 2.4 for details).

Figures 2.2-4 to 2.2-6 illustrate schematically the central-cell ion-particle flows, central-cell ion-power balance, and central-cell electron-power balance, respectively, for the MARS-mode of MFTF-B. These

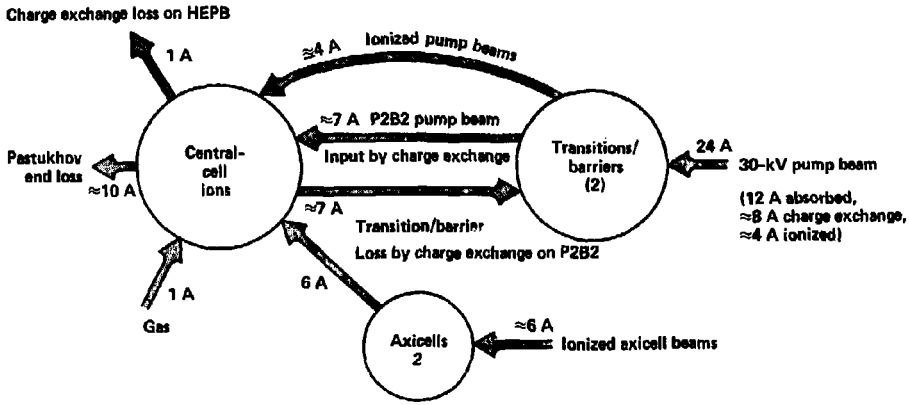

Fig. 2.2-4. Typical central-cell particle balance for MARS mode of MFTF-B.

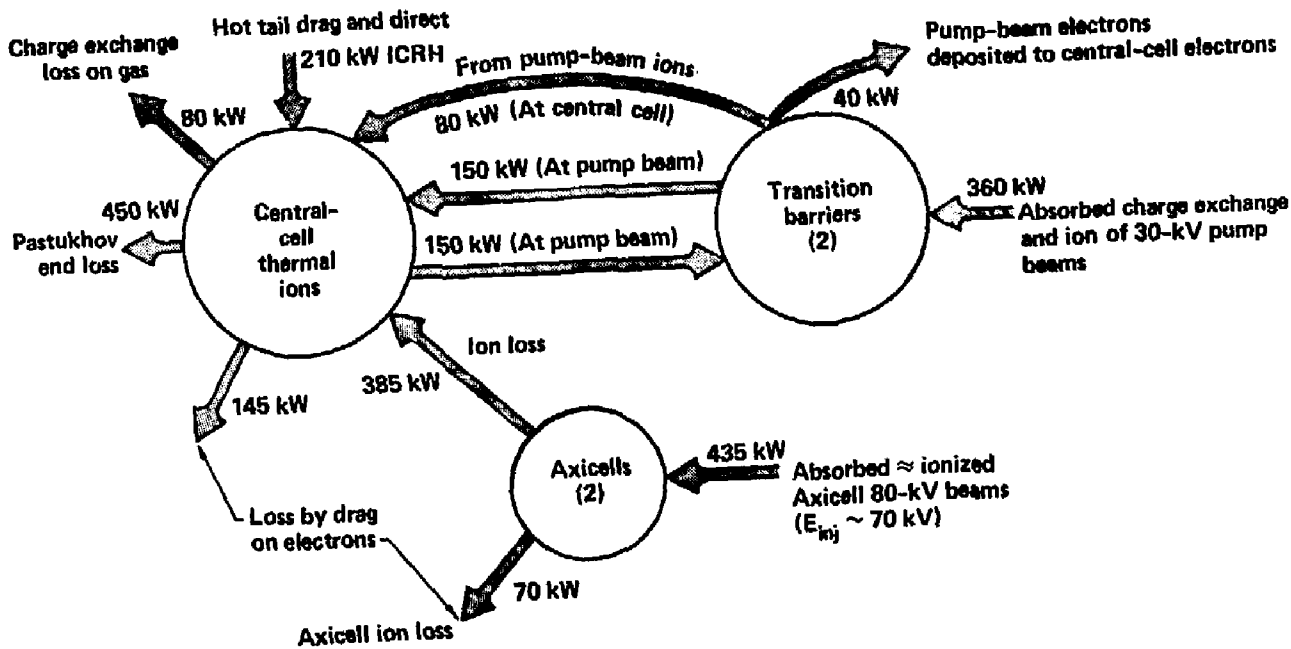

Fig. 2.2-5. Typical central-cell ion-energy balance for MARS mode of MFTF-B.

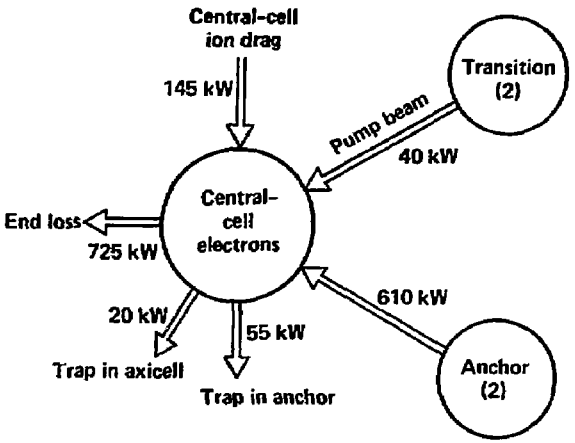

Fig. 2.2-6. Typical central-cell electron-energy balance for MARS mode of MFTF-B.

values correspond to the parameters in Table 2.2-6. Essentially, Fig. 2.2-4 shows that the central cell is fueled by the axicell beams (since the lowest axicell mirror is towards the central cell) and by the 30-kV pump beams of the transition regions, which have enough energy to pass deposited ions over the axicell-potential hill and into the central cell but not over the ϕ_c potential peaks at the extreme ends of the plugs. The axicell-beam power can be varied by a factor of at least two to control the amount of central-cell fueling and heating.

Figure 2.2-5 shows that the central-cell-ion power input from the axicells must be supplemented by ICRH, because an 80-kV beam-voltage limit does not provide enough energy per ion lost.

Figure 2.2-6 shows a simplified electron-power balance (leaving out many of the details) that involve the major parts of the power flow. Input power to the central-cell electron is dominated by the ECRH in the anchors. Hot and warm ECRH electrons in the plugs/anchors originate from the passing central cell electrons reaching the ECRH resonance zones. Furthermore, the electron-confining potential is maximum at the outermost yin-yang mirror. Therefore, scattering and drag losses of these heated electrons, for the most part, ends up rethermalizing back into either the transition or central cell by conduction and convection.

Stability Considerations

Having described the reference-case MARS-mode of MFTF-B, which is consistent with power balance and engineering constraints, we now show it is reasonably consistent with nominal theoretical criteria for plug microstability, trapped-particle stability, and MHD stability for interchange beta limits and MHD-response of hot electrons. Indeed the stability criteria described by Baldwin (Sec. 1 of this report) were used to guide the evolution of this design. We are still in the process of solving MHD stability, including ballooning at low mode numbers, with finite Larmor radius (FLR) and conditions for null parallel current in the transitions and anchors. However, we believe we still have flexibility to lower the beta in the axicell to 10 to 15%, if needed for ballooning (by lowering axicell beam voltage somewhat and raising ICRH power in the central cell), and to further modify the transition-coil design, if needed to reduce the equilibrium parallel currents in the ends.

With respect to plug/anchor microstability, we note that this design for MFTF-B, which puts the thermal barrier in the yin yang with a larger mirror ratio, is very similar to the TMX-U, which is designed stable with respect to present theory for drift-cyclotron-loss-cone (DCLC), axial-loss-cone, and Alfvén-ion-cyclotron modes. Data from testing these predictions will be available in time to guide the location of beams and ECRH in the MFTF-B yin yangs. For the reference-case thermal-barrier MARS mode of MFTF-B, the microstability analysis of Appendix F in this report indicates that a midplane warm-ion fraction, $n_{warm}/n_{hot} \approx 0.75$ at $T_{warm}/T_{hot} > 0.3$, should be nominally stable. This is consistent with the parameters in Table 2.2-6: $n_{warm}/n_{hot} = g_b\, n_{pass}\,(B_A)/n_{slosh}\,(B_A) = 0.8$, and $T_{warm}/T_{hot} \approx T_{iwC}/\left(\frac{2}{3}\, E_{inj}^{slosh}\right) = 0.32$. As noted in Appendix F, the stability boundary varies with the hot-electron axial profile, which can in principle be controlled by the location of the ECRH resonances. Also, to add flexibility, the sloshing-ion density can be decreased some 20% with respect to the passing-ion density.

The stability criteria of Baldwin for conversion of trapped-particle modes to stable drift waves by charge separation in the anchors (see Eq. 1.2 in Sec. 1) can be written for the m = 1 mode as:

$$\omega_{*i}^2 > 4\,\gamma_{MHD}^2\,(1 + A_r)/A_r^2 \quad , \tag{2.2.1}$$

where

$$A_r \equiv \left(\frac{r_c}{\rho_{ic}}\right)^2 \left(\frac{B_c}{B_a}\right) \left(\frac{\overline{g_b\, n_{pass}}}{n_c}\right) \left[\frac{2\, L_A(\text{eff})}{L_c}\right] \tag{2.2.2}$$

is the Rosenbluth parameter; $g_b\, n_{pass}$ is the effective passing-ion density into the anchor minus the passing-electron density, averaged over the good curvature regions of the anchors of effective length $L_A(\text{eff})$. The effective length depends in part on the assumed shape of the trapped-particle mode $\phi(z)$, which has not yet been precisely determined, so therefore $L_A(\text{eff})$ and $g_b\, n_{pass}$ cannot be precisely determined.

Figure 2.2-7 indicates that $g_b\, n_{pass}$ would be about 2×10^{12} cm^{-3} in the MFTF-B yin yang, over a characteristic length of about 2.5 m, if the worst trapped-particle eigen mode rolls off just where the pressure-weighted good

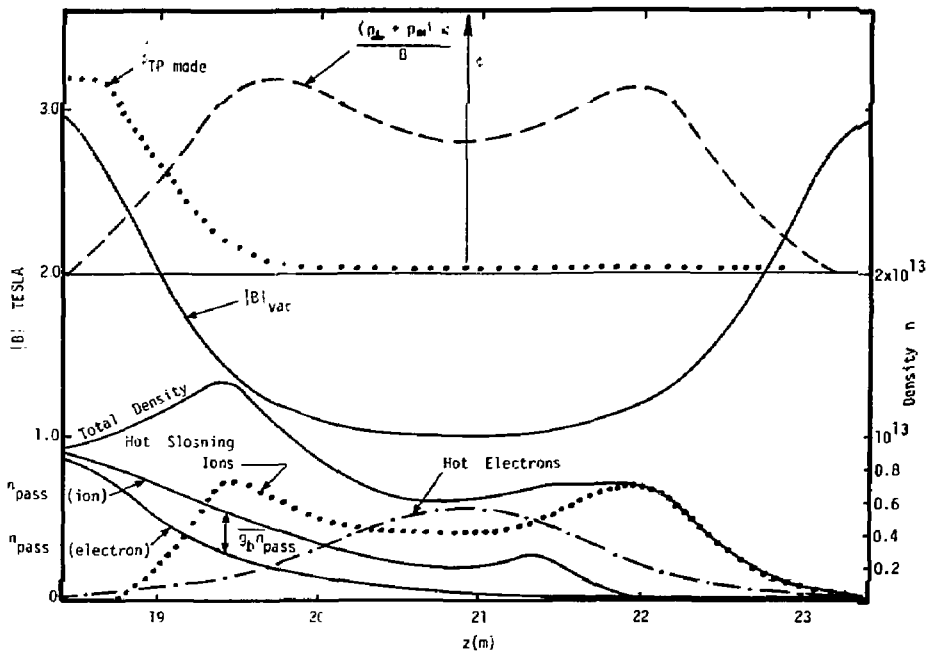

Fig. 2.2-7. Comparison of passing ions and electrons in MFTF-B yin-yang anchor.

curvature in the yin yang begins to rise. Since the trapped cold ions of density $(g_b - 1)n_{pass}$ turn well beyond the mode's roll off (in fact way back near the 12-T high-field mirror) they also contribute to the charge separation [although somewhat (~30%) less effectively than strictly passing ions from the central cell] for yin-yang transition lengths only a few times longer than L_A(eff) (according to Baldwin's analysis using a coupled, three-square-well region model).

The actual effective g_b to use in Eqs. 2.2.1 and 2.2.2 is uncertain to the extent it still depends on the actual "worst" eigenmode shape. Given these uncertainties, we cannot make firm statements now regarding the "margin of safety" for the particular reference case we have chosen for MFTF-B. However, we will shortly indicate how we can vary the operating parameters of MFTF-B to accommodate, up to a factor of four or so, a "worse"-stability boundary than that represented by Eq. 2.2.1. In Eq. 2.2.1, γ_{MHD} is the average MHD growth rate (without anchors), averaged over all the bad MHD drives of the central cell, axicell, and yin-yang transition regions. Since all three regions have comparable drives at present, but the axicell and transition drives might be reduced relative to the center cell by future design optimization, we can characterize γ_{MHD} in terms of the irreducible central-cell drive $\propto R_c^{-1} \propto r_c/L_{tran}^2(cc)$. Hence

$$\gamma_{MHD}^2 \equiv D\,\gamma_{cc}^2 \simeq D\,\frac{2\,T_{ic}\left(\frac{r_c}{p_c}\right)\left(\frac{dp_c}{dr}\right)\,L_{tran}(cc)}{M_i\,r_c\,R_c\,L_c}\quad , \tag{2.2.3}$$

where the proportionality constant D depends on the aggregate bad-curvature regions (being unity in the limiting case of central-cell drive only) and where $L_{tran}(cc)$ is the characteristic central-cell (axisymmetric) transition length. Then using

$$\omega_i^* \simeq \frac{T_{ic}\left(\frac{r_c}{p_c}\right)\left(\frac{dp_c}{dr}\right)}{q\,E_c\,r_c^2}\quad , \tag{2.2.4}$$

where $(r_c/p_c)(dp_c/dr)$ is the pressure-gradient length normalized to central-cell radius, Eq. 2.2.1 can be solved to estimate the required passing density (times the effective g_b):

$$\frac{\overline{g_b n_{pass}}}{n_c} > \frac{8\,D}{\left(\frac{r_c}{p_c}\right)\left(\frac{dp_c}{dr}\right)} \qquad \left(\frac{r_c^{\,2}}{L_{tran(cc)}\, L_{A(eff)}}\right) \left(\frac{B_A}{B_c}\right) . \tag{2.2.5}$$

The interesting feature exhibited by Eq. 2.2.5 is that the required passing-ion-density fraction for trapped-particle stability actually decreases with plasma radius r_c, in spite of the fact that $A_r \propto r_c^2/\rho_{ic}^2$ would be reduced. This is because $\omega_*^2 \sim 1/r_c^4$ overpowers the r_c^2 dependence of A_r. Thus smaller radius plasmas, relative to axial scale lengths, allow smaller $g_b n_{pass}/n_c$ and hence higher tandem-mirror Q:

$$Q \propto \frac{P_{fusion}(\text{central cell})}{P_{injection}(\text{plugs})} \propto \left(\frac{n_c}{g_b\, n_{pass}}\right)^2 . \tag{2.2.6}$$

One caution is that r_c cannot be made too small relative to ρ_{ic} or else other instabilities such as ion hybrid drift waves might become dominant.

Table 2.2-7 presents key stability-related parameters for MFTF-B and also for reactors to show that the high $\omega_*/\gamma_{MHD} > 1$ regime for MFTF-B can also be utilized in reactors. Note in Table 2.2-7 that $r_c/\rho_{ic} \sim 13$ in MFTF-B, while $r_c/\rho_{ic} \sim 40$ still allows $\omega_* > \gamma_{MHD}$ in reactors (because γ_{MHD} is small in long, thin aspect-ratio plasmas).

Some flexibility exists in the MFTF-B operation to accommodate a larger passing-ion fraction than is estimated by Eq. 2.2.5, by means other than simply reducing the plasma radius further (which would begin to limit $r_c/\rho_{ic} < 10$). In the event n_{pass}/n_c needs to be increased by more than a factor of two, it would have to be done in part by reducing n_c, since n_{pass} could not be increased more than twice in the anchor without exceeding available ECRH power or, just beyond that limit, exceeding the cutoff density for microwave penetration. Thus, n_c would be limited beyond that which could otherwise be supported by the combination of axicell-potential bump and the 12-T mirror. The limiting case in which the axicell beam and the transition pump beam are turned off, allowing the transition to fill to a Maxwellian ion distribution, is the TMX-U mode described in Sec. 2.3.2 (Fig. 2.3-3). By varying the amounts of transition pump beams and axicell beams, one could vary n_c over a range of four while keeping the anchor/plug parameters essentially constant (see Fig. 2.2-8). If the central-cell ICRH

TABLE 2.2-7. Trapped-particle stability parameters for MFTF-B and for axicell tandem-mirror reactors.

Parameter	MFTF-B (reference case thermal barriers)	Mirror-Advanced Reactor Study (MARS) (candidate)	Original Axicell Reactor (FY81 report UCID 19271)
r_C (m)	0.3	0.4	1.0
T_{iwC} (keV)	15	35	40
B_C (T)	1	4.7	3.0
r_C/ρ_{ic}	13	40	60
n_C (cm^{-3})	4.5×10^{13}	4.5×10^{14}	1.6×10^{14}
B_A (T)	1	2	1.4
$g_b\, n_{pass}$ (B_A)	2×10^{12}	1×10^{13}	$\sim 1 \times 10^{11}$
$\frac{r}{p}\frac{dp}{dr}$ (gradient parameter)	2.8	3.0	3.0
$D \equiv \gamma_{MHD}/\gamma_{cc}$	3	6	9
ω_{*i}/γ_{MHD}	1.6	1.0	0.21
L_{tran}(cc) (m)	5	12	12
L_A(eff) (m)	2.5	4	3
L_c(eff) (m)	16.5	150	150
A_r (Rosenbluth Parameter)	2.3	4.5	0.2
$g_b\, n_{pass}/n_c$	4×10^{-2}	2.2×10^{-2}	6.3×10^{-4} vs 0.3 required for stability

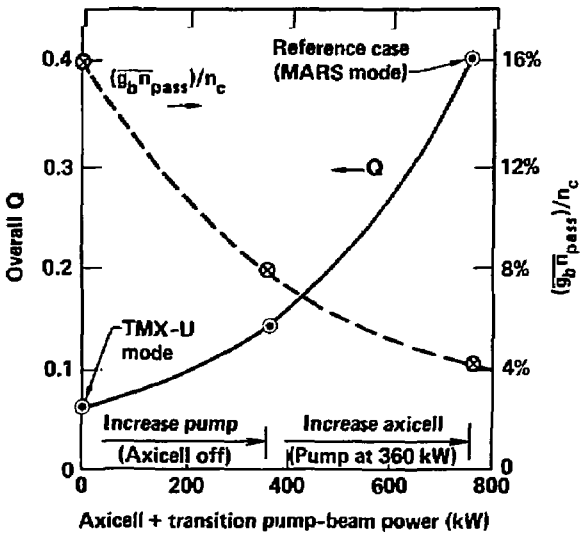

Fig. 2.2-8. Variation of overall Q and of ion fraction passing into the yin-yang anchor as a function of axicell- and pump-beam power.

heating is also varied appropriately, T_{ic} and $(n\tau)_c$ could also be kept nearly constant.

We turn now to MHD-interchange stability. Figure 2.2-9 shows an example of a flute interchange calculation using TEBASCO (see Appendix B) for the vacuum magnetic fields of the coil set of Fig. 2.2-4, with pressure models appropriate for the reference-case thermal barrier (MARS) mode of MFTF-B operation. Although the flute beta limits would change with finite beta fields and for coils readjusted to null parallel current, Fig. 2.2-9 indicates that overall flute interchange stability is roughly consistent with the betas required in the reference case (see Table 2.2-6). These betas ($\beta_c = 0.5$ in the central cell, $\beta_x = 0.2$ in the axicell, and $\beta_T = 0.05$) give rise to comparable contributions to bad curvature drive (weighted with pressure) from each of those three regions, as can be seen in Fig. 2.2-9. Thus, MHD-interchange stability requires a *nominal* anchor beta $\beta_A \approx 0.5$. In order for this anchor beta to count as good MHD pressure (as assumed in the flute interchange calculation of Fig. 2.2-9), the local midplane sloshing-ion beta must well exceed the Lee-Van Dam criterion so that the hot electrons, which make up most of the $\beta_A = 0.5$, will have an MHD response:

$$\beta_{slosh} \gg \frac{2\, r_n}{R_A} \quad . \tag{2.2.7}$$

For the reference case, $\beta_{slosh} \approx 0.05$, $r_n \approx 0.15$ m (for a parabolic radial density profile) and $r_A = 0.3$ m anchor radius. The TEBASCO code calculates a radius of normal curvature $R_A = 0.5\, r_A/(YAH) \approx 15$ m at the anchor midplane. Thus, the Van-Dam limit (Eq. 2.2.7) is exceeded by a factor of about 2.5. Thus, according to Eq. 1.1 in Sec. 1, the effective hot-electron beta is degraded by a factor of about 0.7, and the effective anchor beta is $0.5\ (0.7) + 0.05 = 0.4$. That may still be sufficient for interchange stability at $\beta_c = 0.5$, since Fig. 2.2-9 shows marginal stability at $\beta_c = 0.6$. Otherwise, the hot-electron beta could be increased above 0.5 to compensate, provided ion adiabaticity is maintained.

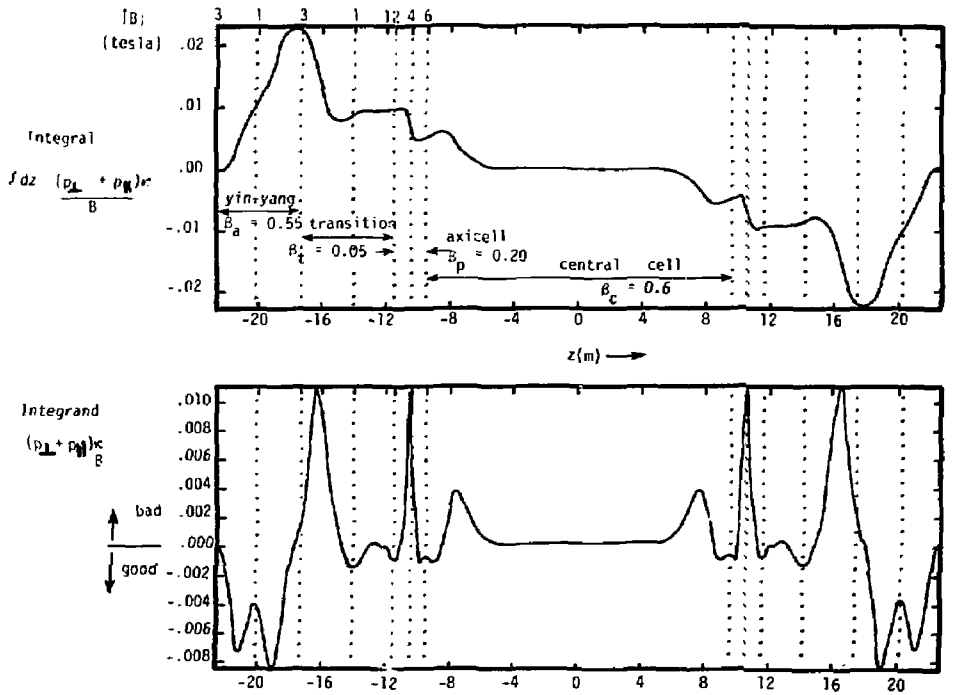

Fig. 2.2-9. MARS-mode (vacuum) flute interchange.

2.2.4. START-UP SCENARIO FOR THE MARS MODE

Evaluation of start up of MFTF-B with thermal barriers shows that the scenario planned for TMX-U is also appropriate to MFTF-B. Therefore, for MFTF-B, we will be able to take advantage of the testing and further developing of these ideas in TMX-U. The start-up of MFTF-B with thermal barriers in an improved axicell mode differs from start-up scenarios for MFTF-B in an A-cell mode in one major way. Rather than build up to high density as rapidly as possible in a tandem mode and then form the thermal barrier in an outboard A-cell, we must form thermal barriers at a low density ($< 10^{12}$ cm^3), then continue the buildup in a thermal-barrier mode. The reason is that the hot-electron power balance requires heating electrons to mirror-confined energies ($>> 10^4$ eV) at low densities; otherwise, collisional losses will clamp the electron energy below a few kiloelectron volts.[2.7] With an A-cell outboard from the MHD anchor, the hot-electron A-cell could start up at low density after the anchors and central cell were at high density. With the axicell, hot electrons for the thermal barrier are in the anchor; MHD stability then requires that the beta (throughout MFTF-B) be within an order of magnitude of the plug betas; hence, the plasma density must build up slowly throughout.

We examine start up from the viewpoint of satisfying the following set of physics constraints:

- Particle and power balance for each species in each cell.
- MHD stability.
- Microstability for both hot ions and hot electrons, and trapped-particle modes.

For two reasons the most difficult period in which to satisfy these constraints is before thermal-barrier formation.

- First, more power is required at this time, because the plasma is confined only by magnetic mirrors, with little enhancement by electrostatic plugging.
- Second, more power is required because absolute microstability is not assured without substantial electrostatic confinement of warm ions.

We have evaluated several of these constraints at times before barrier formation and find that, even then, they define an operating window in

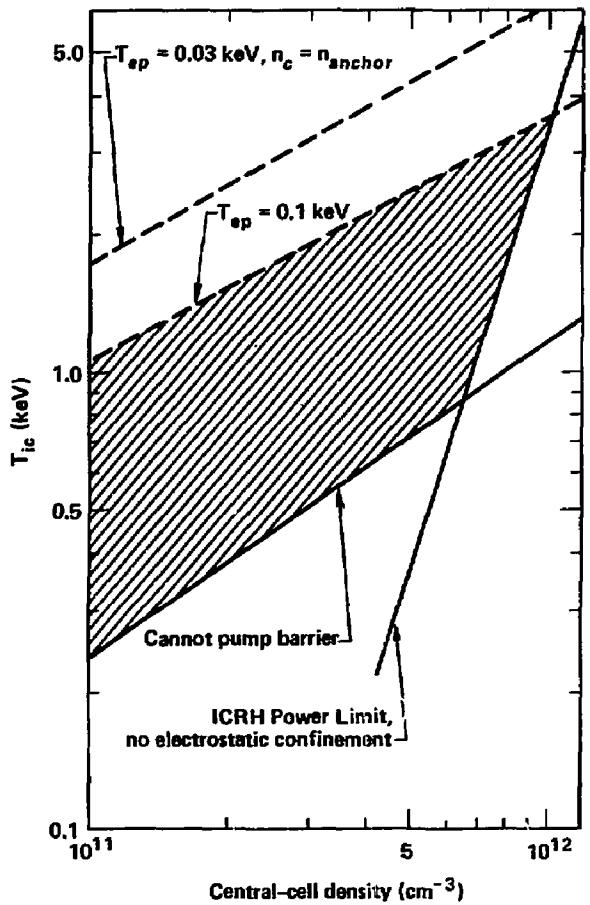

Fig. 2.2-10. Operating window during start-up of MFTF-B.

temperature-density space, as shown in Fig. 2.2-10; the central-cell ion-particle and power balance will limit the maximum density to $n \approx 10^{12}$ cm^{-3}, similar to the initial limit from hot-electron power balance. The requirements for pumping the barriers provide a lower bound on the ion temperature. Hot-ion DCLC stability, because of streaming ions alone, provides a soft upper limit to the ion temperature.

We are continuing to evaluate the other constraints; until these evaluations are complete, we will use qualitative arguments. The MHD stability was satisfactory and was less restrictive than stream stabilization of DCLC on TMX-U, and we expect similar results for MFTF-B. Stability to trapped-particle modes is less restrictive during start up than at design level, as discussed in the next paragraph. We expect the microstability of the plugs to be substantially enhanced by sloshing ions and by mirror-confined electrons, thus increasing the upper T_{ic} limit above that resulting from microstability by streaming ions alone (see Fig. 2.2-10).

Stability to trapped-particle modes requires maintaining an adequate ratio of passing to central-cell ions. This, as well as MHD stability, will be improved during start up by keeping the central-cell density low until the anchor-plasma parameters are near design level. Then the central-cell density can be increased to its limits. The greatest susceptibility to trapped-particle modes will occur before thermal-barrier formation, when the passing-ion density will be lower because of the lack of a potential peak to reflect these ions. But, because the planned ICRH power of 400 kW into the plasma is four times the computed power losses during this time, we can tolerate a substantial degradation of the confinement because of instabilities without impairing our ability to start up MFTF-B.

The plasma parameters will be kept in the operating window by controlling the timing and the power or current of the following "knobs" as indicated in Fig. 2.2-11:

- Plasma streaming guns.
- Gas boxes.
- ECRH.
- Central-cell ICRH.
- 0.5- and 30-s, 80-keV, sloshing-ion neutral beams in the anchors.
- 0.5- and 30-s axicell, 80-keV neutral beams.
- Axial and axicell pump neutral beams.

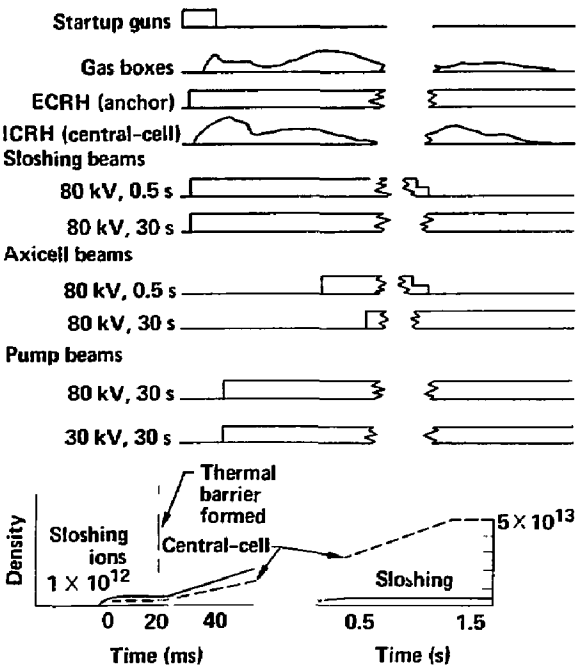

Fig. 2.2-11. Start-up of MFTF-B Axicell with thermal barriers.

We expect the knobs to be used as follows: Plasma streaming guns will provide a seed plasma of minimum density. The ECRH will be used at maximum power to build up the hot-electron density as fast as possible. The hot electrons provide several benefits: they aid MHD stability and hot-ion microstability; they improve the operation of the thermal barriers; and they prevent the plug plasma from being destroyed by incident gas. It is the ions associated with the hot electrons that provide sufficient trapping of sloshing beams to balance charge exchange losses on gas and pump beams. In previous scenarios that lacked hot electrons, a rapid buildup to high density was required to allow the trapping rate to exceed the charge-exchange loss rate.

Central-cell ICRH will be turned on near full power before the central-cell density exceeds 10^{12} cm^{-3} in order to heat the central-cell and passing ions to a low collisionality. The power level will then be programmed down to keep T_{iwC} below the DCLC and MHD boundaries.

Sloshing-ion beams must be turned on at full power soon after the ICRH in order to maintain MHD stability.

The gas boxes will be turned on to fuel the plasma after the plasma streaming guns are turned off. They will be programmed initially to keep the density within the window just discussed. After a thermal barrier is formed at low density, the gas will be programmed to maintain the plug density sufficiently higher than the hot-electron density to achieve hot-electron microstability.

In steady state, most of the fueling and power for the central cell will come from the axicell and pump beams. But, the gas box and central-cell ICRH are available during buildup so that operational flexibility is not restricted by both the pumping and the central-cell heating being tied to these beams. Pump neutral beams will be off until the other conditions for establishing a thermal barrier are either established or are within a pumping time constant (a few milliseconds) of being established. The axicell beams provide a small potential peak to reduce the fraction of the central-cell ions that become passing ions. The passing ions are further reduced by the pump beams. The pump beams must be turned on to form the thermal barrier. The axicell beams enhance the performance of the thermal barrier, so are turned on when required by the particle or power balance.

The transition from 0.5- to 30-s-duration neutral beams can be staged to avoid a sudden decrease in the beam current without a simultaneous decrease in the gas associated with the 0.5-s beams. The gas incident on the plasma will decrease along with the beam current if one beam is turned off at a time and one gas-pumping time (approximately 50 to 100 ms) is allowed before turning off another.

An approximate central-cell power balance used for start up analysis is shown in Fig. 2.2-12, both before and after thermal-barrier formation. The maximum power requirement is 600 kW at design level. However, the axicell beams contribute about 200 kW to the central cell, leaving 400 kW to be supplied by the ICRH system. We plan to use the fundamental resonance, ω_{ci}, for start up and initial heating because that directly heats the bulk of the ion distribution, as required to minimize collisional filling of the thermal barrier. Evanescent fast-wave heating at ω_{ci} has been demonstrated on the Phaedrus tandem mirror (see discussion and references in Ref. 2.8) to couple sufficient power to meet the requirements shown in 2.2-12. After the density increases sufficiently for a fast wave to n to propagate, we expect that the fundamental resonance will no longer heat effectively. We will then use $2\omega_{ci}$ heating. At these high densities ($> 2 \times 10^{13}$ cm^{-3}), heating the tail of the ion distribution will not be a problem because collisions will transfer sufficient power from the tail to the bulk. An attractive way to accomplish this heating using one transmitter and an antenna is to place the antenna near the 2-T field of the central cell and operate the transmitter near 15 MHz. This provides heating at ω_{ci} in the near field of the antenna until the density exceeds $\sim 2 \times 10^{13}$ cm^{-3}, at which point the wave will propagate to the midplane where heating will occur at $2\omega_{ci}$. We will continue to evaluate whether a more flexible two-frequency system might be more effective. The ICRH experiments in TMX-U, as well as in other tandem mirrors, will provide additional data on which to base a decision.

Operation outside the desired window can be corrected in the following ways. Too collisional a barrier can be corrected by increasing the ICRH power or varying its timing to increase T_{ic}, by decreasing the gas-feed rate or start-up-gun power, or by varying their timing to decrease the density. The MHD stability can be regained by increasing the sloshing neutral-beam current, decreasing the pump-beam current, or by decreasing the current of neutral gas incident on the plasma core, all of which will increase the density of

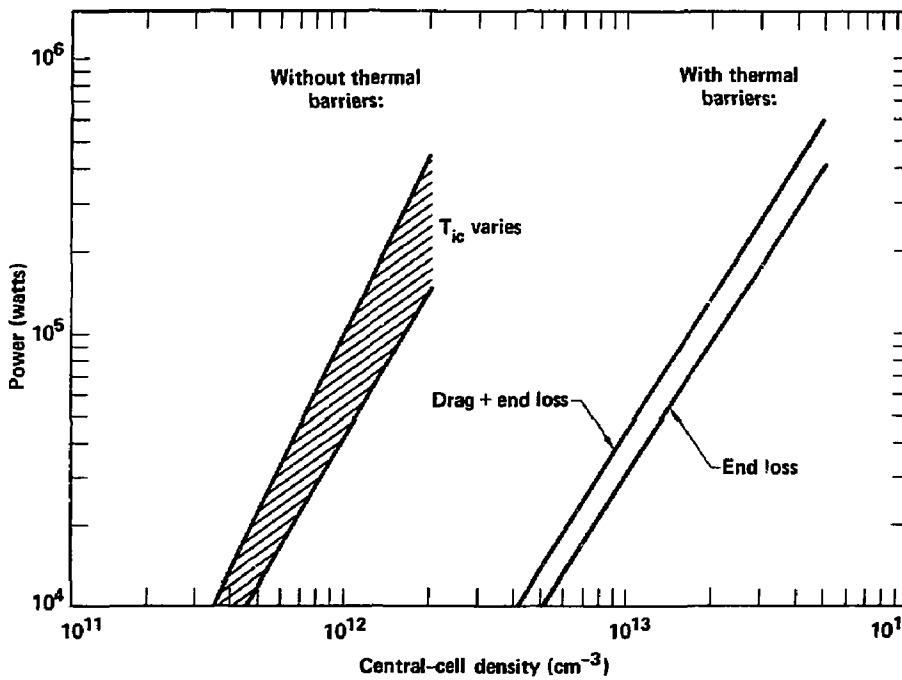

Fig. 2.2-12. Approximate central-cell power balance used for start-up.

sloshing ions. MHD stability can also be increased by decreasing the axicell beam current. Control of the neutral gas current reaching the plasma core may require controlling the plasma boundary density and temperature. Both MHD and DCLC stability can be regained by programming the ICRH power downwards. Programming the density would have no effect if the ICRH power coupled into the plasma were exactly proportional to the density, but since the proportionality is only approximate, some control over T_{ic} is available by varying the gas-box input. Operation at too high a density can be corrected by reducing the start up gun power or duration and by reducing the gas-box current.

REFERENCES

2.7. B. W. Stallard, Y. Matsuda, and W. M. Nevins, "Fokker-Planck Calculations of Electron Cyclotron Resonant Heating (ECRH) in Mirror Geometry", in Proc. of Second Workshop on Hot Electron Ring Physics, San Diego, CA, December 1981, LLNL Report, UCRL-86826 (1981).

2.8. A. W. Molvik and S. Falabella, Use of ICRH for Start-Up and Initial Heating of the TMX-U Central Cell, LLNL Report, UCID-19342 (1982).

2.3. ALTERNATE OPERATING MODES

2.3.1. KELLEY TDF-LIKE MODE

The Kelley TDF-like mode differs from the thermal-barrier MARS mode mainly by the introduction in the central cell of a neutral-beam injected, hot component that is predominantly mirror confined. The hot component dominates the neutron production because of its higher temperature and density compared to the central-cell warm component, which is potentially confined and Maxwellian. The warm component is required for microstability of the hot component. Axial profiles of B, ϕ, and n are given in Fig. 2.3-1, and the parameters are given in Table 2.3-1. The axicell is eliminated (see MHD discussion) in the Kelley-TDF mode. Although the Kelley-TDF mode has a higher physics Q_c than the thermal-barrier MARS mode (0.7 compared to 0.6), the scaling associated with mirror confinement, compared to potential confinement, reverses the ordering for reactor conditions. However, as pointed out by Fowler and Logan,[2.9] the physics associated with the TDF mode indicates that a tandem-mirror machine about the size of TMX could provide fusion nuclear-engineering data. The lower τ value (0.16 s for the TDF mode compared to 1 s for the MARS mode) allows equilibrium to be reached with 0.5 s beams without the aid of 30 s duration beams. Here we describe for the TDF-mode the physics constraints involving microstability, MHD, thermal-barrier formation, the trapped-particle instability suggested by Berk and Rosenbluth,[2.10] and power flow.

Microstability

As with the thermal-barrier MARS mode, the microstability requirements of the anchor are satisfied by passing ions, which become potentially trapped in the anchor. The warm component within the central cell has a density level high enough to establish a monotonic distribution.

Magnetohydrodynamics (MHD)

The predicted experimental value of β_c, at a fixed B_c value for the Kelley-TDF mode, is higher than in the thermal-barrier MARS mode because of the mirror-confined hot ions. By increasing the central-cell magnetic field from 1.0 to 1.6 T, lowering the transition beta, and eliminating the unstable drive

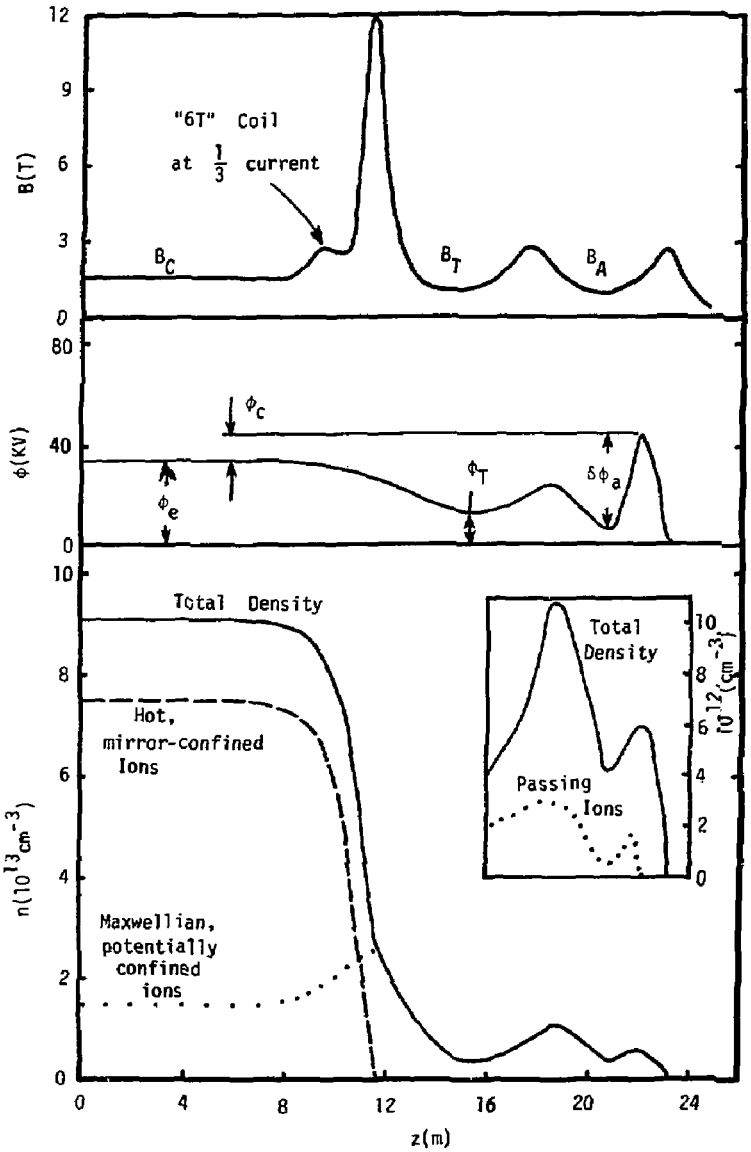

Fig. 2.3-1. Axial profiles in Kelley mode of MFTF-B Axicell.

Table 2.3-1. Central-cell plasma parameters.

Central cell (C)	Thermal barrier-MARS	Kelley-TDF	TMX-U
B_C (T)	1	1.6	1
ϕ_e (kV)	50	34	50
ϕ_C (kV)	30	11	30
n_{eC} ($10^{13}cm^{-3}$)	4.8	9.1	1.3
n_{iwC} ($10^{13}cm^{-3}$)	4.4	1.6	1.2
n_{ihC} ($10^{13}cm^{-3}$)	0.4	7.5	0.1
T_{eC} (kV)	9	6	9
T_{iwC} (kV)	15	15(⊥), 10(∥)	15
T_{ihC} (kV)	35	35	35
$(n\tau)_{eC}$ ($10^{13}cm^{-3} \cdot s$)	4	1.9	5
$(n\tau)_{iwC}$ ($10^{13}cm^{-3} \cdot s$)	5	0.6	5
$(n\tau)_{ihC}$ ($10^{13}cm^{-3} \cdot s$)	2	1.4	2
P_C^{Fusion} (kW)	640[a]	4200	80
$P_{C\ trapped}^{ICRH}$ (kW)	210	0	60
$P_{C\ trapped}^{Beam}$ (kW)	0	5600	0
β_C	0.5	0.54	0.12
r_C (cm)	30	24	30
$i_{C\ trapped}^{gas}$ (Atom Amps)	1.3	0	1.3
Q_C	0.6	0.7	0.6
Q_{Total}	0.4	0.6	0.06
$L_C^{effective}$ (cm)	1650	2060	2810

[a]An additional 190 kW of fusion power are generated by the axicells.

from the axicell, we find the theoretically predicted β_C limit is higher than the experimental value required. The "6-T" coil is energized at a current level equal to one-third the full value. Any less current results in a dip in the magnitude of B before it reaches the axicell, which could lead to potential MHD problems. The "12-T" coil remains energized at full current to allow the plasma column to clear its smaller internal-diameter-coil case.

Thermal-Barrier Formation

The potential depth of the thermal barrier $\delta\phi_a$, with respect to the peak confining potential, is approximately half as large in the Kelley-TDF mode as in the thermal-barrier MARS mode (40 kV compared to 70 kV). Therefore, less ECRH power is required for the former. For $\delta\phi_a$, the temperature of the potentially trapped warm electrons within the anchor is the controlling factor along with the sloshing-ion density. The neutral-beam pumping requirements are approximately the same because the sloshing-ion density depression (3 to 1 between its turning point and midplane value) does not change between the operating modes and because the passing ion density is the same.

Trapped-Particle Instability

The physics constraints imposed by the trapped particle instability are evaluated in terms of the required passing density, n_{pass}, normalized to the central-cell density, n_C. The requirement is given by Eq. 2.2.5, except that in the TDF mode the required value of n_{pass}/n_C is increased by the ratio of the mirror-confined ion energy to the warm potentially confined ion temperature of the central cell. On the other hand, changes in other plasma parameters (e.g., central-cell radius and magnetic field), along with a smaller value of the transition beta, lowers the value of n_{pass}/n_C that is necessary for stability in the TDF mode to about half the value required in the MARS mode.

Power Flow

The physics model developed in Sec. 2.4 can be simplified when applied to the alternate modes of MFTF-B (Kelley TDF-like and TMX-U-like). All the terms involving the axicell are eliminated and the power and particle inputs from the P2B2 pumping beams are either absent or extremely small compared to the remaining terms. A generalized power-flow diagram of the central cell,

derived from Eq. 2.4.42 is given in Fig. 2.3-2. A hot-ion component is added to allow a beam-driven or ICRH-produced tail in the ion distribution to be present. In Table 2.3-1 the central-cell plasma parameters for the alternate modes are compared with those for the thermal-barrier MARS-mode reference.

The anchor beam and ECRH requirements for the Kelley-TDF can easily be scaled from the numbers for the thermal-barrier mode (Sec. 2.2.3), using the equations of Sec. 2.4. The hardware requirements never exceed those of the thermal-barrier mode.

The central-cell plasma Q value, Q_c, is given by

$$Q_C = \frac{E_{D-T}^{Fusion}}{4} \left\{ \frac{n_{ihC}^2 \langle\sigma v\rangle^h + n_{iwC}^2 \langle\sigma v\rangle^w + 2n_{ihC}n_{iwC}\langle\sigma v\rangle^{hw}}{\frac{n_{ihC}^2}{(n\tau)_{ihC}^{mirror}}(E_{ihC} + \phi_e + T_{eC}) + \frac{n_{iwC}^2}{(n\tau)_{iwC}^{Pastukhov}}(\phi_C + T_{iwC} + \phi_e + T_{eC})} \right\}, \tag{2.3.1}$$

where a 50:50 mix of D-T is assumed for both the hot and warm species and E_{D-T}^{Fusion} = 17.6 MeV. For T_{ihc} = 35 keV and T_{iwc} = 15 keV, we used $\langle\sigma v\rangle^h = 7.4 \times 10^{-16}$, $\langle\sigma v\rangle^w = 2.6 \times 10^{-16}$, and $\langle\sigma v\rangle^{hw} = 3.2 \times 10^{-16}$ cm^3•s^{-1}. The value of Q_{Total} is calculated by adding the fusion power and the power losses from the other cells.

The central-cell magnetic-field strength for the Kelley-TDF mode is at the maximum value of 1.6 T rather than at 1 T, as in the thermal-barrier mode, to allow $n_{ihC} \propto \beta_C B_C^2$ to reach a maximum level. Given that the hot-ion component is generated from neutral-beam injection, the value of E_{ihc} can be derived from the Logan-Mirin-Rensink model.[2.11] The MHD-limited value of β_C gives in turn n_{ihC}, with n_{iwC} determined from Fokker-Planck studies of the central-cell ion distribution.

The ϕ_C value was chosen high enough to minimize the power flow through the warm-ion channel $I_{iwC}^{loss} \propto 1/(n\tau)_{iwC}^{Pastukhov}$ but low enough to keep $(\phi_e + \phi_C)$ below the thermal-barrier mode. After determining (ϕ_e/T_{eC}) from equating electron- and ion-Pastukhov-particle losses, the values of T_{iwC} and T_{eC} can be determined from the power-balance equations described in Fig. 2.3-2. The trapped neutral-beam power must support the power losses associated with both the ion- and electron-particle losses.

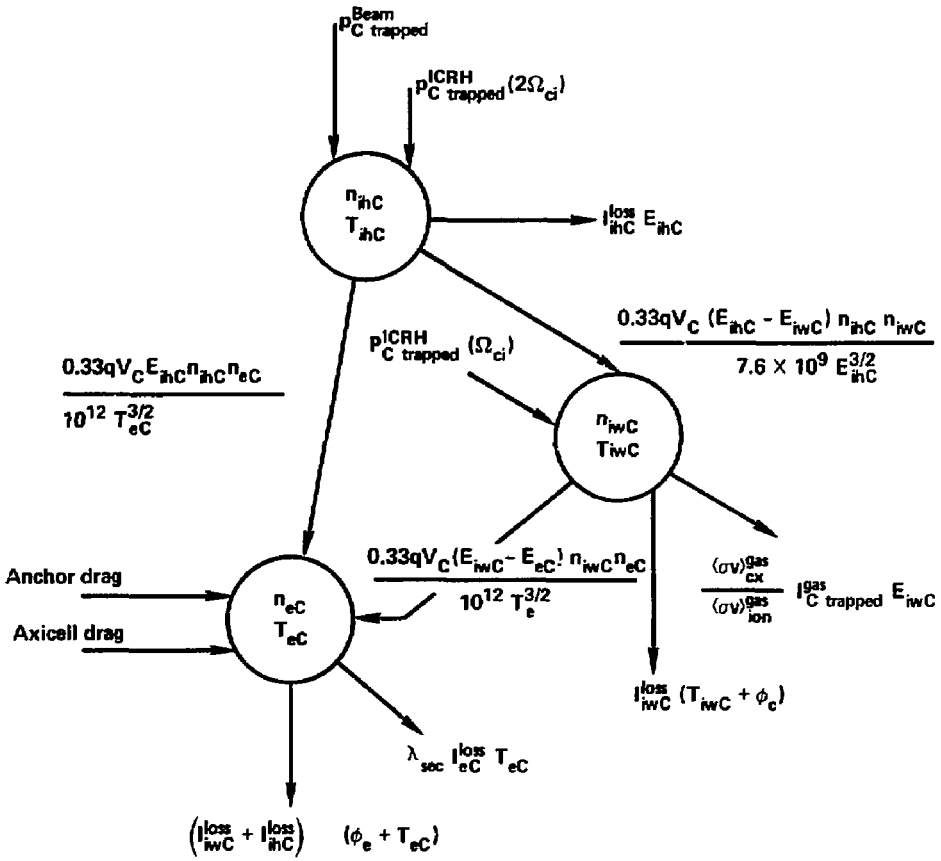

Definitions:

$\langle n^2 \rangle = 1/3\,n^2$ for $n(r) = n(o)\,[1 - (r^2/r_C^2)]$

$I_{ihC}^{loss} = 1/3\,q\,V_C\,n_{ihC}^2 / (n\tau)_{ihC}^{mirror}$

$I_{iwC}^{loss} = 1/3\,q\,V_C\,n_{iwC}^2 / (n\tau)_{iwC}^{Pastukhov}$

$I_{eC}^{loss} = 1/3\,q\,V_C\,n_{eC}^2 / (n\tau)_{eC}^{Pastukhov}$

$\lambda_{sec} = I^{sec} / I_{eC}^{loss}$

$V_C = \pi r_C^2\,L_C^{effective}$ with $L_C^{effective} = B_{mid} \int dl/B$

Fig. 2.3-2. Central-cell power flow for alternate modes.

The pumping requirements in the transition are no greater than the thermal-barrier numbers because the warm-ion losses are less in the Kelley-TDF mode. The ECRH heating is also less since ($\phi_e + \phi_c$) is approximately half the thermal-barrier value. No gas-current feed is required because of the large amount of trapped neutral-beam current that eventually joins the warm-ion distribution.

2.3.2. TMX-U-LIKE MODE

The TMX-U-like mode is very similar to the thermal-barrier MARS mode in terms of B, ϕ_e, ϕ_c, and $(n\tau)_{iwC}$ but operates at lower n_{iwC} (1.2×10^{13} compared to 4.4×10^{13}). The axial profiles of B, ϕ, and n are given in Fig. 2.3-3, and the parameters are given in Table 2.3-1 of Sec. 2.3.1. The TMX-U mode differs from the previously discussed MARS and TDF modes by the absence of neutral-beam pumping within the transition region between the central cell and the anchor. The only neutral beams required are those associated with the anchor. Because of the long particle lifetimes (approximately 4 s), the 0.5-s beams are not able to support this experiment alone. Long pulse (30-s) beams and ECRH and ICRH are required but at no larger power levels than for the thermal-barrier mode.

Microstability

The plasma parameters within the anchor that are associated with the sloshing ions and ECRH electrons are identical in the TMX-U and MARS modes. The passing-ion density, however, at the inside 3-T mirror of the anchor is four times greater for the TMX-U mode (1.2×10^{13} cm^{-3} compared to 0.3×10^{13} cm^{-3}). All microstability requirements of the anchor are, therefore, easily satisfied. The central cell has only a small percentage of hot ions (less than 10%). This amount does not perturb the inherent microstability of the Maxwellian distribution, which is potentially confined.

Magnetohydrodynamics (MHD)

The theoretically predicted limit of β_c is lower in the TMX-U mode (12% compared to 50% in the MARS mode) because of the increase in the destabilizing drive associated with having the transition density, n_T, equal to the central-cell density, n_c.

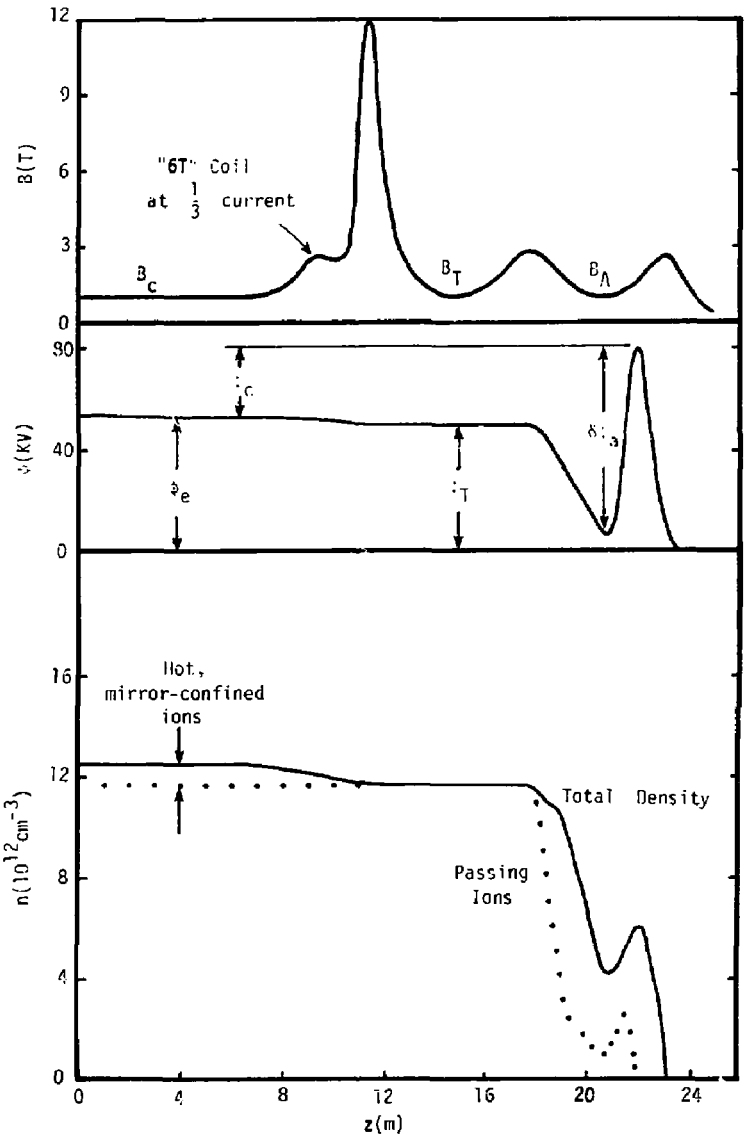

Fig. 2.3-3. Axial profiles in TMX-U mode of MFTF-B Axicell.

Thermal-Barrier Formation

Because the anchor parameters are the same for the TMX-U and MARS modes, the barrier formation will be the same in terms of ECRH power. The increased passing density mentioned in the microstability discussion might require additional neutral-beam pumping.

Trapped-Particle Instability

Because the "worst picture" of this instability allows the amplitude of the fluctuations to locate where the growth rate is maximized and because the anchor parameters are the same in the TMX-U mode, the minimum n_{pass}/n_c required for stability (and hence maximum n_c) is the same in the TMX-U and MARS modes. However, since barrier pumping only occurs in the yin yang, the 12-T coil does not affect n_c, which is limited to a value four times lower in the TMX-U mode compared to the MARS mode. Thus, trapped-particle stability is satisfied by a margin of four.

Power Flow

The long particle lifetime ($\sim$ 4 s) requires the duration of power input into the central cell to exceed the 0.5-s-duration beams. The ICRH power available (see Sec. 2.2.3) for the thermal-barrier MARS mode more than satisfies the needs of the TMX-U mode. The amount of trapped ICRH power, $P_{C\ trapped}^{ICRH}$, necessary to support T_{iwC} of 15 keV is estimated by using the Logan-Mirin-Rensink model (Ref. 2.11) to calculate E_{ihC} and by using the power flow in the warm-ion channel (see Fig. 2.3-1). Central-cell particle losses from charge-exchange with the high-energy pump beam and from passing particles trapped within the anchor have been ignored. Enough ICRH power is available so that additional power losses can be met if these charge-exchange losses become important or if the E_{ihC} estimate is inappropriate for ICRH heated plasmas. The value of $P_{C\ trapped}^{ICRH}$ does not scale with n_{iwC}^2 because a large fraction of the power input into the central cell in the thermal-barrier case came from the axicell beam and the transition pumping beam (see Eq. 2.4.42 in Sec. 2.4).

The effective central-cell length, $L_c^{effective}$, includes the $B_T \int \frac{dl}{B}$ contribution to $B_c \int \frac{dl}{B}$, because the density is uniform from the central cell through the transition (see Fig. 2.3-3), as is the case for the present TMX-U experiment.

2.3.3. TARA-LIKE MODE

In the event some as-yet undiscovered effect other than charge separation can stabilize the trapped particle mode, it would be prudent to design the axicell in MFTF-B in such a way as to allow conversion to the TARA-like configuration (see Ref. 2.1), to have the thermal barrier generated in a larger mirror ratio axicell, and to require a minimum of conversion time and cost. At present, we require the 6-T and 12-T axicell coils for the MARS-mode to be usable in a TARA-mode; we switch their order along the z-axis and spreading them apart from 2 to 4 m to allow ECRH at 1 T and sloshing-ion injection into a larger mirror ratio. Figure 2.3-4 shows an early MFTF-B design for a TARA-configuration magnet set, along with the appropriate axial profiles of field, density, and potential. Corresponding plasma parameters for this early TARA-mode set are given in Table 2.3-2.

The only differences between this early TARA-mode design and one suitable with the present magnet set converted to the TARA-configuration would be that the yin yang would have a mirror ratio of 3:1 instead of 2:1, and a longer length of 5.2 m instead of 3.4 m, as well as a slightly shorter central cell (with 14 solenoid coils as planned). Since the midplane yin-yang field ($B_A \approx 1$ T) and beta value ($\beta_A \approx 0.5$) would be the same, anchor parameters might be similar to those given in Table 2.3-2.

In the conversion to the TARA-mode, the perpendicular axicell beam of the MARS-mode is expected to remain approximately in place and serve as a sloshing-ion beam when the inner axicell mirrors are moved further toward the central cell to get the desired mirror ratio. The axicell beams thus would hit perpendicularly at a mirror ratio of 1.5 to 2 to make sloshing ions. The 30-kV pump beams (P2B2), however, would have to be translated about 4 m towards the central cell (still at about 30^0 angle) to pump the axicell. Moving ECRH from the yin yangs to the axicells would then mostly complete the conversion to the TARA-mode. Present best estimates are that it will take a few months and about two million dollars to make the conversion.

Because the estimated achievable plasma parameters and performance levels (Q) of this early design for the TARA-configuration (Table 2.3-2) are roughly comparable to the reference-case MARS-mode (Table 2.2-6), what would be the advantages of the TARA-mode compared to the MARS-mode? One advantage would be that radial transport of central-cell ions that are due to the

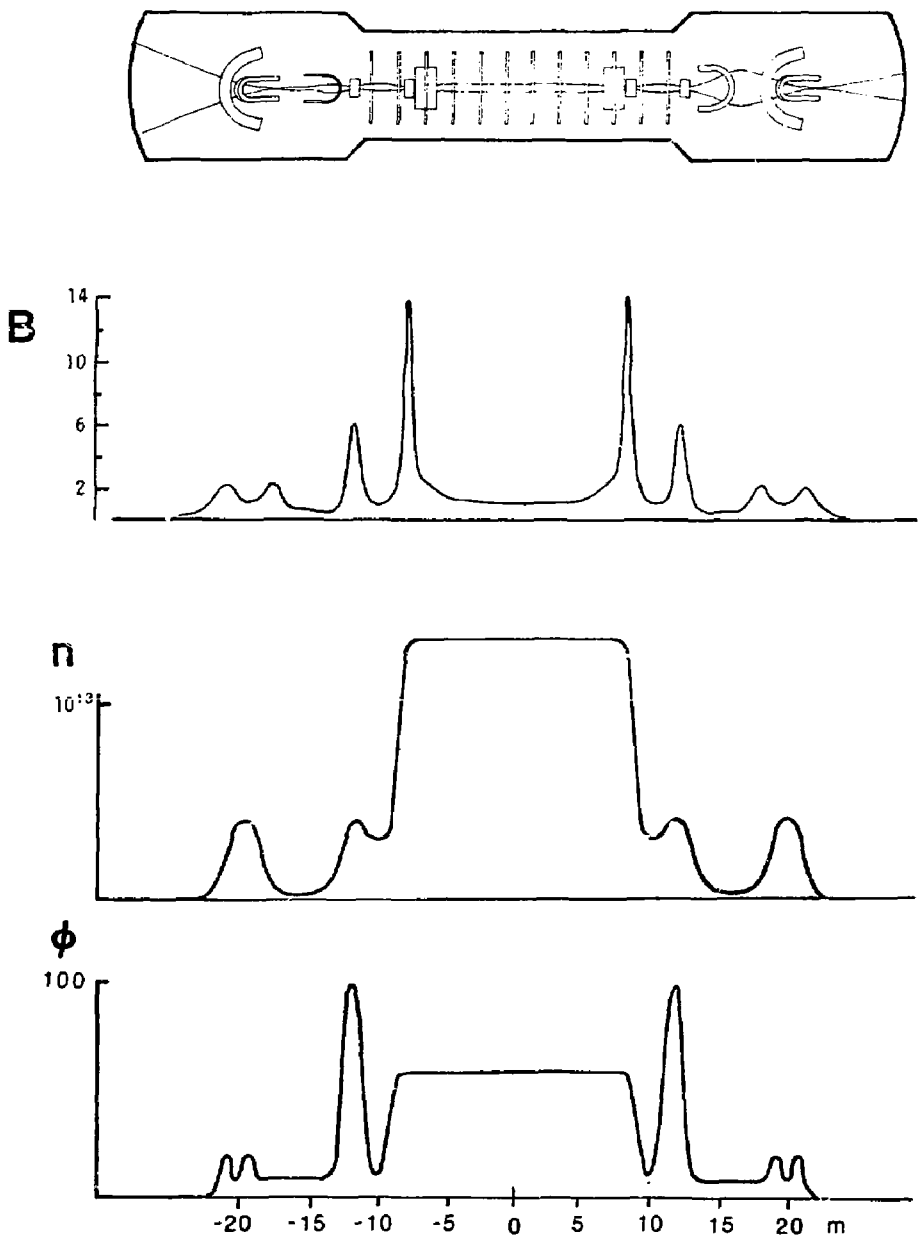

Fig. 2.3-4. Axial profiles in the TARA-like configuration of MFTF-B.

TABLE 2.3-2. Parameters for MFTF-B Axicell in the TARA-like mode (for an earlier design), Q = 0.37, Q_c = 1, P_{fusion} = 330 kW.

Central cell:

B_c = 1T	n_{ih} = 1.95 x 10^{12}	T_{ic} = 20 keV
L_c = 12.5 m	β_c = .356	T_{ec} = 12 keV
r_c = 30	ϕ_c = 33.7	$(n\tau)_c$ = 5 x 10^{13}
n_{ic} = 2.78 x 10^{13}	ϕ_e = 44.1	

Axicell barrier:

B_b = 1T	T_{ew} = 60 keV	n_{ia} = 6.89 x $10^{12}cm^{-3}$
B_{xi} = 6T	β_b = 0.11	ϕ_b = 38.1 kV
B_{x0} = 6T	F_{ec} = 0.13	$\delta\phi_a$ = 71.8 kV
L_x = 4 m	n_b = 3.59 x $10^{12}cm^{-3}$	I_{trap} = 0.670 A
E_{eh} = 88 keV		

Beam requirements:

I_{loss} = 2.93 A	I_{slosh} (abs) = 0.470 A	I_{anchor} (abs) = 0.4 A
I_c (ion) = 0.776 A		

Microwave power:

P_a = 81.9 kW	P_{cc}(ICRH) = 47.3 kW	P_b = 86.1 kW
P_{ANCHOR} = 39.4 kW		

quadrupole anchor would be negligible in the TARA-mode but still be significant in the MARS-mode. On the other hand, some radial transport is beneficial for impurity removal. Perhaps the main advantage of the TARA-mode would be to test the idea that MHD anchors might still work even though isolated from the confined axicell plasma, thus permitting evolution of much simpler and lower field anchors. This, after all, was one of the main attractions of the original TARA concept.

REFERENCES

2.9. T.K. Fowler and B.G. Logan, Tandem Mirror Technology Demonstration Facility, LLNL Report, UCID-19193 (1981).

2.10. M. N. Rosenbluth, H. L. Berk, N. V. Wong, D. E. Baldwin, and T. Antonsen, "Fast-Growing Trapped Particle Modes in Tandem Mirrors;" also L. D. Pearlstein, D. E. Baldwin, R. H. Cohen, T. K. Fowler, and B. G. Logan, "Stabilization of Tandem Mirror Trapped Particle Modes by Incomplete Cancellation of Particle Drifts." Both papers presented at the 1982 Sherwood Meeting, Annual Controlled Fusion Theory Conference, Santa Fe, NM, April 25-28, 1982.

2.11. B.G. Logan, A.A. Mirin, and M.E. Rens Nucl. Fusion 20, 1613 (1980).

2.4. PHYSICS MODELS FOR CALCULATIONS OF PARAMETERS

The plasma parameters for the axicell version of MFTF-B shown in Table 2.3-2 were calculated using the following physics models, which are similar to those used in determining the operating scenario for the A-cell version of MFTF-B.[2.12] Where further model developments and Fokker-Planck calculations occurred, we incorporated the improvements in the present calculation. The models were developed for the MARS-like mode but can be used with suitable modifications for the other modes.

2.4.1. CENTRAL-CELL PARAMETERS

As in the earlier calculation,[2.12] we chose a design point based on a set of central-cell parameters that are near the limit of MHD stability for our magnet design.[2.13] In this case, we choose a central cell β_c of 0.5 with an axicell β_x of 0.20. To maximize the fusion power achievable from a 50:50 D-T mix, we chose the thermal-ion temperature in the central cell to be T_{iwC} = 15 keV. The electron temperature is estimated to be about 60% of this value (as in Ref. 2.12), and hence T_{eC} = 9 keV. The desired ion Pastukhov confinement parameter is chosen as $(n\tau)_{iwC} \approx 5 \times 10^{13}$, and this determines the required ion-confining potential ϕ_c. This value of ϕ_c is near the maximum that can be generated with 80-kV beams and ECRH.

The electron-confining potential ϕ_e is initially chosen to give an electron Pastukhov ($n\tau$) equal to the ion value. This tends to give an overestimate of ϕ_e because the presence of secondary electrons flowing in from the end walls would produce an electron-confinement time that is less than the ion Pastukhov-confinement time. However, this estimate for ϕ_e is a satisfactory starting value that can be easily refined in one iteration, as will be shown later. The nomenclature used in this report is similar to that used in Ref. 2.12 and follows the axicell system shown in Fig. 2.1-2.

2.4.2. AXICELL PARAMETERS

The plasma density and potential profile in the axicell as well as the neutral beam required are calculated in a manner similar to that of Ref. 2.12. The potential rise from the central cell to the axicell midplane, $\Delta\phi_{pc}$, is calculated from

$$\Delta\phi_{pc} = T_{eC} \ln\left(\frac{n_{eX}}{n_{eC}}\right), \tag{2.4.1}$$

where the electron density at the axicell midplane is determined from,

$$n_{eX} = n_{iwX} + n_{ihX} \cdot \tag{2.4.2}$$

The warm-ion density is assumed to be nearly Maxwellian. Hence,

$$n_{iwX} = n_{iwC}\, e^{-\Delta\phi_{pc}/T_{iwC}} \cdot \tag{2.4.3}$$

The hot ions are determined by assuming the perpendicular β in the axicell is given by the MHD-stability limit. Then

$$n_{ihX} \simeq \frac{2.5 \times 10^{15}\, \beta_{\perp}\, B_X^2 - n_{iwX}\,(T_{iwC} + T_{eC})}{(0.9\, E_{ihX} + T_{ec})} \cdot \tag{2.4.4}$$

The solution of Eqs. 2.4.1 to 2.4.4 gives $\Delta\phi_{pc}$ and the plasma density in the axicell.

The potential drop from the axicell midplane to the outboard mirror is calculated from

$$\Delta\phi_{pb} = T_{eC} \ln\left[\frac{n_{eX}}{n_{eX}(m)}\right], \tag{2.4.5}$$

where $n_{eX}(m)$ is the electron density at the outboard axicell mirror. This density is taken as a factor $g_b(m)$ times the cold-passing-ion density at the mirror given by $n_{iX}^{pass}(m)$ where,

$$n_{iX}^{pass}(m) = n_{iC}\, \ell\, e^{-\Delta\phi_{pc}/T_{iw}} \left\{ e^{\Delta\phi_{pb}/T_{iw}}\, \mathrm{erfc}\left[\left(\frac{\Delta\phi_{pb}}{T_{iw}}\right)^{1/2}\right] \right.$$

$$\left. + 2\left(\frac{R_0 - 1}{\pi}\right)^{1/2} D\left[\left(\frac{\Delta\phi_{pb}}{T_{iw}(R_0 - 1)}\right)^{1/2}\right]\right\}, \tag{2.4.6}$$

where

$$R_0 = B_{mXo}/B_X \sqrt{1 - \beta_X} \cdot$$

and Dawson's integral is

$$D(x) = e^{-x^2} \int_0^x e^{u^2}\, du \quad .$$

The plasma lifetime is calculated using the Logan-Rensink model as in Ref. 2.12. Assuming that the hot-ion lifetime is determined by scattering losses and electron drag and also that charge-exchange losses are negligible, the hot-ion-confinement parameter is given by

$$(n\tau)_p = \left\{(n\tau)_s^{-1} + \left[(n\tau)_D \ln (E_{inj}/\bar{E}_L)\right]^{-1}\right\}^{-1} \quad , \tag{2.4.7}$$

where

$$(n\tau)_s = \frac{3.9 \times 10^{12} (E_{inj})^{3/2}}{\ln \Lambda_{ii}} \log_{10}(R_{eff}) \quad ,$$

$$R_{eff} = \frac{B_{mXi}/B_X}{\left(1 + \frac{\Delta\phi_{pc}}{E_{inj}}\right)\sqrt{1 - B_X}} \quad ,$$

$$(n\tau)_D = \frac{2 \times 10^{13}}{\ln \Lambda_{ei}} T_{eC}^{3/2} \quad ,$$

and E_{inj} is the beam-injection energy. The average energy of the ions escaping from the yin yang is $\bar{E}_L$ and is obtained from,

$$\frac{\bar{E}_L}{E_{inj}} = \frac{1}{1 + \tau_s/\tau_D} + \frac{E_p\,(\tau_s/\tau_D)/E_{inj}}{1 + \tau_s/\tau_D} \quad , \tag{2.4.8}$$

$$\frac{\tau_s}{\tau_D} \simeq \frac{0.11}{\sqrt{A}} \left(\frac{E_{inj}}{T_{ec}}\right)^{3/2} \frac{\log (R_{eff})}{\ln (E_{inj}/\bar{E}_L)} \frac{\ln \Lambda_{ei}}{\ln \Lambda_{ii}} \quad , \tag{2.4.9}$$

where A is the ion mass in amu and

$$E_p = \frac{\Delta\phi_{pc}}{\left(\frac{B_{mXi}}{B_X}\right) - 1} \quad .$$

The calculation of $\Delta\phi_{pc}$ and $\Delta\phi_{pb}$ required a value of E_{ihX}, the hot-ion energy. This energy can be calculated by balancing the drag losses of the ions on the electrons with the net energy injected by the axicell beams. Neglecting charge exchange, the hot-ion energy is given by

$$E_{ihX} = (E_{inj} - \bar{E}_L) \frac{(n\tau)_{drag}}{(n\tau)_p} + E_{eC} \quad . \tag{2.4.10}$$

Since the hot-plasma-confinement parameter $(n\tau)_p$ and hence E_{ihX} depends on $\Delta\phi_{pc}$, and because $\Delta\phi_{pc}$ depends on the value of E_{ihX}, it is clear that an iterative procedure is required to solve for the potential profile and plasma-confinement parameter $(n\tau)_p$.

The axicell beam current required to maintain the axicell is given by balancing the scattering losses,

$$I_{X\ ion} = q \frac{n_{ihX}\, n_{eX}\, V_X}{(n\tau)_p} \quad . \tag{2.4.11}$$

2.4.3. BARRIER PARAMETERS

With our choice of β_b, the beta in the midplane of the anchor, and ϕ_e, we can solve for the barrier potential ϕ_b as a function of the fraction F_{ec} of the cold electrons at the barrier midplane by applying a quasi-neutrality relation at the barrier midplane. As in Ref. 2.12, the warm-passing-ion density is mapped from the central-cell value, accounting for the variation in magnetic field and the change in potential. The cold-electron-density distribution in the barrier midplane region is assumed to follow a cut-off distribution,

$$n_{ecA}(\phi_b) = g_b(m)\, n_{iwX}(\text{mirror}) \left(\frac{e^{-\frac{\phi_b - \Delta\phi_{pb}}{T_{ec}}} - e^{-\phi/T_{ec}}}{1 - e^{-\phi/T_{ec}}} \right) \quad , \tag{2.4.12}$$

where

$$\phi = \phi_e + \Delta\phi_{pc} - \Delta\phi_{pb} \quad .$$

The density thus equals the electron density at the 12-T mirror when $\phi_b = \Delta\phi_{pb}$, and is zero when $\phi_b = \phi_e + \Delta\phi_{pc}$.

The quasi-neutrality relation, which is solved for the barrier potential, then is

$$n_{ecA}(\phi_b) = n_i^{pass}(b)\, G_b\, F_{ec} \quad , \tag{2.4.13}$$

where the passing-ion density $n_i^{pass}(b)$ is scaled from the central-cell density by

$$\begin{aligned}\frac{n_i^{pass}(b)}{n_{iwC}} = e^{-\Delta\phi_{pc}/T_{iwC}} \Bigg\{ & e^{\phi_b/T_{iwC}}\, \mathrm{erfc}\left[\left(\frac{\phi_b}{T_{iwC}}\right)^{1/2}\right] \\ & - \sqrt{1-R_0}\left\{ e^{\frac{\phi_b}{T_{iwC}(1-R_0)}}\, \mathrm{erfc}\left[\left(\frac{\phi_b}{T_{iwC}(1-R_0)}\right)^{1/2}\right] \right. \\ & \left. - e^{\frac{\phi_b+\varepsilon'}{T_{iwC}}}\, \mathrm{erfc}\left[\left(\frac{\varepsilon^*+\varepsilon'}{T_{iwC}}\right)^{1/2}\right]\right\} \\ & - \sqrt{1-R_m}\, e^{\frac{\phi_b-\varepsilon^*+\phi^*}{T_{iwC}}}\, \mathrm{erfc}\left[\left(\frac{\phi^*}{T_{iwC}}\right)^{1/2}\right]\Bigg\}, \end{aligned} \tag{2.4.14}$$

where

$$R_0 = \frac{B_b\sqrt{1-\beta_b}}{B_X\sqrt{1-\beta_X}} \quad ,$$

$$R_m = \frac{B_b\sqrt{1-\beta_b}}{B_{mX_0}} \quad ,$$

$$\varepsilon^* = \frac{R_0\phi_b - R_m(\phi_b - \Delta\phi_{pb})}{R_0 - R_m} \quad ,$$

$$\phi^* = \varepsilon^* + \frac{R_m(\phi_b - \Delta\phi_{pb})}{1-R_m} \quad ,$$

$$\phi' = \frac{R_0\,\phi_b}{R_0 - 1} - \varepsilon^* \quad ,$$

$$\varepsilon' = \frac{R_0\,\phi_b}{1 - R_0} \quad ,$$

and erfc (x) is the complementary error function of x. Here, B_b is the magnetic field at the barrier (anchor) midplane, B_x is the field at the axicell midplane, and B_{mXo} is the outer (12-T) mirror of the axicell.

Equation 2.4.13 is solved for the barrier potential ϕ_b. Then the passing density at the barrier midplane is given by Eq. 2.4.14 while the trapped- and total-ion densities at the barrier midplane are obtained from

$$n_i^{trap}(b) = (g_b - 1)\, n_i^{pass}(b) \quad , \tag{2.4.15}$$

$$n_{iA}(b) = G_b\, n_i^{pass}(b) \quad , \tag{2.4.16}$$

where g_b is the ratio of total warm-ion to passing-ion density, and G_b is the ratio of total ion density to passing-ion density.

The hot-electron energy is determined by assuming that the ions and hot electrons at the barrier midplane supply a known value for ß. Hence, for energy in keV,

$$E_{ehA} = \left(2.5 \times 10^{15}\, \beta_b B_b^2 - E_1(a)\, \frac{B_b}{B_A} \sqrt{1 - \beta_b}\, n_{ihA} \right.$$

$$\left. - T_{iw}\, \frac{B_b \sqrt{1 - \beta_b}}{B_{mAi}}\, g_b(b)\, n_{iwA} \right) / [n_{iA}(b)\,(1 - F_{ec})] \quad , \tag{2.4.17}$$

where B is in tesla and the density is per cubic centimeter.

2.4.4. WARM-ELECTRON AND CONFINING-POTENTIAL PARAMETERS

The peak in the potential profile for the anchor occurs at the position shown as a in Fig. 2.1-2. The potential and density peak are produced by 90^0 injection of the sloshing ions at the 1.2 tesla point in the vacuum field. Fokker-Planck calculations[2.14] indicate that the potential and

density peak occur inboard of the injection point. The potential peak is enhanced by auxiliary electron heating by microwave power applied near the 1.2-T position.

As in Ref. 2.12, the warm-electron density at a is obtained from a quasi-neutrality condition,

$$n_{ewA}(a) = n_{iA}(a) - n_{ehA}(a) - n_{ecA}(a) \quad . \tag{2.4.18}$$

The hot-ion density at a is taken to be a factor R_s times the density at the barrier midplane. As shown in Figs. 2.4.1 and 2.4.2, Fokker-Planck calculations indicate that a value of $R_s = 2.8$ can readily be achieved. The hot- and cold-electron densities at a are mapped from the known values at b, using

$$n_{ehA}(a) = n_{ehA}(b)\left(\frac{B_{mAo} - B_a}{B_{mAo} - B_b}\right)\left(\frac{E_{eh_{\parallel}}}{\delta\phi_a + E_{eh_{\parallel}}}\right)^{1/2} \tag{2.4.19}$$

and

$$n_{ecA}(a) = n_{ecA}(b)\,\frac{B_a}{B_b}\left(\frac{T_{ecA}}{T_{ecA} + \pi\delta\phi_a}\right)^{1/2} \quad . \tag{2.4.20}$$

$E_{eh\parallel}$ is the parallel component of the hot electron energy at b and is assumed to be about 20% of the total hot-electron energy.

The confining potential for the warm electrons, $\delta\varphi_a$, is defined as

$$\delta\phi_a = \phi_c + \phi_b - \Delta\phi_{pc} \quad . \tag{2.4.21}$$

If we use the model of Ref. 2.1, the warm-electron temperature can then be determined from

$$\frac{\delta\phi_a}{T_{ewA}} = \ln\left(N_{cw}\,\frac{1 + J_{AB}}{1 + N_{cw}\,J_{AB}}\right) , \tag{2.4.22}$$

as a function of the cold-electron ionization source J_e. In Eq. 2.4.22,

$$J_{AB} = \frac{\sqrt{\pi}}{4}\left(1 + \frac{B_b}{B_a}\right)\frac{\tau_{ee}\,J_e}{n_{ew}(a)} \quad , \tag{2.4.23}$$

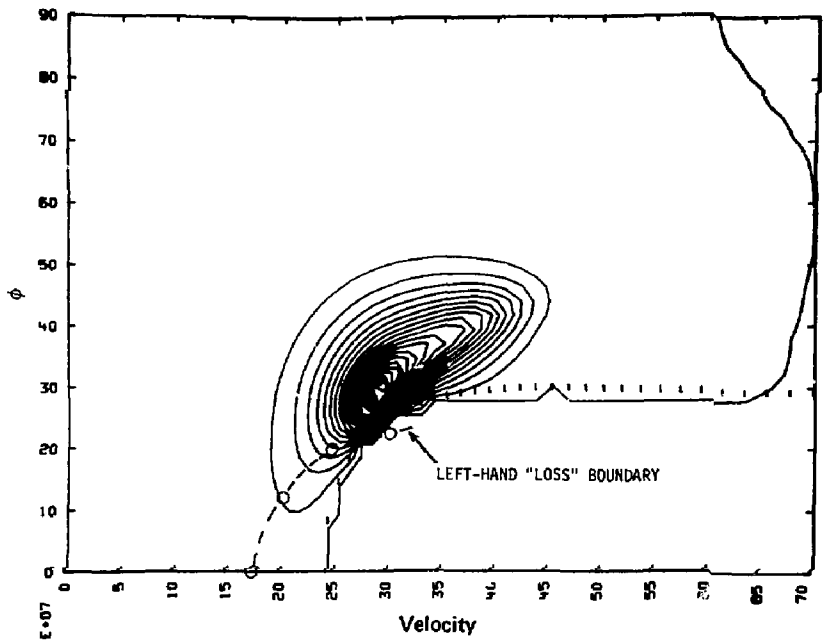

Fig. 2.4-1. Loss boundary and distribution-function contours for sloshing-ion injection in yin-yang anchor.

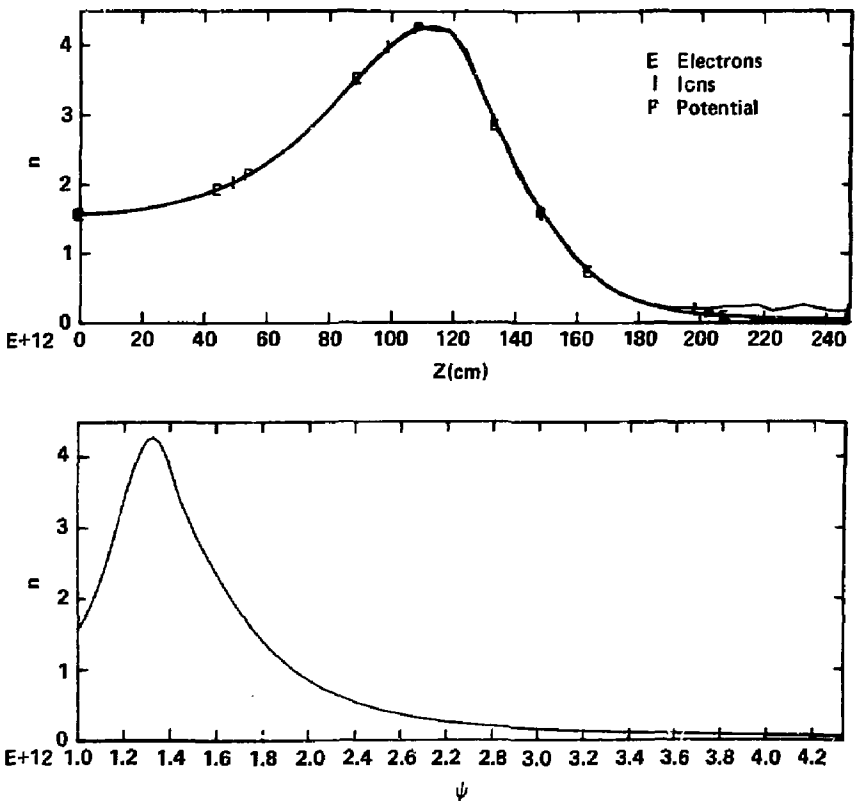

Fig. 2.4-2. Potential and density profiles obtained for sloshing-ion injection in yin-yang anchor.

$$\tau_{ee} = \frac{8.19 \times 10^9 \, T_{ew}^{3/2}(\text{keV})}{[n_{ewA}(a) + n_{ecA}(a)] \ln \Lambda_{ee}} , \tag{2.4.24}$$

$$N_{cw} = \frac{n_{ewA}(a)}{n_{ecA}(b)} \left(\frac{T_{ec}}{T_{ew}}\right)^{1/2} . \tag{2.4.25}$$

The cold-electron-source results from the ionization of the sloshing-ion beam and the axial high-energy pump beam at the position a. Since the value of J_e will be determined subsequently, we can find the warm-electron temperature that is consistent with the neutral-beam requirements and the required potential profile.

2.4.5. ANCHOR-CELL BEAM REQUIREMENTS

The neutral beams injected into the barrier region in the anchor include the high-energy sloshing-ion beam, incident at 90^0 at the 1.2-T outboard position, and an axial high-energy pump beam (HEPB). The HEPB is designed to pump out the warm trapped ions, which would otherwise build up in the potential well in the barrier. In addition, the HEPB pumps the hot sloshing ions and maintains the appropriate ratio of peak to minimum sloshing-ion density in the anchor (R_s).

The potentially trapped ion current in the anchor and transition regions is determined using a bounce-averaged Fokker-Planck calculation[2.15] with the loss boundaries and distribution functions shown in Fig. 2.4-3. The magnetically trapped current is calculated as in Ref. 2.1 with a correction factor (Devoto[2.16]) included. The magnetically trapped current then is given by

$$I_\mu = \frac{q \, g_b(b^*) \, n_{iwA}^2(b^*) \, V_b^*}{2.5 \times 10^{10} \, T_{iw}^{3/2} \, (2\theta^*/\pi)^2 \, D} , \tag{2.4.26}$$

where the Devoto correction factor for the MFTF-B Axicell geometry is

$$D \simeq 8 ,$$

and

$$\sin \theta^* \simeq \frac{B_b + B_a}{2B_{mAo}} \left(1 + \frac{\phi_c}{2T_{iw}}\right) . \tag{2.4.27}$$

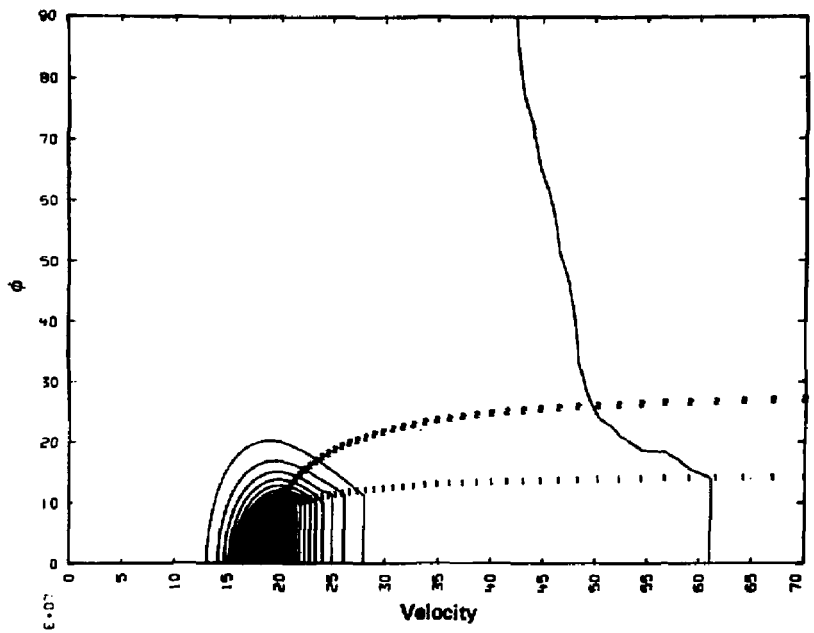

Fig. 2.4-3. Loss boundary and distribution-function contours for passing and trapped ions in the transition region.

The position b* is the point where the potential on the outboard side of the barrier rises back to the value in the central cell; V_b^* is the effective volume in this region; and $g_b(b^*) = 2.75$. The value of I_μ is generally quite small and equal to about 10% of the potentially trapped ions. The total trapped current is then taken to be the sum of the potentially and magnetically trapped currents.

The magnitude of the HEPB is determined by the requirement that the charge-exchange pumping rate in the bottom of the barrier matches the pumping rate necessary to maintain the sloshing-ion-density distribution with the required ratio of peak density to minimum density as determined by bounce-averaged Fokker-Planck[2.17] calculations of the anchor. Since the HEPB is absorbed and also pumps in the other regions of the barrier and transition regions, the total pumping by the HEPB is about 15% of I^{trap}. The remaining 85% is to be pumped by the passing-particle barrier beam (P282).

The ionization current of the sloshing-ion beam in the anchor balances the scattering losses of the hot sloshing ions and the charge-exchange losses off the HEPB. If, in addition, the one-half and one-third energy components of the sloshing beam were not confined when injected at the 1.2-tesla point, they would act as a charge-exchange pump removing the hot sloshing ions that are confined. The ionization current would then be written

$$I_{slosh}^{(ion)} = \frac{I_{scat} + I_{cx}^{HEPB}}{1 - F_2} \quad . \tag{2.4.28}$$

Here I^{scat} is the scattering-loss current obtained by Logan[2.18] from modeling Fokker-Planck calculations of the scattering loss of the sloshing ions,

$$I^{scat} = \frac{q\, n_{ihA}^2(b)\, V_{slosh}}{(n\tau)_{slosh}} \quad , \tag{2.4.29}$$

and

$$(n\tau)_{slosh} = 2.23 \times 10^{10} \, (\bar{E}_t)^{3/2} \, \log_{10}\left(\frac{B_{mAo}/B_{inj}}{1 - \frac{\phi_m - \phi_{inj}}{\bar{E}_t}}\right), \quad (2.4.30)$$

$$\bar{E}_t = \frac{\sum_{j=1,1/2,1/3} \left[\frac{\langle\sigma v\rangle_{ij}}{v_j} f_j E_j + \frac{\langle\sigma v\rangle_{cxj}}{v_j} f_j (E_j - \bar{E}_{in})\right]}{\sum_{j=1,1/2,1/3} \frac{\langle\sigma v\rangle_{ij}}{v_j} f_j}, \quad (2.4.31)$$

$$\bar{E}_{in} = \frac{\sum_{j=1,1/2,1/3} \frac{\langle\sigma v\rangle_{ij}}{v_j} f_j E_j}{\sum_{j=1,1/2,1/3} \frac{\langle\sigma v\rangle_{ij}}{v_j} f_j}. \quad (2.4.32)$$

When the one-half and one-third beam-energy components are not confined, the term F_2 is the ratio of the charge-exchange rate of the one-half and one-third beam-energy components to the ionization rate of the full-energy component of the sloshing beam. For our standard case, all the beam-energy components are confined, and F_2 is zero; I_{cx}^{HEPB} is the charge-exchange loss current resulting from charge-exchange interactions between the sloshing ions and the HEPB ions as they traverse the anchor. For the reference-case parameters, the scattering loss of the sloshing ions is comparable to the charge-exchange losses of the HEPB.

The summations indicated in Eqs. 2.4.31 and 2.4.32 are over the full, the one-half, and the one-third beam-energy components of the beam; $\langle\sigma v\rangle_{ij}$ and $\langle\sigma v\rangle_{cxj}$ are the total ionization and charge-exchange rates for beam component j. Similarly, E_j and f_j are the energy and atomic fraction for each beam component; and v_j is the velocity of beam component j, corresponding to the energy E_j; $(\phi_m - \phi_{inj})$ is the potential difference between the outer mirror and the point of beam injection.

The ionization current from the sloshing beam and the ionization current of the HEPB deposited in the region of the potential peak provide the cold electrons that form the cold-electron source J_e in Eq. 2.4.23. This value of J_e places a limit on the maximum sloshing-ion current and HEPB current

that can be used in the axicell. When J_e becomes too large, the model Eq. 2.4.22 only has solutions for $T_{ewA} > \delta\phi_a$, a regime where the model becomes inaccurate. In practice, the value of J_e is limited to several microamps per cubic centimeter.

2.4.6. MICROWAVE POWER REQUIREMENTS

The microwave power supplied to the potential peak region a and the thermal barrier region b in the axicell is calculated in a manner similar to that in Ref. 2.11. The power per unit volume at a is given by

$$P_a = J_{in} \frac{B_b}{B_a} (T_{ewA} - T_{ecA}) + J_e \left(\delta\phi_a + \frac{B_b}{B_a} T_{ewA}\right) + \frac{1}{2} J_{in} (T_{ewA} - T_{ecA}) \quad . \quad (2.4.33)$$

This is the so-called "weak ECRH" limit of Ref. 2-11, where

$$J_{in} = \frac{n_{ecA}(b)\, n_{ewA}(a)}{(n\tau)} \left(\frac{T_{ewA}}{T_{ecA}}\right)^{1/2} e^{\delta\phi_a/T_{ewA}} \quad (2.4.34)$$

and

$$(n\tau) = \frac{\sqrt{\pi}}{4} \left(1 + \frac{B_b}{B_a}\right) n_{ewA}(a)\, \tau_{ee} \left(e^{\delta\phi_a/T_{ewA}} - 1\right) . \quad (2.4.35)$$

The dominant term in Eq. 2.4.33 is the one involving J_e. Hence, the power at a is controlled by the magnitude of the cold-electron source at a.

The microwave power needed to produce the hot electrons is modeled as the sum of scattering and synchrotron radiation losses. The scattering loss per unit volume is

$$P_{SCATT} = \frac{q\, n_{iA}^2(b)\, (1-F_{ec})\, (E_{ehA}/2)}{n\tau} , \quad (2.4.36)$$

where

$$n\tau = 1.65 \times 10^8\, E_{ehA}^{3/2} \log (R_{eff}) \quad . \quad (2.4.37)$$

The numerical coefficient of Eq. 2.4.38 is low by comparison with recent electron Fokker-Planck calculations in this geometry,[2.19] which are best fitted with the coefficient 2.8×10^8. However, those calculations include

only the hot-electron population and neglect drag effects between the hot electrons and the other electron populations whose spatial distributions overlap. Depending on the details of the spatial distribution, the drag effects might add as much as 50 to 60% to the power estimate for the hot electrons at b. Thus, retaining the lower coefficient in Eq. 2.4.38 is tantamount to correcting for these drag effects, giving a more realistic modeling of the total microwave power needed at b. However, because some of this drag power is transferred to the warm electrons at a, we would expect the power estimate P_a given by Eq. 2.4.33 to be higher than necessary.

The value of R_{eff} is taken as the smaller of R_{eff} for losses to the inner-mirror point or the outer-mirror point, where

$$R_{eff}\ (\text{inner}) = \frac{B_{mAi}/B_b\ (1 - \beta_b)^{1/2}}{1 + \phi_b/E_{ehA}} \quad , \tag{2.4.38}$$

$$R_{eff}\ (\text{outer}) = B_{mAo}/B_b\ (1 - \beta_b)^{1/2} \quad . \tag{2.4.39}$$

Here we assume that the potential at the outer-mirror point is the same as that at the bottom of the thermal barrier. In general, because B_{mAi} is so much larger than B_{mAo}, $R_{eff} = R_{eff}(\text{outer})$.

2.4.7. CENTRAL-CELL ION-PARTICLE AND ENERGY BALANCE

This model assumes all the central-cell ions are thermal ions with a temperature T_{iwC}. In the most general case, some of these ions are supplied by ionization of gas and by a neutral beam in the central cell. In addition, some of the ions produced by charge exchange and ionization of the passing-particle barrier beam (P2B2) in the transition region become trapped in the central cell. A third source of ions for the central cell is the ionization current from the axicells adjacent to the central cell. The balance equation for the thermal ions then becomes

$$I_i^{loss} + 2I^{trap} + 2I_{abs}^{P2B2}\, f_{cx}^{P2B2}$$

$$= I_{C\ ion}^{gas} + 2I^{P2B2}\, f_{trap}^{P2B2} + I_{C\ ion} + 2I_{X\ ion} \quad . \tag{2.4.40}$$

The axial loss current I_i^{loss} of the warm central-cell ions is given by

$$I_i^{loss} = q \frac{n_{iwC}^2 V_c}{(n\tau)_{iwC}} \quad , \tag{2.4.41}$$

where $(n\tau)_{iwC}$ is the ion Pastukhov confinement parameter for the warm ions; f_{trap}^{P2B2} is the fraction of ions from the passing-particle barrier beam that are eventually confined in the central cell; f_{cx}^{P2B2} is the fraction of the absorbed P2B2 that charge-exchanges on the passing ions in the transition region; I^{trap} is the current of ions from the central cell that traps in the transition and anchor regions; I_{abs}^{P2B2} is the total passing-particle barrier-beam current absorbed in the transition region; $I_{C\ ion}^{gas}$, $I_{C\ ion}$, and $I_{X\ ion}$ are the ionization currents for the central-cell gas and neutral beams and the axicell neutral beam, respectively. The factors of two in Eq. 2.4.40 account for the particle losses and inputs from each end of the system.

The ion-energy equation is obtained by balancing the energy carried out by each ion with the energy input of each source ion. The difference in potential between the point of production of the ion and the central cell is also considered in the energy bookkeeping. The equation is

$$\begin{aligned}
&I_{C\ ion} f_{ii} \bar{E}_{trap} + P_C^{ICRH} + 2I_{abs}^{P2B2} (E_{P2B2} - 6\phi_L + \Delta\phi_{pc}) f_{trap}^{P2B2} \\
&\quad + 2I_{X\ ion} (E_{loss} + \Delta\phi_{pc}) \\
&\quad + 2I_{X\ ion} (E_{loss} + \Delta\phi_{pc} - E_{ic}) \frac{\langle\sigma v\rangle_{cx}}{\langle\sigma v\rangle_{ion}} \frac{n_{iX}^{pass}}{n_{iX}} \\
&= I_i^{loss} (T_{iwC} + \phi_c) + 2I^{trap} E_{iwC} \\
&\quad + \frac{\langle\sigma v\rangle_{cx}^{gas}}{\langle\sigma v\rangle_{ion}^{gas}} I_{C\ ion}^{gas} E_{iwC} + 2f_{cx}^{P2B2} I_{abs}^{P2B2} E_{iwC} \\
&\quad + \frac{q\, n_{iwC}^2 V_c}{(n\tau)_{drag}} (E_{iwC} - E_{eC}) \quad ,
\end{aligned} \tag{2.4.42}$$

where E_{trap} is the mean beam energy trapped per beam neutral ionized, and f_{ii} is the fraction of this energy deposited in the ions. The values of E_{trap} and f_{ii} are calculated with the formulism of Ref. 2.12 using the atomic fractions,

$$f_1 = 0.833 \ ,$$

$$f_{1/2} = 0.075 \ ,$$

$$f_{1/3} = 0.092 \ ,$$

calculated for the 80-kV neutral beams with a 90:5:5 molecular mix in the arc chamber.

The absorbed fraction of the P2B2 supplies to the central cell an energy per particle, $(E_{P2B2} - \delta\phi_L + \Delta\phi_{pc})$, where E_{P2B2} is the average beam energy and $\delta\phi_L$ is the average potential drop between the potential peak in the axicell and the location where the P2B2 ion is born. The neutral beam in the axicell contributes energy equal to its loss energy (calculated in Eqs. 2.4.8 and 2.4.9 from the axicell plus the change in potential $\Delta\phi_{pc}$. Moreover, because the passing ions from the central cell can charge-exchange with the axicell beam, there is a second term in the energy balance that depends on the axicell ionization current.

The loss terms in the energy balance include the axial energy carried out by the ions, the energy lost by ion trapping in the transition and anchor regions, the charge exchange losses by passing ions in the transition and by interactions with gas in the central cell, and also the energy lost by electron drag.

In the general problem of particle and energy balance, we solve (2.4.40) for the gas current (for a given ion-confining potential) and substitute into Eq. 2.4.42. This gives the rf power, P^{ICRH}, as a function of the central-cell-beam ionization current, $I_{C\ ion}$, or vice versa. However, to find the optimum $(n\tau)_{iwC}$ for the system, we solve the balance equations with the restriction that $I^{gas}_{C\ ion} = 0$. In addition, we set the central-cell-beam current to zero and obtain the maximum $(n\tau)_{iwC}$ that can be achieved with the other given beam inputs. With the gas and central-cell beams set to zero, we solve Eq. 2.4.40 for I^{loss} (and hence ϕ_c) to give particle balance, and then use Eq. 2.4.42 to solve for the value of P^{ICRH}, which gives energy balance.

2.4.8. CENTRAL-CELL ELECTRON-PARTICLE AND ENERGY BALANCE

The electron-particle losses are all assumed to be axial losses, so that the electron-loss current is written as

$$I_e^{Loss} = \frac{q\, n_{eC}^2\, V_c}{(n\tau)_{eC}} \quad . \tag{2.4.43}$$

Here, $(n\tau)_{eC}$ is the Pastukhov confinement for electrons in the confining potential ϕ_e.

The electron sources result from the ionization of the gas, the central cell and axicell beams, as well as the HEPB, P2B2 and sloshing-ion beams in the anchor and transition regions. In addition, a source of secondary electrons I_{sec} flow in from the end walls. This current is given in terms of the primary electron loss current by[2.20]

$$I^{sec} = \lambda\, I_e^{Loss} \quad , \tag{2.4.44}$$

where λ is the secondary-emission coefficient. In terms of the total ion loss out the ends of the system, I_{tot},

$$\lambda = \frac{I^{sec}}{I^{sec} + I^{tot}} \quad , \tag{2.4.45}$$

where

$$I^{tot} = \frac{q\, n_{iwC}^2\, V_c}{(n\tau)_{iwC}} + 2\left(I_{A\ ion}^{slosh} + I_{ion}^{HEPB} + I_{ion}^{P2B2} + I_{X\ ion}\right) .$$

The electron-particle balance then becomes

$$I^{sec} + I_{C\ ion} + I^{gas} + 2\left(I_{A\ ion}^{slosh} + I_{ion}^{HEPB} + I_{ion}^{P2B2} + I_{X\ ion}\right) = \frac{q\, n_{eC}^2\, V_C}{(n\tau)_{eC}} . \tag{2.4.46}$$

In the central-cell electron energy balance, the position of ionization is taken into consideration. The potential change between this point and the central cell is then added or subtracted appropriately, depending on whether the electron is a net energy source or sink to the central-cell electron population. The rate equation then is

$$\frac{q\, n_{iwC}^2\, V_c}{(n\tau)_{drag}} (E_{iwC} - E_{eC}) + I^{sec}\, \phi_e + P_C + 2(P_a + P_b)$$

$$+ I_{C\ ion} (1 - f_{ii})\, \bar{E}_{trap} + 2\left[I_{ion}^{HEPB}\, \bar{\phi} + I_{ion}^{P2B2}\, (\delta\phi_L - \Delta\phi_{pc})\right]$$

$$= \frac{q\, n_{eC}^2 V_c}{(n\tau)_{eC}} (\phi_e + T_{eC}) + 2I_{A\ ion}^{slosh}\, \phi_c + 2I_{X\ ion}\, \Delta\phi_{pc} \quad . \qquad (2.4.47)$$

In this model, the secondary electrons carry in the energy ϕ_e obtained from the potential drop from the wall to the central cell. We assume that all the microwave power that produces the thermal barrier at b and the potential peak at a eventually ends up in the central cell. This tends to overestimate the central-cell power input, since some of the hot, magnetically confined electrons that form the thermal barrier are lost to the end walls, rather than to the central cell.

The term P_C allows us to introduce power for direct electron heating of the central-cell electrons. A portion $(1 - f_{ii})$ of the trapped energy from the central-cell neutral beams goes directly into the electrons. The electrons produced by ionization of the HEPB and P2B2 in the anchor and transition carry in energy obtained from their change in potential in entering the central cell. The electrons produced by ionization of the sloshing-ion beam in the anchor must climb a potential approximately equal to ϕ_c to reach the central cell, and hence appear as an energy-loss term in the central cell. Similarly, the axicell electrons must climb the potential $\Delta\phi_{pc}$ to reach the central cell.

The solution of the two rate Eqs. 2.4.46 and 2.4.47 gives us the secondary-electron current and a new value for the electron-confining potential ϕ_e. Recall that we initially set ϕ_e by requiring that the ion and electron Pastukhov-confinement parameters be equal. Now when we introduce the secondary electrons, the electron-confinement parameter and ϕ_e are appropriately smaller. This new value of ϕ_e is then used to recalculate the barrier parameters, beam requirements, and microwave power needs. Using the electron-balance equations with these revised parameters gives the next iteration value for ϕ_e. Experience has shown that ϕ_e converges to better than 1% in one iteration.

Along with the secondary-electron current, we can calculate the secondary-emission coefficient using Eq. 2.4.45 and compare it to the value of the coefficient when the secondary-electron current is assumed to be limited by space-charge effects. The space-charge limited value of the secondary-emission coefficient has been approximated by Logan[2.21] as

$$\lambda_{scl} = \left[0.15 \ln\left(\frac{T_{eC}}{\phi_e + \phi_c + T_{iw}}\right) + 0.656\right]^{1/4} . \qquad (2.4.48)$$

If $\lambda < \lambda_{sec}$, then clearly some suppression scheme would have to be invoked to get I_{sec} below the space-charge limited value.

The ECRH power necessary to achieve the electron-particle and energy balance is larger than the ECRH power required to maintain the hot-electron and warm-electron populations against the mainly classical loss processes modeled by Eqs. 2.4.33 to 2.4.39. While this extra power cannot be directly fed to the electrons in the central-cell region, the energy can be supplied to the central-cell electrons by an appropriately designed microwave system in the barrier region. The design would be flexible enough so that we would supply the power necessary to maintain the hot and warm electrons as well as heat some of the cold electrons that pass to the central cell. This extra power capability in the barrier region could also be used to supply more energy to the hot and warm electrons in the event that non-classical processes enhance the electron losses in the barrier region.

REFERENCES

2.12. D. E. Baldwin, B. G. Logan, and T. C. Simonen, Eds., Physics Basis for MFTF-B, LLNL Report, UCID-18496, Pt. 1 (January 1980).

2.13. R. H. Bulmer, private communication, April 1982.

2.14. M. E. Rensink, private communication, February 1982.

2.15. A. H. Futch and G. W. Leppelmeier, private communication, April 1982.

2.16. R. S. Devoto, Memorandum, January 1982.

2.17. M. E. Rensink, private communication, April 1982.

2.18. B. G. Logan, private communication, December 1981.

2.19. J. W. Shearer, private communication, February 1982.

2.20. D. Porter, Effect of Gas Recycling and Secondary Emission on the Axial Power Flow in an Open-Ended Device, LLNL Report, UCRL-85847 (June 1981).
2.21. F. H. Coensgen, T. C. Simonen, A. K. Chargin, and B. G. Logan, TMX-U Major Project Proposal, LLNL Report, LLL-Prop-172 (April 1980).

APPENDIX A

Analytic equilibria with quadrupole symmetry in the paraxial limit

L. D. Pearlstein, T. B. Kaiser, and William A. Newcomb

Lawrence Livermore National Laboratory, University of California, Livermore, California 94550
(Received 15 December 1980; accepted 11 March 1981)

Mirror equilibria for arbitrary mirror ratio and flux-tube eccentricity are obtained to leading order in the plasma pressure (beta expansion) in the paraxial limit (axial scale lengths long compared with radial scale lengths). The solutions are given in terms of quadratures over known functions. The theory is applied to a tandem-mirror configuration.

I. INTRODUCTION

Adiabatic confinement in conventional mirrors is controlled primarily by the z component of the axisymmetric part of the applied magnetic field. However, to create a stable configuration (interchange motion being the problem) it is necessary to generate a "minimum-B well." This is usually done by adding a quadrupole (sometimes even a higher order multipole) component to the main field. This addition, of course, makes the guiding-center equilibrium problem three-dimensional. In general, the solution of this equilibrium set of equations requires large sophisticated codes and state-of-the-art digital computers.[1,2] Even then results tend to be relatively crude, because of the limitations of computer memory capacity and speed. However, because the symmetry breaking field is weak compared with the main axisymmetric field, and because the radius of curvature of the main axisymmetric field is large compared with other characteristic lengths, an important simplification can be made. This simplication in the equilibrium model has been called the "long-thin" or paraxial approximation. Specifically, if we identify the small parameter λ as the ratio of radial scale length to axial scale length, then it can be systematically seen that: the perpendicular components of the magnetic field are of order λ compared with the main z component; the radius of curvature is of order λ^{-2} compared with the radial scale length; and the local parallel current is of order λ compared with the local perpendicular current.

Using this ordering, we generate a reduced set of equations in flux coordinates for the equilibrium in Sec. II. These equations are nonetheless a formidable set, and solving them is still an extensive numerical problem, even though they have the further advantage that z is a time-like coordinate in the partial differential equation determining the flux-line geometry. That is, the equation can be formally integrated from one plane of constant z to the next and then information from the original plane can be discarded. Hence, in principle, the required computer storage becomes that of a two-dimensional problem. Unfortunately, the axial boundary conditions come from both ends.

To make further progress, we look for a self-consistent equilibrium to first order in the plasma pressure. That is, we expand the equilibrium equations treating the ratio of plasma to magnetic field pressure (beta) as a small expansion parameter, but large compared with λ^2. This expansion is carried out for quadrupole symmetry in Secs. III and IV; in Sec. III we develop the general perturbation scheme and in Sec. IV we obtain explicit solutions. The solutions are given as quadratures over known vacuum-magnetic-field quantities (functions of z) and over prescribed pressure profiles (functions of mod-B and the principal flux). We emphasize that, given the natural smallness parameter λ, we need only assume low beta to obtain analytic solutions; the mirror ratio minus one and flux-tube eccentricity are arbitrary differing from zero by terms of order unity.

Section V gives our results. There are two features of the equilibrium which we indicate here. We find, as Stupakov did,[3] that there is a breakdown in the perturbation expansion, an apparent bifurcation point when the flute instability criterion is marginal. This we believe to be an interesting point; whether there is, in fact, another equilibrium we are not able to say at this time. The other feature, which is very favorable, is that the self-consistent equilibrium reduces the strong ellipticity in the transition regions of tandem mirrors. This is contrary to the results in Ref. 3. The reasons for this difference are discussed in Sec. V.

The Heaviside–Lorentz system of units, in which $\epsilon_0 = \mu_0 = 1$, is used throughout.

II. EQUILIBRIUM EQUATIONS IN THE PARAXIAL APPROXIMATION

Our starting point is the general tensor-pressure magnetostatic equilibrium conditions,[4]

$$(\nabla P)_\perp = Q\boldsymbol{\kappa}\,, \tag{1}$$

and

$$\frac{dP}{dB} = B\frac{d}{dB}\left(\frac{Q}{B}\right), \tag{2}$$

where

$$P = B^2/2 + p_\perp\,, \tag{3}$$

$$Q = B^2 + p_\perp - p_\parallel\,, \tag{4}$$

B is the magnetic flux density, $\boldsymbol{\kappa}$ is the curvature vector, and $p_\perp$ and $p_\parallel$ are the pressure components perpendicular and parallel to $\mathbf{B}$. The derivatives d/dB in Eq. (2) should be understood as directional derivatives

 0031-9171/81/071326-10$00.90

in the parallel direction, i.e.,

$$\frac{d}{dB} = (\mathbf{B}\cdot\nabla B)^{-1}\mathbf{B}\cdot\nabla . \tag{5}$$

Here and elsewhere, $|\mathbf{B}|$ is abbreviated as B and $\hat{b}$ denotes the unit vector parallel to B. Then

$$\kappa = \hat{b}\cdot\nabla\hat{b} = -\hat{b}\times(\nabla\times\hat{b}) . \tag{6}$$

Apply the operator $\hat{b}\cdot\nabla\times$ to Eq. (6) to obtain

$$\hat{b}\cdot\nabla\times\kappa = B\hat{b}\cdot\nabla(i/B) , \tag{7}$$

where i, the parallel current per unit magnetic flux, is

$$i = \hat{b}\cdot\nabla\times\hat{b} . \tag{8}$$

Next, apply the same operator to Eq. (1) and obtain

$$\hat{b}\cdot\nabla\times Q\kappa = -iB\hat{b}\cdot\nabla(Q/B) .$$

Then, with Eq. (7) we have the usual parallel current equation

$$\hat{b}\cdot\kappa\times\nabla Q = B^2\hat{b}\cdot\nabla(Qi/B^2) . \tag{9}$$

These equations, given the requisite conditions for well-posedness[5] (or local stability)

$$\frac{dP}{dB} > 0 \text{ (mirror mode)}$$

and

$$Q > 0 \text{ (firehose mode)},$$

determine the equilibrium.

We now introduce flux coordinates α, β with the property that

$$\mathbf{B} = \nabla\alpha\times\nabla\beta , \tag{10}$$

and

$$\hat{b}\cdot\nabla\alpha = \hat{b}\cdot\nabla\beta = 0 . \tag{11}$$

The pressure distribution is assumed to be of the special form

$$p_{\perp,\parallel} = p_{\perp,\parallel}(\alpha, B) . \tag{12}$$

That is, aside from its dependence on B, it is a function of only one flux coordinate, the so-called principal flux coordinate. We will say more about this later.

From Eq. (2), [remember $d/dB = \partial/\partial B)_{\alpha,\beta}$] we obtain the usual relationship between $p_\perp$ and $p_\parallel$.

$$p_\perp = -B^2\frac{d}{dB}\left(\frac{p_\parallel}{B}\right) , \tag{13}$$

so that only $p_\parallel(\alpha, B)$ need be specified.

Henceforth, we assume a large-aspect-ratio system so that we make the paraxial (or long-thin) approximation.[6] That is, lengths in the x, y plane are small (of order λ) compared with the axial scale length (in the z direction), and the field components B_x, B_y are similarly small, of order λ, compared with B_z, and B_z vanishes nowhere. In all calculations henceforth, all terms of relative order λ^2 are systematically dropped. If we take the unit of length to be on the order of the transverse scale length, then all gradients in the z direction are of order λ, and because of this κ is of order λ^2. With ds denoting the element of arc length along a flux line (constant α, β), we have

$$ds = dz . \tag{14}$$

Furthermore, to this order

$$B_z = B . \tag{15}$$

From Eq. (1) it follows that

$$P = P(z) = \tfrac{1}{2}B_v^2(z) , \tag{16}$$

where B_v denotes the vacuum field. Given $P(z)$ and $p_\parallel(\alpha, B)$, only a functional inversion is required to determine B, $p_\parallel$, $p_\perp$ as functions of α, z. All are independent of β.

To complete the description of the equilibrium requires a determination of the coordinate transformation (α, β, z) to (x, y, z). It is thus necessary to determine the flux-line geometry $x(\alpha, \beta, z)$, $y(\alpha, \beta, z)$.

One equation in the two unknowns x, y is immediately obtainable from the definition of α, β as flux coordinates, viz.,

$$\frac{\partial(x, y)}{\partial(\alpha, \beta)} = \frac{1}{B} \tag{17}$$

(see Appendix A), where B is a known function of α and z. (The standard notation is used here to denote the Jacobian of x and y with respect to α and β.) To obtain a second relation, we first define the covariant curvature components $\mathcal{A}$ (normal curvature), $\mathcal{K}$ (geodesic curvature) so that

$$\kappa = \mathcal{A}\nabla\alpha + \mathcal{K}\nabla\beta . \tag{18}$$

Thus (primes are used to denote partial derivatives with respect to z for fixed α, β),

$$\mathcal{A} = x''\frac{\partial x}{\partial\alpha} + y''\frac{\partial y}{\partial\alpha} , \tag{19}$$

and

$$\mathcal{K} = x''\frac{\partial x}{\partial\beta} + y''\frac{\partial y}{\partial\beta} . \tag{20}$$

Furthermore, the definition Eq. (8) reduces to

$$i = B\left(\frac{\partial(x', x)}{\partial(\alpha, \beta)} + \frac{\partial(y', y)}{\partial(\alpha, \beta)}\right) \tag{21}$$

(see Appendix A), and finally, from Eq. (9), we obtain the desired second equation in x and y of the form

$$\mathcal{K}\frac{\partial Q}{\partial\alpha} = -B\left(\frac{Qi}{B^2}\right)' , \tag{22}$$

where again Q is a known function of α, z. (The partial $\partial Q/\partial\alpha$ is taken for fixed z.) Presumably Eqs. (17)–(22), in conjunction with the appropriate boundary conditions, would suffice to determine the unknown coordinates $x(\alpha, \beta, z)$ and $y(\alpha, \beta, z)$. In the next section we linearize these equations about their vacuum values to obtain the equations which define the flux line geometry to leading order in beta (the ratio of the plasma energy density to field energy density).

III. FLUX-LINE GEOMETRY (LEADING ORDER IN BETA)

To lowest order the flux-line geometry is determined by the vacuum fields. For quadrupole symmetry in the paraxial approximation, the field line trajectories can be written

$$x_v = \sigma(z)x_0\,, \tag{23}$$

$$y_v = \tau(z)y_0\,, \tag{24}$$

where σ and τ satisfy

$$\sigma\tau = (B_0)_v/B_v(z)\,, \tag{25}$$

and where x_0 and y_0 are the coordinates of the field lines at the midplane ($z=0$) of the configuration, and $B_0 = B(0)$. In what follows, we assume the type of symmetry defined by the two conditions

$$B_v(z) = B_v(-z)\,, \tag{26}$$

and

$$\sigma(z) = \tau(-z)\,, \tag{27}$$

This, of course, is the symmetry of the standard minimum-B mirror (with the fans rotated through an angle of 90° relative to each other) and of tandem mirrors such as TMX, Ambol, and Phaedrus. We also identify the transverse vacuum-field components

$$B_x = x'B = x_0 B_v\sigma'\,,$$

$$B_y = y'B = y_0 B_v\tau'\,, \tag{28}$$

where the first equality is valid for any field in the paraxial limit, and the second is valid for the vacuum field only. The components B_x, B_y, as such, will not appear explicitly in further calculations but are written down here for completeness.

Next, we identify the principal flux coordinate to this order. From the parallel-current constraint (22), we force

$$\int_{-L}^{L}\frac{dz}{B}\frac{\partial Q}{\partial\alpha}\mathrm{FO} = 0 \tag{29}$$

in order that the parallel current will vanish at the ends of the device (a necessary condition for a plasma to be *confined and isolated from the surrounding environment*). Since

$$\frac{\partial Q}{\partial\alpha} = -2\frac{\partial p}{\partial\alpha}\,, \tag{30}$$

where $p \equiv (p_\perp + p_\parallel)/2$, is already of order beta, we need only the vacuum values of the remaining quantities in (29). If we now make the identification of

$$\alpha = \psi = r^2 B_v(0)/2\,,\quad r^2 = x_0^2 + y_0^2\,, \tag{31}$$

$$\beta = \theta = \tan^{-1}(y_0/x_0)\,, \tag{32}$$

we see that constraint (29) is satisfied by symmetry, since

$$\mathrm{FO} = -r^2(\sigma\sigma'' - \tau\tau'')\sin\theta\cos\theta \tag{33}$$

is antisymmetric. Thus, the leading-order expression for the parallel current is

$$i = r^2\sin 2\theta\int_z^L\frac{dz'}{B_v}(\sigma\sigma'' - \tau\tau'')\frac{\partial p}{\partial\psi}\,. \tag{34}$$

To next order, we set

$$x = x_v + \xi\,, \tag{35}$$

$$y = y_v + \eta\,, \tag{36}$$

and obtain, after linearizing Eq. (17),

$$\frac{\partial(\xi,y)}{\partial(\psi,\theta)} + \frac{\partial(x,\eta)}{\partial(\psi,\theta)} = \delta\left(\frac{1}{B}\right)\,;$$

but, now let us change coordinates from ψ, θ to x_0, y_0. Using Eq. (3), we obtain

$$\tau\frac{\partial\xi}{\partial x_0} + \sigma\frac{\partial\eta}{\partial y_0} = \frac{B_0}{B^3}(p_\perp - \delta P)\,. \tag{37}$$

In Eq. (37) δP is the change in the vacuum solution due to the presence of plasma currents. If there is a boundary where the flux is fixed (a perfectly conducting shell at some boundary denoted by ψ^*), then

$$\delta P = \frac{\int_0^{\psi^*} d\psi' p_\perp/B^3}{\int_0^{\psi^*} d\psi'/B^3}\,. \tag{38}$$

Henceforth, all quantities refer to their vacuum values (in the absence of plasma) unless otherwise stated. Since the right-hand side of Eq. (37) is independent of θ, we can immediately construct the general solution to this equation, viz.,

$$\xi = k\sigma x_0 + \sigma\frac{\partial\phi}{\partial y_0}\,, \tag{39}$$

$$\eta = k\tau y_0 - \tau\frac{\partial\phi}{\partial x_0}\,, \tag{40}$$

where, at this stage,

$$\phi = \phi(x_0, y_0, z) \tag{41}$$

is an arbitrary stream function, and the particular solution satisfies

$$2\frac{B_0}{B}\frac{\partial}{\partial\psi}(k\psi) = \frac{B_0}{B^3}(p_\perp - \delta P)\,,$$

so that

$$k = \frac{1}{2\psi}\int_0^\psi d\psi'\frac{p_\perp - \delta P}{B^2}\,. \tag{42}$$

To determine the stream function uniquely, we use our second equation for the flux-line coordinates, Eq. (22), and the definition of i, Eq. (21). Linearizing these equations generates

$$\frac{\partial(x',\xi)}{\partial(\psi,\theta)} + \frac{\partial(y',\eta)}{\partial(\psi,\theta)} + \frac{\partial(x,\xi')}{\partial(\psi,\theta)} + \frac{\partial(y,\eta')}{\partial(\psi,\theta)} = \frac{i}{B}\,. \tag{43}$$

Again, let us put it in terms of x_0, y_0:

$$\sigma'\frac{\partial\xi}{\partial y_0} - \sigma\frac{\partial\xi'}{\partial y_0} - \tau'\frac{\partial\eta}{\partial x_0} + \tau\frac{\partial\eta'}{\partial x_0} = i\frac{B_0}{B}\,. \tag{44}$$

If we now substitute Eqs. (34), (39), and (40), we finally obtain

$$\tau^2\frac{\partial^2\phi'}{\partial x_0^2} + \sigma^2\frac{\partial^2\phi'}{\partial y_0^2} = 2\sin 2\theta\psi\frac{\partial}{\partial\psi}S(\psi,z)\,, \tag{45}$$

with

$$S(\psi,z) = \frac{1}{B}\int_z^L\frac{dz'}{B}p(\sigma\sigma'' - \tau\tau'') - \frac{1}{2}(\sigma^2 - \tau^2)k'\,. \tag{46}$$

At this point, several remarks are in order. First, all field quantities refer to their vacuum values. Second, Eq. (45) is an elliptic equation for $\phi'(x_0, y_0, z)$ in which the coefficients are functions only of z (i.e., only of a parameter, at this level). Consequently, to solve for ϕ we first solve Eq. (45) subject to the lateral boundary condition that ϕ' vanish at some $\psi = \psi^a$ for all z and θ. We then construct

$$\phi(x_0, y_0, z) = \int_0^z \phi'(x_0, y_0, z')dz' + \phi_0(x_0, y_0). \tag{47}$$

That is, having solved for ϕ', we know ϕ to within an arbitrary function of x_0, y_0 (or equivalently, of the flux coordinates).

To determine ϕ_0 we demand that the parallel current still vanish at the ends to this order in the flux-line geometry. Thus, we once again apply Eq. (22) so that

$$\int_{-L}^{L} dz\, \delta\text{IO}\,\delta\left(\frac{1}{B}\frac{\partial Q}{\partial \psi}\right) + \int_{-L}^{L} dz (\delta\text{IO})\frac{1}{B}\frac{\partial Q}{\partial \psi} = 0. \tag{48}$$

Again, the first term vanishes by symmetry. Thus, we need only compute the correction to the geodesic curvature

$$\delta\text{IO} = \xi^a \frac{\partial x}{\partial \theta} + x^a \frac{\partial \xi}{\partial \theta} + \eta^a \frac{\partial y}{\partial \theta} + y^a \frac{\partial \eta}{\partial \theta}. \tag{49}$$

Let us write this as $\delta\text{IO}_1 + \delta\text{IO}_2$, wherein the two terms represent the contributions of k and ϕ in the formulas for ξ and η. We first have

$$\delta\text{IO}_1 = x_0 y_0 [-(\sigma k)^a \sigma + (\tau k)^a \tau - k\sigma\sigma^a + k\tau\tau^a]. \tag{50}$$

Now, since δIO_1 is an odd function of z, it too does not contribute to Eq. (48). Finally, the remaining piece is

$$\delta\text{IO}_2 = -\sigma y_0 \left(\sigma \frac{\partial \phi}{\partial y_0}\right)^a + \sigma\sigma^a x_0 \frac{\partial}{\partial \theta}\left(\frac{\partial \phi}{\partial y_0}\right) - \tau x_0 \left(\tau \frac{\partial \phi}{\partial x_0}\right)^a - \tau\tau^a y_0 \frac{\partial}{\partial \theta}\left(\frac{\partial \phi}{\partial x_0}\right).$$

After rearranging,

$$\delta\text{IO}_2 = \sigma\sigma^a \frac{\partial}{\partial \theta}\left(x_0 \frac{\partial \phi}{\partial y_0}\right) - \tau\tau^a \frac{\partial}{\partial \theta}\left(y_0 \frac{\partial \phi}{\partial x_0}\right) - y_0 \left(\sigma^2 \frac{\partial}{\partial y_0}\phi'\right)' - x_0 \left(\tau^2 \frac{\partial}{\partial x_0}\phi'\right)',$$

or, in polar coordinates,

$$\delta\text{IO}_2 = \frac{\sigma\sigma^a + \tau\tau^a}{2}\frac{\partial^2 \phi}{\partial \theta^2} + \frac{\sigma\sigma^a - \tau\tau^a}{2} \times \frac{\partial}{\partial \theta}\left(r\sin 2\theta \frac{\partial}{\partial r} + \cos 2\theta \frac{\partial}{\partial \theta}\right)\phi - r\frac{\partial}{\partial r}\left(\frac{\sigma^2 + \tau^2}{2}\phi'\right)' + \left(r\cos 2\theta \frac{\partial}{\partial r} - \sin 2\theta \frac{\partial}{\partial \theta}\right)\left(\frac{\sigma^2 - \tau^2}{2}\phi'\right)'. \tag{51}$$

Finally, making use of symmetry, we obtain the defining equation for ϕ_0

$$\Pi \frac{\partial^2 \phi_0}{\partial \theta^2} = -\Sigma, \tag{52}$$

where

$$\Sigma = \int_{-L}^{L} \frac{dz}{B}\frac{\partial p}{\partial \psi}\left\{(\sigma\sigma^a + \tau\tau^a)\int_0^z dz' \frac{\partial^2 \phi'}{\partial \theta^2} + (\sigma\sigma^a - \tau\tau^a)\int_0^z dz' \frac{\partial}{\partial \theta}\left(r\sin 2\theta \frac{\partial}{\partial r} + \cos 2\theta \frac{\partial}{\partial \theta}\right)\phi' - r\frac{\partial}{\partial r}[(\sigma^2 + \tau^2)\phi']' + \left(r\cos 2\theta \frac{\partial}{\partial r} - \sin 2\theta \frac{\partial}{\partial \theta}\right)[(\sigma^2 - \tau^2)\phi']'\right\}, \tag{53}$$

and

$$\Pi = \int_{-L}^{L} \frac{dz}{B}\frac{\partial p}{\partial \psi}(\sigma\sigma^a + \tau\tau^a). \tag{54}$$

This same integral, Π, appears in the familiar low-β flute-instability criterion: $\Pi > 0$.

At this stage several points need to be made. For one, we see that the perturbation procedure breaks down when the flute-instability parameter, Π, is actually equal to zero. Thus, there is apparently a bifurcation in the equilibrium at the marginal point. A second point is that the parallel current constraint is trivially satisfied beyond the lateral boundary of the plasma since the pressure vanishes. Consequently, *there is not a unique value of ϕ_0 in the vacuum region, any one will do. Different ϕ_0's only correspond to different positions in the vacuum.* With a conducting shell, ϕ_0 is chosen to force $\psi = \psi^a$ on the boundary. In general, our only interest is in the flux-line geometry within the confined plasma; consequently, we do not examine the exterior region.

Thus, we see that Eqs. (45) and (52), along with the appropriate definitions, completely determine the equilibrium. All that remains is to solve the elliptic differential equation (45), which is done in the next section. *From this point on, we consider only the case* in which the boundary is at infinity, where ϕ' must be well-behaved.

IV. SOLUTION FOR ϕ

We solve Eq. (45) by transforming it to Poisson's equation in the stretched coordinates $(\tau^{-1}x_0, \sigma^{-1}y_0)$, which we then invert by means of the appropriate Green's function. In terms of the coordinates (r, θ) defined in (31) and (32), the Green's function is

$$G(r, \theta | r', \theta') = \frac{1}{4\pi}\ln\Lambda,$$

$$\Lambda = \frac{1}{\tau^2}(r\cos\theta - r'\cos\theta')^2 + \frac{1}{\sigma^2}(r\sin\theta - r'\sin\theta')^2,$$

and ϕ' is

$$\phi' = \frac{1}{2\pi\sigma\tau B_0}\mathrm{Im}\int_0^\infty d\psi' \psi' \frac{\partial S(\psi', z)}{\partial \psi'}\int_0^{2\pi} d\theta' e^{2i\theta'}\ln\Lambda, \tag{55}$$

where we have again used (31) to express r' in terms of ψ'.

Next, we integrate by parts with respect to ψ' to ob-

tain

$$\phi' = \frac{1}{2\pi\sigma\tau B_0}\,\mathrm{Im}\int_0^\infty d\psi' S(\psi',z)\int_0^{2\pi} d\theta' e^{i\theta'} \times\left\{\ln\Lambda + \frac{1}{\Lambda}\left[r'^2\left(\frac{\cos^2\theta'}{\tau^2}+\frac{\sin^2\theta'}{\sigma^2}\right) - rr'\left(\frac{\cos\theta\cos\theta'}{\tau^2}+\frac{\sin\theta\sin\theta'}{\sigma^2}\right)\right]\right\}.$$

We then transform the logarithmic term by integrating by parts on θ' and obtain, after some algebraic reduction,

$$\phi' = \frac{1}{2\pi\sigma\tau B_0}\,\mathrm{Im}\int_0^\infty d\psi' S(\psi',z)\int_0^{2\pi} d\theta' e^{i\theta'}\frac{r'^2}{\Lambda} \times\left[\frac{\cos\theta'}{\tau^2}+i\frac{\sin\theta'}{\sigma^2}-\frac{r}{r'}\left(\frac{\cos\theta}{\tau^2}+i\frac{\sin\theta}{\sigma^2}\right)\right].$$

We evaluate the integral over θ' by converting it to a contour integral over the unit circle: $e^{i\theta'}=\zeta$,

$$\phi' = \frac{1}{\pi\sigma\tau B_0}\,\mathrm{Im}\int_0^\infty d\psi' S(\psi',z)\, i\oint d\zeta\,\frac{\zeta\left[(1/\tau^2)(\zeta^2-2\rho\zeta\cos\theta+1)+(1/\sigma^2)(\zeta^2-2i\rho\zeta\sin\theta-1)\right]}{(1/\tau^2)(\zeta^2-2\rho\zeta\cos\theta+1)^2-(1/\sigma^2)(\zeta^2-2i\rho\zeta\sin\theta-1)^2}, \tag{56}$$

where $\rho \equiv r/r'$. The ζ integrand has four poles. Two are roots of

$$\zeta^2 - 2\rho\chi^-\zeta - \mu^- = 0,$$

and two are roots of

$$\zeta^2 - 2\rho\chi^+\zeta - \mu^+ = 0,$$

where

$$\chi^\pm \equiv \tfrac{1}{2}(e^{i\theta} - \mu^\pm e^{-i\theta}), \tag{57}$$

and

$$\mu^\pm \equiv (\tau \pm \sigma)/(\tau \mp \sigma). \tag{58}$$

We henceforth assume that $\tau > \sigma$, implying that $\mu^+ > 1$, $\mu^- < 1$. The final answer will be independent of this choice. We write the roots as

$$\zeta_j^\pm = \rho\chi^\pm + \Gamma_j^\pm, \quad j = 1,2, \tag{59}$$

where

$$\Gamma_j^\pm = \mp(-1)^j[\rho^2(\chi^\pm)^2 + \mu^\pm]^{1/2}, \quad j = 1,2. \tag{60}$$

It is then possible to show that the residue at each of the poles is given by the general formula

$$R_j^\pm = (i/4)\mu^\pm(\rho\chi^\pm/\Gamma_j^\pm + 1). \tag{61}$$

With Eq. (61), Eq. (56) reduces to

$$\phi' = -\frac{1}{2\sigma\tau}\frac{1}{B_0}\,\mathrm{Im}\int_0^\infty d\psi' S(\psi',z)\sum_{\text{poles}}\rho\frac{\mu^\pm\chi^\pm}{\Gamma_j^\pm}, \tag{62}$$

the sum including only those poles lying inside the unit circle.

All that remains is to locate the poles. Consider those at $\zeta = \zeta_j^+$. We note that at $\rho = 1$, $|\zeta_j^+|$ is independent of θ. In particular,

$$|\zeta_1^+|_{\rho=1} = 1, \quad |\zeta_2^+|_{\rho=1} = \mu^+.$$

We also observe that

$$|\zeta_j^+|_{\rho=0} = \sqrt{\mu^+},$$

independent of θ. Now consider $|\zeta_j^+|$ for $\theta = 0$. We see that

$$|\zeta_j^+|_{\theta=0} = -(-1)^j\tfrac{1}{2}\rho(1-\mu^+) + [\tfrac{1}{4}\rho^2(1-\mu^+)^2 + \mu^+]^{1/2},$$

a monotonic function of ρ. For $\theta = \pi/2$, there are two possibilities, depending on the value of ρ. If $\rho < 2\sqrt{\mu^+}/(1+\mu^+)$, Γ_j^+ is real, and

$$|\zeta_j^+|_{\theta=\pi/2} = \sqrt{\mu^+}.$$

If $\rho > 2\sqrt{\mu^+}/(1+\mu^+)$, on the other hand, Γ_j^+ is purely imaginary, and we find

$$|\zeta_j^+|_{\theta=\pi/2} = \tfrac{1}{2}\rho(1+\mu^+) + (-1)^j[\tfrac{1}{4}\rho^2(1+\mu^+)^2 - \mu^+]^{1/2},$$

again, a monotonic function of ρ. Finally, it can be shown that $d|\zeta_j^+|/d\theta = 0$ if, and only if, $\theta = 0$ or $\pi/2$, or if $\rho = 0$ or 1. The net result of the foregoing considerations is that all possible values of $|\zeta_j^+|$ are confined to the shaded region of Fig. 1.

A similar diagram could be constructed for $|\zeta_j^-|$ by recognizing that

$$(\zeta_j^\pm)^* = -\mu^\pm\zeta_j^\mp,$$

or

$$|\zeta_j^-| = (1/\mu^+)|\zeta_j^+|. \tag{63}$$

From Fig. 1 and Eq. (63) we conclude that for $\rho < 1$, i.e., $\psi' > \psi$, the contributing poles are ζ_j^+. Referring to Eq. (62), we see that in this case the sum over the poles is proportional to $(\Gamma_1^+)^{-1} + (\Gamma_2^+)^{-1} = 0$. The effect is to restrict the ψ' integration to the range $[0, \psi]$. Again referring to Fig. 1 and Eq. (63), we see that, for $\rho > 1$ ($\psi' < \psi$), only the poles at $\zeta = \zeta_1^+$ contribute.

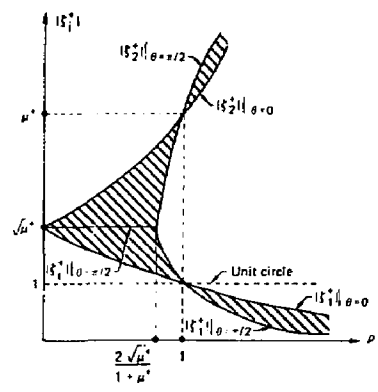

FIG. 1. Sketch showing the location of the poles $\zeta = \zeta_j^+$ relative to the boundary of the unit circle $|\zeta| = 1$.

Thus, from Eq. (62),

$$\phi' = -\frac{1}{2\sigma\tau}\frac{1}{B_0}\,\mathrm{Im}\int_0^{\psi} d\psi' S(\psi', z)\rho\left(\frac{\mu^+\chi^+}{\Gamma_1^+}+\frac{\mu^-\chi^-}{\Gamma_1^-}\right).$$

We can simplify further by noting that $(\chi^+/\Gamma_1^+)^* = \chi^-/\Gamma_1^-$. Therefore, finally,

$$\phi' = -\frac{2}{(\tau+\sigma)^2 B_0}\frac{1}{\mu}\,\mathrm{Im}\int_0^{\psi} d\psi' S(\psi', z) \times\left(1+4\frac{\psi'}{\psi}\frac{\mu e^{i2\theta}}{(1-\mu e^{i2\theta})^2}\right)^{-1/2}. \tag{64}$$

In Eq. (64) and henceforth we define

$$\mu \equiv \mu^-. \tag{65}$$

After considerable algebra this solution has been shown to satisfy Eq. (45) by direct substitution. It can easily be shown that if S is a polynomial in ψ of order N, then, for $\psi < \psi_B$, ϕ' has harmonics up to $\sin 2(N+1)\theta$. On the other hand, for $\psi > \psi_B$, all harmonics are generated (although, of course, falling off as ψ^{-N}). To complete the solution, the stream function itself is given by

$$\phi = \int_0^{z} \phi'(\psi, \theta, z')dz' + \phi_0(\psi, \theta), \tag{66}$$

where $\phi_0(\psi, \theta)$ is obtained from Eqs. (52) through (54).

In Appendix B we write down the explicit equations for the equilibrium inside the plasma source for the following pressure profiles:

$$p_u = (1-\psi/\psi_B)\hat{p}_u(B), \tag{67}$$

and

$$p_u = (1-\psi/\psi_B)^2\hat{p}_u(B), \tag{68}$$

where $\hat{p}_u(B)$ is chosen to fit the various tandem mirror configurations, and the ψ dependence is assumed to be the same in different regions of the system. Although configurations in which the weighting function varies from one region to another are conceivable, we do not consider such complications.

V. DISCUSSION

It should be emphasized that equilibrium based on the anisotropic magnetohydrodynamic equations does not in itself guarantee long time equilibrium. These equations only assume (μ, J) invariance. To ensure equilibrium on a drift time scale, the particle distribution must satisfy the drift kinetic equation

$$\frac{\partial F}{\partial t}+\frac{c}{e}\left(\frac{\partial K}{\partial \psi}\frac{\partial F}{\partial \theta}-\frac{\partial K}{\partial \theta}\frac{\partial F}{\partial \psi}\right)=0, \tag{69}$$

where the partial derivatives imply (μ, J) held constant; K is the Hamiltonian defined in terms of the action as

$$J = \int ds[2(K-\mu B-e\Phi)/m]^{1/2}; \tag{70}$$

and its derivatives are proportional to the respective ∇B drifts. Now, the ∇B drifts due to finite β are large (of order λ^{-2}) compared with the curvature drifts and since B is a function of ψ only (θ dependence is of order λ^3), the drift kinetic equation is automatically satisfied to the lowest order in λ since F is not a function of θ.

Next, before we present a detailed equilibrium, the following points should be made. We note that the β correction to the flux surface defined by $p(\psi, B)$, is inversely proportional to the instability criterion [note the definition of Π, Eq. (54)]. At the marginal point the perturbation expansion breaks down, i.e., $\phi_0 \to \infty$, which implies a bifurcation in the equilibrium. Whether the other equilibrium is physical or not we cannot say at this time.

Another observation regarding this term is that the signs of ϕ_0 and Π are the same. The numerator on the right side of Eq. (52) for the tandem mirror configuration is positive definite; to see this consider Eq. (B9). Given that the central cell is generally axisymmetric over most of its length, only the second term proportional to k_1 in Eq. (B7) is scaled with this longest length. All other terms in the integrand are zero in the axisymmetric region and can be dropped. Then, for this term we have

$$\Sigma = \frac{16\psi^2}{3B_0\psi_B}\sin 4\theta\int_{-L}^{L} dz\,\frac{\hat{p}}{B}(\sigma\sigma'' - \tau\tau'') \times\int_0^{z}\frac{dz'}{B(\sigma+\tau)^2}\int_{z'}^{l} dz''\,\frac{\hat{p}}{B}(\sigma\sigma''-\tau\tau'').$$

Now define $z = \pm l$ as the boundary of the axisymmetric region such that $l/(L-l) \gg 1$ and consequently,

$$\Sigma = \frac{32\psi^2}{3B_0\psi_B}\sin 4\theta\int_{l}^{L} dz\,\frac{\hat{p}}{B}(\sigma\sigma''-\tau\tau'') \times\int_0^{l}\frac{dz}{B(\sigma+\tau)^2}\int_{l}^{L} dz\,\frac{\hat{p}}{B}(\sigma\sigma''-\tau\tau'') \approx \frac{8}{3}\frac{\psi^2}{B_0\psi_B}\sin 4\theta\left(\int_{l}^{L} dz\,\frac{\hat{p}}{B}(\sigma\sigma''-\tau\tau'')\right)^2\int_0^{l}\frac{dz}{B},$$

and finally we have

$$\phi_0 = -\frac{1}{12}\frac{\psi^2}{B_0\psi_B}\int_0^{l}\frac{dz}{B}\,\frac{\left[\int_l^L dz\,\hat{p}(\sigma\sigma''-\tau\tau'')/B\right]^2}{\int_0^L dz\,\hat{p}(\sigma\sigma''+\tau\tau'')/B}\sin 4\theta. \tag{71}$$

The form of Eq. (71) is the same as that derived by Stupakov[3] who considered only the case where l was very large.

Now the flux surface at the midplane is easily seen to be, Eqs. (39) and (40),

$$\frac{1}{2}[r(0)^2B(0)] = \psi(1+2k) + B_0\frac{\partial\phi_0}{\partial\theta}. \tag{72}$$

Hence if $\Pi < 0$ (denominator >0), which it must be for a stable configuration, the octupole distortion squares off the surface. With the other sign the surface exhibits a diamond-shaped distortion.

This property explains the difference between our results and those of Stupakov[3] that led to a diamond-shaped distortion. He argued that a proper boundary condition was $j_u = 0$ at the mirror peak separating the central cell from the plug, thus discarding any influence of the plug on the central cell. In general, the flute-instability criterion [Eq. (54)] is positive (unstable) for the central-cell alone. Because of this change in sign, he was led to the constraint that the central cell could not be too long or else field lines would migrate to the walls because of the finite distor-

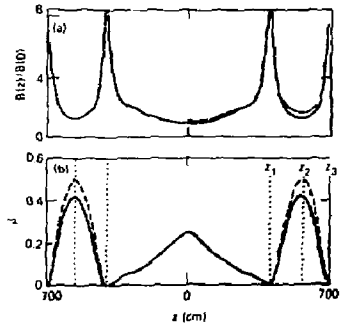

FIG. 2. Field strength and plasma beta on axis. (a) $B(z)$ on axis, both *in vacuo* (dashed curve) and with plasma present (solid curve), normalized to $(B_c)_0$. (b) Plasma beta on axis. $\beta_\perp = 2p_\perp/B_0^2$ is shown dashed and $\beta = (p_\perp + p_\parallel)/B_0^2$ solid. Vertical dotted lines mark the inboard mirror peaks and midplanes of the end cells.

tion of the flux. As we will subsequently show we obtain the opposite effect, that is, because beta is finite, field lines reduce their maximum excursion from the axis in the central-cell region.

Now, which boundary condition is correct? Obviously, if we assume that the mirror is isolated from the outside world, $j_\parallel = 0$ at the axial edge of the confined plasma. This boundary condition, along with the lateral boundary condition, completely determines the equilibrium. There is no freedom to specify the parallel current at the interface of the central cell and the plug. We, of course, find that it is not simultaneously zero at both interfaces.

We now present results based on the linear flux dependence of the pressure profile for a standard tandem

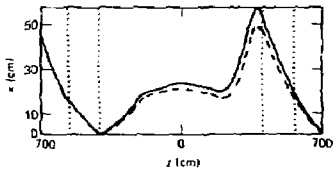

FIG. 4. The r coordinate of the field line $\psi = \psi_B$, $\theta = \pi/4$, *in vacuo* (dashed curve) and with plasma present (solid curve). Vertical dotted lines are as in Fig. 2.

mirror configuration (the TMX Upgrade) for which $(B_0)_c = 3 \times 10^3$ G, and $\psi_B = 1.35 \times 10^6$ G cm^2. The computer code EFFI[7] and the experimental coil configuration were used to generate the vacuum field functions $B(z)$, $\sigma(z)$ on a fine grid (typically 200–400 points). Cubic spline interpolation was used between grid points so that the quadratures arising in the calculation of ϕ could be evaluated using the Gear method.[8] In Fig. 2 we show the dependence of mod-B and pressure on z. In Fig. 3, we plot the parallel current per unit flux as a function of z in both the total field and the vacuum field. In Fig. 4, we compare a field-line trajectory at finite beta with its trajectory in the vacuum for the same flux coordinates. In Figs. 5 and 6, we have similar comparisons for the normal and geodesic curvatures. Note that although the $O(\lambda^2)$ quantity $2\psi R$ approaches unity in the transition regions for the extreme case shown ($\psi = \psi_B$), it is small over the bulk of the plasma because it scales as r^2. In Fig. 7, we compare flux surfaces in the finite-beta field with those in the vacuum field at the midplane of the machine, the mirror peaks, and the midplane of the plug. We see squaring off of the flux surface at the midplane of the machine (octupole distortion). We also note the reduced eccentricity at the inboard mirror, the plasma currents are attempting to recircularize. Conversely, the eccentricity at the outboard mirror is increased.

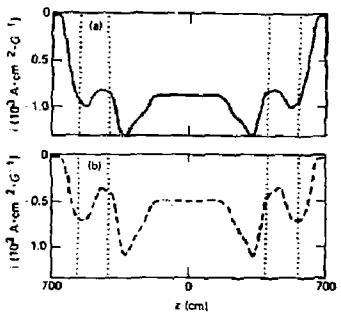

FIG. 3. Parallel current per unit magnetic flux calculated from Eq. (22) on the field line $\psi = \psi_B$, $\theta = \pi/4$. In (a) the equilibrium magnetic field was used in the calculation, while in (b) the vacuum field was used. Vertical dotted lines are as in Fig. 2.

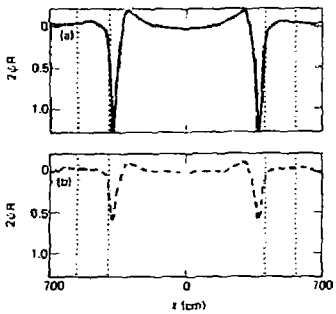

FIG. 5. The quantity $2\psi R$ on the field line $\psi = \psi_B$, $\theta = \pi/4$, in both the equilibrium magnetic field (a) and *in vacuo* (b). Vertical dotted lines are in Fig. 2.

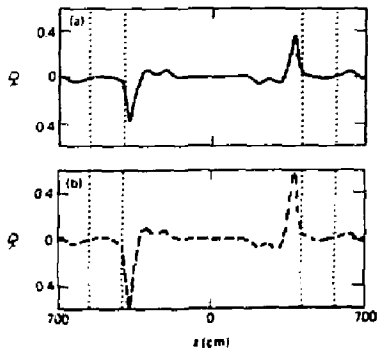

FIG. 6. The geodesic curvature on the field line $z=z_0$, $\theta=\pi/4$, in both the equilibrium magnetic field (a) and *in vacuo* (b). Vertical dotted lines are as in Fig. 2.

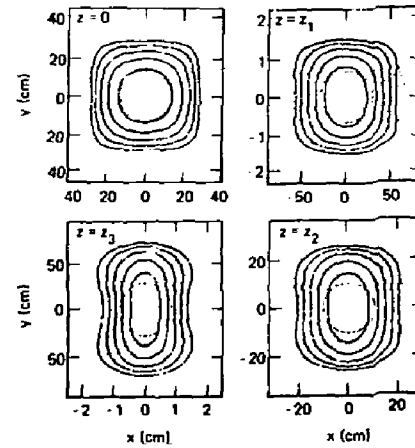

FIG. 7. Constant-pressure-surface cross sections perpendicular to the magnetic axis *in vacuo* (dotted curves) and at finite beta (solid curves). Contours are at equally spaced flux intervals shown at four different axial positions.

In these comparisons we have used

$$\hat{p}_\perp = \hat{p} = (\beta_{ce}/2)\,B^2(0), \quad z < z_1$$

and

$$\hat{p}_\perp = \frac{\beta_{s\parallel m}}{2}\,B^2(z_2)\,\frac{B_m^2 - B^2}{B_m^2 - B^2(z_2)} + \delta p_\perp, \quad z_1 < z < z_2,$$

where

$$\delta p_\perp = \frac{\beta_{ce}}{2}\,B^2(0)\,\frac{B^2(z) - B^2(z_1)}{B^2(z_2) - B^2(z_1)}, \quad z_1 < z < z_2,$$

$$\delta p_\perp = 6\beta_{ce}\,\frac{B^2(0)B^2(z)[B(z) - B(z_1)][B_m - B(z)]}{[B(z_1) + B(z_2)][B_m - B(z_2)]^3},$$

$$z_2 < z < z_3,$$

where $B_m = \min[B(z_1), B(z_3)]$.

To close, $\delta p_\parallel$ is obtained from the integral of the parallel pressure balance equation

$$\frac{d}{dB}\frac{p_\parallel}{B} = -\frac{p_\perp}{B^2}. \tag{73}$$

Note that these combinations were chosen to force $\hat{p}_\parallel$ to be zero at the plasma boundary. Also note that z_1 is the position of the inboard mirror, z_3 is the position of the outboard mirror, and z_2 is the position of the plug minimum (see Fig. 2). These choices are used to represent the penetration of the central-cell plasma and to identify the solenoid and plug beta values. For these computations $\beta_c = 0.25$ and $\beta_p = 0.5$. These high values were picked to emphasize the effects of the plasma currents. At lower values the results are qualitatively the same.

We conclude with a word of caution. The analysis is perturbative and so field line displacements should be small relative to their vacuum positions to be believed. Also, to quantify the accuracy it is necessary to calculate to next order in β, a project not contemplated at this time.

ACKNOWLEDGMENTS

We have benefited greatly from the helpful comments of L. S. Hall.

This work was performed under the auspices of the U. S. Department of Energy by the Lawrence Livermore National Laboratory under contract number W-7405-ENG-48.

APPENDIX A. LONG-THIN DIFFERENTIAL GEOMETRY

Here, we derive Eqs. (17) and (21), which, with Eq. (22), determine the field-line geometry. Both follow from the large-aspect-ratio limit of a standard differential geometric relationship among the variables of any invertible coordinate transformation. This result is most concisely stated if we denote the Cartesian coordinates (x,y,z) as (x_1,x_2,x_3) and the flux coordinates (α,β,s) by $(\bar{x}_1,\bar{x}_2,\bar{x}_3)$. Then, it is easily shown that

$$\frac{\partial \bar{x}_i}{\partial x_j} = \epsilon_{imn}\epsilon_{jkl}\,\frac{\partial(x_k,x_l)}{\partial(\bar{x}_m,\bar{x}_n)}\,\frac{\partial(\bar{x}_1,\bar{x}_2,\bar{x}_3)}{\partial(x_1,x_2,x_3)}, \tag{A1}$$

where $\epsilon_{imn} = 0$ if any two indices are equal and $=\pm 1$ according to whether (i,m,n) is an even or odd permutation of $(1,2,3)$; the standard notation for the Jacobian is used; and the summation convention is not used. An equivalent equation with barred and unbarred variables interchanged clearly also holds.

From Eq. (10) we find that

$$\frac{\partial(\bar{x}_1,\bar{x}_2,\bar{x}_3)}{\partial(x_1,x_2,x_3)} = \nabla\alpha \times \nabla\beta \cdot \nabla s = \mathbf{B}\cdot\nabla s = B. \tag{A2}$$

Then, Eq. (17) follows immediately from the long-thin limit of the special case of Eq. (A1) for which $i=j=3$:

$$\frac{\partial s}{\partial z} = \frac{\partial(x,y)}{\partial(\alpha,\beta)}\,B. \tag{A3}$$

To $O(\lambda)$, however, Eq. (14) implies that

$$\frac{\partial \bar{x}_j}{\partial \bar{x}_i}\frac{\partial x_3}{\partial \bar{x}_i} = \delta_{j3}, \tag{A4}$$

with which Eq. (A3) becomes

$$\frac{\partial(x, y)}{\partial(\alpha, \beta)} = B^{-1},$$

i.e., Eq. (17).

To obtain Eq. (21) we note that in the large-aspect-ratio limit, the components of the unit vector $\hat{b}$ are [see Eqs. (15), (28)]

$$b_x = x', \quad b_y = y', \quad b_z = 1. \tag{A5}$$

Inserting Eqs. (A5) in Eq. (8) gives

$$i = \hat{b}\cdot\nabla\times\hat{b} = -x'y'' + y'x'' + \frac{\partial y'}{\partial x} - \frac{\partial x'}{\partial y}. \tag{A6}$$

The first two terms on the right side of Eq. (A6) are $O(\lambda^2)$ relative to the last two, leaving

$$i = \frac{\partial y'}{\partial x} - \frac{\partial x'}{\partial y} = \frac{\partial y'}{\partial \alpha}\frac{\partial \alpha}{\partial x} + \frac{\partial y'}{\partial \beta}\frac{\partial \beta}{\partial x} - \frac{\partial x'}{\partial \alpha}\frac{\partial \alpha}{\partial y} - \frac{\partial x'}{\partial \beta}\frac{\partial \beta}{\partial y}. \tag{A7}$$

If we now use Eqs. (A4) in Eqs. (A1) to evaluate the necessary partial derivatives, we find that Eq. (A7) becomes

$$i = B\left(\frac{\partial y'}{\partial \alpha}\frac{\partial y}{\partial \beta} - \frac{\partial y'}{\partial \beta}\frac{\partial y}{\partial \alpha} + \frac{\partial x'}{\partial \alpha}\frac{\partial x}{\partial \beta} - \frac{\partial x'}{\partial \beta}\frac{\partial x}{\partial \alpha}\right)$$
$$= B\left(\frac{\partial(x', x)}{\partial(\alpha, \beta)} + \frac{\partial(y', y)}{\partial(\alpha, \beta)}\right),$$

which is Eq. (21).

APPENDIX B. LINEAR AND QUADRATIC PRESSURE PROFILES

In this appendix, we obtain the explicit solutions for the two pressure profiles given by Eqs. (67) and (68). First, define

$$k_1(z) = \frac{4}{B}\frac{1}{(\sigma+\tau)^2}\int_z^L dz\,\frac{\hat{p}}{B}\,(\sigma\sigma'' - \tau\tau''), \tag{B1}$$

and

$$k_2(z) = \mu(\hat{p}_\perp/B^2)'. \tag{B2}$$

Now considering first the linear pressure profile, we have from Eqs. (42), (46), and (64)

$$\phi_1' = -\frac{1}{2\mu B_0}\,\mathrm{Im}\int_0^\psi d\psi'\left[(k_1+k_2) - \frac{\psi'}{\psi_B}\left(k_1+\frac{k_2}{2}\right)\right]$$
$$\times\left(1 + \frac{4\psi'}{\psi}\frac{\eta}{(1-\eta)^2}\right)^{-1/2}, \tag{B3}$$

with the definition

$$\eta = \mu e^{2i\theta}. \tag{B4}$$

Integrating by parts twice generates

$$\phi_1' = -\frac{\psi}{2\mu B_0}\,\mathrm{Im}\left[(k_1+k_2)\frac{1-\eta}{2\eta}(1+\eta-1+\eta)\right.$$
$$\left. - \frac{\psi}{\psi_B}\left(k_1+\frac{k_2}{2}\right)\frac{1-\eta^2}{2\eta} - \frac{1-\eta}{12\eta^2}[(1+\eta)^3 - (1-\eta)^3]\right],$$

or collecting terms,

$$\phi_1' = -\frac{\psi}{2\mu B_0}\,\mathrm{Im}\left[(k_1+k_2)(1-\eta) - \frac{i}{4}\left(k_1+\frac{k_2}{2}\right)\left(\frac{1}{2} - \frac{2}{3}\eta + \frac{1}{6}\eta^2\right)\right]. \tag{B5}$$

Taking the imaginary part produces the answer

$$\phi_1' = \frac{\psi}{B_0}\left\{\left[\frac{1}{2}(k_1+k_2) - \frac{\psi}{3\psi_B}\left(k_1+\frac{k_2}{2}\right)\right]\sin 2\theta\right.$$
$$\left. + \mu\left(k_1+\frac{k_2}{2}\right)\frac{\psi}{12\psi_B}\sin 4\theta\right\}. \tag{B6}$$

Turning to the expressions for ϕ_0, Eqs. (52) through (54), and noting that k_1 and k_2 are even functions of z, we have for the numerator:

$$\Sigma = \frac{4\psi^2}{3B_0\psi_B}\sin 4\theta\int_{-L}^{L} dz\,\frac{\hat{p}}{B}\left\{(\sigma\sigma'' + \tau\tau'')\int_0^z dz'\,\mu\left(k_1+\frac{k_2}{2}\right)\right.$$
$$+ (\sigma\sigma'' - \tau\tau'')\int_0^z dz'\left(k_1+\frac{k_2}{2}\right) + \frac{1}{4}\left[(\sigma^2+\tau^2)\mu\left(k_1+\frac{k_2}{2}\right)\right.$$
$$\left.\left. + (\sigma^2-\tau^2)\left(k_1+\frac{k_2}{2}\right)\right]'\right\}. \tag{B7}$$

Note that the term linear in ψ cancels. Next integrating by parts and combining the integrated part, we have with

$$\left(\frac{\hat{p}}{B}\right)' = \frac{B}{2}\left(\frac{\hat{p}_\perp}{B^2}\right)' \tag{B8}$$

[see Eq. (2)] and Eq. (25),

$$\phi_{0,1} = -\frac{\psi^2}{12B_0\psi_B}\left\{\int_{-L}^{L} dz\,\frac{\hat{p}}{B}\left[(\sigma\sigma'' + \tau\tau'')\int_0^z dz'\,\mu\left(k_1+\frac{k_2}{2}\right)\right.\right.$$
$$\left. + (\sigma\sigma'' - \tau\tau'')\int_0^z dz'\left(k_1+\frac{k_2}{2}\right)\right] + \frac{B_0}{4}\int_{-L}^{L} dz\,k_2\left(k_1+\frac{k_2}{2}\right)\Bigg\}$$
$$\times\frac{\sin 4\theta}{\int_{-L}^{L} dz\,\hat{p}(\sigma\sigma'' + \tau\tau'')/B}. \tag{B9}$$

Next, we turn to the quadratic source. Here we have

$$\phi_2' = -\frac{1}{2\mu B_0}\,\mathrm{Im}\int_0^\psi d\psi'\left\{(k_1+k_2) - 2\frac{\psi'}{\psi_B}\left(k_1+\frac{k_2}{2}\right)\right.$$
$$\left. + \left(\frac{\psi'}{\psi_B}\right)^2\left(k_1+\frac{k_2}{3}\right)\right\}\left(1 + \frac{4\psi'}{\psi}\frac{\eta}{(1-\eta)^2}\right)^{-1/2}. \tag{B10}$$

Integrating by parts three times produces

$$\phi_2' = -\frac{\psi}{2\mu B_0}\,\mathrm{Im}\left((k_1+k_2)(1-\eta) - \frac{\psi}{\psi_B}\left(k_1+\frac{k_2}{2}\right)\right.$$
$$\times\left(1 - \frac{4}{3}\eta + \frac{1}{3}\eta^2\right) + \left(\frac{\psi}{\psi_B}\right)^2\left(k_1+\frac{k_2}{3}\right)\left\{\frac{1-\eta^2}{2\eta} - \frac{1-\eta^2}{6\eta^2}(1+\eta)^2\right.$$
$$\left.\left. + \frac{1}{60\eta^3}(1-\eta)[(1+\eta)^5 - (1-\eta)^5]\right\}\right), \tag{B11}$$

where we have used Eq. (B5) (note that the term quadratic in ψ/ψ_B is multiplied by two here). Again collecting terms in the braces we obtain for that term

$$\left(\frac{\psi}{\psi_B}\right)^2\left(k_1+\frac{k_2}{3}\right)\left(\frac{1}{3} - \frac{\eta}{2} + \frac{\eta^2}{5} - \frac{\eta^3}{30}\right).$$

Finally we have for the imaginary part

$$\phi_2' = \frac{\psi}{B_0}\left[\frac{1}{2}(k_1+k_2)\sin 2\theta - \frac{1}{2}\frac{\psi}{\psi_B}\left(k_1+\frac{k_2}{2}\right)\right.$$
$$\times\left(\frac{4}{3}\sin 2\theta - \frac{1}{3}\mu\sin 4\theta\right) + \frac{1}{2}\left(\frac{\psi}{\psi_B}\right)^2\left(k_1+\frac{k_2}{3}\right)$$
$$\left.\times\left(\frac{1}{2}\sin 2\theta - \frac{1}{5}\mu\sin 4\theta + \frac{1}{30}\mu^2\sin 6\theta\right)\right]. \qquad \text{(B12)}$$

Closing, we compute the expression for ϕ_0. We immediately see that

$$\phi_{0,2} = 2\phi_{0,1} + \delta\phi_0, \qquad \text{(B13)}$$

where $\delta\phi_0$ comes from the new term proportional to $(k_1 + k_2/3)$ in Eq. (B12). For that term we have

$$\delta\phi_0 = \frac{\psi^2}{10B_0\psi_B^2}\left(\int_{-L}^{L} dz\,\frac{\hat{\rho}}{B}\left\{(\sigma\sigma'' + \tau\tau'')\int_0^z dz'\,\mu\left(k_1+\frac{k_2}{3}\right) + (\sigma\sigma'' - \tau\tau'')\int_0^z dz'\left(\frac{5}{4} - \frac{1}{4}\mu^2\right)\left(k_1+\frac{k_2}{3}\right)\right.\right.$$
$$\left.\left. - \left[\frac{\mu}{2}\sigma\tau\left(k_1+\frac{k_2}{3}\right)\right]'\right\}\right)\frac{\sin 4\theta}{\int_{-L}^{L} dz\,\hat{\rho}(\sigma\sigma'' + \tau\tau'')/B}$$

and, after integrating by parts

$$\phi_{0,2} = 2\phi_{0,1} + \frac{\psi^2}{10B_0\psi_B^2}\left\{\int_{-L}^{L} dz\,\frac{\hat{\rho}}{B}\left[(\sigma\sigma'' + \tau\tau'')\int_0^z dz'\,\mu\left(k_1+\frac{k_2}{3}\right) + (\sigma\sigma'' - \tau\tau'')\int_0^z dz'\left(\frac{5}{4} - \frac{1}{4}\mu^2\right)\left(k_1+\frac{k_2}{3}\right)\right]\right.$$
$$\left. + \frac{B_0}{4}\int_{-L}^{L} dz'\,k_2\left(k_1+\frac{k_2}{3}\right)\right\}\frac{\sin 4\theta}{\int_{-L}^{L} dz\,\hat{\rho}(\sigma\sigma'' + \tau\tau'')/B}. \qquad \text{(B14)}$$

[1] L. S. Hall and B. McNamara, Phys. Fluids 18, 552 (1975).
[2] B. McNamara, D. V. Anderson, J. K. Boyd, J. A. Byers, R. Cohen, T. A. Cutler, L. S. Hall, R. F. Post, and M. E. Rensink, in *Plasma Physics and Controlled Nuclear Fusion Research* (International Atomic Energy Agency, Vienna, 1977), Vol. 1, p. 161.
[3] G. V. Stupakov, Fiz. Plasmy 5, 871 (1979) [Sov. J. Plasma Phys. 5, 486 (1979)].
[4] W. A. Newcomb, Lawrence Livermore National Laboratory Report, UCRL-85188 (1980).
[5] H. Grad, in *Proceedings of Symposia in Applied Mathematics* (American Mathematical Society, Providence, Rhode Island, 1967), Vol. XVIII, p. 162.
[6] H. P. Furth and M. N. Rosenbluth, Phys. Fluids 7, 764 (1964).
[7] S. J. Sackett, Lawrence Livermore National Laboratory Report, UCRL-52402 (1978).
[8] C. W. Gear, Commun. ACM 14, 176 (1971).

APPENDIX B

GYROKINETIC MAGNETOHYDRODYNAMICS (MHD)

W. M. Nevins and T. B. Kaiser

1. INTRODUCTION

Quadrupole tandem mirrors rely for MHD stability on high pressure-weighting of regions of favorable curvature (MHD anchors) relative to those of destabilizing curvature. This guarantees stability to curvature-driven modes when the plasma β-values in the unstable region of destabilizing curvature is less than some critical value that depends on the value of β in the anchors and on details of the magnetic geometry.

To determine the critical β-value, we must formulate and solve the equation of motion for the modes of interest. At low β, the characteristic perturbations are electrostatic flute modes whose stability criterion is simple and well-known.[B-1,9] At higher values of β, magnetic-field perturbations make flux-line bending possible. This allows modes to localize in regions of unfavorable curvature. The stability properties of such ballooning modes ultimately will determine the critical β-values achievable in tandem mirrors.

Here in Appendix B we present a full three-dimensional analysis of "large-n" ballooning modes in the axicell configuration of MFTF-B. Since this analysis was performed, the proposal coil set for MFTF-B has been altered. While the resulting changes in the equilibrium magnetic field can be expected to change quantitative results, we do not expect a change in our main qualitative result: in a machine the size of MFTF-B ($a_i/R_p \approx 0.06$ in the central cell), localized modes will not limit the central-cell β.

In Sec. 2 we discuss flute stability, and in Sec. 3 we review the "large-n" formalism[B-2] as it applies to tandem mirrors. In Sec. 4 we present the ideal MHD central-cell beta limit due to large-n ballooning modes. In Sec. 5 we show how the formalism of "quasi-classical" mechanics may be used to obtain a global-dispersion relation, which includes both kinetic effects[B-3,4]

and the "1/n" corrections.[B-3] We present marginal-stability boundaries for the axicell configuration of MFTF-B in Sec. 6 and discuss our results in Sec. 7.

2. FLUTE STABILITY

In the low-β limit, the MHD eigenmodes of a tandem mirror are flute-like.[B-1] A sufficient condition for the instability of such modes is that

$$\int_{-L}^{L} \frac{dz}{B} \frac{\partial}{\partial \psi} p\mathcal{R} > 0 \quad , \quad p = \frac{p_\perp + p_\parallel}{2} \quad , \tag{B.1}$$

where B is the magnetic-field strength ($\underset{\sim}{B} = \hat{B}b$); ψ is the principal flux coordinate ($\underset{\sim}{B} = \nabla\psi \times \nabla\theta$); $P_{\perp,\parallel}(\psi,B)$ are components of the plasma-pressure perpendicular and parallel to $\underset{\sim}{B}$; and $\mathcal{R}$ is the normal curvature ($\underset{\sim}{K} = \hat{b} \cdot \nabla\hat{b} = \mathcal{R}\nabla\psi + \mathcal{D}\nabla\theta$). Thus, it is necessary for stability that the flux-tube average of the pressure-weighted normal curvature be positive.

This condition along with minimization of plasma current flowing parallel to $\underset{\sim}{B}$ through the central cell have been the major constraints on the design of the MFTF-B magnetic-field coils. While the design continues to evolve toward one with acceptably small central-cell parallel current, we examine the flute stability of our latest design, which has not yet satisfied all constraints. We consider two pressure models for the transition region; one in which the pressure is constant ($\beta \approx 0.05$) and the other in which $p \sim B$ represents a passing and trapped population with a $g_B \approx 3$. Stable central-cell beta-values (β_c) are listed in Table B-1 for both equilibrium and vacuum-field configurations for an axicell beta of 0.2 and an anchor beta of 0.55, the reference-case values. These central-cell beta values are to be

Table B-1. Critical beta-values for the central cell.

	Equilibrium field	Vacuum field	Mars-mode
$p_{TR} \sim B$	$\beta_c = 0.36$	$\beta_c = 0.6$	$\beta_c = 0.5$
p_{TR} constant	$\beta_c = 0.53$	$\beta_c = 0.96$	$\beta_c = 0.5$

compared with the value of 0.5 of the reference case (Mars mode). While the precise value of the critical central-cell β for flute stability will probably be somewhat different for MFTF-B, the qualitative result should be the same: flute modes are not expected to impose a serious constraint on performance of the machine.

3. LARGE-n THEORY AND OTHER APPROXIMATIONS

In the past few years a great deal of progress has been made in analyzing ballooning modes by employing the "large-n" expansion.[B-2] Although this formalism was originally developed to analyze ballooning modes in tokamaks[B-2,3], it has been extended to non-axisymmetric systems like tandem mirrors.[B-4] The large-n formalism describes modes in which the typical scale length for variation of the perturbation across the magnetic field is short in comparison to either the equilibrium scale lengths or the scale length for variations of the perturbation parallel to $\underset{\sim}{B}$. An eikonal approximation, $\phi \simeq \tilde{\phi}(s) \exp [iS(\theta,\psi)]$, is then employed to describe the perpendicular variations in the stream function, ϕ, which describes the perturbation. The assumption of rapid perpendicular variation allows one to reduce the MHD ballooning mode problem to the solution of a second-order ordinary differential equation along each magnetic-field line.[B-2,3]

This equation is most simply written in magnetic-flux coordinates, (s,θ,ψ); where the enclosed magnetic flux ψ labels a particular flux surface; θ is an angle-like variable that labels a particular magnetic field line on this flux surface; and s measures the position along this magnetic-field line. In the work reported here, we use the long-thin or paraxial expansion.[B-5] To lowest significant order in the long-thin parameter, $\lambda = R/L$ (R is a typical radial dimension and L is a typical axial dimension), no difference exists between s and the axial distance z. Hence, we may write the ballooning-mode equation as a second-order differential equation in z:

$$\left[\frac{\partial}{\partial z}\frac{Q|\underset{\sim}{\nabla}S|^2}{B^3}\frac{\partial}{\partial z} + \frac{p(z)}{B^3}|\underset{\sim}{\nabla}S|^2(\omega^2 - \omega\omega^*S_\theta)\right.$$

$$\left. + \frac{1}{B^3}[\underset{\sim}{\nabla}(P_\perp + P_{\parallel})x\hat{b}]\,(\underset{\sim}{K}\times\hat{b}) : \underset{\sim}{\nabla}S\,\underset{\sim}{\nabla}S\right]\tilde{\phi} = 0\,, \qquad (B.2)$$

where $Q = B^2 + P_\perp - P_\parallel$ is the parallel component of the total stress tensor;[B-5] ∇S is the gradient of the eikonal $S(\theta,\psi)$; $\rho(z)$ is the mass density; ω is the wave frequency; $\Omega^* = (T_i/eB)(1/rR_p)$ is the angular velocity of diamagnetic rotation [R_p is the scale length for variation in the perpendicular ion pressure, $R_p^{-1} \equiv -(rB/P_{i\perp})(\partial P_{i\perp}/\partial\psi)$]; while $S_\theta \equiv \partial S/\partial\theta$ is proportional to the surface component of the wave vector. Hence, $\Omega^* S_\theta$ is the usual diamagnetic drift frequency. In writing this equation we have ignored the finite-β corrections to Ω^* (see Ref. B-4). This approximation is justified because we find that Eq. B.2 properly describes the most unstable modes only at modest values of the central-cell beta, $\beta \lesssim 0.1$.

We will solve this equation subject to the boundary condition $\partial\tilde{\phi}/\partial z = 0$ at the axial boundaries of the plasma. Physically, this boundary condition follows from requiring that the perturbed current vanish in the vacuum external to the plasma. A consequence of this boundary condition is that, while the labels of magnetic-field lines beyond the axial boundaries of the plasma may be interchanged by the perturbation, the structure of the external magnetic field is left unaltered.

It is necessary to find MHD equilibria in order to evaluate the coefficients in Eq. B.2. Nonaxisymmetric tandem-mirror equilibria are obtained by using the expansion described in Ref. B-6. This evolves expanding in both the long-thin parameter λ and in $\beta \equiv 2P/B^2$.

A final approximation is to treat Ω^* as constant, independent of θ, ψ, and z. The lack of dependence on θ and ψ is justified if Ω^* varies little over the region in θ and ψ, over which the modes are localized. This approximation is analogous to the approximation $\partial\omega^*/\partial r = 0$ used in the nonlocal analysis of electron-drift waves in toroidal systems.[B-7] Diamagnetic effects are most important in the long central cell of tandem mirrors.[B-8] and Ω^* is nearly constant in this region. Hence, we believe that the approximation $\partial\Omega^*/\partial z$ is justified. We will see in Sec. 6 that the approximation Ω^* = constant greatly simplifies the system of equations that must be solved numerically to obtain the marginal-stability boundary for ballooning modes in a given magnetic configuration.

4. IDEAL MHD RESULTS

Previous analysis of beta limits in MFTF-B were based on a study[B-9] of ideal MHD ballooning modes in the large-n limit. We review the principle results of ideal MHD-ballooning-mode theory here because they provide a basis for understanding the full three-dimensional treatment, including both the kinetic term and the "1/n corrections" described in the next section. The ideal MHD-ballooning-mode equation may be obtained from Eq. B.2 by taking the limit $\Omega^* \to 0$. Since Ω^* is proportional to a_i/R_p, this is equivalent to considering a very large machine, in which the ion gyroradius a_i is very much less than a radial-scale length R. In the ideal MHD limit, each term in the ballooning-mode equation is proportional to $|\nabla S|^2$. Upon dividing the equation through by the value of $|\nabla S|^2$ at the midplane of the central cell, one obtains an equation that depends only on the orientation of ∇S and that is independent of the magnitude of ∇S. Hence, Eq. B.2 can provide no information about the magnitude of ∇S.

The orientation of ∇S is determined by

$$\Gamma \equiv 2\psi S_\psi / S_\theta \quad . \tag{B.3}$$

The marginal stability condition for ideal MHD ballooning modes in nonaxisymmetric tandem mirrors depends on both the field-line labels, (θ,ψ), and on Γ. At small to moderate values of β_c, the "worst" field line (i.e., the last field line on which ideal MHD-ballooning modes are unstable as β_c is decreased) always occurs at $\theta = N\pi/2$. These field lines lie on one of the principle axes of the elliptical flux surfaces in and near the MHD anchor cells. The stability properties are the same for any value of N as a result of quadrupole symmetry. Hence, we need only consider MHD stability in the neighborhood of $\theta = 0$.

The worst value of ψ generally lies about midway out in the radial profile, which is Gaussian for the assumed constant Ω^*. Figure B-1 shows the critical value of β_c for marginal stability in the axicell configuration of MFTF-B vs ψ. The peak value of beta in the MHD anchor cell is held fixed at $\beta_a = 0.55$, while the peak value of beta in the axicell (where the central-cell ions are plugged by the ambipolar potential) is set at $\beta_p = 0.11$. Values of θ and Γ have been chosen at each value of ψ to minimize β_c. We see that the

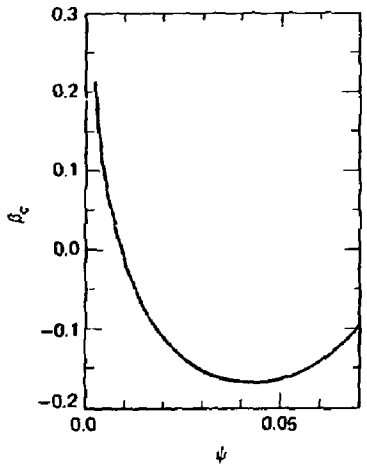

Fig. B-1. Critical value of β_c as a function of ψ. The values of beta in the MHD anchor cell and the axisymmetric plug cell are held fixed at $\beta_a = 0.55$ and $\beta_p = 0.11$. Theta and Γ were chosen at each value of ψ to minimize β_c.

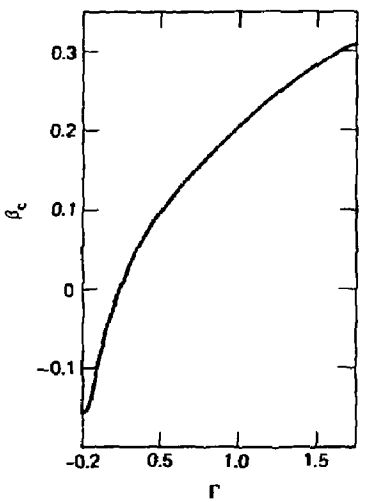

Fig. B-2. Critical value of β vs Γ for $\beta_a = 0.55$, $\beta_p = 0.11$, and $\theta = 0$; ψ is held fixed at $\psi/\psi_{edge} = 0.043$.

worst flux surface at $\psi = 0.043$ lies at the bottom of a quite gentle well in critical β_c.

Similarly, in Fig. B-2 we show the critical value of β_c vs Γ for the same values of β_a and β_p. In Fig. B-2, θ is held fixed at zero and ψ is fixed at $\psi/\psi_{edge} = 0.43$, the worst field line for $\Gamma = 0$. We see that worst orientation, $\Gamma = 0$, lies at the bottom of a very steep well in β_c. When Γ is less than about 0.25, we see that the critical value of β_c is negative. That is, the axicell configuration of MFTF-B is found to be unstable to ideal MHD-ballooning modes even at zero central-cell beta. Increasing β_a makes the system more stable, while increasing β_p makes the system more unstable.

We find in Sec. 6 that this result is far too pessimistic. When effects associated with the perpendicular structure (i.e., "1/n corrections") and diamagnetic drifts (i.e., "kinetic terms") are included, the beta limit is greatly increased and falls somewhere in the range $0.1 \lesssim \beta_c \lesssim 0.4$. This result, first, is in part due to the stabilizing kinetic term, which acts over the entire axial length of a tandem mirror, while the destabilizing pressure-curvature term acts only in the axicell and the transition region between the axicell and the MHD anchor cell. Second, the result is in part due to the "1/n corrections"; that is, the orientation of the perpendicular wave vector, as described by Γ, is determined by the perpendicular structure of the mode and is no longer free to be adjusted so that it fits into the deep well in Fig. B-2 near $\Gamma = 0$.

5. METHOD OF SOLUTION

The stabilizing kinetic effects enter Eq. B.2 through a term proportional to S_θ. Unfortunately, the single-field-line problem provides no information about the magnitude of S_θ; this information must be obtained from a solution of the eigenvalue problem in the plane perpendicular to $\underline{B}$. This is in contrast to the ballooning-mode problem in axisymmetric systems, like tokamaks, where S_θ is replaced by the toroidal-mode-number n. In axisymmetric systems n is a constant, so one can independently analyze the kinetic term and the radial-mode structure, which leads to the "1/n corrections".[B-3] In nonaxisymmetric systems, like the axicell MFTF-B configuration, these two problems are coupled through S_θ, so that they must be treated together.

Equation B.2 describes the behavior of large-n (i.e., $S_\theta \gg 1$) ballooning modes on each magnetic-field line. A numerical solution of this equation along a particular field line yields the local dispersion relation,

$$D(\theta,\psi,\Gamma,\Omega^2 \; ; \; \beta_c,\beta_a,\beta_p \; \ldots) = 0 \quad . \tag{B.4}$$

The explicit dependence on S_θ enters through the parameter

$$\Omega^2 \equiv \omega(\omega - \Omega^* \, S_\theta) \quad . \tag{B.5}$$

Note that the local dispersion relation depends not only on the field-line labels (θ,ψ), the wave parameters $\underset{\sim}{\nabla}S$, and ω, but also on the equilibrium parameters Ω^*, β_c, etc.

Our problem is to "sew" together the solutions on each field line in a self-consistent way to obtain both the mode structure in the (θ,ψ) plane and the global dispersion relation. We accomplish this by using the theory of quasi-classical mechanics--essentially WKB theory generalized to many dimensions.[B-10] In the quasi-classical formalism, the local dispersions relation D may be viewed as the Hamiltonian governing the motion of a ray in the four-dimensional phase space: $(\theta, \psi, S_\theta, S_\psi)$, where the field line labels (θ,ψ) are the coordinates and the covariant components of $\underset{\sim}{\nabla}S$, (S_θ, S_ψ), are the conjugate momenta. The ballooning mode ray then obeys the equations of motion

$$\dot{\theta} = \frac{\partial D}{\partial S_\theta} \quad , \tag{B.6a}$$

$$\dot{\psi} = \frac{\partial D}{\partial S_\psi} \quad , \tag{B.6b}$$

$$\dot{S}_\theta = - \frac{\partial D}{\partial \theta} \quad , \tag{B.6c}$$

and

$$\dot{S}_\psi = - \frac{\partial D}{\partial \psi} \quad . \tag{B.6d}$$

The ray motion described by Eqs. B.6a-d may be either integrable or stochastic.[B-11] The Hamiltonian D is clearly a constant of the ray motion since the ray must stay on the surface D = 0. If there is a second independent constant of the motion, then the ray orbit must lie on a two-dimensional surface, Σ, embedded in the four-dimensional phase space. It may be shown that the surface Σ is topologically a torus. This surface is central to the quasi-classical theory of mechanics, where it is known as the "invariant torus". Ray orbits that lie on an invariant torus are said to be integrable.

If a second constant of motion does not exist, then the ray orbit fills a three-dimensional region of phase space (the energy shell), and the ray orbit is said to be stochastic.

The theory of quasi-classical mechanics is concerned primarily with integrable systems. If the ray orbits are stochastic, little can be said about the mode spectrum; while if the ray orbit is integrable, then the dispersion relation may be obtained by quantizing the two independent actions,

$$I_k = \oint_{C_k} \underset{\sim}{\nabla} S \cdot d\underset{\sim}{q} \quad . \tag{B.7}$$

These two independent actions are obtained by following a closed path that goes either once around the invariant torus the short way (C_1) or else once around the torus the long way (C_2). This is illustrated in Fig. B-3. The quantization condition for the systems considered here is

$$I_k = (2n_k + 1)\pi \quad . \tag{B.8}$$

We find that the modes associated with the larger values of n_k are more stable than the $n_k = 0$ modes. Hence, in studying marginal stability one need only consider normal modes satisfying

$$I_k = \pi \quad . \tag{B.9}$$

Before attempting to apply the methods of quasi-classical mechanics we must determine if the ray orbits associated with "large-n" ballooning modes in the axicell configuration of MFTF-B are integrable. This is accomplished by a direct numerical integration of the ray equations of motion. A ray is initialized with a particular set of phase variables (θ_0, ψ_0, $S_{\theta 0}$). The fourth phase variable, $S_{\psi 0}$, is chosen such that the ray lies on the "energy shell", D = 0. The orbit is advanced in time using Eqs. (B.6) together with

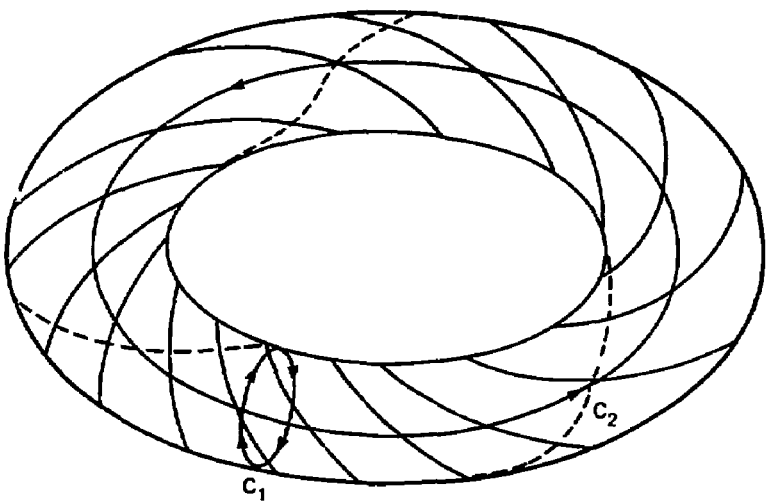

Fig. B-3. Phase-space trajectory and invariant toroid for two degrees of freedom. The C_1 and C_2 curves are for defining the action integrals I_1 and I_2. The toroidal helix is the trajectory; normally it is not closed. (Shown with permission of I. C. Percival, Ref. B-10.)

the Livermore Solver for Ordinary Differential Equations (LSODE).[B-12] At each time step, the ballooning-mode equation B.2, is integrated on the current field line to calculate D and its derivatives. The value of D is monitored to check the accuracy of the integration. Integrability may then be determined from a Poincaré map; each time that the ray passes through the hyperplane $\psi = \psi_0$, the current values of θ and S_θ are plotted. If the ray orbit is integrable, then these points will lie on a smooth curve as in Fig. B-4, while if the ray orbit is stochastic then they will fill an area in the (θ, S_θ) plane. Figure B-5 shows a stochastic orbit. We did not follow this orbit long enough to see this area-filling property in the Poincaré map.

We find that the ray orbits are often but not always integrable. When the equilibrium parameters are in the general vicinity of ideal MHD marginal stability, the ray orbits are found to be integrable; while as we move further from ideal MHD marginal stability (by increasing β_c for example), this integrability breaks down. The assumption that $S_\theta >> 1$ also breaks down for the most unstable modes far from ideal MHD marginal stability, so that this loss of integrability does not by itself limit our calculation.

It is really somewhat remarkable that any ray orbits are found to be integrable, as it is an unfortunate fact of classical mechanics that most two-dimensional Hamiltonian systems are not integrable. Two general cases exist in which two-dimensional systems become integrable. Either there is a symmetry (perhaps a hidden one) or there is a separation of time scales. Our system is an example of one in which there is a separation in characteristic time scales of the ray motion. This may be seen in the projection of the ray orbit into the (θ, ψ) plane shown in Fig. B-4. There is a rapid motion directed generally parallel to $\nabla\psi$ superimposed on a slow precession in θ. We believe that this separation of time scales is associated with the extreme ellipticity of the equilibrium flux surfaces in the transition region between the MHD anchor cell and the axicell. Ballooning modes are associated with the bending of flux bundles in this transition region. When a flux bundle with a circular cross section in the central cell is mapped into this region, it also takes on an elliptical cross section. These elliptical flux bundles act much like pieces of tin; they are easily bent perpendicular to the flat plane but are very stiff when bent parallel to the flat plane. Hence, the ballooning ray has a rapid quiver associated with bending the elliptical flux bundles parallel to their major axis in the transition region. The action associated

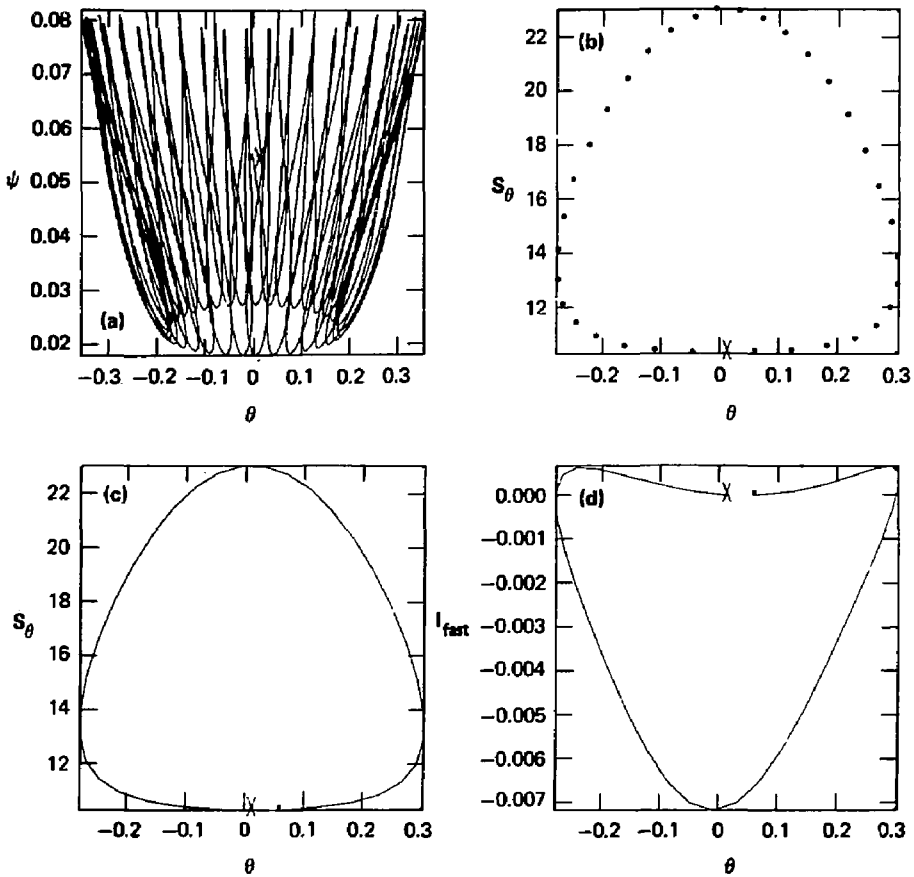

Fig. B-4. Example of an integrable ballooning ray orbit: (a) Projection of the ray orbit onto the ψ,θ plane; (b) surface of section plot of S_θ vs θ; (c) points connected to form a smooth curve; and (d) our computed value at I_{fast}, which is shown to be well conserved.

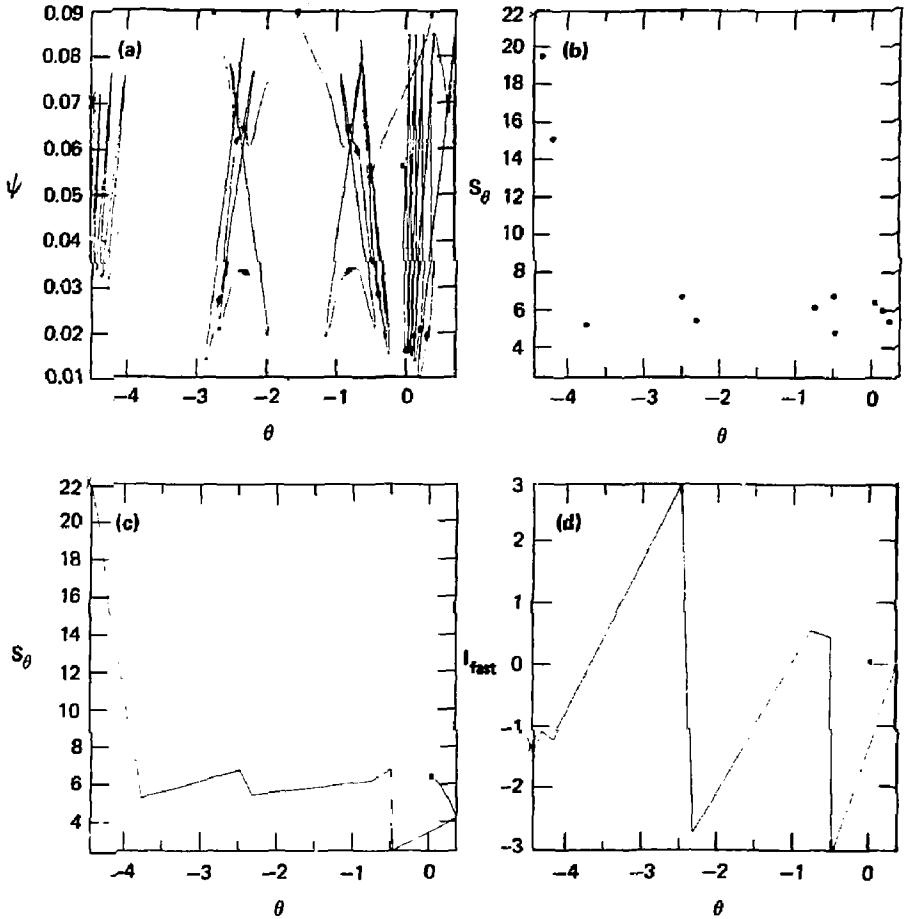

Fig. B-5. Plots same as in Fig. B-4 except for a stochastic orbit.

with this rapid motion, I_{fast}, is then an adiabatic invariant over the slow motion. Hence, I_{fast} is the second independent constant of motion that guarantees the integrability of ray orbits.

A numerical approximation to I_{fast} may be obtained by following the ray orbit once around the torus the short way, accumulating $\int \nabla S \cdot d\underset{\sim}{q}$ along the ray orbit and then closing the loop by using a two-point, Simpson's rule integration to step back to the initial point along a line of constant ψ. This scheme allows us to evaluate I_{fast} once for each point on the Poincaré map. The numerically determined value of $I_{fast}-\pi$ is plotted in Figs. B-4 and B-5. The initial phase variables were chosen such that $I_{fast} = \pi$ for the first loop so that the dispersion relation, Eq. B.9, is satisfied. We see from Figs. B-4 and B-5 that I_{fast} is indeed well conserved on the integrable orbit, while it is not conserved on the stochastic orbit.

The separation of time scales also provides us with some information about the frequency spectrum. The separation in frequency between modes with neighboring values of n_{fast} is $\Delta\omega \sim 2\pi/T_{fast}$, where

$$T_{fast} = \frac{\partial}{\partial\omega} I_{fast}$$

$$= \oint d\underset{\sim}{q} \cdot \frac{\partial}{\partial\omega} \nabla S \quad , \tag{B.10}$$

and the integral is to be taken once around the torus the short way. Noting that $|\partial \nabla S/\partial \omega|$ may be interpreted as $1/v_{group}$, we see that T_{fast} is essentially the period of the fast motion. Similarly, the frequency separation between modes with neighboring values of n_{slow} is $\delta\omega \sim 2\pi/T_{slow}$, where

$$T_{slow} = \oint d\underset{\sim}{q} \cdot \frac{\partial}{\partial\omega} \nabla S \quad , \tag{B.11}$$

with the integral taken once around the torus the long way (I_{slow} is essentially the area enclosed by the line segments connecting the points on the Poincaré map in Fig. B-4). Hence,

$$\frac{\delta\omega}{\Delta\omega} \sim \frac{T_{fast}}{T_{slow}} << 1 \quad . \tag{B.12}$$

That is, the line spectrum must be like that shown in Fig. B-6.

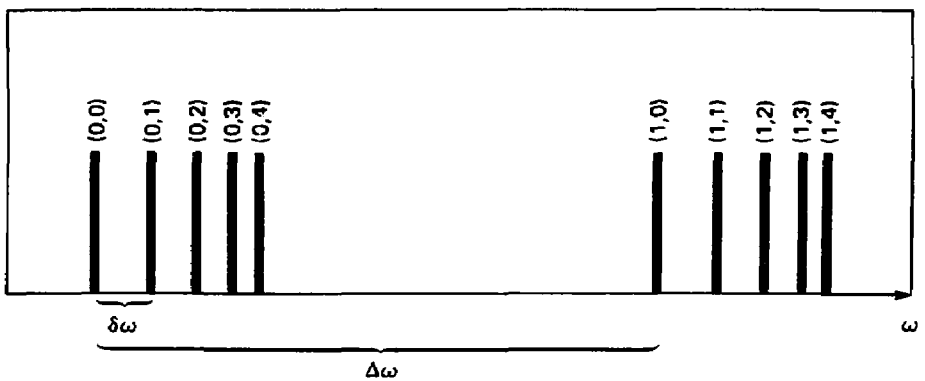

Fig. B-6. Sketch of line spectrum that is characteristic of a system with well-separated time scales. Each normal-mode frequency is labeled by the EBK mode number (n_{slow}, n_{fast}).

It follows that we need only do a careful job in quantizing I_{fast}, while the remaining parameter that determines I_{slow} may be chosen to maximize instability. This will put us within $\delta\omega$ of the most unstable mode. Instability is maximized when the derivative of I_{fast} with respect to the remaining parameter vanishes. This approximation is analogous to estimating the dispersion relation in a plasma slab by using local theory at the most unstable value of the inhomogeneous coordinate. This procedure generally does reasonably well, although it misses WKB corrections (which are usually stabilizing) that are associated with the radial-mode structure. In the present instance, we retain WKB corrections associated with the fast motion but ignore small stabilizing corrections associated with the slow motion. This is an important practical simplification because it is now only necessary to follow a ray once around the torus the short way and compute just I_{fast}. This in turn requires on the order of 10^3 integrations of the balloon equation and takes several seconds of CPU time on a CRAY-1. A numerical computation of I_{slow} (which we are avoiding) would require that we follow the ray for at least one full period of the slow motion. This requires between five and ten minutes of CPU time on a CRAY-1. Hence, ignoring corrections to the mode frequency of order $\delta\omega$ as compared to corrections of order $\Delta\omega$ saves hours of computer time in computing marginal stability boundaries.

6. MARGINAL STABILITY BOUNDARIES

It is necessary to find the invariant torus associated with the unstable "large-n" ballooning modes to obtain the dispersion relation and the marginal stability boundary. We expect that the most unstable ballooning modes will be localized in the neighborhood of the worst field line of ideal MHD theory. Hence, we may fix θ_0 and ψ_0 as the labels of this field line. The initial value of S_θ, $S_{\theta 0}$, then selects a particular invariant torus from among those intersected by the curve

$$\theta = \theta_0 \quad ,$$

$$\psi = \psi_0 \quad , \tag{B.13}$$

$$D(\theta, \psi, \Gamma, \Omega^2) = 0 \quad .$$

Given a particular set of equilibrium parameters, the frequency of the most unstable mode satisfies the equations

$$I_{fast}(\theta_0, \psi_0, S_{\theta 0}, \Omega^2; \beta_c, \ldots) = \pi \tag{B.14}$$

and

$$\frac{\partial I_{fast}}{\partial S_{\theta 0}} = 0 \quad . \tag{B.15}$$

If we require this mode to be marginally stable, we must satisfy the additional equation

$$\frac{\partial I_{fast}}{\partial \omega} = 0 \quad . \tag{B.16}$$

In general, it would be necessary to simultaneously solve Eqs. B.14 to B.16. Fortunately, the assumption Ω^* = constant, together with the fact that S_θ has only a small fractional variation during one period of the rapid motion allows us to replace the third equation with the condition

$$\frac{\partial \Omega^2}{\partial \omega} = 0 \quad ; \tag{B.17}$$

or, from Eq. (B.5),

$$\omega = \frac{\Omega^* S_{\theta 0}}{2} \quad . \tag{B.18}$$

This results in a considerable simplification, as it is now only necessary to solve Eqs. B.14 and B.15 simultaneously with Ω^2 set equal to $-(\Omega^* S_{\theta 0}/2)^2$.

These equations may be solved numerically to find the marginally stable value of Ω^* for a particular set of equilibrium parameters, β_c, β_a, β_p ... . Then one of these parameters, say β_c, may be varied to produce a stability boundary like that shown in Fig. B-7. We are able to track the stability boundary from ideal MHD marginal stability at $\beta_c = -0.167$ to $\beta_c = 0.1$. At this point an examination of the ray orbit shows that, while the orbit performs several rapid oscillations, it ultimately escapes like the ray orbit shown in Fig. B-5. Hence, the ray orbit is no longer integrable, and the quasi-classical procedure outlined in Sec. 5 is no longer justified. As long

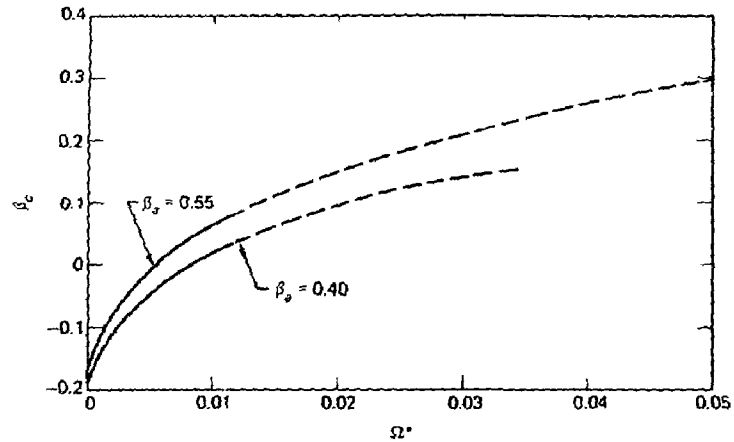

Fig. B-7. Marginal stability boundary in the β_c, Ω^* plane. The projected operating point with this coil set is $\Omega^* = 0.1$. The value of beta in the axicell is $\beta_p = 0.11$, while the MHD anchor-cell beta is $\beta_a = 0.55$ (upper curve) or 0.40 (lower curve). The flute average-beta limit for β_a is 0.55, as shown by heavy line near $\beta_c = 0.4$.

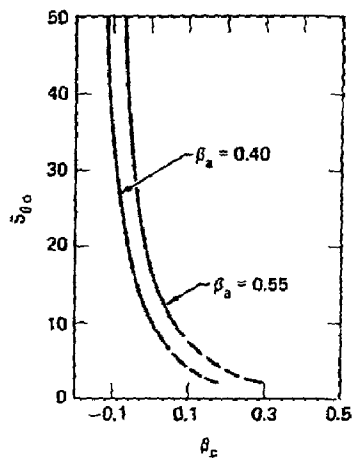

Fig. B-8. A plot of S_θ vs β_c at marginal stability.

as the ray orbit continues to perform even one rapid oscillation it is possible to define I_{fast} and to solve Eqs. B.15 and B.16. Points on the marginal-stability boundary obtained in this manner are connected by a dashed line in Fig. B-7.

Figure B-8 shows the values of $S_{\theta 0}$ on the marginal-stability boundary. We see that the condition $S_\theta >> 1$, required in the derivation of Eq. (B.2), also breaks down near $\beta_c \simeq 0.1$. Hence, there is little significance to the dashed portion of the marginal-stability curve.

The effect of varying beta in the MHD anchor cell, β_a, is shown by the lower curve in Fig. B-7, in which β_a has been reduced from 0.55 to 0.40. Just as in ideal MHD ballooning-mode theory, we find that decreasing β_a tends to destabilize the system.

7. SUMMARY

The main result of this calculation is the marginal-stability boundary shown in Fig. B-7. An important feature of the marginal-stability boundary is the fact that the characteristic value of S_θ at the marginal stability decreases as β_c and Ω^* increase (see Fig. B-8) until the calculation breaks down at $\beta_c \simeq 0.1$. At this point, $\Omega^* = 1.4 \times 10^{-2}$ and $S_\theta = 7.27$. It is possible to extend the calculation to larger values of β_c, as indicated by the dashed curves in Figs. B-7 and B-8, but two assumptions underlying this calculation ($S_\theta >> 1$ and integrability of the ray orbits) are not satisfied in this regime.

The axicell configuration of MFTF-B lies off to the right of Fig. B-7 at $\Omega^* \simeq 0.1$ in our units. It is clear from Figs. B-7 and B-8 that "large-n" ballooning modes will not limit the central-cell beta at these large values of Ω^*. The rapid decrease in S_θ on the marginal-stability boundary suggests that at larger values of β_c and Ω^*, the most dangerous modes will be low-m modes with a global structure in the plane perpendicular to $\underset{\sim}{B}$. The beta limit imposed by such modes is certainly bounded from above by the flute average-stability condition, $\beta_c < 0.4$, as this limit is found to be relatively insensitive to the field-line labels, (ψ, θ). Hence, we may expect the central-cell beta limit to fall in the range $0.1 \lesssim \beta_c \lesssim 0.4$.

The extension of large-n theory beyond its domain at validity gives a marginal-stability curve (the dashed line in Fig. B-7) that appears to asymptote to the flute-stability limit as Ω^* increases. This suggests that at the rather large values of Ω^* in the axicell configuration of MFTF-B ($\Omega^* = 0.1$) the actual central-cell beta limit will be closer to the flute average limit of 0.4. Theoretical and computational studies of the low-m modes that will determine this β limit are currently in progress.

REFERENCES

B-1. L.S. Hall and B. McNamara, Phys. Fluids 18, 552 (1975).

B-2. J.W. Conner, R.J. Hastie, and J.B. Taylor, Phys. Rev. Letters 40, 396 (1978); A.H. Glasser, in Proceedings of the Finite Beta Theory Workshop, Varenna, Italy, Sept. 1977, B. Coppi and W. Sadowski, Eds. (National Technical Information Service, Springfield, VA., 1979) p. 55.

B-3. R.L. Dewar, J. Manickam, R. C. Grimm, and M. S. Chance, Nuclear Fusion 21, 493 (1981).

B-4. W.M. Tang and P.J. Catto, Phys. Fluids 24, 1314 (1981); X.S. Lee and P.J. Catto, Phys. Fluids 24, 2010 (1981).

B-5. W.A. Newcomb, J. Plasma Physics 26, 529 (1981).

B-6. L.D. Pearlstein, T.B. Kaiser, and W.A. Newcomb, Phys. Fluids 24, 1326 (1981).

B-7. See, for example, W.M. Tang, Nucl. Fusion 18, 1089 (1978).

B-8. D.E. Baldwin, Tandem Mirror Geometry Enhancement of FLR Effects, Lawrence Livermore National Laboratory, personal communication (1980).

B-9. T.B. Kaiser, in Physics Basis for MFTF-B, Ed. by D.E. Baldwin, B. G. Logan, and T. C. Simonen, Lawrence Livermore National Laboratory, Rept. UCID-18496, Part 2 (1980), Sec. IV-B.

B-10. See, for example, I.C. Percival, Adv. in Chem. Phys. 36, 1 (1977).

B-11. See, for example, B.V. Chirikov, Phys. Reports 52, 263 (1979).

B-12. A.C. Hindmarsh, Linear Multistep Methods for Ordinary Differential Equations, Lawrence Livermore National Laboratory, Rept. UCRL-51186 (1972).

APPENDIX C

SOME EFFECTS OF HOT-ELECTRON STABILITY IN TANDEM-MIRROR GEOMETRY

D. E. Baldwin

A hot, anisotropic electron component will continue to play an important role, it appears, in tandem-mirror (TM) confinement, either as a potential-depressing component in a thermal barrier or as a pressure-enhancing component in an magnetohydrodynamic (MHD) anchor. The theory of the interactions of these hot electrons with low-frequency interchange and ballooning modes follows closely that of Elmo Bumpy Torus (EBT) stability, but some features are special to the TM geometry. In this note, some of these special features are examined by using a model balloon-mode equation.

The most immediate special feature of TM's are the several axial regions having particles of quite different energies and, therefore, different drift speeds. We model this by treating each region as a localized slab having magnetic curvature simulated by a local effective gravity. These regions are then coupled by a balloon-mode equation obtained by setting $\nabla\cdot\tilde{j}$ (perturbed) = 0. We introduce the curvature-drift frequency ω_k and the ∇B-drift frequency ω_B for each species and assume that β exceeds the ratio of the plasma-density scale length r_n to the magnetic radius of curvature R_c. Then for each species $\omega_B >> \omega_k$. Hot-species quantities are labeled by subscript "h", and warm-species quantities by "w", with hot and warm defined by drift speeds relative to wave frequency in the ordering $\omega >> \omega_{Bw} >> \omega_{kw}$ and $\omega_{Bh} >> \omega \sim \omega_{kh}$.

The balloon equation for eikonal solutions in finite Larmor radius (FLR) ordering and this frequency ordering is given by

$$B\frac{d}{ds}\left(\frac{k_\perp^2 Q}{B^3}\frac{d\phi}{ds}\right) + \frac{k_\perp^2}{V_A^2}\left[\omega(\omega - \omega_{*i}) + \frac{\omega - \Lambda\omega_{kh}}{\omega - \omega_{kh}(1+\Lambda)}\sum\frac{\alpha\omega_{*i}\omega_k}{b}\right]\phi = 0 \ , \quad (C.1)$$

where ϕ is proportional to the displacement; $Q = B^2 + p_\perp - p_{//}$; V_A is the local Alfvén speed; ω_{*i} is the diamagnetic drift frequency; α is the local species-density fraction; $b = 1/2\ k_\perp^2 a^2$ with "a" the species gyroradius; Σ is the sum over all species; $\sum_w$ is the sum over only warm species; and

$$\Lambda \equiv \frac{\sum_{w} \frac{\alpha\omega_{*i}\omega_B}{b}(1+\beta)}{\sum \frac{\alpha\omega_{*i}\omega_k}{b}} \approx \frac{1}{2}\beta_w \frac{1+\beta_{tot}}{1-\beta_{tot}} \frac{R_c}{|r_n|} \quad .$$

The ω_{*i} term is due to finite ion gyroradius. Being nonvanishing over the entire solenoid, its effect is enhanced for long solenoids to the point that only low-m modes are unstable. We model $m = 1$ by setting $\omega_{*i} \to 0$ and taking $k_\perp \approx r_n^{-1}$. When $\omega >> \omega_{kh}$, Eq. C.1 then reduces to the familiar MHD balloon equation.

The parameter Λ, which has the sign of the local curvature, is that obtained by Van Dam and Lee[C-1] in their analysis of EBT stability. When $\omega_{kh} >> \omega$, the drive term

$$\frac{\Lambda}{1+\Lambda}\sum \frac{\alpha\omega_{*i}\omega_k}{b}$$

is locally stabilizing (i.e., < 0) in a well having $\omega_{*i}\omega_k > 0$ only when $-1 < \Lambda < 0$. When $|\Lambda| << 1$, the denominator of Λ replaces the Σ-drive by the Σ_w-numerator of Λ. This latter term describes the warm species moving in the VB-well dug by the hot electron (through ω_B); the hot electrons otherwise drop out of the problem, as in the "rigid ring" description. If $|\Lambda| > 1$, the hot electrons respond as MHD fluid in the negative-curvature well.

In the positive-curvature MHD anchor of a TM, Λ (now > 0) is again important when most of the anchor β appears in hot electrons. Again, only the portion $\Lambda/(1+\Lambda)$ of the total pressure contributes; or equivalently, only the anchor β excluding hot electrons contributes, although it does so in the enhanced well dug by the hot electrons.

A second class of modes can appear near the hot-electron-drift frequency in a well having $\Lambda < 0$. Berk and Dominguez[C-2] show that when $\omega_{kh} < \Omega_{ci}$, the ion gyrofrequency, stability in a slab requires

$$\frac{n_h}{n_{total}} \lesssim \frac{1}{4}\frac{\omega_{kh}}{\Omega_{ci}} \quad . \tag{C.2}$$

This originates from a condition in which there is enough ion mass to preclude the high-frequency motions, $\omega \lesssim \omega_{kh}$.

It has been assumed that in a TM the ions of the central cell will serve the function of eliminating the Berk-Dominguez modes. We find that, although

this is true for a flute mode, a long, TM central cell can actually have a destabilizing effect.

To illustrate this for a TM configuration having a central cell and a double-end cell, one of positive and one of negative curvature (such as MFTF-P or TARA) we assume modes that are flute through the entire end region and sinusoidal through the central cell. There will be curvature-driven contributions from the plugs ($R_c < 0$), anchor ($R_c > 0$), and transition ($R_c < 0$) between the central cell and end region. Introducing the frequency associated with Alfven-wave propagation in the central cell $\omega_A = 2\ V_A/L_c$, we obtain a dispersion relation by equating logarithmic derivative of $\tilde{\phi}$ at $s = \pm\ L_c/2$:

$$\frac{2\omega}{L_c\ \omega_A}\begin{bmatrix} -\tan\ \omega/\omega_A \\ \cot\ \omega/\omega_A \end{bmatrix} = B_c \int_{p+a+t} \frac{ds}{BV_A^2}\left[\omega^2 + \frac{\omega - \Lambda\omega_k}{\omega - (1+\Lambda)\ \omega_k}\sum \frac{\alpha\omega_{*i}\omega_k}{b}\right], \quad (C.3)$$

where p = plug, t = transition, and a = anchor. The upper term describes even modes and the lower term, odd modes. With $x = \omega/\omega_A$, $x_k = \omega_k/\omega_A$,

$$A = \frac{B_c\ L_c\ \omega_A^2}{2}\int_{p+a+t}\frac{ds}{BV_A^2}\ , \quad \gamma_{t,p}^2 = \frac{\int_{t,p}\frac{ds}{B}\sum\frac{\alpha\omega_{*i}\omega_k}{b}}{\int_{p+a+t}\frac{ds}{B}}\ ,$$

and

$$\omega_a^2 = -\frac{\int_a \frac{ds}{B}\sum\frac{\alpha\omega_{*i}\omega_k}{b}}{\int_{p+a+t}\frac{ds}{B}}\ , \quad \text{and } \omega_{ka} \to \infty\ ;$$

this becomes

$$\frac{x}{A}\begin{bmatrix} -\tan x \\ \cot x \end{bmatrix} = x^2 + \gamma_t^2 - \omega_a^2\frac{\Lambda_a}{1+\Lambda_a} + \gamma_p^2\frac{x - \Lambda_p\ x_{kp}}{x - (1+\Lambda_p)\ x_{kp}}\ . \quad (C.4)$$

Here, for simplicity we set $\omega_{kh} \to \infty$ in the anchor cell.

To analyze roots of this dispersion relation, we plot the right and left sides of Eq. C.3 vs x, as shown in Fig. C-1 for the even solution.

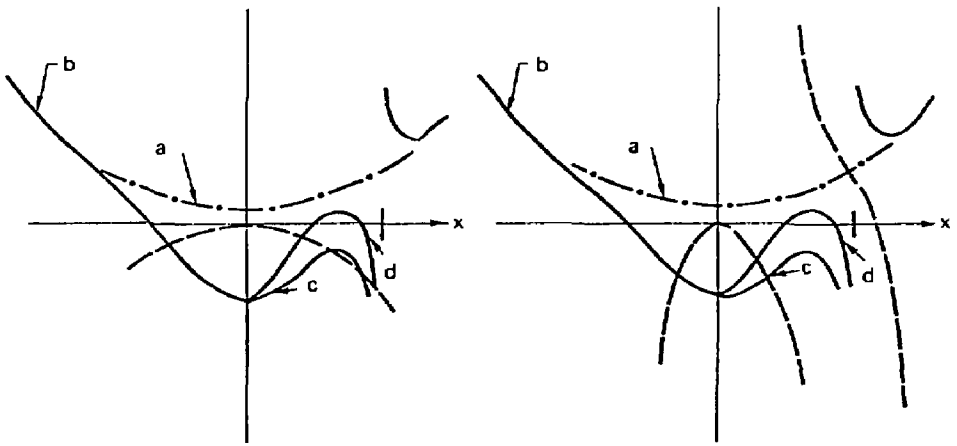

Fig. C-1. Frequency dependence of right side (solid curves) and left side (dashed curves) of the dispersion relation. On the x-axis, the mark to the right of the d-curve intercept locates the point $x = (1 + \Lambda_p)\, x_{kp}$. See text for explanation.

Consider first the solid curve alone, which would be the local condition or that appropriate formally as $A \to \infty$. Extension "a" of the solid curve is that which would pertain in pure MHD. The dip at $x = 0$, generating curve "b", arises from the plug term at $x = 0$. In EBT, "a" lies above the axis and stabilization is generated by conversion to "b" by electrons having large x_k.

Again for $A \to \infty$, a second branch of modes is unstable if curve "c" pertains, rather than "d". The condition for "d" is given by Eq. C.2 when $\omega_{kh} < \Omega_{ci}$. Note that even when local stability is achieved, a negative energy wave exists, as indicated by the negative slope of the solid curve at the root having $\omega > 0$.

When the dashed curves are added, the actual roots occur at the intercepts with the appropriate solid curve. When $x_k << 1$, all of the tan structure is pushed to high x, i.e., x tan $x \to x^2$ as in Fig. C-1. The only change is a less restrictive Berk/Dominguez condition (e.g., "c" as shown is stable). This corresponds to adding the central-cell-mass weighting in a flute mode.

Decreasing ω_A by increasing L_c pulls the tan structure in until a pair of real roots is lost for $\omega_{kh} \approx \pi\omega_A$. Physically, the otherwise stable negative energy mode in the end cells has coupled to a positive energy shear Alfvén wave standing in the central cell to produce instability. Similarly, for a long solenoid, a solution Im $\omega > \omega_A$ can be found by setting tan $x \to i$.

These modes that originate from the coupling to the solenoid disappear if

$$(1 + \Lambda_p)\, x_{kp} < 0 \quad ,$$

which can be achieved either by a good-curvature plug, $\omega_k > 0$, or by the Van Dam-Lee condition being exceeded in a bad curvature plug, $\Lambda_p < -1$. The former case is that of TARA; the latter, that of MFTF-B. This result does not bode well for a simple axisymmetric TM stabilized by hot electrons in a bad-curvature well; if $\Lambda_p < -1$, it would be low-frequency (MHD) unstable, and if $-1 < \Lambda_p < 0$, it would be high-frequency (ω_{kh}) unstable.

REFERENCES

C-1. J. W. Van Dam and Y. C. Lee, Proc. Workshop on EBT Ring Physics, Oak Ridge, TN 1979, p. 471.

C-2. R. R. Dominguez and H. L. Berk, Phys. Fluids 21, 827 (1978).

APPENDIX D

ELECTROSTATIC BALLOONING MODES

D.E. Baldwin

The low-frequency stability analysis described in Appendices B and C was predicated on the assumption that $\tilde{E}_{\parallel} = 0$, as in conventional MHD theory. Normally, this condition is well satisfied; an electrostatic field $\partial\tilde{\phi}/\partial s$ drives a parallel current and a subsequent inductive component $\tilde{A}_{\parallel}$, forcing $\tilde{E}_{\parallel}$ to zero while introducing bending of the magnetic lines. The energy required for this bending is a stabilizing effect that offsets the tendency of modes to localize in regions of unfavorable magnetic curvature.

The response to $\partial\tilde{\phi}/\partial s$ is quite different for electrons confined in a potential well, as in any open geometry, when their axial bounce frequency exceeds the wave frequency. Then, on successive bounces, they receive nearly compensating impulses on passing through regions of parallel electric fields, and little net parallel current is generated. There results a mode that is substantially flute-like through the solenoid and end-cell regions of unfavorable curvature, and vanishing in regions of favorable curvature. This is an electrostatic (ES) ballooning mode, localized to regions of unfavorable curvature without requiring a bending energy. The transition between the flute-like portion of the perturbation and the region where it vanishes can occur when the equilibrium reflects a significant number of particles, such as a mirror or potential gradient.

In such low-frequency electrostatic disturbances, the electron response is to Debye shield the perturbation, just as in the analogous situation of electron Debye shielding in an ion acoustic wave. There is a similar parallel ion response when the ion bounce frequency is also large. However, both Debye shielding contributions can be small in geometries having small fractions of particles that pass between regions of good and bad curvature.

We neglect here the axial variations in the electric field drifts and, after transforming to a rotating frame, drop all such drifts. Similarly, because the dominant finite-β effect is to introduce a $\tilde{B}_{\parallel}$ that cancels the magnetic-well effect of the equilibrium ∇B-drift, we consider only electrostatic perturbations in low β. Axial variations of both the

equilibrium E x B drift and the ∇B-drift introduce a number of complications whose effects remain to be evaluated, although there do not appear to be any really significant effects arising from these variations.

An eikonal approximation gives the equation for perturbed charge-neutrality,

$$0 = \sum \frac{q^2}{m} \int \frac{d\varepsilon d\mu}{v_{\parallel}} \left[\left(\bar{\phi} - \overline{\phi J_0^2} \right) \frac{\partial f}{\partial \varepsilon} - \frac{\overline{\phi J_0^2}}{\omega - \bar{\omega}_D} \left(\Omega^{-1} \, \underline{kxb} \cdot \nabla f + \bar{\omega}_D \frac{\partial f}{\partial \varepsilon} \right) \right] ,$$

where the sum is over species,

$$\overline{(\ldots)} \equiv \frac{1}{\tau_B} \int \frac{ds}{v_{\parallel}} (\ldots) \qquad , \qquad \tau_B \equiv \int \frac{ds}{v_{\parallel}} ,$$

ω_D is the magnetic-drift frequency, and J_0 is the Bessel function introduced to allow for FLR effects. This equation may be put in a variational form by multiplying by ϕ and integrating over the field line to obtain

$$\sum \frac{q^2}{m} \int d\varepsilon d\mu \, \tau_B \frac{\partial f}{\partial \varepsilon} \left\{ \overline{(\phi - \bar{\phi})^2} + \bar{\phi}^2 \left[\left(\frac{\omega_* - \bar{\omega}_D}{\omega - \bar{\omega}_D} \right) + k^2 \rho^2 \left(\frac{\omega - \bar{\omega}_D}{\omega - \bar{\omega}_D} \right) \right] \right\} = 0 \quad , \qquad (D.1)$$

where we have introduced the Larmor radius ρ upon expanding J_0^2 and defined

$$\hat{\omega}_* \equiv - \frac{\underline{kxb} \cdot \nabla f}{\Omega \, \partial f / \partial \varepsilon} \quad .$$

Charge neutrality (or its radial derivative) can be expressed in the same notation by

$$\sum \frac{q^2}{m} \int d\varepsilon d\mu \, \tau_B \frac{\partial f}{\partial \varepsilon} \left(\overline{\phi^2} \, \hat{\omega}_* - \overline{\phi^2} \, \omega_D \right) = 0 \quad , \qquad (D.2)$$

which has been obtained by multiplying the local charge condition by ϕ^2 and integrating over the field line.

The drift frequency $\omega_D = \omega_E + \omega_B$ contains the $\underline{E} \times \underline{B}$ drift,

$$\omega_E = \frac{c}{B} \underline{kxb} \cdot \nabla \Phi \quad ,$$

and the magnetic drift,

$$\omega_B = \frac{1}{\Omega} \underline{k} x \underline{b} \cdot (\mu \nabla B + v_{||}^2 \underline{\kappa}) \quad ,$$

where $\underline{\kappa} \equiv \underline{b} \cdot \nabla \underline{b}$. Equation D.1 becomes quite complex when the variation in ω_D, which is due primarily to variation in ω_E, is comparable to ω. We do not consider here such circumstances and assume that ω_D can be written as

$$\omega_D = \omega_0 + \omega_B \quad ,$$

where ω_0 is the constant, species- and z-independent E x B-drift frequency of the central cell. We take $\omega_B << \omega - \omega_0$, and expand the denominators of Eq. D.1. When this is added to Eq. D.2 and divided by $\omega - \omega_0$, with $\omega \to \omega + \omega_0$ and higher order quantities are discarded, we obtain the result

$$\sum \frac{q^2}{m} \int d\epsilon d\mu \, \tau_B \frac{\partial f}{\partial \epsilon} \left\{ \left[\overline{(\phi - \bar{\phi})^2} + k^2 \rho^2 \bar{\phi}^2 \right] (\omega + \omega_0 - \hat{\omega}_*) \right.$$

$$\left. + \frac{\bar{\phi}^2 \, \overline{\omega_B}}{\omega} (\hat{\omega}_* - \omega_0) \right\} = 0 \quad . \tag{D.3}$$

In this approximation, $\hat{\omega}_* - \omega_0$ corresponds to the total density gradient because of the flux dependence of f and of Φ, so that $\hat{\omega}_* - \omega_0 = \omega_*$ is the familiar diamagnetic drift frequency.

In this form, one can identify the Debye shielding, the polarization, the FLR, and the bounce-averaged curvature-drive terms. The term $\overline{(\phi - \bar{\phi})^2} (\omega_* - \omega_0)$ describes a coupling to drift waves brought about by the ϵ, μ, q dependence of particle turning points and, therefore, $\bar{\phi}$, in the combined magnetic and electrostatic fields. This term is absent in the equivalent tokamak calculation.

When the drift and FLR effects are neglected, the variational form becomes an energy principle for ω^2, which is a minimum at the eigenfrequency

$$\omega^2 = - \frac{\sum \frac{q^2}{m} \int d\epsilon d\mu \, \tau_B \frac{\partial f}{\partial \epsilon} \bar{\phi}^2 (\omega_* - \omega_0) \omega_B}{\sum \frac{q^2}{m} \int d\epsilon d\mu \, \tau_B \frac{\partial f}{\partial \epsilon} \left[\overline{(\phi - \bar{\phi})^2} + k^2 \rho^2 \bar{\phi}^2 \right]} \quad . \tag{D.4}$$

provided trial functions are chosen that vanish in the anchor where $(\hat{\omega}_* - \omega_0)\,\omega_B < 0$, there is always an instability in this approximation. If the $\overline{(\phi - \bar{\phi})^2}$ factor is small, the growth rate will be the MHD growth rate in the absence of the anchors. This Debye term can be small when very few particles pass between the regions of good and bad curvature. In such circumstances, a perturbation such as that sketched in Fig. D-1 minimizes ω^2. In the long central cell, $\phi \approx \bar{\phi}$, so that all particles trapped there do not contribute. For those that do pass between the regions, i.e., in and out of the perturbation,

$$\overline{\tau_B\,(\phi - \bar{\phi})^2} = \int \frac{ds}{v_{\parallel}}\,(\phi - \bar{\phi})^2 \approx \frac{2L_a}{v_{\parallel}}\,\phi_c^2 \quad ,$$

where L_a is the length of one anchor and ϕ_c is the perturbation level in the central cell. If we define the characteristic MHD growth rate of the unfavorable curvature region alone as

$$\gamma_c^2 \equiv -\frac{\sum \frac{q^2}{m} \int d\varepsilon d\mu\, \tau_B \frac{\partial f}{\partial \varepsilon}\, \bar{\omega}_B\, (\hat{\omega}_* - \omega_0)}{\sum \frac{q^2}{m} \int d\varepsilon d\mu\, \tau_B\, k^2 \rho^2 \frac{\partial f}{\partial \varepsilon}} \quad , \tag{D.5}$$

we find

$$\omega^2 = \frac{\gamma_c^2}{1 + \Sigma \frac{1}{k^2 \rho^2} \frac{B_c}{n_c L_c} \int_{\phi=0} \frac{ds}{B}\, \hat{n}} \quad , \tag{D.6}$$

where $\hat{n}$ is the density of particles passing into and out of the perturbation, and the integration is carried out over the region that the perturbation vanishes. According to how many ions are trapped in the transition region, in addition to those passing directly from the central cell, the eigenfunction will minimize this integral of $\hat{n}$. When both the positive potential peak and thermal barrier are placed in the axicell, as is possible in one operating mode of the axicell configuration, $\hat{n}/n_c$ is very small. The special susceptibility of this operating mode to ES ballooning was first pointed out by Berk and Rosenbluth[D-1].

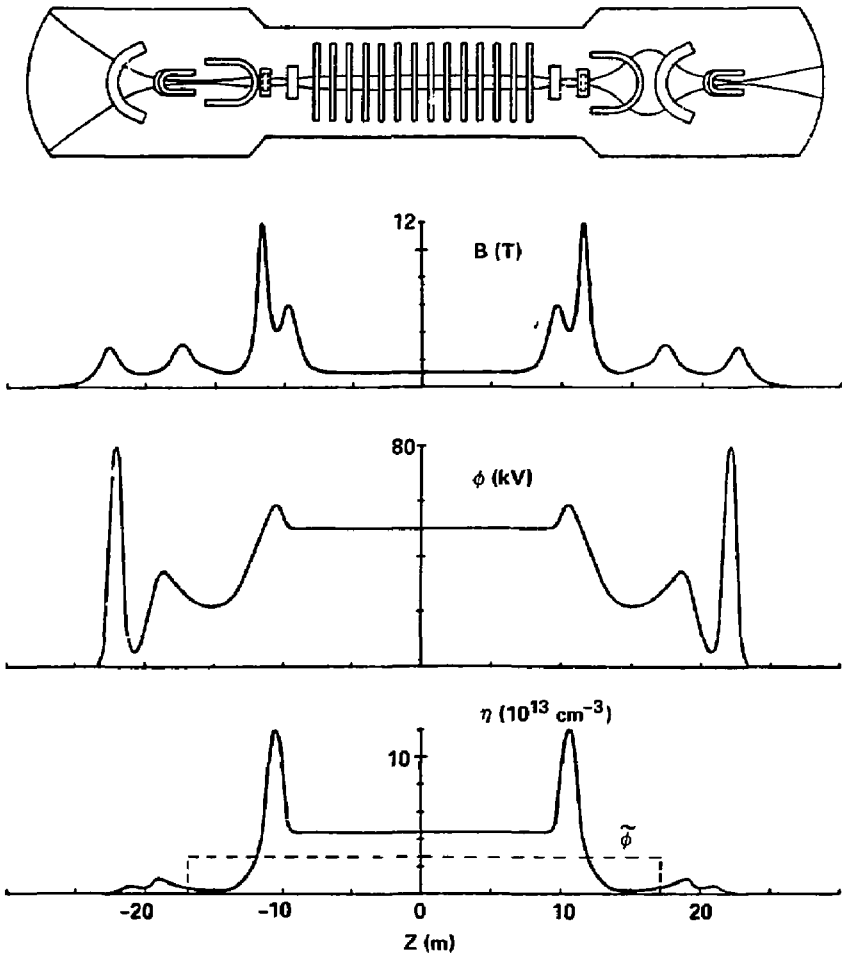

Fig. D-1. Profiles of field B, density n, and potential ϕ for the MFTF-B Axicell design. The dashed line represents the worst ES ballooning mode, which occurs when the density in the transition is very low.

The drift term in Eq. D.1, neglected in obtaining Eq. D.6, can play an important role in stabilizing the basic mode described by Eq. D.6 by coupling it to a drift wave[D-2,D-3]. The process is very similiar to familiar FLR stabilization of curvature-driven modes and is described by including $\omega_* - \omega_0$ in Eq. D.3. As may be observed in Eq. D.3, particles trapped in a region of constant ϕ have no drift contribution, just as they have no Debye contribution. The FLR term, of course, contributes everywhere.

A second point to be recognized from Eq. D.3 is that the ion-drift term has the same sign as the ion-FLR term and is, therefore, additive. The electron-drift term has the opposite sign. The magnitude of each term is weighted by $(\overline{\phi - \bar{\phi}})^2$, and this term is in turn increased by the "overshoot", or the distance of reflection of a particle beyond the place where ϕ goes to zero. Thus, configurations are preferred in which ions carry further beyond the perturbation than the electrons, and the axicell configuration is of this type.

The variational form of Eq. D.3 can be used to compare the axicell and A-cell geometries with regard to stability to the ES ballooning mode. Consider first the axicell design shown in Fig. D-2. As a trial function, take $\phi = 1$ through the central cell, $\phi = 1 - \alpha$ in the transition, and $\phi = 0$ in the anchor or yin yang. The parameter α will be varied to achieve a minimum in the stabilizing contribution. Changes in ϕ are located at the high mirror peak of the axicell and the inside edge of the thermal barrier (see dashed line in Fig. D-2).

The ion distribution in the transition is composed of a portion that streams directly from the central cell (to be confined by the positive potential of the anchor, n_{pass}) and a population of ions that have become trapped between this potential and the high-field coil of the axcicell. With good pumping in the transition region, the distribution of these trapped ions is close to that of the passing component and, therefore, is beam-like in character. We denote their relative density by $g_b - 1$ (g_b is the total density in the transition normalized to the passing component; the two spatial profiles throughout the transition and anchor regions are nearly equal). We then compute different averages for different classes of ions. Introducing the bounce time in each region--central cell, transition, and anchor (τ_c, τ_t, τ_a, respectively)--we have for those ions trapped in the central cell,

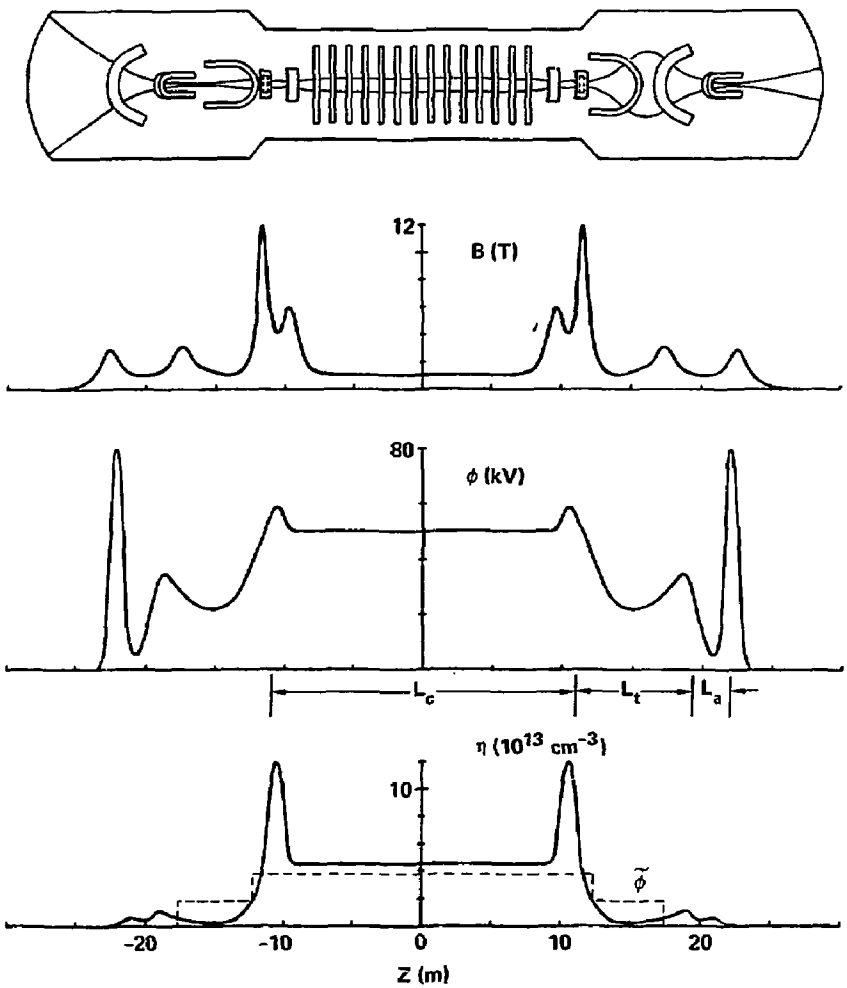

Fig. D-2. Field, density, and potential profiles for the MFTF-B Axicell design. The dashed line represents the trial function, having variable transition-region value, when the plasma density in the transition is low but significant.

$$\bar{\phi} = 1 \quad ;$$

for those untrapped in the central cell and confined by the anchor potential,

$$\bar{\phi} = \frac{\tau_c + 2(\tau_t + \tau_a)(1 - \alpha)}{\tau_c + 2(\tau_t + \tau_a)} \xrightarrow[\tau_c >> \tau_t, \tau_a]{} 1 \quad ;$$

and for those trapped in the transition-anchor region,

$$\bar{\phi} = (1 - \alpha) \frac{\tau_t}{\tau_t + \tau_a} \quad .$$

Here τ_c, τ_t, τ_a are proportional to the lengths shown in Fig. D-2.

Although the ion distribution in the transition region is of a streaming type, the electrons that neutralize these ions will be locally Maxwellian and very few of them will pass through the high-field axicell coil. Thus, to a good approximation, the electrons in each cell are confined to that cell, their $\bar{\phi}$ in each cell, and they drop out of the shielding and drift terms of Eq. D.7.

To calculate the effect of the beam-like ion distribution in the transition regions, we temporarily restore the definition of ω_* and rewrite Eq. D.3 as

$$\sum \frac{q^2}{m} \int d\varepsilon d\mu \, \tau_B \left\{ \left[\overline{(\phi - \bar{\phi})^2} + k^2 \rho^2 \bar{\phi}^2 \right] \left[(\omega + \omega_0) \frac{\partial f}{\partial \varepsilon} + \frac{1}{\Omega} \underline{k} \times \underline{b} \cdot \nabla f \right] \right.$$

$$\left. - \frac{\bar{\phi}^2 \, \bar{\omega}_B}{\omega} \left[\omega_0 \frac{\partial f}{\partial \varepsilon} + \frac{1}{\Omega} \underline{k} \times \underline{b} \cdot \nabla f \right] \right\} = 0 \quad . \qquad (D.7)$$

Because $\partial f / \partial \varepsilon > 0$ for trapped ions, such terms must be treated with some care. As implied above, we treat $\bar{\Phi}$ as independent of ε, μ, except for the differences arising from the trapped and untrapped orbits. Thus, for the term not containing $\partial f / \partial \varepsilon$, we obtain

$$\int d\varepsilon d\mu\, \tau_B \overline{(\phi - \bar{\phi})^2}\, \frac{1}{\Omega}\, \underline{k}\times\underline{b} \cdot \nabla f$$

$$= \frac{2\hat{\omega}_*}{T_c}\left[\frac{\alpha^2\tau_t + \tau_a}{\tau_t + \tau_a} + (g_b - 1)(1-\alpha)^2 \frac{\tau_t\tau_a}{(\tau_t + \tau_a)^2}\right] \int_{t+a} \frac{d\ell}{B}\, n_{pass} \quad , \tag{D.8}$$

where T_c is the central-cell ion temperature, and the passing density n_{pass} is integrated over the transition and anchor regions. In the $\partial f/\partial\varepsilon$ term, we integrate in energy, expressing the result in terms of the common value of f at the separatrix and $\Delta\overline{(\phi - \bar{\phi})^2}$, which is the jump in $\overline{(\phi - \bar{\phi})^2}$ between passing and trapped ions. Estimating

$$\int d\mu\, \tau_B f\big|_{separatrix} \approx \frac{1}{T_c}\, 2\int_{t+a} \frac{d\ell}{B}\, n_{pass} \quad ,$$

we obtain

$$\int d\mu\, \tau_B f\, \overline{\Delta(\phi - \bar{\phi})^2}_{separatrix}$$

$$\approx -\frac{1}{T_c}\left[\frac{\alpha^2\tau_t + \tau_a}{\tau_t + \tau_a} - (1-\alpha)^2 \frac{\tau_t\tau_a}{(\tau_t + \tau_a)^2}\right] \int \frac{d\ell}{B}\, n_{pass} \quad . \tag{D.9}$$

Integrals containing $\bar{\phi}^2$ have their principal contributions from the central cell when these considerations do not apply because of the nearly Maxwellian nature of the distributions there.

Combining these results, we obtain from Eq. D.3 and the assumed perturbation (neglecting the FLR term so as to model a rigid perturbation),

$$\omega(\omega = \omega_0)\left[\frac{\alpha^2\tau_t + \tau_a}{\tau_t + \tau_a} - (1-\alpha)^2\frac{\tau_t\tau_a}{(\tau_t+\tau_a)^2}\right]2\int_{t+a}\frac{d\ell}{B}\,n_{pass}$$

$$- \omega\hat{\omega}_*\left[\frac{\alpha^2\tau_t + \tau_a}{\tau_t + \tau_a} + (g_b - 1)(1-\alpha)^2\frac{\tau_t\tau_a}{(\tau_t+\tau_a)^2}\right]2\int_{t+a}\frac{d\ell}{B}\,n_{pass}$$

$$+ \left[\omega^2k^2\rho^2 + \bar{\omega}_B\,(\omega_* - \omega_0)\right]\int_c\frac{d\ell}{B}\,n_c = 0 \quad , \tag{D.10}$$

where the subscript c denotes the central cell.

The choice of α to yield the most unstable mode, in general, involves the parameters $\hat{\omega}_*/\omega_0$ and $\hat{\omega}_*/\bar{\omega}_B$. Here we set $\alpha = 1$, thereby eliminating the stabilizing effects of positive $\partial f/\partial\varepsilon$ and $g_b \neq 1$ in the transition region. This perturbation has $\phi = 0$ in the transition region and anchor. Solutions are stable provided

$$\frac{1}{4}\bar{\omega}_B\,(\hat{\omega}_* - \omega_0)\int_c\frac{d\ell}{B}\,n_c < \frac{(\hat{\omega}_* - \omega_0)^2\left(2\int_{t+a}\frac{d\ell}{B}\,n_p\right)^2}{\left(k^2\rho^2\int_c\frac{d\ell}{B}\,n_c + 2\int_{t+a}\frac{d\ell}{B}\,n_p\right)} \quad . \tag{D.11}$$

In terms of the growth rate γ_c introduced in Eq. D.5, this becomes

$$\frac{\omega_*^2}{\gamma_c^2} > \frac{4A^2}{(1+A)} \quad , \tag{D.12}$$

where

$$A = \frac{1}{k^2\rho^2}\frac{2\int_{t+a}\frac{d\ell}{B}\,n_p}{\int_c\frac{d\ell}{B}\,n_c} \quad ,$$

and we have introduced the familiar ω_*.

In the A-cell geometry shown in Fig. D-3, we assume that the worst mode is one that vanishes in the yin yang and the A-cell. All but a fraction of electrons are free to pass through the anchor, and only these see an average potential

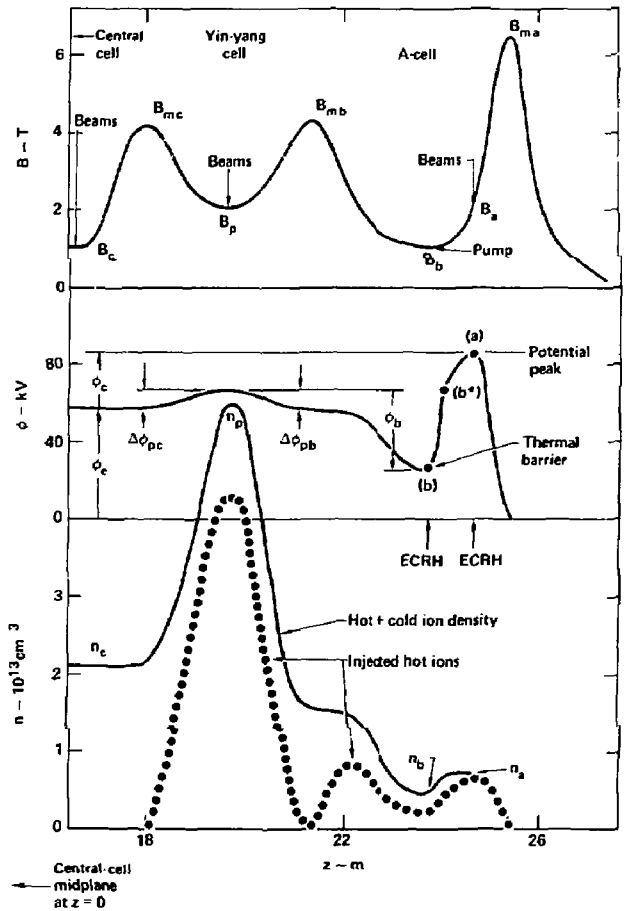

Fig. D-3. Profiles of field, potential, and density at one end of MFTF-B when operated with thermal barriers of the A-cell type. The dashed line represents the assumed worst perturbation that excludes the favorable yin-yang curvature.

$$\bar{\phi}_e = \frac{\tau_c}{\tau_c + 2(\tau_A + \tau_a)} ,$$

where A refers to A-cell and, as before, a to the anchor, or yin-yang.

If there is no local potential rise $\Delta\varphi_p$ in the anchor, the same fraction of ions pass through as electrons and there is no drift term at all. In the presence of $\Delta\varphi_p$, a drift term develops. However, because it is generated by electrons, this term has the opposite sign as the familiar ion FLR term.

Neglecting the ε, μ dependence of the various transit times, we arrive at the following estimates,

$$\left\langle \overline{\tau_B(\phi - \bar{\phi})^2} \right\rangle_{\text{ions}} = \frac{1}{R_c} e^{-\Delta\varphi_p/T_{ic}} \frac{2(L_a + L_A)}{L_c}$$

$$\left\langle \overline{\tau_B(\phi - \bar{\phi})^2} \right\rangle_{\text{electrons}} = \frac{1}{R_c} \frac{2(L_a + L_A)}{L_c}$$

where $\langle \ldots \rangle$ denotes the ε, μ average, and R_c is the mirror ratio seen by the central cell. When allowance is made for $\omega_{*e} = -\omega_{*i} T_e/T_i$, these results lead to the dispersion relation

$$\left(1 + \frac{A_1}{m^2}\right)\omega^2 - \omega_{*i}\left(m - 1 + \frac{A_2}{m}\right)\omega + \gamma_c^2 = 0 ,$$

where

$$A_1 = \frac{1}{R_c}\left(\frac{T_{ic}}{T_{ec}} + e^{-\Delta\phi_p/T_{ic}}\right)\frac{r_c^2}{\rho_i^2}\frac{2(L_a + L_A)}{L_c} ,$$

$$A_2 = -\frac{1}{R_c}\left(1 - e^{-\Delta\phi_p/T_{ic}}\right)\frac{r_c^2}{\rho_i^2}\frac{2(L_a + L_A)}{L_c} .$$

Evaluations of the A-factors for the two magnet sets are given in Sec. I. Comparisons of the two geometries shows the A-values for the A-cell configuration are larger. However, the sign of the drift term is such as to cancel the FLR term, giving instability at finite m.

REFERENCES

D-1. H.L. Berk and M.N. Rosenbluth, LLNL, private communication.

D-2. H.L. Berk, M.N. Rosenbluth, H.V. Wong, T. Antonsen, and D.E. Baldwin, Fast-Growing Trapped-Particle Modes in Tandem Mirrors, Institute for Fusion Studies, University of Texas, Austin, TX, Report IFSR-59 (1982).

D-3. L.D. Pearlstein, D.B. Baldwin, R.H. Cohen, T.K. Fowler, and B.G. Logan, "Stabilization of Tandem-Mirror Trapped-Particle Modes by Incomplete Cancellation of Trapped-Particle Drifts," presented at 1982 Sherwood Meeting, Annual Controlled Fusion Theory Conference, Santa Fe, NM, April 25-28, 1982.

APPENDIX E

SLOSHING IONS IN THE MFTF-B ANCHOR

M. E. Rensink

1. INTRODUCTION

In both the A-cell and axicell configurations for MFTF-B, sloshing ions play a key role in microstability considerations and in creation of the potential that plugs the solenoid. In the A-cell configuration the sloshing-ion distribution and plugging potential were produced in the A-cell itself. For the new axicell configuration, the sloshing-ion distribution and plugging potential are produced in the anchor (yin yang). Here, we report on some bounce-average Fokker-Planck calculations for sloshing ions in the MFTF-B anchor. As in the previous designs, sloshing ions are formed by off-midplane neutral-beam injection perpendicular to the magnetic field.

2. MAGNETIC FIELD

The axial magnetic field profile for the stretched yin-yang configuration is shown in Fig. E-1. The vacuum magnetic field, $B_{vac}(z)$, is obtained from an EFFI code run. The finite-beta depression of the vacuum magnetic field is estimated by means of the long-thin approximation,

$$B(z) = B_{vac}(z)\sqrt{1 - \beta(z)}$$

where our model for $\beta(z)$ is

$$\beta(z) = \beta(0)\left(\frac{B_M - B_{vac}(z)}{B_M - B_{vac}(0)}\right) .$$

We assume a midplane ($z = 0$) beta value $\beta(0)$ of 0.55, so the vacuum mirror ratio of 2.91 increases to 4.34, mainly because of the hot magnetically-confined electrons.

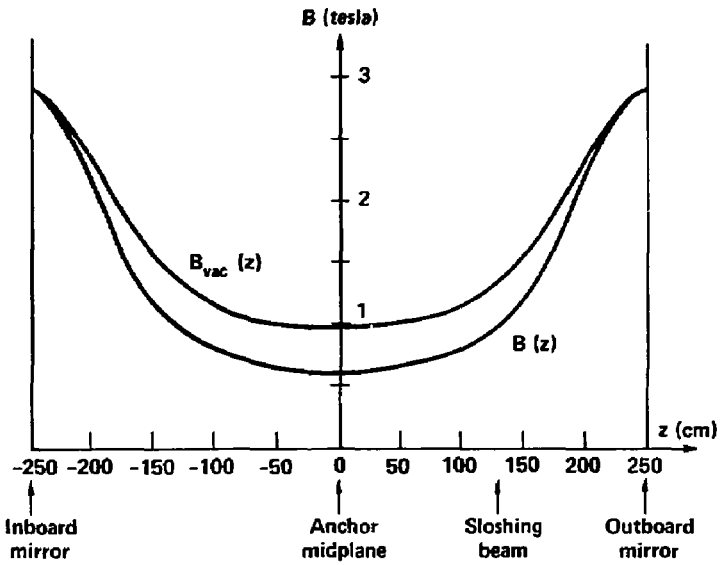

Fig. E-1. Axial magnetic-field profile in anchor.

3. ELECTROSTATIC POTENTIAL

The axial potential profile, $\Phi(z)$, is sketched in Fig. E-2. This potential is derived by setting the local charge density to zero, including contributions from cold, warm, and hot electrons as well as passing, trapped, and sloshing ions. The self-consistent calculation of this potential is a formidable problem, so for the sloshing-ion calculations described here we assume a fixed form for the potential as part of our input data.

On the outboard side of the anchor midplane, we assume a piece-wise quadratic form for $\Phi[\psi]$, where $\psi \equiv B(z)/B(0)$ is the local mirror ratio;

$$\Phi[\psi] = \Phi_a - (\Phi_a - \Phi_0)\left(\frac{\psi_a - \psi}{\psi_a - 1}\right)^2 \quad , \quad 1 \le \psi \le \psi_a \quad ;$$

$$= \Phi_a - (\Phi_a - \Phi_m)\left(\frac{\psi - \psi_a}{\psi_m - \psi_a}\right)^2 \quad , \quad \psi_a \le \psi \le \psi_m \quad .$$

The parameters used in our simulations were:

$$\Phi_0 = 20.0 \text{ keV} \quad ;$$

$$\Phi_a = 80.0 \text{ keV} \quad , \quad \psi_a = 1.50 \quad ;$$

$$\Phi_m = 0.0 \text{ keV} \quad , \quad \psi_m = 4.34 \quad .$$

On the inboard side of the anchor midplane we assume a net mirror ratio $R_L = 4.34$ and a potential rise (midplane to inboard mirror) $\Delta\Phi_L$ of 32.5 keV. These parameters are important in mapping the passing- (solenoid-) ion distribution from the inboard mirror to the midplane, which is the reference point for the bounce-average Fokker-Planck code. The detailed profile of Φ on the inboard side does not enter the calculations because in performing orbit averages, the code assumes symmetry with respect to the midplane.

4. NEUTRAL BEAM INJECTION

Neutral-beam injection is represented by various source and loss terms in the Fokker-Planck equation for the ions. These may be written schematically in the form

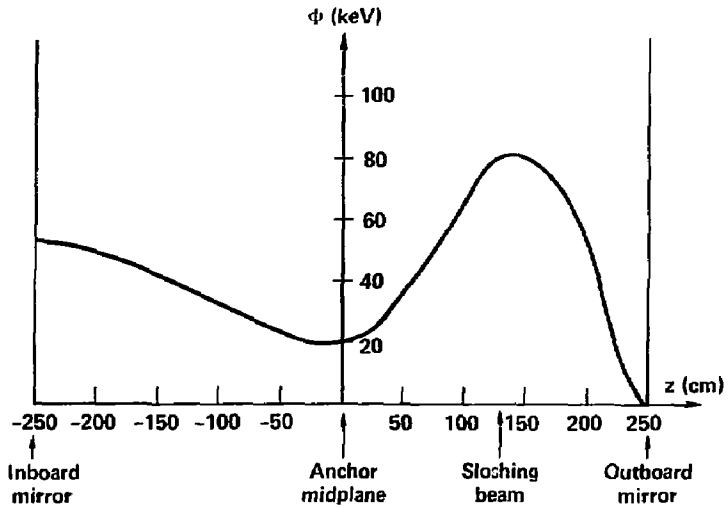

Fig. E-2. Potential profile in anchor.

$$\frac{\partial}{\partial t} f_i\,(z,v,\theta) = C(f_i) + \sum_b \alpha_b(z)\,[(\nu_I^b + \nu_{cx}^b) n_i(z) S_b(v,\theta)$$

$$- \nu_{cx}^b\, f_i(z,v,\theta)] \quad .$$

The first term, $C(f_i)$, is the Fokker-Planck collision term. The remaining terms represent ionization and charge exchange for each beam in the problem. The factor $\alpha_b(z)$ defines the spatial profile of the incident neutral beam. Typically, we assume the Gaussian form

$$\alpha_b(z) = \exp[-(z - z_b)^2/(\Delta z_b)^2] \quad ,$$

where z_b is the injection point and Δz_b is the axial extent of the beam. For sloshing beams in the MFTF-B anchor, we inject at the position of the potential peak, z_b = 130 cm, as indicated in Figs. E-1 and E-2. For well-collimated beams focused at the magnetic axis the spatial extent is $\Delta z_b = \pm 10$ cm for perpendicular injection.

The local source strength (particles/cm^3/s) at the injection point is proportional to the local ion density for ionization and charge-exchange processes. The rate coefficients ν_I^b and ν_{cx}^b are specified as input parameters. These are related to incident neutral-beam currents and ionization and charge-exchange cross sections, e.g.,

$$\nu_I^b = n_b\,(\overline{\sigma v})_I^b \quad ,$$

$$n_b = J_b/e v_b \quad ,$$

where J_b is the incident neutral-beam current density, v_b is the beam velocity, and $(\overline{\sigma v})_I^b$ is the impact-ionization rate parameter (from both electrons and ions).

The velocity-space shape factor, $S_b(v,\theta)$, describes the energy and orientation of the neutral beam and has the form

$$S_b(v,\theta) = K_b \exp[-\lambda_b(v - v_b)^2 - \gamma_b\,(\cos\theta - \cos\theta_b)^2] \quad ,$$

where (v_b,θ_b) specify the mean velocity and pitch angle and (λ_b,γ_b)

define the spread in these quantities. The normalization constant, K_b, is defined such that

$$\int d^3, S_b(v,\theta) = 1 \quad .$$

5. BEAM SPECIES MIX

There are three energetic components for the injected neutral beams. Most of the incident neutrals have the full 80-keV energy, but there are smaller fractions with half-energy (40 keV) and third-energy (27 kev). For our sloshing-ion beams, we have assumed a 90/5/5 molecular-source-current mix, which leads to incident atomic currents at the plasma in the ratio 83/8/9 when beam divergences are taken into account. The half- and third-energy beam components tend to reduce the mean energy of the trapped ions because they constitute a finite fraction of the total incident beam. This effect is accentuated because the charge-exchange cross section at 27 keV and 40 keV is larger than at 80 keV, leading to a larger trapping fraction for the half- and third-energy components. Also, if the half- and third-energy ions from the sloshing beam are not trapped, then charge exchange between these components and the sloshing ions acts as a loss mechanism for the ions and leads to increased sloshing beam current requirements.

6. HIGH-ENERGY PUMP BEAM (HEPB)

The high-energy pump beam is directed along the magnetic axis so that any charge-exchange of this beam with the sloshing or trapped ions produces an untrapped ion. Thus, the HEPB removes ions from the anchor. The rate parameter $(\overline{\sigma v})_{cx}^{HEPB}$ can vary significantly with axial position because the charge-exchange cross section is a strong function of the relative velocity between the axially directed HEPB and the co- or counter-streaming components of the sloshing ions. This effect is included in the specification of the profile factor $\alpha_b(z)$ for the HEPB. For the MFTF-B anchor, $n_{HEPB}(z)$ is approximately uniform for the axially-directed HEPB, and the spatial variation of $(\overline{\sigma v})_{cx}^{HEPB}$ is modelled by

$$\alpha_{HEPB}(z) = \exp[-z^2/L_{cx}^2] \quad ,$$

where $L_{cx} \approx 250$ cm fits the estimated fall off in $(\sigma v)_{cx}^{HEPB}$ as one moves out from the midplane.

7. LOSS-CONE BOUNDARIES AND PASSING IONS

The velocity-space loss boundary at the midplane of the anchor consists of several segments, as shown in Fig. E-3. For ions to escape through the outboard mirror from the midplane, they must first be able to pass over the potential peak Φ_a at ψ_a. Ions to the right of curve A satisfy this condition. If the magnetic moment of these ions is not too large, they will be able to pass through the outboard-mirror throat and escape from the plasma. Ions to the right of both curves A and M satisfy these conditions. It is also

'ble for ions to escape through the inboard mirror and join the passing ions in the solenoid or in the transition region between the axicell and potential peak at ψ_a in the anchor. Ions in the shaded region to the right of curve L but to the left of curve A satisfy this condition, and we call these the "passing" ions.

We assume that the passing ions have a Maxwellian distribution characterized by the solenoid-ion temperature ($T_{ic} = 15$ keV for nominal MFTF-B operation). The density of the passing ions depends on the strength of the charge-exchange pumping in the transition region. In this report we present results for several plausible values of the passing-ion density.

8. RESULTS

We present results for three different values of the passing-ion density at the inboard-mirror throat, i.e., $n_M = 2 \times 10^{12}$, 4×10^{12}, and 8×10^{12} cm^{-3}. The incident sloshing beam is held fixed, and in each case the HEPB has been adjusted in intensity to maintain a midplane ion density $n_0 \approx 3.2 \times 10^{12}$ cm^{-3}. Table E-1 summarizes input parameters common to all three cases. Results are summarized in Table E-2 and in Figs. E-4 to E-7. It should be noted that the density profiles in Fig. E-4 apply only to the outboard side of the anchor.

From Table E-2 we see that the ratio of warm (passing and trapped) ions to sloshing ions is largest for case C ($n_M = 8 \times 10^{12}$ cm^{-3}) so we expect this to be the most favorable case for microstability. An examination of the

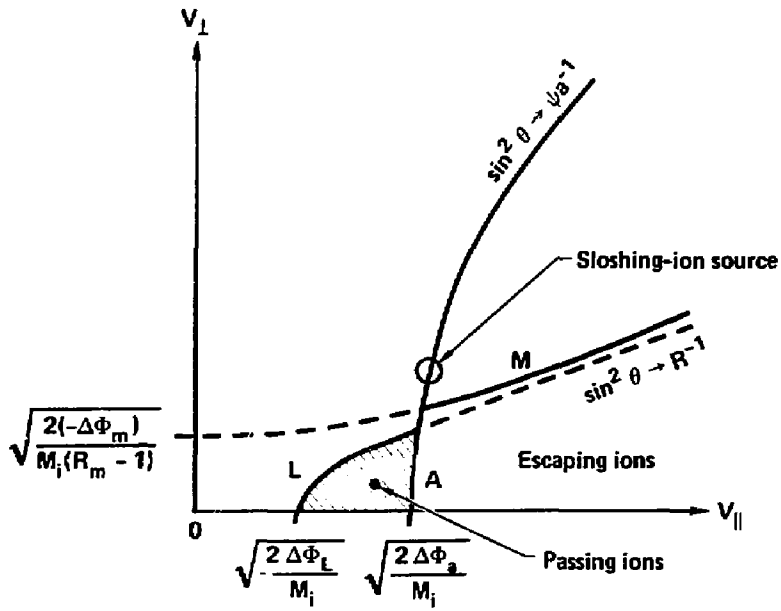

Fig. E-3. Loss-cone boundaries in midplane velocity space of anchor.

Table E-1. Input parameters for sloshing-ion anchor.

Magnetic Field	
Outboard-mirror ratio (net)	$R_M = 4.34$
Inboard-mirror ratio (net)	$R_L = 4.34$
Midplane-to-mirror axial distance (symmetric)	$z_m = 248$ cm
Potential	
Potential drop (midplane to outboard mirror)	$\Delta\Phi_m = -20$ keV
Potential rise (midplane to peak of plug)	$\Delta\Phi_a = +60$ keV
Mirror ratio to peak of plug potential	$\psi_a = 1.5$
Potential rise (midplane to inboard mirror)	$\Delta\Phi_L = +32.5$ keV
80-keV Sloshing Beams	
Mirror ratio (midplane to injection point)	$\psi_{inj} = 1.5$
Axial distance (midplane to injection point)	$z_{inj} = 130$ cm
Axial extent of beam	$\Delta z_{inj} = \pm 10$ cm
Local injection angle	$\theta_{inj} = 90^o$
Equivalent midplane injection energy	$E_{inj}^{(0)} = 140$ keV
Equivalent midplane injection angle	$\theta_{inj}^{(0)} = 38^o$
Rate coefficients for full/half/third-energy beam components	$\nu_I^{SL} = 13.75/3.62/7.07$ $\nu_{cx}^{SL} = 5.34/2.27/5.25$
Incident sloshing-beam current density (at injection point on <u>each</u> side of midplane)	$J_{incident}^{SL} = 10.4$ mA/cm^2
80-keV HEPB	
e-folding length for fall off of $(\sigma v)_{cx}^{HEPB}$	$L_{cx} = 248$ cm

Table E-2. Effect of passing-ion density on anchor parameters.

	Case number			
	A	B	C	D
Fokker-Planck run	MF25N	MF25K	MF25M	MF25Q
Passing-ion density at inboard-mirror throat, n_m $(cm^{-3})(10^{12})$	2	4	8	0
HEPB-rate coefficient needed to maintain to constant midplane density, ν_{cx}^{HEPB} (s^{-1})	1.50	1.83	3.30	1.83
Incident HEPB current density; $J_{incident}^{HEPB}$ (mA/cm^2)	1.03	1.26	2.26	1.26
Total midplane-ion density, $n(cm^{-3})(10^{12})$	3.22	3.33	3.12	2.08
Passing warm-ion density, $n_p(cm^{-3}(10^{12})$	0.10	0.30	0.40	0
Trapped warm-ion density, $n_T(cm^{-3})(10^{12})$	0.77	1.52	2.25	0
Sloshing-ion density, $n_{SL}(cm^{-3})(10^{12})$	2.35	1.61	0.47	2.08

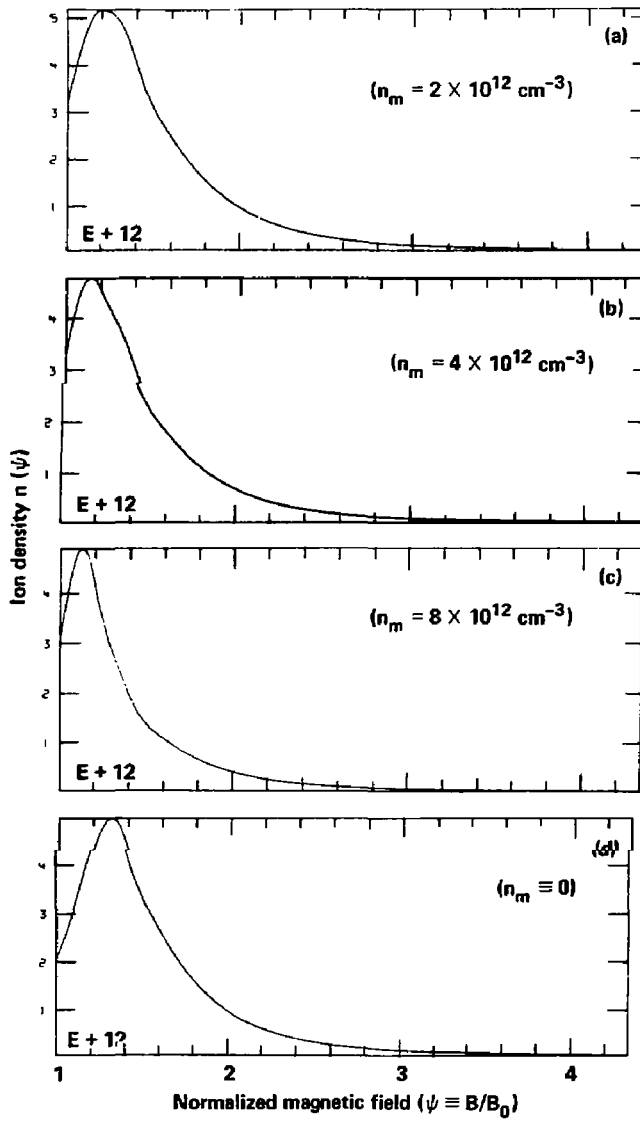

Fig. E-4. Ion density as a function of magnetic field for four values of n_m.

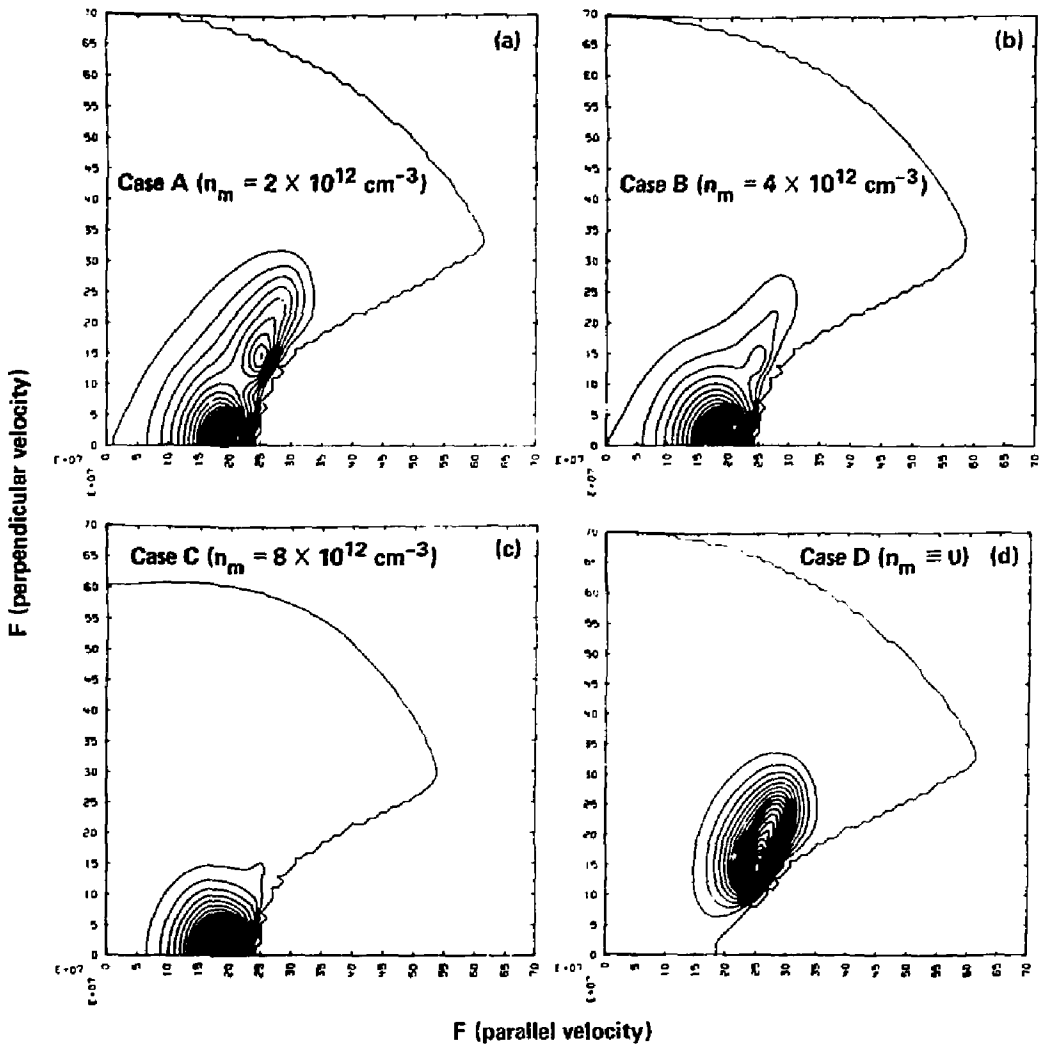

Fig. E-5. Contour plots of ion-distribution function, $f_0(v_\perp, v_\parallel)$, at anchor midplane for four values of n_m.

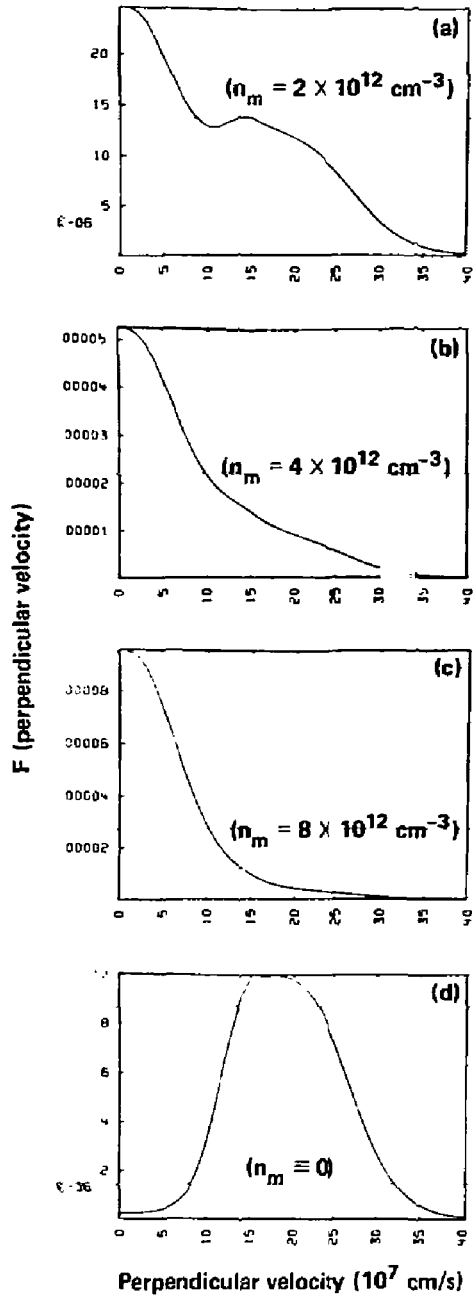

Fig. E-6. Distribution of perpendicular velocities at anchor midplane for four values of n_m.

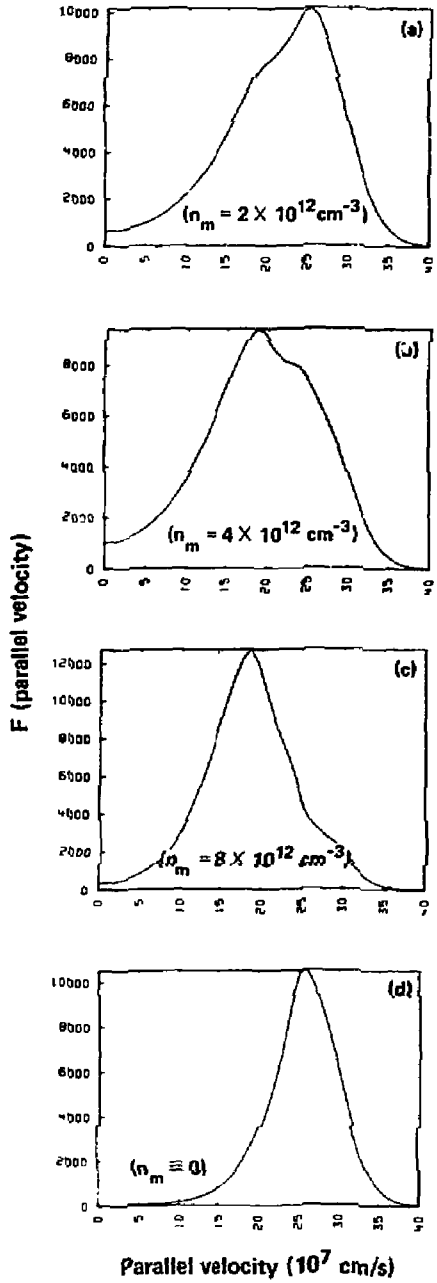

Fig. E-7. Distribution of parallel velocities at anchor midplane for four values of n_m.

midplane-$v_\perp$ distributions in Fig. E-6 confirms this expectation. If the higher value of the passing-ion density in case C should turn out to be the most plausible, but a larger fraction of sloshing ions is required (e.g., to produce a larger potential peak), then both the HEPB and the sloshing-beam currents would have to be increased relative to the values given in Tables E-1 and E-2.

The presence of the warm (passing + trapped) ions in cases A, B, and C tends to obscure some of the features of the sloshing ions, so to obtain a clearer picture we examine case D in which there are no warm ions. Here we use the same HEPB as in case B but arbitrarily set the passing-ion density to zero. Results are given in Table E-2 and Figs. E-4 to E-6. The sloshing-ion midplane density for this case is $n_0 = 2.08 \times 10^{12}$ cm^{-3}; the peak density is 2.84 times higher. The peak, which occurs at a mirror ratio $\psi_{pk} = 1.3$, is shifted toward the midplane from the injection point at $\psi_{inj} = 1.5$. This inward shift is due to ion-ion scattering, which tends to broaden the midplane pitch-angle distribution of the sloshing ions. Ions that scatter toward smaller pitch angles escape through the loss cone, while ions that scatter toward $\theta_0 = 90^0$ are trapped closer to the midplane.

The particle confinement time for the sloshing ions is limited by a combination of charge exchange on the HEPB and axial loss because of ion-ion scattering into the loss cone. This can be seen from the particle balance equation which we write in the form

$$\frac{\partial N_{SL}}{\partial t} = + J^{SL}_{ionization} - \frac{N_{SL}}{\langle \tau_{cx}^{HEPB} \rangle} - \frac{N_{SL}}{\langle \tau_{end\text{-}loss} \rangle} \ ,$$

where the line-integrated particle and current densities are

$$N_{SL} = \oint \frac{dz\ n(z)}{\psi(z)} \ ,$$

$$J^{SL}_{ionization} = \oint dz \frac{\nu_I^{SL}(z)\ n(z)}{\psi(z)} \ .$$

In steady state, for case D, we find that the lifetimes for loss from charge exchange and scattering are comparable,

$$\langle \tau_{cx}^{HEPB} \rangle = 0.65 \text{ s} ,$$

$$\langle \tau_{end\text{-}loss} \rangle = 0.88 \text{ s} .$$

The somewhat shorter lifetime for charge exchange is typical of most cases we have considered for sloshing ions in the anchor.

APPENDIX F

ION MICROSTABILITY

L. D. Pearlstein and G. R. Smith

This section contains assessments of both loss-cone and Alfvén ion-cyclotron instabilities and an overall conclusion.

1. LOSS-CONE STABILITY (L. D. Pearlstein)

The background for the material presented here on stability to loss-cone modes was detailed in Physics Basis for MFTF-B,[B-1] and will not be repeated here. Rather, I will update the physics and the status of the stability to loss-cone modes in the axicell configuration. In this configuration, there are still two cells (the axisymmetric mirror and the quadrupole anchor) with loss-cone distribution of ions. As in the A-cell yin-yang, the axicell ion distribution averaged over the parallel velocity is a monotonic function of the perpendicular velocity and thus is stable to loss-cone modes. After such an average, the yin-yang anchor-barrier cell, like the A-cell, does maintain a loss-cone between the midplane and the outboard mirror (see Fig. F-1 and its stability must be ascertained.

I begin with a brief description of the modes. In general, the electrons generate the waves while the ions provide the instability mechanism. Stability rests on the control of the ion distributions. An important property of these modes are the various space scales. The wavelengths perpendicular to the magnetic field are short ($k_\perp \rho_i \gtrsim 1$) compared to equilibrium scale lengths and, consequently, the eikonal approximation can be used for this variation. Wavelengths along the magnetic field are comparable to equilibrium scale lengths (variations in the magnetic field, density, and the like). Hence, we solve a second-order ODE along the magnetic field[F-1] with $k_\perp(s)$, to find the eigenvalues, that is, the standard "balloon" equation. The form of this differential equation follows:

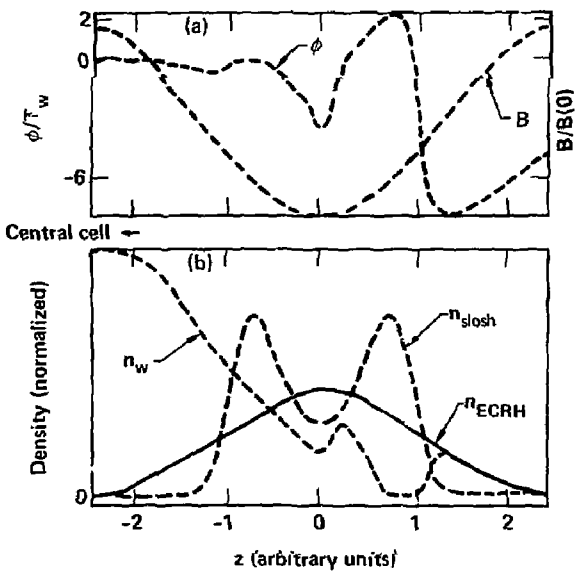

Fig. F-1. Stability of axicell configuration to loss-cone modes: (a) Electrostatic potential ϕ and magnetic field B as a function of z, distance along the magnetic field; (b) sloshing-ion density, the thermal-ion density, and the magnetically confined ECRH-generated electron density, all shown as functions of z. The central cell is off to the left. All densities are normalized to the peak sloshing-ion density.

$$\omega_{ci} \frac{d}{ds} \frac{\omega_{pe}^2}{\omega^2 \omega_{ci}} \frac{k_\perp^2 c^2}{k_\perp^2 c^2 + \omega_{pe}^2} \frac{d\phi}{ds} = k_\perp^2 (\phi + F_e \phi + F_i[\phi]) \quad , \tag{F.1}$$

where

$$F_e = \frac{\omega_{pe}^2}{\omega_{ce}^2} + \frac{1}{k_\perp^2 \lambda_D^2} \left[\left(1 - \frac{\omega_i}{\omega}\right) \left(1 + \frac{\hat{\beta}}{2}\right) - 1 \right] \quad , \tag{F.2}$$

(Electromagnetic)

with

$$\hat{\beta} = \frac{1 - \frac{\beta}{2} \phi_2 - \frac{\omega}{\omega_{ci}} (1 + \phi_2)}{1 - \frac{\omega}{\omega_{ci}} (1 + \phi_2)} \tag{F.3}$$

and

$$\phi_2 = - \int_0^\infty dv_\perp^2 \, f_e(v_\perp^2) \frac{\omega - \omega_{*e}}{\omega + \omega_{*e} v_\perp^2 \frac{\beta}{2}} \quad . \tag{F.4}$$

All undefined notation is standard (for definitions see Ref. F-1). Also the new form ($\hat{\beta}$) of the finite β term added to the basic equations arises from the ∇B electron drift with $k_\perp \rho_e << 1$.[F-2] Note that in the limit $T_e \to 0$, we recover the standard result $\hat{\beta} = \beta$. Also $F_i[\phi]$ is as defined in Ref. F-1. One further addition has been an improved self-consistent barrier-potential model.[F-3]

In Fig. F-2 I present results for the vacuum mirror ratio 2.8, $\beta_{vac} = 0.55$ (actual mirror ratio 4.) for the sloshing-ion profile shown. Also shown is the density of magnetically trapped electrons and the density of thermal ions and the potential, all as functions of s. The potential profile shown differs somewhat from that calculated in Sec. II, although the warm-plasma-density profile is quite similar. This difference is due to our approximate model distribution function, which must be an analytic function of mod-B (see Ref. F-3) for the stability analysis.

In Fig. F-2, stability boundaries are shown for the two worst modes (solid line) of the configuration described above and stability boundaries for a configuration with a 20% broader ECRH profile (dashed line), thus also a more flattened well. The ordinate is the ratio of the thermal-ion density to

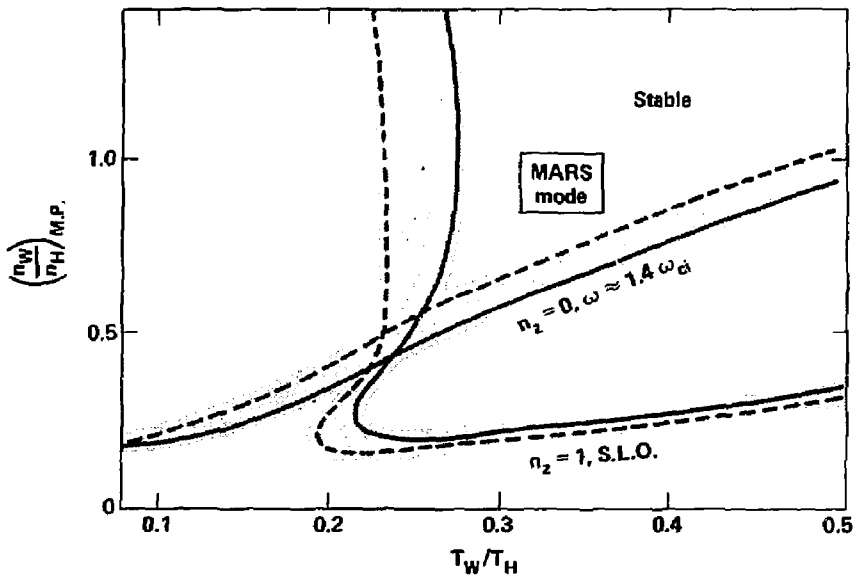

Fig. F-2. Marginal stability for two worst modes (solid lines) and for a configuration with a 20% broader ECRH profile (dashed lines). The two curves of each set correspond to two magnetically contained electron profiles varying by 20% (see text). The vertical axis is the ratio of thermal-ion to sloshing-ion density at the mirror midplane. The horizontal axis is the ratio of thermal-ion to sloshing-ion energy. The shaded regions imply the existence of uncertainty in profiles. The square region depicts the nominal operating regime for the MARS mode.

the sloshing-ion density evaluated at the midplane of the mirror, and the abscissa is the ratio of the thermal-ion energy to the energy of the sloshing ions evaluated at the midplane of the mirror. The curve labelled $n_z = 0$ (the lowest axial mode) is the stability boundary for the analog of the drift-cyclotron-loss-cone (DCLC) mode in a symmetric well, but here $\omega \approx 1.4\ \omega_{ci}$ and is near a resonant frequency in the region of no warm plasma. The curve labelled $n_z = 1$ (the next mode) is the stability boundary to the axial loss-cone mode (ALC) computed from straight-line orbits where $\omega > 5.5\ \omega_{ci}$. The normal operating regime is denoted by the rectangle shown in the figure.

The basic conclusion of this study is that stable regions for loss-cone driven modes overlap the operating regime of the MFTF-B Axicell configuration. The shaded area on the graph represents the sensitivity to details and is a measure of the uncertainty of the theory. Obviously, a more extreme variation in profiles can expand the shaded area to include the operating point. It should be emphasized that this sensitivity to moderate changes in scale length is primarily a property of the large hole in the perpendicular sloshing-ion distributions, a signature common to both the A-cell and axicell configurations.

Further properties of a marginally stable point are shown in Figs. F-3 and F-4. The marginally stable distribution function averaged over the parallel velocity is shown in Fig. F-3. The values generated from a bounce-averaged Fokker-Planck code (circles) are used as input to the various scenarios. Last, Fig. F-4 shows the magnitude and phase of typical eigenfunctions.

2. ALFVÉN ION-CYCLOTRON STABILITY (G. R. Smith)

Each of the operating modes of MFTF-B has at least one mirror cell for which Alfvén ion-cyclotron (AIC) stability must be considered. Here, we give a preliminary assessment of AIC stability in each type of cell. More detailed assessments will be undertaken as Fokker-Planck results for each cell become available. Also, we describe briefly the flexible, model ion distribution function being used for each type of cell.

The various operating modes have two qualitatively different types of mirror cells, those containing sloshing ions and those without a sloshing-ion component.

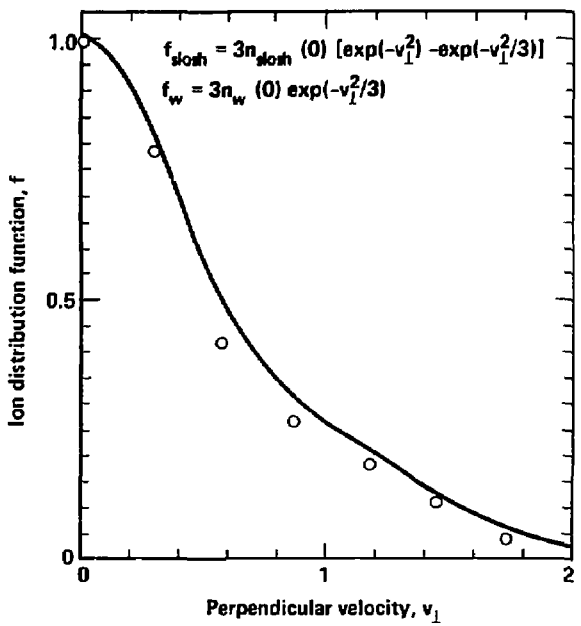

Fig. F-3. Ion-distribution function f as a function of perpendicular velocity at midplane of anchor at marginal stability. The circles depict values obtained from a Fokker-Planck run.

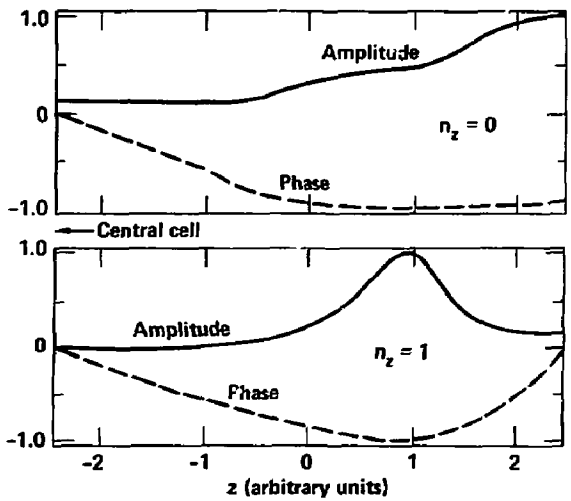

Fig. F-4. The amplitude and phase of the eigenfunction of marginal stability for the $n_z = 0$ mode and for the $n_z = 1$ mode.

2.1 Anchor-Plug Cell With Sloshing Ions

For three operating modes (axicell, Kelley, and TMX-U-like) the anchor plug implemented in the yin-yang magnet has a strong sloshing-ion component. Hot electrons provide most of the β; the β of the sloshing ions is moderate, of order 10%, a few times the value expected in TMX-U.

In initial calculations of the effect of a sloshing-ion component on AIC instability, a strong stabilizing effect has been discovered. Crudely, the sloshing energy of the ions can be included in calculating the anisotropy $\langle v_\perp^2 \rangle / \langle v_\parallel^2 \rangle - 1$ that drives the instability. Thus, a sloshing-ion component with mean pitch angle of 45^0 contributes weakly, at most, to driving AIC instability.

Because of this strong stabilizing effect, the largest drive for AIC instability may come from the region where the ions reflect from the inner mirror, since the anisotropy and ion energy (and therefore β) are both high there. This region is fairly short ($\lesssim$ 100 cm) in terms of the typical unit of length (inverse wavenumber) for AIC instability

$$\frac{c}{\omega_{pi}} = \frac{2.3 \times 10^7}{Z} \left(\frac{\mu}{n}\right)^{1/2} \text{cm} \quad ,$$

where Z and μ are the ion charge and mass numbers and n is in cubic centimeters. For MFTF-B, Z = 1, μ = 2, $n \approx 6 \times 10^{12}$, and $c/\omega_{pi} \approx 15$ cm. The shortness of this region of high sloshing-ion density shows the need for calculations that take into account the axial equilibrium variations.

Detailed calculations including sloshing ions and axial variations are necessary to refine the parameters of this anchor-plug cell.

2.2 Cells Without Sloshing Ions

2.2.1 Anchor-Plug Cell of TMX-Like Operating Mode. This cell, also implemented in the yin-yang magnet, has high ion β, like the successful 2XIIB experiment. However, unlike 2XIIB, the stabilizing effect of finite length is negligible in MFTF-B since for $n \approx 10^{14}$,

$$\frac{c}{\omega_{pi}} \approx 4 \text{ cm} \ll L_{plasma} \sim 150 \text{ cm} \quad .$$

Counteracting the destabilizing effect of larger plasma size is the potentially stabilizing effect of larger mirror ratio in MFTF-B. The vacuum mirror ratio of 2 in 2XIIB was not fully utilized because of the maintenance by electron drag and charge exchange of an ion distribution much shorter than the mirror-to-mirror distance. If means can be found in MFTF-B to build an ion distribution that fills this cell of vacuum mirror ratio 3, AIC stability can probably be achieved in spite of the long plasma length.

2.2.2 Axicell. The axicell operating mode of MFTF-B (and of the similar MARS reactor study) contains an axisymmetric mirror cell with moderate ion β (comparable to the TMX end cell). In this respect, the axicell is much superior to the yin-yang cell of the A-cell design of MFTF-B, which requires β to be many times that achieved in TMX. The smaller mirror ratio of the axicell (1.5 on the central-cell side) allows confinement of only a rather anisotropic distribution. The anisotropy could, however, be somewhat less than in TMX and in the A-cell design, which (like 2XIIB) did not utilize their full mirror ratios. An estimate of the anisotropy limit can be obtained by adapting the convective-absolute boundary calculation of Hedrick[F-4]

$$\frac{\beta_\perp}{\beta_\parallel} \approx 1.9\, \beta^{-1/2} \quad .$$

For β of 20%, this predicts that absolute instability can be avoided if

$$\frac{\beta_\perp}{\beta_\parallel} \lesssim 6 \quad ,$$

which should be achievable. This calculation neglects the stabilizing effect of the central-cell ions that seem to be present in TMX. In MFTF-B the effect may be stronger than in TMX, because the central-cell ions have significant density throughout the axicell.

The axicell thus seems more stable than the yin-yang of the A-cell design.

2.2.3 Central Cell for Kelley Operating Mode. In this operating mode, which is similar to that of the Technology Development Facility (TDF) strong neutral-beam injection and short confinement time can lead to a significantly non-Maxwellian ion distribution in the central cell. Furthermore, high β is

required, and the plasma is extremely long in units of c/ω_{pi}, which may imply that suppression of absolute AIC instability is not adequate to avoid deleterious effects; convectively growing waves might heat and trap ions in the bad-curvature transition region. Ameliorating these effects is the very large vacuum mirror ratio of about 10. The large mirror ratio may allow a sufficiently Maxwellian distribution to be built so that AIC instability can be avoided.

2.3 Model Ion-Distribution Function

An ion-distribution function that is very useful for modeling the various cells of a tandem-mirror machine leads to a numerically tractable dispersion relation for Alfvén ion-cyclotron instability, as described in this section.

The ion-distribution function f is a superposition of distributions f_j of one or more ion components (e.g., sloshing, passing, trapped):

$$f(\underline{v}) = \sum_j f_j(\underline{v}) \quad .$$

The following two models for f_j allow a large variety of mirror cells to be studied. The first model has f_j separable in perpendicular and parallel velocity $v_\perp$ and $v_\parallel$, while the second has f_j separable in speed $v \equiv (v_\perp^2 + v_\parallel^2)^{1/2}$ and pitch angle $\phi \equiv \tan^{-1}(v_\perp/v_\parallel)$. Thus,

$$f_j(\underline{v}) = A_j\, f_\perp(v_\perp) \left\{ \exp\left[-\alpha_j (v_\parallel - u_j)^2 \right] + (v_\parallel \to -v_\parallel) \right\} \quad ,$$

$$f_j(\underline{v}) = F_j(v)\, G_j(\phi), \quad G_j(\phi) = G_j(\pi - \phi) \quad .$$

Both models have the required symmetry under $v_\parallel \to -v_\parallel$. For perpendicular wave number $k_\perp = 0$, the form of $f_\perp$ does not enter the dispersion relation, only the density and temperature moments enter. Even for $k_\perp \neq 0$ the first model allows both velocity-space integrals to be done analytically.

For the second model, a particular class of $F_j(v)$ allows one velocity-space integral (speed) to be done analytically for $k_\perp a_j \lesssim 1$, where a_j is the mean gyroradius of ion component j:

$$F_j(v) = C_j v^{2\ell_j} \exp(-\alpha_j v^2), \quad \ell_j = 0, 1, 2, \ldots \quad .$$

For $k_\perp = 0$, a rather simple form of the dispersion relation results even for the model $f_j = F_j(v)G_j(\phi)$. Suppressing the subscript j for brevity, we can write the dispersion relation for a plasma with cold electrons as

$$0 = D(\omega,k) = k^2c^2 - \omega^2 + \frac{\omega_{pe}^2\omega}{|\Omega_e|} + D_i(\omega,k) \quad ,$$

$$D_i = \omega_{pi}^2 \left(1 + \frac{2\pi^{1/2}}{\Gamma(\ell + 1.5)} \int_{\phi_{loss}}^{\pi/2} d\phi \tan\phi\, G(\phi) \right.$$

$$\left. \left\{ \sin\phi \tan\phi \left[(2 + \ell)Z_{3+2\ell} - Z_{5+2\ell}\right] - \frac{\Omega\alpha^{1/2}}{k} Z_{2+2\ell} \right\} \right) \quad ,$$

where the generalized plasma dispersion functions,

$$Z_m(z) \equiv \pi^{-1/2} \int_{-\infty}^{\infty} du \frac{u^m \exp(-u^2)}{u - z} \quad ,$$

have argument

$$z = \frac{\omega - \Omega}{k \cos\phi} \alpha^{1/2} \quad .$$

Here, Ω is the ion-cyclotron frequency. These functions can be computed accurately and rapidly. Only a single integral (over pitch angle ϕ) must be done numerically. Nonzero $k_\perp \lesssim a_j^{-1}$ does not force the numerical evaluation of both velocity-space integrals but merely introduces a determinant with elements no more complicated than D shown above.

3. CONCLUSION

The conclusion of this study is that both the A-cell and axicell configurations look the same with regard to ion microstability. Further, provided the predicted operating parameters can be achieved and some care is taken in forming the ion distributions, we anticipate that the plasma will be stable to these modes.

REFERENCES

F-1. D. E. Baldwin, B. G. Logan, and T. C. Simonen, Physics Basis for MFTF-B, Lawrence Livermore National Laboratory, Rept. UCID-18496, Part 2 (1980) Sec. IV.E.

F-2. R. C. Davidson, N. T. Gladd, C. S. Wu, and J. D. Huba, Phys. Fluids 20, 301 (1977)

F-3. L. D. Pearlstein and W. M. Nevins, The Barrier Potential Model, Lawrence Livermore National Laboratory, Rept. UCID-19159 (August 1981).

F-4. C.L. Hedrick, Convective-Absolute Boundary for Whistler Modes, Oak Ridge National Laboratory, Rept. ORNL-TM-3143 (Sept. 1970).

APPENDIX G

ELECTRON MICROSTABILITY

Y.-J. Chen, W.M. Nevins, and G.R. Smith

1. INTRODUCTION

The hot-electron plasmas in tandem mirrors may be unstable at frequencies comparable to the electron-cyclotron frequency Ω. By studying these instabilities we hope to prevent deleterious effects by learning how to operate experiments without strong instabilities.

An early review of microinstabilities of ECRH plasmas was provided by Guest and Sigmar.[G-1] The instabilities that led to the most stringent constraints on plasma parameters were the electromagnetic whistler instability and the electrostatic "upper-hybrid loss-cone" (UHLC) instability. Later work on the whistler instability shows that relativistic effects are significantly stabilizing even for mean electron energies much less than the rest energy.[G-2 to G-4] The UHLC instability was the subject of a detailed study for plasma parameters appropriate to the earth's magnetosphere.[G-5]

In this previous work[G-1 to G-5] it was found that the wavelengths associated with these high-frequency electron modes are short in comparison to typical macroscopic scale lengths of the plasma. Hence, requiring stability in the case of these modes tends to constrain the electron-distribution function rather than the configuration of an experimental plasma.

In this article we describe our present numerical study of instabilities of ECRH plasmas. Our work improves on earlier work by more accurately modeling the electron-distribution functions suggested by recent Fokker-Planck studies of electron-cyclotron-resonance heating (ECRH) in a magnetic-mirror field.[G-6,G-7]

2. MODELING THE ELECTRON DISTRIBUTION

Fokker-Planck studies of ECRH plasmas in the TMX-Upgrade Experiment have found distributions $f(\underline{v})$ like the one shown in Fig. G-1.[G-6,G-7] The distribution for MFTF-B will be similar to that shown in Fig. G-1. The moments

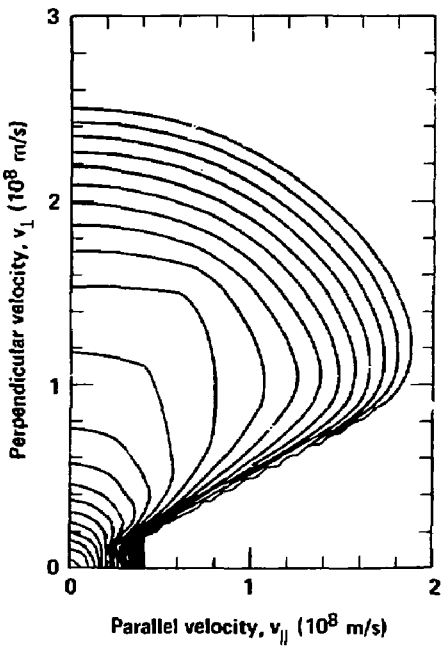

Fig. G-1. Contour plot of electron distribution found in Fokker-Planck studies of the ECRH plasma in the TMX-U experiment. The total electron density is given by $\omega_p^2/\Omega^2 = 1.55$. Contours are logarithmically spaced, adjacent contours being separated by a factor of two.

$f_\perp \equiv \int dv_\parallel f(\underline{v})$ and $f_\parallel \equiv 2\pi \int v_\perp dv_\perp f(\underline{v})$ are monotonically decreasing functions of perpendicular and parallel energy, respectively. It does not follow, however, that loss-cone instabilities are absent, because the distribution in Fig. G-1 is poorly approximated by $f_\perp f_\parallel$, i.e., $f(\underline{v})$ is not a separable function of perpendicular and parallel energies. Separable distributions have been used in most previous studies; exceptions are the whistler-instability studies of Scharer[G-8] and Jacquinot and Leloup.[G-2] Loss-cone instabilities with finite $k_\parallel$ can be driven by wave-particle interactions at $v_\parallel = (\omega - n\Omega)/k_\parallel$, along which the perpendicular-velocity distribution is inverted for appropriate n, ω, and $k_\parallel$. Here, n is an integer, ω is the wave frequency, and $k_\parallel$ is the parallel component of the wavevector. Failure to recognize the nonseparability of $f(\underline{v})$ would lead to overly optimistic stability assessments for loss-cone instabilities. Therefore, we have developed the following nonseparable model for the distribution function of an ECRH plasma.

We superpose a number N of electron components with various parameters:

$$f(\underline{v}) = \sum_{s=1}^{N} f_s(\underline{v}) \quad . \tag{G.1}$$

Each species has a separable distribution

$$f_s(\underline{v}) = \frac{n_s}{\pi^{3/2}\, \alpha_{\perp,s}^2\, \ell_s!\, \alpha_{\parallel,s}} \left(\frac{v_\perp}{\alpha_{\perp,s}}\right)^{2\ell_s} \exp\left(-\frac{v_\perp^2}{\alpha_{\perp,s}^2} - \frac{v_\parallel^2}{\alpha_{\parallel,s}^2}\right) . \tag{G.2}$$

By appropriate choices of the densities n_s, thermal speeds $\alpha_{\perp,s}$ and $\alpha_{\parallel,s}$, and indices ℓ_s, we achieve a good reproduction of Fig. G-1, as shown in Fig. G-2.

Superposing separable distributions to model a nonseparable distribution allows us to avoid numerical velocity-space integrations, a considerable computational advantage. The distribution in Eq. G.2 is precisely that used by Callen and Guest,[G-9] who provided all the formulae necessary for numerical calculation of the dielectric function $D(\omega,\underline{k}) = \det[\underline{D}(\omega,\underline{k})]$, whose roots describe the small-amplitude waves of a collisionless plasma in a uniform magnetic field, $\underline{B}_0$.

We have written a computer code that solves the fully electromagnetic dispersion relation $D(\omega,\underline{k}) = 0$ for the non-separable model distribution given by Eqs. G.1 and G.2. The direction of wave propagation $\underline{k}$ with

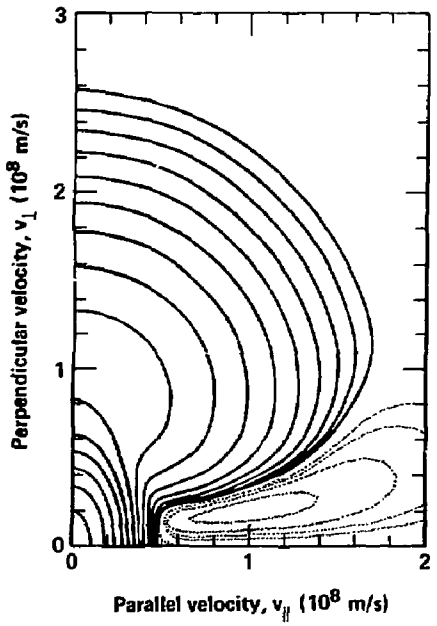

Fig. G-2. Model electron distribution formed by superposing five separable distributions (see Eq. G.2). The logarithmically spaced contours are separated by a factor of two. The plasma frequencies ω_p, perpendicular temperatures $T_\perp \equiv (\ell + 1)\, m\alpha_\perp^2/2$, parallel temperatures $T_\parallel \equiv m\alpha_\parallel^2/2$, and indices ℓ are given by $\omega_p^2/\Omega^2 = 0.64$, 0.92, -0.037, 0.046, and -0.018, respectively; $T_\perp$ = 3, 40, 12, 12, and 4 keV; $T_\parallel/T_\perp$ = 0.3, 0.35, 4, 2, and 6; and ℓ = 0, 1, 1, 1, and 1. Dotted contours give unphysical negative values of the distribution function. The spacing between adjacent dotted contours is also by a factor of two. The magnitude of the most negative value of the distribution function is less than 1/2000th of the most positive value.

respect to $\underline{B}_0$ can be arbitrary, but the plasma is assumed to be spatially uniform and nonrelativistic.

The uniform-plasma approximation is a reasonable first approximation because high-frequency instabilities have wavelengths much shorter than typical equilibrium scale lengths of the plasma. The non-relativistic approximation is known to be pessimistic for the whistler instability: Gladd has found growth-rate reductions of a factor of two or more for mean electron energies of 250 keV, one-half the rest energy.[G-3,G-4] Relativistic effects are stabilizing only for instabilities with $\omega < \Omega$. Nevertheless, at the 200-600 keV energies envisioned for MFTF-B, even the UHLC instability, which has $\omega > \Omega$, will have to be treated relativistically. The results in the next section were found with the non-relativistic approximation.

3. NUMERICAL RESULTS

Only two instabilities, the whistler and upper-hybrid loss-cone modes, are found in a plasma with the non-separable model electron distribution shown in Fig. G-2 by applying the Nyquist technique thoroughly over the $\underline{k}$ plane. We have used our computer code to calculate the real frequencies and temporal growth rates of these instabilities. For the whistler mode the maximum growth rate occurs at $k_\perp = 0$ and $k_\parallel c/\Omega = 1.41$, where $\omega/\Omega = 0.55 + i\ 0.025$. When we double the total electron density without changing the shape of the distribution, we find that the wave vector that maximizes the growth rate shifts to $k_\parallel c/\Omega = 1.74$, where the frequency is given by $\omega/\Omega = 0.51 + i\ 0.049$.

For the UHLC instability we show in Fig. G-3 a contour plot of Im ω in the $k_\perp k_\parallel$ plane. The maximum growth rate occurs at $k_\perp c/\Omega = 9.9$ and $k_\parallel/k_\perp = 0.071$, where $\omega/\Omega = 1.15 + i\ 0.0064$. These values of $k_\parallel$ and $k_\perp$ for the most unstable mode are in line with estimates presented by Guest and Sigmar.[G-1] Note that the growth rate of the UHLC mode goes to zero as $k_\parallel$ goes to zero, as expected for our monotonically decreasing $f_\perp$. Doubling the total electron density shifts the maximum growth rate to $k_\perp c/\Omega = 10.9$ and $k_\parallel/k_\perp = 0.13$, where $\omega/\Omega = 1.24 + i\ 0.008$.

Defining $\langle T_\parallel \rangle$ and $\langle T_\perp \rangle$ to be the averaged parallel and perpendicular temperature, respectively, for the distribution given by Eqs. G.1 and G.2, our model distribution shown in Fig. G-2 has $\langle T_\parallel \rangle / \langle T_\perp \rangle = 0.32$. We vary $T_\parallel$ of all components, keeping ratios of $T_\parallel$ between all five components constant.

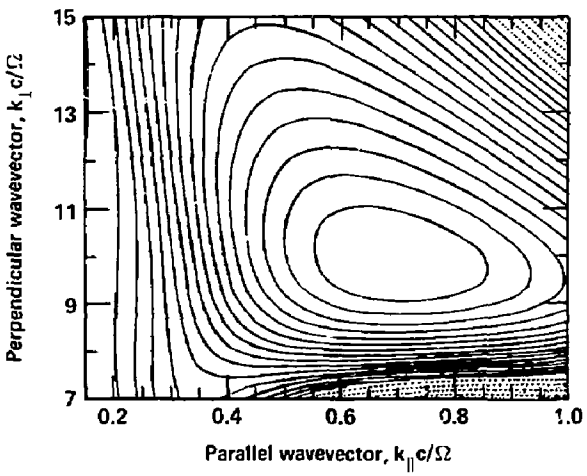

Fig. G-3. Temporal growth rate of the upper-hybrid loss-cone instability for the electron distribution shown in Fig. G-2. Solid contours give Im $\omega \geq 0$, dotted contours give Im $\omega < 0$. The interval between adjacent contours is 4.0×10^{-4} Ω.

We find that increasing $\langle T_{\parallel}\rangle/\langle T_{\perp}\rangle$ stabilizes the whistler mode, but destabilizes the upper-hybrid loss-cone mode as shown in Fig. G-4. The maximum growth rates of both modes are less than 0.008 Ω when $\langle T_{\parallel}\rangle/\langle T_{\perp}\rangle \gtrsim 0.5$. Doubling the $\langle T_{\parallel}\rangle/\langle T_{\perp}\rangle$ to 0.64 shifts the maximum growth rates to $k_{\parallel}c/\Omega = 0.9$ for the whistler mode, where $\omega/\Omega = 0.32 + i\ 0.004$, and $k_{\perp}c/\Omega = 9.25$ and $k_{\parallel}/k_{\perp} = 0.056$ for the upper-hybrid loss-cone mode, where $\omega/\Omega = 1.16 + i\ 0.008$.

Figure G-5 shows curves of constant temporal growth rates in the $\langle T_{\parallel}\rangle/\langle T_{\perp}\rangle$ versus ω_{ptot}^2/Ω^2 plane, maximized over the $\underline{k}$ plane, for the whistler and the upper-hybrid loss-cone instabilities. $\omega_{ptot}^2 = \sum_s \omega_{ps}^2$ is proportional to the total electron density. In the $\langle T_{\parallel}\rangle/\langle T_{\perp}\rangle$ versus ω_{ptot}^2/Ω^2 plane, the value of $T_{\parallel}$ and ω_p^2 for each component is varied, such that the ratios of $T_{\parallel}$ and of ω_p^2 between all five components remain constant. The maximum growth rates of both modes are less than 0.004 Ω, if we require that $\langle T_{\parallel}\rangle/\langle T_{\perp}\rangle \gtrsim 0.4$ and $\omega_{ptot}^2/\Omega^2 \lesssim 0.55$. Along the growth rate $\gamma_{max}/\Omega = 0.004$ curves, the convective growth length of the whistler mode varies from 20 cm to 8 cm, and that of the upper-hybrid loss-cone mode varies from 3.6 cm to 1.3 cm, when ω_{ptot}^2/Ω^2 increases from 0.55 to 3.05 and B = 1 tesla.

Figure G-6 shows the boundary between conditions for absolute and convective whistler instability when the ratios of $T_{\parallel}$ and ω_p^2 between all five components remain constant. Since increasing ω_{ptot}^2/Ω^2 increases the required temperature anisotropy $\langle T_{\parallel}\rangle/\langle T_{\perp}\rangle$ for convective instability, increasing the total electron density has a destabilizing effect.

4. SUMMARY

Our work to date has found two instabilities, the whistler and upper-hybrid loss-cone modes, in a plasma with an electron distribution function similar to that produced by electron-cyclotron-resonance heating. In the hope of preventing deleterious effects in future experiments, we continue to study these instabilities, both in the uniform-plasma approximation discussed here and with effects of spatial nonuniformity.

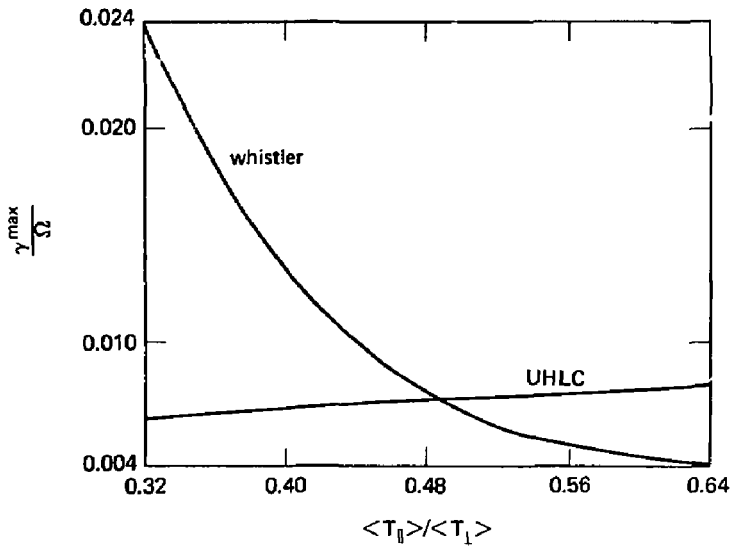

Fig. G-4. Growth rates, maximized over $\underline{k}$, of the whistler and upper-hybrid loss-cone (UHLC) instabilities as a function of the temperature anisotropy $<T_{\parallel}>/<T_{\perp}>$.

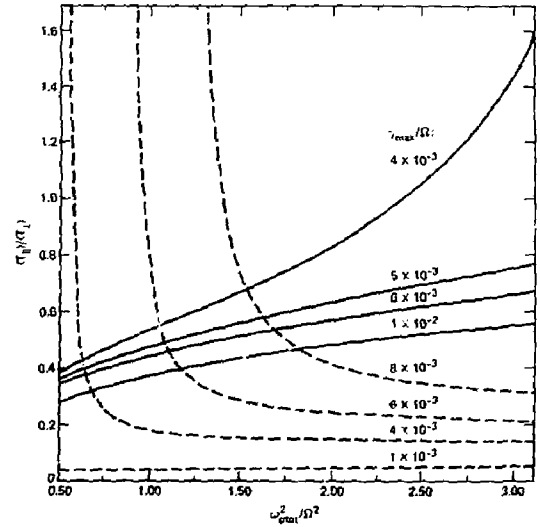

Fig. G-5. Constant-growth-rate curves for the whistler and UHLC modes. The temperature anisotropy, $\langle T_{\parallel} \rangle / \langle T_{\perp} \rangle$, is shown as a function of total electron density, ω_{ptot}^2/Ω^2. Growth rates are maximized over the $\underline{k}$ plane. Solid curves are for the whistler mode; dashed curves for the upper hybrid loss-cone (UHLC) mode.

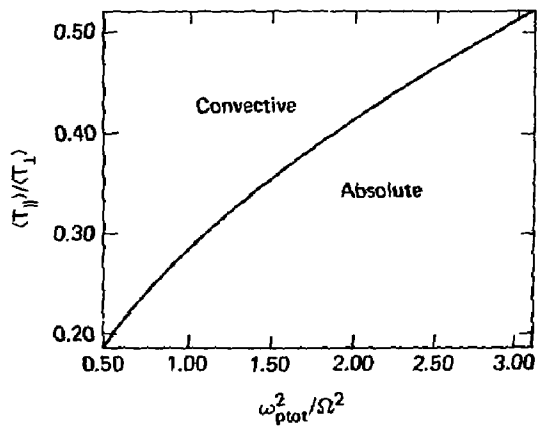

Fig. G-6. Convective-absolute instability boundary for whistler mode.

REFERENCES

G-1. G. E. Guest and D. J. Sigmar, Nucl. Fusion 11, 151 (1971).

G-2. J. Jacquinot and C. Leloup, Phys. Fluids 14, 2440 (1971).

G-3. N. T. Gladd, et al., "Microstability of the EBT Boundary," Sec. IV, in Proc. Workshop on EBT Stability Theory, N. A. Uckan, Ed., Oak Ridge, TN, May 1981.

G-4. N. T. Gladd, "The Whistler Instability at Relativistic Energies," in Proc. 2nd EBT Ring Physics Workshop, N. A. Uckan, Ed., San Diego, CA, Dec. 1981.

G-5. M. Ashour-Abdalla and C. F. Kennel, J. Geophys. Res. 83, 1531 (1978).

G-6. Y. Matsuda, W. M. Nevins, and R. H. Cohen, "Electron-Cyclotron Resonant Heated Electron Distribution Functions," in Proc. Workshop on EBT Stability Theory, N. A. Uckan, Ed., Oak Ridge, TN, May 1981.

G-7. B. W. Stallard, Y. Matsuda, and W. M. Nevins, "Fokker-Planck Calculations of Electron Cyclotron Resonant Heating (ECRH) in Mirror Geometry," in Proc. 2nd EBT Ring Physics Workshop, N. A. Uckan, Ed., San Diego, CA, Dec. 1981.

G-8. J. E. Scharer, Phys. Fluids 10, 652 (1967).

G-9. J. D. Callen and G. E. Guest, Nucl. Fusion 13, 87 (1973).

APPENDIX H

RADIAL TRANSPORT

R. H. Cohen and J. M. Gilmore

We assess here the importance of various mechanisms for transport of ions and ion energy in the solenoid of the proposed MFTF-B Axicell configuration. The transport mechanisms considered are resonant transport and classical diffusion, both resulting from charged-particle encounters and ion-neutral encounters. The principle conclusions are:

- The axicell reduces resonant transport by a factor of order $R^{-1} \exp(-\Delta\phi_{pi}/T)$ compared to a configuration with the same geodesic-curvature profile but without the axicell between the yin-yang cell and the solenoid. (Here R is the ratio of the minimum field strength on-axis in the axisymmetric region to the mid-solenoid value.) However, the simplest axicell magnet designs tend to have large geodesic curvature in the transition region, producing unacceptably large transport. We anticipate the final design for MFTF-B will result in a radial loss rate less than the axial loss rate.
- The classical charged-particle energy diffusion rate is about a third of the axial loss rate.
- Ion-neutral transport is a rather weak ($n\tau \gtrsim 1.5 \times 10^{14}$ cm^{3}s^{-1}) effect in the plasma but is much larger in the halo.

1. RESONANT TRANSPORT

As of this writing, the magnetic-field design for MFTF-B has not been finalized. The issue delaying this process, namely the lack of a satisfactory equilibrium, is closely related to resonant transport, as both the parallel current and the radial drift per bounce are proportional to a line integral $\int ds\, \partial\Omega$ of the geodesic curvature. We have analyzed a preliminary field design and found that the solenoid ions passing into the transition and yin-yang cells satisfy the criterion for intrinsically stochastic transport, thereby implying unacceptably high radial-transport rates. However, a drop in $\int ds\, \partial\Omega$ by a factor of order five would cause the transport to change from stochastic to banana transport and would be accompanied by a precipitous drop in the diffusion coefficient. Reduction of $\int ds\, \partial\Omega$ by at least such a factor

is deemed necessary for a good equilibrium. We estimated the banana-diffusion coefficients for the preliminary design to be two orders of magnitude smaller than the stochastic diffusion coefficients, implying a radial lifetime of the order of the axial lifetime.

The axicell configuration proposed for MFTF-B has a potentially strong advantage over the A-cell magnetic configuration vis-a-vis resonant transport. The axicell mirrors and potential hill confine most of the solenoid ions to a purely axisymmetric region, so that, in a bounce time, only a fraction of order $R^{-1} \exp(-\Delta\phi_{pi}/T)$ of the ions experience the quadrupole field, implying a scaling of the diffusion coefficient by the same factor. The scaling with $\Delta\phi_{pi}$, the size of the potential hill in the axicell, is only very crudely given by the exponential factor, as will be explained later.

If we approximate the radial drift per bounce $\Delta r \equiv a \cos 2\beta$ as independent of pitch angle over the range of pitch angles for which particles pass into the nonaxisymmetric region, then in the stochastic limit (large electric field, azimuthal drift per bounce $\Delta\beta > r/a$), we can calculate the scaling with R. The stochastic particle-diffusion coefficient is[H-1]

$$D_0 = \frac{\pi B}{r L_s m^2 n} \int d\varepsilon \, d\mu \, a^2 f \quad . \tag{H.1}$$

Taking f to be Maxwellian and independent of $v_{\parallel}/v$ over the range $(1 - R^{-1})^{1/2} < v_{\parallel}/v < 1$, we find $D_0 \propto 1 - (1 - R^{-1})^{1/2}$ which is proportional to R^{-1} for large R. For more moderate electric fields, the diffusion coefficient depends on the velocity space location of individual resonances, as well as the collisionality regime (banana/plateau); the scaling remains O(1/R), although a precise general scaling cannot be written.

Calculation of resonant transport in the axicell configuration is simpler than in previous configurations, because solenoid ions which pass into the non-symmetric region all have $v_{\parallel}/v = 1$ at the midplane of the solenoid, and all reflect off of the potential hill in the yin-yang cell. Thus, the general expression for the change of flux coordinate α in a bounce,

$$\Delta\alpha = 2 \frac{mc}{e} \int_0^{s_t} ds \, (v_{\parallel} + v_{\perp}^2/2v_{\parallel}) \Omega \; ; \tag{H.2}$$

where κ is the geodesic curvature, s = 0 denotes the solenoid midplane, and s_t denotes the turning point; becomes

$$\Delta\alpha \approx \begin{cases} \dfrac{2mcv_t}{e}\displaystyle\int_0^{s_\phi} ds\kappa\,, & (v_{\parallel}/v_s) > (1 - 1/R)^{1/2}\,,\ \tfrac{1}{2}mv_s^2 > \Delta\phi_{pi} \\ 0 & \text{elsewhere} \end{cases} \tag{H.3}$$

where now s_ϕ denotes a point part way up the side of the potential hill in the yin-yang cell. In Eq. H.3 and henceforth, a subscript t denotes evaluation of a quantity in the transition region, whereas a subscript s denotes a solenoid value.

Equations H.2 and H.3 are usually evaluated along a field line, a procedure that is only accurate as long as the azimuthal drift $\Delta\beta_e$ during the time an ion spends in the transition and yin-yang regions is negligible. In the opposite limit $\Delta\beta_e \gg 1$, $\Delta\alpha$ should become exponentially small, in $\Delta\alpha \propto -\Delta\beta_e$. Following in the spirit of Ref. H-3, we assume Eq. H.2 is valid for $\omega_{\beta t} L_e/v_{\parallel} < 1$, where ω_β is the azimuthal drift frequency, and take

$$\Delta\alpha = 0 \quad , \qquad \omega_{\beta t} L_e/v_{\parallel} > 1 \quad . \tag{H.4}$$

Here L_e is an effective length for the transition region; a plot of vs s for the preliminary MFTF-B design indicates that most of the contribution to $\int ds$ comes from a narrow spike about 2 m in length in the transition region; hence we take L_e = 2 m in the numerical calculations described below.

The integral in Eq. H.3 is available as output in the TEBASCO equilibrium code; hence we can estimate $\Delta\alpha$ without numerically calculating drift orbits. (Furthermore, use of Eqs. H.3 and H.4 with $\omega_\beta = \omega_{ExB}$ and approximating the bounce time by $t_{\parallel} = L/v_{\parallel}$ when L is the distance between yin-yang centers, allows the integrals in the resonant-banana, resonant-plateau and stochastic diffusion coefficients[H-1,H-2] to be evaluated analytically. These results will be described in a separate communication.)

The criterion[H-1] for stochastic transport can be approximately written as $K \approx 2\,a\Delta\beta/r > 1$; here, $\Delta\beta$ is the azimuthal drift in a bounce. Approximating $\Delta\beta$ by $\underline{E}x\underline{B}$ drift alone, this becomes

$$E > \frac{T_i}{er}\frac{r^3}{\rho L\, a}. \tag{H.5}$$

From Eq. H.3 and TEBASCO output for the vacuum field of case EGZ24 (generated by the EFFI code), we find $\int ds/B$ = 24 cm at r = 21 cm, implying that with energy of 45 keV in the transition region (15 keV in the central cell), a/r = 0.47 for ions. Then, for the reference MFTF-B parameters of Table 2.1-1 (MARS mode), we find stochasticity for E > 70 V/cm. For E ~ T_e/er, the design studied satisfies H.5 by about a factor of five. Integration of Eq. H.1 using Eqs. H.3 and H.4 gives

$$D_0 = \frac{a^2}{4\pi^{1/2} LR} \left(\frac{2T}{m}\right)^{1/2} \exp(-\Delta\phi_{pi}/T)\, G(x_0, x_1) \quad ,$$

where $x_0 = (eEr/T)^2 (2L_e \rho/\pi r)^2$, $x_1 = \Delta\phi_{pi}/T$, and

$$G = \begin{cases} x_1^2 + 2x_1 + 2 + \Phi (x_1 + 1) & x_1 - x_0 > x_1/R \\ (x_1 - x_0)(x_1 - 2) + 2 + \Phi (x_1 - x + 1) - g + h, & 0_1 < x_0 - x_1 < x/R \\ \exp (x_1 - x_0)[2 + \Phi + h] - g & x_0 > x_1 \end{cases} .$$

Here, $x_L = x_0 (1-R^{-1})^{-1}$, $\Phi \equiv T^{-1} \times$ (potential difference between solenoid and transition region),

$$g = \exp (x_1 - x_2)[(x_2 - x_0)(x_2 - 2) + 2 + \Phi (x_2 - x_0 + 1)] \quad ,$$

and $h = R^{-1} (x_2^2 + 2x_2 + 2)$. For MFTF-B parameters this gives $D_0 \approx 5.5 \times 10^{-4}$ cm^2 s^{-1} and a corresponding lifetime of order 10^{-2} s. This time is shorter than the classical time to scatter into the loss cone, τ_{ii} lnR. Thus the transport would act to produce a loss-cone distribution.

The above estimates for the diffusion rate can be considered as an upper bound. Additional effects could reduce the diffusion rate, at least mildly, in the design studied and perhaps drastically in the final design.

For example, the above estimate is obtained by neglecting the azimuthal drift in the transition region until it is large enough to rotate particles by order $\pi/2$ in a single transit through the spike in the geodesic curvature. However, before that limit is reached, the azimuthal drift will be large enough to cause particles to drift by order $\pi/2$ between their pre- and post-bounce passages through the spike in B. The radial displacements accompanying these successive passages no longer add in phase, as previously

assumed. At least, the successive phases will be effectively random, reducing the (stochastic) transport by about a factor of two. Also, for a (perhaps uninteresting) range of parameters, the orderly variation of the phase change with radius can lead, as in Ref. H-7, to regions of stochasticity separated by annular nonstochastic bands. The radial lifetime would then be approximately determined by the time to diffuse (under the influence of collisions) across the nonstochastic bands.

A more important effect is that reduction of $\int ds|\Omega|$ by a factor of order five causes the transport to become resonant rather than stochastic; such a reduction is required for production of a satisfactory equilibrium. Because the collisionality in MFTF-B is such that resonant transport is in the banana regime, the transition to nonstochastic dynamics can produce an order-of-magnitude change of two in the transport rate, as the following example shows. The precise reduction in $\int ds|\Omega|$ required is uncertain, as Eq. H.3 is only an estimate of the stochasticity criterion: the stochasticity parameter K is actually $K = 2a\partial\Delta\beta/\partial r$ and so depends on second derivatives of the potential and magnetic field; and the stochasticity boundary for an arbitrary dynamical map is only approximately K = 1. (It is clear, however, that particles with $a/r \sim 1/2$, as in the studied design, are stochastic). The stochasticity boundary will be studied in more detail numerically.

To illustrate the difference between stochastic and nonstochastic diffusion rates, we evaluate the nonstochastic resonant transport for the preliminary design. In Fig. H-1, we plot numerical values for the resonant diffusion coefficients D_0, D_1, and D_2 and the lifetime estimate τ_2, as defined by Eqs. H.1, H.2, and H.9 of Ref. H-4. The diffusion coefficients are obtained by numerical integration of the smaller of the banana and plateau integrands, as described in Ref. H-5. The acceleration and change in ω_β that is due to the axial variation of the ambipolar potential is neglected. We use Eqs. H.3 and H.4, with both ∇B and ExB contributions to ω_β. For all data shown, the collisionality regime is banana. The electric fields E_1 and E_2 in Fig. H-1 correspond to T_e/r and ϕ_c/r, respectively. We see that, except for the narrow spike around E = 200 V/cm, the lifetime τ_2 is always greater than about 1 s, corresponding to $n\tau > 5 \times 10^{13}$ cm^{-3} s^{-1}, or about the same order as the axial lifetime. Changing $\int ds|\Omega|$ by a factor α will change the banana lifetime by about $\alpha^{-1/2}$. Note that the marked difference between

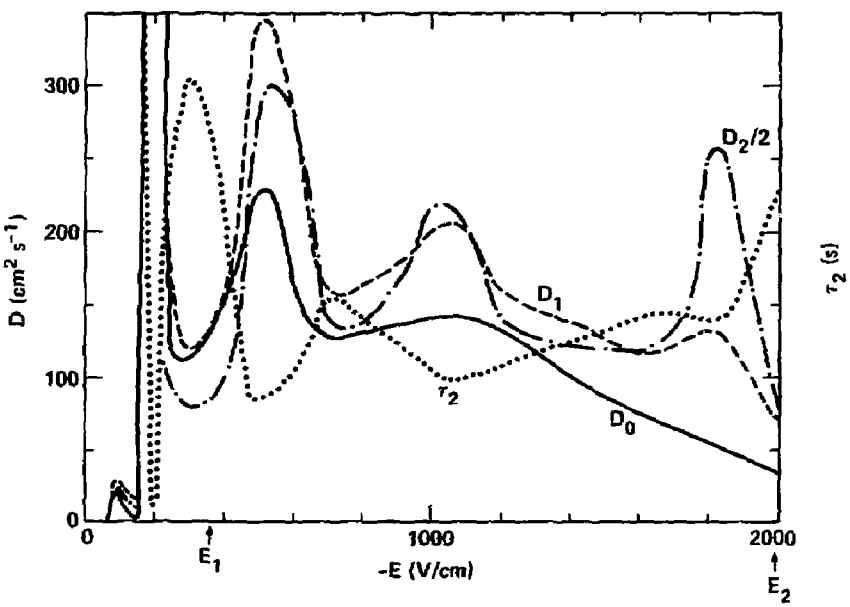

Fig. H-1. Resonant diffusion coefficients (D_0, D_1, and D_2) and lifetime estimate (τ_2) for MFTF-B preliminary design, all shown as a function of electric field.

stochastic and resonant lifetimes is due to the low collisionality in MFTF-B. The resonant-plateau and stochastic lifetimes are comparable.

The route being pursued to minimize $\int ds\,\mathcal{D}$ is to add extra coils, which have the effect of producing two spikes of oppositely signed $\mathcal{D}$ in the transition region. One can, in fact, thus achieve $\int ds\,\mathcal{D} = 0$ along a field line. However, $\int ds\, v\mathcal{D}$ evaluated along a particle orbit will in general not vanish, because of both the azimuthal drift $\Delta\beta_{cr}$ in a single pass through the transition region and the variation in velocity v from the axial variation of the electrostatic potential. Defining I_1 to be the integral of $\mathcal{D}$ over one of the spikes, and $\Delta\phi$ to be the axial change in potential over the region of the spikes, the effective noncancellation of $\int ds\,\mathcal{D}$ because of the azimuthal drift and the axial potential variation are, respectively, of order $2\Delta\beta_{tr}\, I_1$ and $(\Delta\phi/2T)\, I_1$. To ensure nonstochastic dynamics, we must keep these quantities below about 5 cm $\times$ $(r/21\ \text{cm})^2$ (i.e., one-fifth of the value of $\int ds\,\mathcal{D}$ in the preliminary design).

The effect of the potential hill in the axicell on resonant transport can be appreciably larger or smaller than $\exp(-\Delta\phi_{pi}/T)$, depending on the electric field. Because of the large mirror ratio, the principle effect of the potential is to cut off the resonance sum at a resonance number $k = k_\phi$ [azimuthal drift per bounce $\equiv (2k + 1)\,\pi/2$] such that, for $k > k_\phi$, all resonant particles are reflected by either the magnetic field or by the potential. Neglecting ∇B drifts, one has $2k_\phi + 1 = (E/E_*)(T/\Delta\phi_{pi})^{1/2}$, when E_* is the electric field for which a thermal particle drifts $\pi/2$ per bounce. The resonance sum is also cut off when the azimuthal drift in the transition region becomes too large (at a k that is independent of E). Thus, for large enough E, the cutoff due to $\Delta\phi$ becomes irrelevant, while for $E/E_* < (\Delta\phi_{pi}/T)^{1/2}$, resonant transport is effectively eliminated.

For the R^{-1} scaling and Eq. H.3 to apply, the radial transport of ions magnetically trapped in the solenoid-plus-axicell region must be small compared to that of ions passing to the yin-yang cell. This in turn requires that $\int ds\,\mathcal{D}$ in the solenoid-plus-axicell region be small compared to $h(R)$ times $\int ds\,\mathcal{D}$ in the transition-plus-anchor region. Here, $h(R)$ equals R^{-2} in the banana regime and equals $R^{-1/2}$ in the plateau and stochastic regimes. The inequality for banana transport, which is the more severe one, is satisfied for the design studied.

2. CLASSICAL CHARGED-PARTICLE TRANSPORT

The classical ion-heat flux Q is predominately due to ion-ion scattering, $Q \equiv -(2nT/m_i\Omega_i^2\,\tau_{ci})\,\nabla T_i$, where τ_{ci} is the ion-ion collision time. Taking $n/n_0 = T/T_0 = 1 - r^2/r_c^2$, where n_0 and T_0 denote on-axis values and r_c is the central-cell plasma radius, and defining the radial energy lifetime τ_e by the relation $n_0T_0/\tau_e = -\nabla \cdot Q$, we find $\tau_E = r_c^2\,\tau_{ci}/4\,\rho_i^2$, where $\rho_i^2 \equiv 2T_i/m_i\Omega_i^2$. For the MFTF-B parameters of Table H-3, this gives $\tau_E = 25\,\tau_{ci}$. This is to be compared to the lifetime for axial-energy loss, $\tau_{Ea} = (1 + \phi_i/T_{ic})^{-1}\,\tau_p$, where τ_p is the Pastukhov (particle) lifetime; for MFTF-B, one has $\tau_{Ea} \sim 8\,\tau_{ci}$.

For MFTF-B parameters, the classical ion-particle flux is driven, approximately equally by ion-electron and ion-ion [$O(\rho^4/r_c^4)$ terms in flux] scattering; the lifetime is of order $10^4\,\tau_{ci}$ and is, thus, of little concern.

3. ION-NEUTRAL TRANSPORT

The flux of particles arising from ion-neutral collisions, Γ_{in}, can be written as:

$$-\Gamma_{in} = D_{0n}\left(\frac{\partial n}{\partial r} + \frac{ne}{T}\frac{\partial \phi}{\partial r}\right) + D_{1n}\frac{n}{T}\frac{\partial T}{\partial r} \quad ;$$

where $D_{0n} = \rho_i^2\,\nu(1 + \nu^2/\Omega_i^2)^{-1}$, and we estimate $D_{1n} = D_{0n}$. We note

$$\nu^2/\omega_{ii}^2 \ll 1 \quad \text{and} \quad \nu = n_n^{FC}\,\sigma_{in}\,\overline{v_{rel}}\,, \quad \overline{v_{rel}} = v_{ion}\,, \quad \sigma_{in} = 2\,\sigma_{cx}\,.$$

We assume that the density of molecular deuterium neutrals at the plasma edge (r = 40 cm) is $n_n = 2 \times 10^{10}$ cm^{-3}. This implies a Franck-Condon neutral density, n_n^{FC}, of 2.4×10^7 cm^{-3} at r = 20 cm, assuming[H-8] an attenuation of the Franck-Condons through the halo of two orders of magnitude. Adopting parabolic models for the radial density, temperature, and potential profiles gives a flux $\Gamma_{in} = 4.6 \times 10^{13}$ cm$^{-2}\cdot$s^{-1}, corresponding to $n\tau_{in} = 1.45 \times 10^{14}$ cm$^{-3}\cdot$s; the flux further in is smaller yet. On the other hand, in the halo, $\Gamma_{in} = 1.4 \times 10^{13}$ cm$^{-2}\cdot$s^{-1} corresponding to $n\tau_{in} = 7 \times 10^{12}$ cm$^{-3}\cdot$s.

4. CONCLUSIONS

Stochastic transport would seriously limit the operation of the preliminary design studied. However, reduction of the line-averaged geodesic curvature by a factor of about five should be sufficient to change the transport regime to resonant banana; the resultant radial $n\tau$ would be about 10^{14} cm^{-3}•s, which is of the same order as the axial $n\tau$.*

Ion-neutral particle transport and ion-ion energy transport have $n\tau$ values of the order of, but smaller than, the corresponding axial $n\tau$ values; thus these processes will quantitatively affect profile shapes but not qualitatively alter the machine performance.

---

*Note added in proof: The constraints on azimuthal drift in the transition region mentioned at the top of page 213 have proved to be serious. For the current (as of 7/30/82) design it appears necessary to externally control the radial potential profile in the transition region in order to avoid stochastic transport for the design plasma parameters.

REFERENCES

H-1. R.H. Cohen and G. Rowlands, Phys. Fluids 24, 2295 (1981).

H-2. D.D. Rytutov and G.V. Stupakov, Dok. Akad. Nauk SSSR 240, 1086 (1978) [Sov. Phys. Dokl. 23, 412 (1978)].

H-3. J.R. Myra and P.J. Catto, Phys. Rev. Lett. 48, 620 (1982).

H-4. D. E. Baldwin, B. G. Logan, and T. C. Simonen, Physics Basis for MFTF-B, LLNL, Report UCID-18496, Part 2, (1980), Sec. IV.C.

H-5. J.H. Foote, A.K. Chargin, R.H. Cohen, T.B. Kaiser, C.V. Karmendy, T.C. Simonen, and R.L. Wong, TMX-Upgrade Magnet System--Design Characteristics and Physics Considerations, LLNL, Report UCRL-86677 (1981).

H-6. R.H. Cohen, "Effect of Magnetically Confined Electrons on Potential Formation in Tandem-Mirror Thermal Barriers", Poster Paper to be presented at the 1982 Sherwood Theory Meeting, Santa Fe, NM, April 26-28, 1982.

H-7. R.H. Cohen, "Stochastic Motion of Particles in Mirror Machines", in Intrinsic Stochasticity in Plasmas, G. Laval and D. Gresillon, Eds. (Editions de Physiques, Orsay, France, 1979), p. 181.

H-8. G.D. Porter, LLNL, private communication.

APPENDIX I

BARRIER POTENTIAL MODEL

L. D. Pearlstein and W. M. Nevins

We present here a useful model for calculating the variation in the electron density, ion density, and ambipolar potential along magnetic-field lines in the thermal-barrier cell of a tandem mirror. We derive potential profiles in the barrier, sloshing-ion A-cell and use the analytic distribution function suggested by R. H. Cohen[I-1] for the thermal ions. This distribution, being continuous across the separatrix, is less likely to lead to potential sheaths. For the thermal electrons, we use an analytic distribution that is again continuous across the separatrix. The general configuration and notation is depicted in Fig. I-1. In what follows, we only consider the region between B_M and ϕ_c.

We first consider the thermal electrons in the well region (between B_0 and B_c) whose phase space is carved up as shown in Fig. I-2 (note $\phi = |e|\phi$).

To model the hot trapped electrons and the warm passing electrons, we approximate the electron distribution as follows:

$$f = \frac{1}{\sqrt{\pi}} \exp\left(-\varepsilon - \phi_0\right) \quad , \quad \varepsilon > -\phi_0 \quad ; \tag{I.1}$$

and

$$f = \frac{1}{\sqrt{\pi}} \exp\left(-\varepsilon\tau - \phi_0\tau\right) \quad , \quad \varepsilon < -\phi_0 \quad ; \tag{I.2}$$

where

$$\tau = T_{warm}/T_{hot} \quad . \tag{I.3}$$

Thus, for ease of analysis, we assume that the temperatures of passing and weakly trapped electrons are the same. Also, for the same reason, we assume the more deeply trapped electrons and the more deeply trapped Yushmanov electrons have the same temperature.

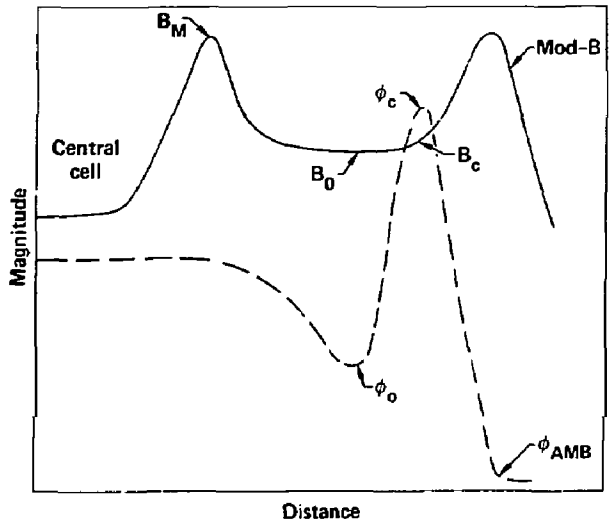

Fig. I-1. Magnetic-field strength (solid line) and ambipolar potential (dashed line) for a typical thermal-barrier cell in a tandem mirror.

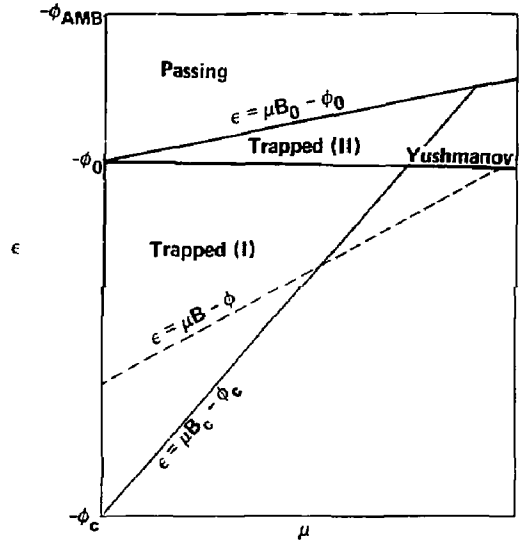

Fig. I-2. Thermal-electron phase space. Electrons in the regions labeled Trapped (I) and Trapped (II) are confined by the potential peak about ϕ_c. Electrons in the shaded region (Yushmanov electrons) are confined by a combination of magnetic forces and the ambipolar electric field.

The thermal electron density is then

$$n_p = \frac{1}{\sqrt{\pi}} \int_{-\phi_0}^{-\phi_{AMB}} d\varepsilon \exp(-\varepsilon - \phi_0) \int_0^{\varepsilon+\phi} \frac{d\mu B}{\sqrt{\varepsilon - \mu B + \phi}}$$

$$= \frac{2}{\sqrt{\pi}} \left[(\phi - \phi_0)^{1/2} - \exp(\phi_{AMB} - \phi_0) (\phi - \phi_{AMB})^{1/2} \right]$$

$$+ \overline{\text{erfc}} (\phi - \phi_0) - \exp(\phi_{AMB} - \phi_0) \overline{\text{erfc}} (\phi - \phi_{AMB}) \quad . \quad (I.4)$$

and

$$n_t = \frac{1}{\sqrt{\pi}} \int_{-\phi}^{-\phi_0} d\varepsilon \exp[-\tau(\varepsilon + \phi_0)] \int_0^{\varepsilon+\phi} \frac{d\mu B}{\sqrt{\varepsilon - \mu B + \phi}}$$

$$= -\frac{2}{\sqrt{\pi}} \frac{(\phi - \phi_0)^{1/2}}{\tau} + \frac{1}{\tau^{3/2}} \overline{\text{erf}} [(\phi - \phi_0)\tau] \quad (I.5)$$

where we have defined

$$\overline{\text{erf}} (u^2) = \frac{2}{\sqrt{\pi}} \exp(u^2) \int_0^u dt e^{-t^2}$$

$$\overline{\text{erfc}} (u^2) = \frac{2}{\sqrt{\pi}} \exp(u^2) \int_u^\infty dt e^{-t^2} \quad (I.6)$$

Next consider the phase space for the thermal ions (see Fig. I-3). The dashed line is the $v_\parallel = 0$ line for positive potentials and the wavy line is the same for negative potentials. Following R. H. Cohen[I-1] we write the distribution for the passing ions as

$$f_p = e^{-\varepsilon} \quad (I.7)$$

and for the trapped ions as

$$f_T = \exp\left(\frac{\varepsilon - \alpha\mu B_M}{\alpha - 1}\right) \quad , \quad (I.8)$$

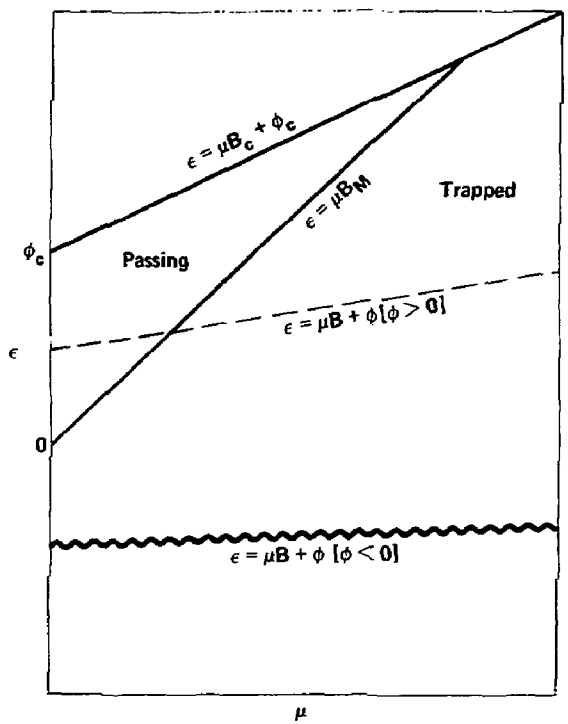

Fig. I-3. Thermal-ion phase space.

which is continuous on the separatrix ($\varepsilon = \mu B_M$). The density of trapped particles increases continuously as α goes from 1 to $+\infty$ and then from $-\infty$ to 0. The limit $\alpha = 1$ corresponds to zero trapped ions, while $\alpha = 0$ corresponds to a completely filled barrier.

We now compute the ion densities for the passing ions. First, for negative potentials we have

$$n_p^- = \frac{1}{\sqrt{\pi}} \int_0^{\phi_p/R} dy \int_{yR}^{\phi_c + yR/R_c} d\varepsilon \exp(-\varepsilon) (\varepsilon - y - \phi)^{1/2} \quad , \qquad (I.9)$$

where here, and in what follows, we have the following definitions:

$$y = \mu B \quad ,$$

$$R = B_M/B \quad ,$$

$$\Psi = \phi \left(\frac{R}{R-1}\right) ,$$

$$\phi_p = \phi_c \frac{R_c}{R_c - 1} \quad ,$$

$$X = \frac{\phi}{\alpha - 1} \quad . \qquad (I.10)$$

Next writing $\varepsilon - y - \phi = x^2$, we have

$$n_p^- = \frac{2}{\sqrt{\pi}} \int_0^{\phi_p/R} dy \exp(-y) \int_{[y(R-1) - \phi]^{1/2}}^{[y(R/R_c - 1) + \phi_c - \phi]^{1/2}} dx \exp(-x^2 - \phi) \, .$$

and integrating by parts on y, we obtain

$$n_p^- = \overline{\text{erfc}}(-\phi) - \overline{\text{erfc}}(\phi_c - \phi) e^{-\phi_c}$$

$$- \left(\frac{R-1}{R}\right)^{1/2} \left[\overline{\text{erfc}}(-\psi) - e^{-\phi_p} \overline{\text{erfc}}(\phi_p - \psi)\right]$$

$$+ \frac{1}{\sqrt{\pi}} \left(1 - \frac{R_c}{R}\right)^{1/2} \int_0^{\phi_p/R_c} dt \, e^{-t} \frac{1}{\left[t + \frac{R}{R - R_c}(\phi_c - \phi)\right]^{1/2}} \quad , \qquad (I.11)$$

which can be written

$$n_p^- = \overline{\text{erfc}}\,(-\phi) - e^{-\phi_c}\overline{\text{erfc}}\,(\phi_c - \phi)$$

$$- \left(\frac{R-1}{R}\right)^{1/2}\left[\overline{\text{erfc}}\,(-\psi) - e^{-\phi_p}\,\overline{\text{erfc}}\,(\phi_p - \psi)\right]$$

$$+ \left(1 - \frac{R_c}{R}\right)^{1/2}\left\{e^{-\phi_c}\,\overline{\text{erfc}}\left[\frac{R}{R-R_c}(\phi_c - \phi)\right] - e^{-\phi_p}\,\overline{\text{erfc}}\left(\frac{R-1}{R-R_c}\right)(\phi_p - \psi)\right\} . \tag{I.12}$$

Next for positive potentials, we have

$$n_p^+ = \frac{1}{\sqrt{\pi}}\left[\int_0^{\phi/(R-1)} dy \int_{y+\phi}^{yR/R_c+\phi_c} d\epsilon\, e^{-\epsilon}\,(\epsilon - \phi - y)^{-1/2}\right.$$

$$\left. + \int_{\phi/R-T}^{\phi_p/R} dy \int_{yR}^{\phi_c+yR/R_c} d\epsilon\, e^{-\epsilon}\,(\epsilon - \phi - y)^{-1/2}\right] . \tag{I.13}$$

Consequently, for the passing ions we have

$$n_p = \left(\left(1 - \frac{R_c}{R}\right)^{1/2}\left\{e^{-\phi_c}\,\overline{\text{erfc}}\left[\frac{R}{R-R_c}(\phi_c - \phi)\right] - e^{-\phi_p}\,\overline{\text{erfc}}\left[\frac{R-1}{R-R_c}(\phi_p - \psi)\right]\right\}\right.$$

$$\overline{\text{erf}}\,(\phi_c - \phi) - \left(\frac{R}{R-1}\right)^{1/2} e^{-\phi_p}\,\overline{\text{erf}}\,(\phi_p - \psi) \qquad \phi > 0$$

$$+$$

$$\left.\overline{\text{erfc}}(-\phi) - e^{-\phi_c}\overline{\text{erfc}}(\phi_c - \phi) - \left(\frac{R-1}{R}\right)^{1/2}\left[\overline{\text{erfc}}\,(-\psi) - e^{-\phi_p}\overline{\text{erfc}}(\phi_p - \psi)\right]\right) \phi < 0. \tag{I.14}$$

Next turn to the trapped plasma. Consider $\phi > 0$, then we have

$$n^+_{tr} = \frac{1}{\sqrt{\pi}} \int_{\phi/R-1}^{\phi_p/R} dy \exp\,(-\alpha yR/\alpha - 1) \int_{y+\phi}^{yR} d\epsilon \exp\,(\epsilon/\alpha - 1)\,(\epsilon - \phi - y)^{-1/2}$$

$$+ \frac{1}{\sqrt{\pi}} \int_{\phi_p/R}^{\infty} dy \exp(-\alpha yR/\alpha - 1) \int_{y+\phi}^{yR/R_c+\phi_c} d\epsilon \exp(\epsilon/\alpha - 1)\,(\epsilon - \phi - y)^{1/2}. \tag{I.15}$$

Again transforming the square root away, we obtain

$$n^+_{tr} = \frac{2}{\sqrt{\pi}} \left[\int_{\phi/R-1}^{\phi_p/R} dy \exp\left(-\,y\,\frac{\alpha R - 1}{\alpha - 1} + \frac{\phi}{\alpha - 1}\right) \int_0^{[y(R-1)-\phi]^{1/2}} dx \exp\left(\frac{x^2}{\alpha - 1}\right)\right.$$

$$\left. + \int_{\phi_p/R}^{\infty} dy \exp\left(-\,y\,\frac{\alpha R - 1}{\alpha - 1} + \frac{\phi}{\alpha - 1}\right) \int_0^{[y(R/R_c-1)+\phi_c-\phi]^{1/2}} dx \exp\left(\frac{x^2}{\alpha - 1}\right)\right]. \tag{I.16}$$

Next, integrating by parts, we find that the integrated parts cancel, leaving

$$n^+_{tr} = \frac{\alpha - 1}{\alpha R - 1} \left\{ e^{-\phi_p} \left(\frac{R - 1}{R}\right)^{1/2} (\phi_p - \psi)\right.$$

$$+ \frac{1}{\sqrt{\pi}} \int_{\phi_p/R}^{\infty} dy \exp\left(-\,y\,\frac{\alpha R - 1}{\alpha - 1} + \frac{\phi}{\alpha - 1}\right)\left(1 - \frac{R_c}{R}\right)^{1/2}$$

$$\left. \frac{R}{R_c} \left(\frac{\alpha - 1}{\alpha R_c - 1}\right)^{1/2} \frac{1}{\left(y + \dfrac{\phi_c - \phi}{R/R_c - 1}\right)^{1/2}} \exp\left[\frac{y(R/R_c - 1) + \phi_c - \phi}{\alpha - 1}\right]\right\}.$$

Finally, combining terms and going through the same algebra for $\phi < 0$, we obtain

$$n_{tr} = \left(\frac{\alpha - 1}{\alpha R - 1}\right) \Bigg\{ e^{-\phi_p}(1 - R_c/R)^{1/2} \left(\frac{\alpha - 1}{\alpha R_c - 1}\right)^{1/2} \overline{\text{erfc}} \left[\frac{\alpha R_c - 1}{\alpha - 1} \frac{R - 1}{R - R_c} (\phi_p - \psi)\right]$$

$$\left(\frac{R - 1}{R}\right)^{1/2} e^{-\phi_p} \overline{\text{erf}}\ (\phi_p - \psi) \quad , \qquad \phi > 0$$

$$+ \left(\frac{R - 1}{R}\right)^{1/2} \left[\overline{\text{erfc}}\ (-\psi) - e^{\phi_p} \overline{\text{erfc}}\ (\phi_p - \psi)\right] + 2 \left(\frac{\alpha - 1}{\pi}\right)^{1/2} D(\chi^{1/2}) \Bigg\}, \quad \phi < 0 \tag{I.17}$$

where the Dawson integral is defined by

$$D(x) = e^{-x^2} \int_0^x dt\, e^{t^2} \quad . \tag{I.18}$$

In terms of Z functions, we have

$$\frac{2}{\sqrt{\pi}} D(x) = i\, e^{-x^2} - \frac{1}{\sqrt{\pi}} Z(x) \quad ,$$

$$\text{erfc}(x^2) = - \frac{i}{\sqrt{\pi}} Z(ix) \quad , \tag{I.19}$$

which defines the analytic continuation [e.g., consider $2\,(\alpha - 1/\pi)^{1/2} D(\chi^{1/2})$ for $\alpha < 0$, note $0 < \alpha < 1$ is forbidden],

$$2 \left(\frac{\alpha - 1}{\pi}\right)^{1/2} D(\chi^{1/2}) \rightarrow (1 - \alpha)^{1/2} \overline{\text{erf}}\ (\chi) \quad .$$

In the remainder of this paper we show several representative solutions for the barrier potential and thermal-ion density profile. The sloshing-ion distribution was chosen to satisfy

$$n_{SLOSH} = \left(\frac{1 - 1/R}{1 - 1/R^*}\right)^{3/2} \exp\left[-\left(\frac{R^*}{R} - 1\right)^2 / \Delta^2\right] \exp\left[+\left(\frac{R^*}{R_c} - 1\right)^2 / \Delta^2\right] \tag{I.20}$$

where R^* is chosen to force n_{SLOSH} to peak at R_c and Δ is fixed by the relative sloshing-ion density at the midplane (R_m). For the magnetically trapped ECRH electrons, we choose

$$n_{ECRH} = n_{ECRH}(0)\left(\frac{1 - 1/R}{1 - 1/R_M}\right)^{3/2} , \qquad (I.21)$$

where $n_{ECRH}(0)$ is determined by forcing charge neutrality together with one further condition needed for closure. A convenient choice is the density ratio of thermal electrons to ECRH electrons at the midplane.

A comparison of the two figures shows the following parameters in common:

$$\frac{n_{SLOSH}(0)}{n_{SLOSH}(R^*)} = 0.3 ,$$

$$\frac{n_{th.e}(0)}{n_{ECRH}(0)} = 0.1 ,$$

$$\frac{T_{e,warm}}{T_i} = 1 \text{ (temperature ratio of thermal electrons to thermal ions)} ,$$

$$\frac{T_{e,warm}}{T_{e,hot}} = \tau = 0.2 ,$$

$$\frac{n_{cc}}{n_{SLOSH}(R^*)} = 1 ,$$

$$n_{th.i}(0)/n_{cc} = 0.085 ,$$

$$R_M = 5 ,$$

$$\Phi_{AMB} = 5 .$$

Note that since the separatrix for the thermal electrons is energy dependent $\nu = 3/2$ (R. H. Cohen's notation, Ref. I-1). To mock up a more realistic $\nu = 1/2$, we raise the $T_{e,hot}$ to get a higher plug potential (ϕ_c). In Fig. I-4, we have various profiles for $\alpha = 1.5$, which results in a $g(R_M) = 1.8$ and $n_{th.i}(0)/n_{cc} = 0.085$. In Fig. I-5, we have the same profiles for $\alpha = 3$, which results in a $g(R_M) = 6.5$ and $n_{th.i}(0)/n_{cc} = 2.4$. We use Logan's definition[I-2] of g, namely $g(R) = n_{th.i}(R)/n_{pi}(R)$.

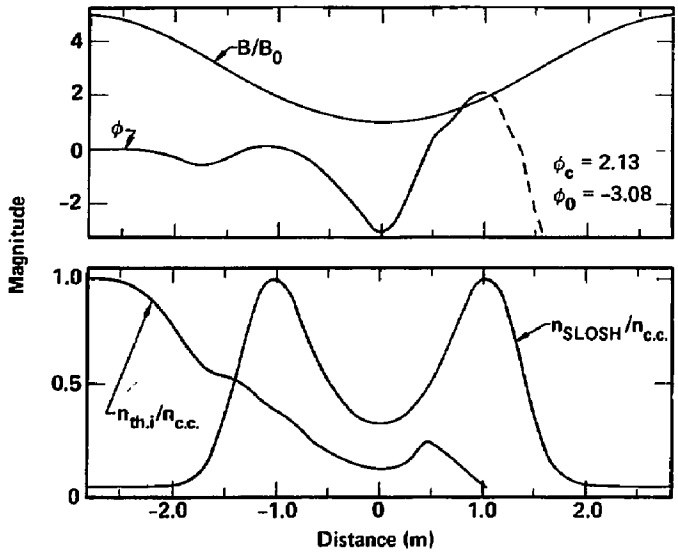

Fig. I-4. Profiles of Mod-B, ambipolar potential ϕ; thermal-ion density $n_{th.i}$; and sloshing-ion density n_{SLOSH} for α = 1.5.

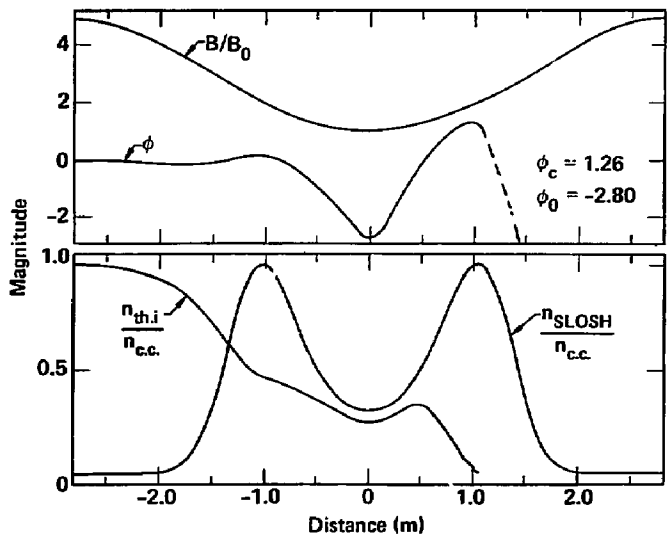

Fig. I-5. The same profiles as in Fig. I-4 but with α = 3.

Note that in this case the barrier potential is roughly symmetric about its minimum. That is, there is no resemblance of a sheath. Using the analytic models for continuous distrbution across separatrices has removed the sheath. It should be emphasized that these are approximate analytic models for equilibrium distribution. Except for extreme cases [too few trapped thermal ions ($\alpha < 1.1$) or too much necking off ($n_{th.e}(0)/n_{ECRH} < 0.025$)], they give rise to continuous potentials and densities and are thus quite useful for obtaining as profiles of n and ϕ for use in composite calculations. Ion microstability is one such case. Using numerical profiles from Fokker-Planck codes would increase computer times by at least an order of magnitude (probably two orders). This is of course the trade off, the potentially inaccurate profiles for computer speed and reliability. In Fig. I-6 we plot various equilibrium quantities as a function of $g(R_M)$.

REFERENCES

I-1. R. H. Cohen, Nuclear Fusion 21, 209 (1981).

I-2. D. E. Baldwin and B. G. Logan, Phys. Rev. Lett. 43, 1318 (1979).

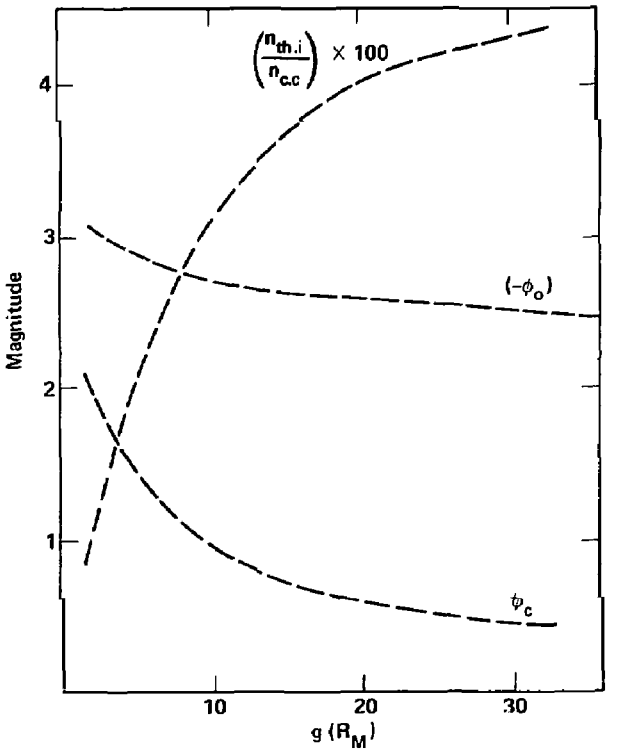

Fig. I-6. Various equilibrium quantities as a function of g(R_M).

DISCLAIMER

Printed in the United States of America
Available from
National Technical Information Service
U.S. Department of Commerce
5285 Port Royal Road
Springfield, VA 22161
Price: Printed Copy $; Microfiche $3.50

Page Range	Domestic Price	Page Range	Domestic Price
001-025	$ 5.00	326-350	$ 18.00
026-050	6.00	351-375	19.00
051-075	7.00	376-400	20.00
076-100	8.00	401-425	21.00
101-125	9.00	426-450	22.00
126-150	10.00	451-475	23.00
151-175	11.00	476-500	24.00
176-200	12.00	501-525	25.00
201-225	13.00	526-550	26.00
226-250	14.00	551-525	27.00
251-275	15.00	526-550	28.00
276-300	16.00	601-up [1]	
301-325	17.00		

[1] Add 2.00 for each additional 25 page increment from 601 pages up.

Technical Information Department · Lawrence Livermore Laboratory
University of California · Livermore, California 94550